CRANFIELD UNIVERSITY

DAVID OSMAN BUSSE

EXTENDING FATIGUE LIFE OF AIRCRAFT FUSELAGE STRUCTURES USING LASER-PEENING

SCHOOL OF AEROSPACE, TRANSPORT AND MANUFACTURING
Materials And Manufacturing

PhD - Doctor of Philosophy
Academic Year: 2017 - 2018

Supervisor: Prof P. Irving and Dr S. Ganguly
October 2017

CRANFIELD UNIVERSITY

SCHOOL OF AEROSPACE, TRANSPORT AND MANUFACTURING
Materials And Manufacturing

PhD

Academic Year 2017 - 2018

DAVID OSMAN BUSSE

EXTENDING FATIGUE LIFE OF AIRCRAFT FUSELAGE STRUCTURES USING LASER-PEENING

Supervisor: Prof P. Irving and Dr S. Ganguly
October 2017

This thesis is submitted in partial fulfilment of the requirements for the degree of PhD - Doctor of Philosophy

Abstract

Fatigue of airframe structures is a constant challenge to aircraft manufacturers when designing, maintaining and repairing new and aging metallic components. Laser-Peening (LP) is a highly flexible and controllable surface treatment and relatively new to manufacturers of large civil aircraft which demonstrated that it can extend the fatigue and crack growth life in aluminium alloys by introducing deep compressive Residual Stresses (RS). Currently there is no application of LP to any components of large civil aircraft. The aim of this research was to demonstrate and explore different LP strategies that can produce significant extension of the fatigue and crack growth performance of aircraft fuselage structures using Laser-Peening.

Two representative samples made from 2000 series aluminium alloy were designed to represent features of the fuselage: A Centre Cracked Tension (CCT) panel made of 1.6 mm thick 2524-T3 represented the fuselage skin. Single overlap Lap-Joints (LJ) of 2.5 mm thick 2024-T3 aluminium with titanium Hi-Lok bolts arrayed in 5 columns and 3 rows embodied longitudinal LJ of aircraft fuselages. Both test samples were laser-peened without protective coating (LPwC) using a range of LP strategies in which LP process parameters and spatial arrangements of laser-peened areas were systematically varied. RS fields were measured before fatigue testing under constant amplitude loading.

RS measurements used Incremental Centre Hole Drilling (ICHD) and X-ray and Neutron diffraction techniques. Laser-peening produced peak compressive RS of 200 – 350 MPa and compression stress penetration depths between 700-1000 µm. These values are superior to RS profiles induced by Shot-Peening. The value of peak compression stress and penetration depth depends on LP process parameters and on the LP layout. The latter defines the location and size of the laser-peened areas.

A study of the effect of different LP strategies to establish the most effective LP treatment to enhance crack growth life of fuselage skins was performed using a Finite Element based crack growth model. The model was first used to introduce balanced RS fields into a cracked CCT sample. The effective stress intensity factor range (ΔKeff) and effective R-ratios (Reff) were then calculated as the crack tip progressed through the sample. Subsequently, fatigue crack growth rates and lives were computed using Walker’s empirical crack growth law. The accuracy of the model was demonstrated by comparison with crack growth test results from laser-peened CCT-samples. Results of the parameter study showed that an increase in the level of compression within the LPS increased life most significantly. Increased width of peen stripe increased the life while increasing the distance of the stripe from the starting position of the crack tip decreased the life.

Four different LP strategies were applied to LJ samples. Subsequent fatigue testing demonstrated fatigue life improvements of between 1.14 to 3.54, depending on the LP strategy.

The LP layout was identified as a key parameter determining the fatigue life. It was found that when small LP areas were used, to leave as much elastic material as possible between the peened areas, larger compressive stresses and minimised balancing tensile stresses were produced. Observations of fatigue fractures on joint samples showed that crack initiation occurred remote from the fastener holes, either in regions of fretting fatigue in peened areas or in regions of balancing tensile stress adjacent to peen boundaries. Optimum fatigue lives occurred when both fracture types occurred in the same sample. Striation spacing measurement and analysis showed that compressive residual stresses had little or no effect on fatigue growth rates at crack lengths > 600 μm. The majority of fatigue life extension was achieved during initiation and crack growth < 600 μm.

The obtained results established evidence of how aircraft fuselage structures made of conventional 2000 series aluminium-copper alloys can be effectively laser-peened to produced fatigue life improvements and also of how to avoid any detrimental reductions in fatigue life which can also occur when LP is applied randomly. The generated research conclusions are applicable to other metals, geometries and components.

Acknowledgements

I would sincerely thank my supervisors from Cranfield University Prof P. Irving and Dr S. Ganguly who always supported and guided me, and without them this thesis would not have been possible. Working at Cranfield University has been inspiring, challenging and productive throughout my time, also because of the many competent people I met here. I thank Barry Walker, Fleming Nielsen, Xianwei Liu and Jim Hurley who supported me in the realms of Cranfield laboratories. Their work is indispensable to PhD students like me.

A very special thanks goes out to Dr Domenico Furfari, my industrial supervisor, who supported me first during my MSc thesis at Airbus Germany and then challenged me to take up a PhD program at Cranfield University. You are the “Don” of Laser-Peening and I sincerely thank you for your trust and confidence that you invested in me.

One of the main pleasures during this PhD project was to work in an industrially guided, cross-university and multinational setting with academic project members from University of Coventry and University of Witwatersrand. I immensely enjoyed working with Prof M. Fitzpatrick, Niall Smyth and of course my PhD colleague Marco Pavan. Thanks for all your support and exchanges which you were always ready to provide. Also, I really appreciate the efforts of Prof C. Polese and her complete Laser-Peening group, especially Dean Van Aswegen, who processed my test samples.

Lastly, I want to thank my mother and my father, their upbringing and encouragement at home have built the fundament for my higher studies. My greatest appreciation I send to my family in Karachi. My many visits to Pakistan have opened my eyes to many realities of this world and in particular to the importance of education and studiousness and therefore changed me forever. As for the lows and the highs, the rain, the thunderstorms and the sunshine of the daily life, I must thank Shireen, my diligent and loving wife, for her continuous support, commitment and love. Life would be pale and dim without you!

List of Conferences

(1) Date: Jun 5, 2017, Title: *“Improving Fatigue Performance of AA 2024-T3 Clad Aeronautical Riveted Lap-Joints Using Laser-Peening”*. at the 35th Conference of International Committee on Aeronautical Fatigue and Structural Integrity (ICAF) 2017 Nagoya, Japan

(2) Date: Nov 2016, Title: *“Fatigue Assessment of AA 2024-T3 Clad Laser-Peened Aeronautical Structural Riveted Lap-Joints”* at the 6th International Conference on Laser Peening and Related Phenomena (6th-ICLPRP) in Johannesburg, South Africa

(3) Date: Oct 20, 2016, Title: *“Extending Fatigue Life of Fuselage Structures using Residual Stress Engineering via Laser Peening”* at the Airbus PhD day in Getafe, Spain

(4) Date: Oct 28, 2015, Title: *“Extending Fatigue Life of Fuselage Structures using Residual Stress Engineering via Laser Peening”* at the Airbus PhD day in Toulouse, France

(5) Date: May 2015, Title: *“Predicting Stress Intensity Factors in Laser-Peened M(T) Samples”* at 5th International Conference on Laser Peening and Related Phenomena (5th-ICLPRP) in Cincinnati, Ohio

Award:

Nov 2016, *"Best Student Contribution to the Field of Laser-Peening"* at the 6th International Conference on Laser Peening and Related Phenomena in Johannesburg, South Africa

Table of Content

Abbreviations

AD	Angle-Dispersive
ALM	Additive Layer Manufacturing
ASTM	American Society for Testing and Materials
BESSY	Berliner Elektronenspeicherring-Gesellschaft für Synchrotronstrahlung
BL	Baseline
BSE	Backscattered Electrons
CAA	Civil Aviation Authority
CCD	Charge-Coupled Device
CCT	Centre Cracked Tension Specimen
CSIR	Council for Scientific and Industrial Research
CT	Compact Tension Specimen
Cx	Cold-Expansion
DEC	Diffraction Elastic Constant
DESY	Deutsche Elektronen-Synchrotron
ED	Energy-Dispersive
EDDI	Energy Dispersive Diffraction
EDM	Electric Discharge Machine
FAA	Federal Aviation Administration
FCGR	Fatigue Crack Growth Rate
FE	Finite Element
FEA	Finite Element Analysis
FEM	Finite Element Method
FSW	Friction Stir Welding
FTI	Fatigue Technology Incorporated
FWHM	Full Width at Half Maximum
GAG	Ground-Air-Ground
ICHD	Incremental Centre Hole Drilling
ILL	Institut Laue-Langevin
LEFM	Linear Elastic Fracture Mechanics
LH	Laser Heating
LJ	Lap-Joint
LP	Laser Peening
LPB	Low Plasticity Burnishing
LPBR	Laser-Peened Boundary Region
LPS	Laser Peening Stripe
LPwC	Laser Peening without Coating

LSP	Laser Shock Peening
MIC	Metal Improvement Company
MIC	Metal Improvement Company
MSD	Multiple Site Damage
NASA	North American Space Agency
Nd: YAG	neodymium-doped yttrium aluminium garnet
OEM	Original Equipment Manufacturer
P-sample	Patch-Sample
RS	Residual Stress
SALSA	Strain Analyser for Large and Small scale engineering Applications
SEM	Scanning Electron Microscope
SERR	Strain Energy Release Rate
SIF	Stress Intensity Factor
SP	Shot Peening
S-sample	Stripe-Sample
UTS	Ultimate Tensile Strength
WFD	Wide-Spread Fatigue Damage
WFM	Weight Function Method
XRD	X-Ray Diffraction
YTS	Yielding Tensile Strength

Nomenclature

$\mu(E)$	linear absorption coefficient	
k	bending factor	
$\mu(E)$	linear absorption coefficient	
a	crack length	[mm]
c	speed of light in vacuum	
d	distance	[mm]
d	spacing between lattices	[Å]
da/dN	Fatigue Crack Growth Rate	[mm/cycle]
E	E-modulus	[MPa]
E	Energy	[keV]
e	Strain	
F	Force	[N]
f	Frequency	[Hz]
G	Strain Energy Release Rate	[J]
h	Planch’s constant	
h,k,l	Miller indices	
I	Intensity	[counts]
K	Stress Intensity Factor	[MPa√m]
k	bending factor	
Kc	Fracture toughness	[MPa√m]
N	Number of cycles	
n	Poisson’s ratio	
p	pitch	[mm]
R	R-ratio	
Rc	Surface roughness	
S	Stress	[MPa]
t	thickness	[mm]
w	width	[mm]
x,y,z	axis coordinates	
θ	reflection angle	[rad/ degrees]
λ	wave length	[Å]
σ	Stress	[MPa]
τ	penetration depth	[μm]
ψ	tilting angle	[rad/ degrees]

Super and Subscripts

0	stress free condition
app	applied
BR	Bearing
c	critical
eff	Effective
FR	Friction
I,II,III	Crack opening modes
LP	Laser-peening
max	maximum
min	minimum
open	opening
res	Residual Stress
RS	Residual Stress
x	Transverse direction
y	Longitudinal direction
z	Thickness direction

List of Figures

List of Tables

1 Introduction

1.1 Background

“An evaluation of the strength, detail design, and fabrication must show that catastrophic failure due to fatigue, corrosion, or accidental damage, will be avoided throughout the operational life of the aeroplane. (...)” CS 25.751 [1]

The above quoted extract of an aviation bill issued by airworthiness and certifying authorities (EASA /FAA) essentially legally demand from any manufacturer of large aeroplane to evaluate and assess the designed airframe in order to prevent any *“catastrophic failure due to fatigue, corrosion or accidental damage”* [1]. This bill also known as certification specification (CS) eventually established the damage-tolerance design philosophy in the aviation industry and became effective in the current complete form in 1978 [2] after years of tragic lessons learnt of how to design against aircraft fatigue [3].

Figure 1-1: Photograph of the Aloha accident aircraft after landing. Front upper fuselage shell is damaged and was lost during flight due to Wide-Spread Fatigue Damage (WFD). (Photograph was taken from [4]**)**

Although it is common practice and even legally required today to design most of aircraft structures according to damage-tolerance principles, the infamous Aloha accident revealed that it does not completely solve the issue of aircraft fatigue. On April 28th in the year 1988 a Boeing 737 operated by Aloha airlines lost part of its upper front fuselage during flight, see Figure 1-1. It was found that so called Multiple Site Damage (MSD) jeopardised the structural integrity of the pressurised fuselage. MSD describes the occurrence of multiple fatigue cracks at different locations which are for themselves small and unproblematic but if coalesced could lead into failure of the structure. In the case of the Aloha incident multiple cracks initiated at the critical rivet row of the longitudinal lap-joint which fastens the upper and lower fuselage skin shells. A detailed analysis of the Aloha accident is given by S. Pitt and R. Jones [5]. Anyhow, since this marking incidence the aviation industry and academia researched the phenomenon of Wide-Spread Fatigue Damage (WFD) which is an overall terms which includes MSD. Especially aircraft fuselage longitudinal lap-joints are of special interest in the research of MSD [6,7] as they are until today recognised as a fatigue critical component of the aircraft fuselage especially in aging fleets.

Today's aircraft fatigue research[1] by the aviation industry or academia addresses not only further improvements of advanced numerical predictive capabilities, fatigue testing techniques or new materials but in addition residual stress engineering has become a vital field of research. Economic and environmental pressures and also the context of global aging aircraft fleets stimulates research to find new technologies to improve the fatigue resistance of fatigue crucial components of aircraft such as the longitudinal lap-joint not only to comply with airworthiness regulation but also to improve the aircraft design. It is well understood that if lap-joints for instance are improved in fatigue resistance there will be overall benefits for aircraft fuselage design in terms of weight, maintenance and overall service life with implication on production and maintenance cost as well as beneficial effect for the environment by reduced emissions. Residual stresses (RS) and effective and controllable techniques to induce them into the designated component are promising to achieve the aim.

1.2 Motivation

Fatigue and damage-tolerance requirements are still one of the main key drivers for the design of large aircraft fuselage structures. Despite the achievement in the development of new aluminium alloys and prediction methodologies to improve and exploit the fatigue performance of modern airframes, extending further the resistance to fatigue cracking of their metallic components in particular, will open up a range of options for airframe manufacturers to offer their customers a more economical and green product. Improved fatigue and damage-tolerance capabilities could be used to either reduce the gross weight or to enlarge maintenance inspection intervals. Both implications provide aircraft operators the desired economic and environmental efficiency of their flight services. Furthermore, the entire aviation industry today faces a major challenge to ensure the continued airworthiness of the ageing global aircraft fleet within the framework of life extension programs. Therefore, the development of appropriate strategies for maintenance and overall aircraft service life extension is evidently necessary.

---

[1] assessed by the selected presentations at the International Conference of Aeronautical Fatigue – ICAF – 2017 Symposium

In recent past years, compressive RSs were suggested as an enabler to increase the fatigue and damage-tolerance properties of metallic aerospace structures. The concept of integrating RSs into the metallic bodies and hence retard fatigue crack initiation and/or crack propagation has been investigated for various different RS techniques [8–27]. Subsequent results demonstrated that compressive RSs have the potential to provide large fatigue and crack growth enhancements. For that reason, methods to induce RS fields into components such as the Cold-Expansion (Cx) technique of fastener holes [8,9,20] or the Shot Peening (SP) [19,28–31] process are already commonly applied by the aerospace industry. Other processes such as Laser-heating (LH) for instance are currently researched by academia [12,17]. However, since all of those RS techniques come along with certain shortcomings and limitations, for example regarding special geometrical features (fastener hole), the maximum quantity of induced RS or maximum penetration depths of compressive RS, industrial stakeholders demand for a more flexible and robust process to induce deep compressive RS fields in a manner which can be smoothly integrated in a large scale manufacturing process or even in the field in the context of Maintenance, Repair and Overhaul (MRO) activities. Therefore, airframe OEMs such as *Airbus* generate stimulus to the research community to explore new techniques which fulfil their cutting-edge requirements. One of the most promising and relatively new processes is Laser-peening (LP) which is a highly flexible process to induce deep compressive RSs by using laser light which provokes a shock wave to travel through the target component. Its superiority over the present industrial standards (Cx and SP) in terms of desired RS profile, flexibility of spatial applicability and controllability can be derived from existing established research data and analogical analyses.

Despite the knowledge about the advantages of LP and the awareness of the vulnerability to fatigue degradation of aircraft fuselage structures, especially the longitudinal lap-joint (LJ), there is currently no application of LP of “flying” large civil aircrafts fuselages. Integrating LP in the design of fatigue susceptible fuselage structures such as the longitudinal LJ and the fuselage skin field has been, therefore, identified as prospective LP applications motivated by the potential beneficial economic and environmental advances.

1.3 Aim and Objectives of Research

Following the above outlined motivation, the presented work aims to demonstrate firstly that LP is an effective approach for fatigue life enhancement of longitudinal Lap-Joints (Fatigue) and to retard fatigue crack growth in typical fuselage skin type specimens (Damage-tolerance). Secondly, this thesis aims to explore and optimise different strategies of LP to maximise the effectiveness of the process.

In this context, the thesis objectives can be broken down to:

(1) Measure experimentally and characterise RSs in laser-peened aircraft fuselage skin type structures and aircraft fuselage longitudinal LJ to develop an understanding of the influence of relevant LP parameters on the resulting RS field.

(2) Establish experimental quantifiable proof that LP can
   a. retard crack growth in aircraft fuselage skin type specimens and
   b. enhance the fatigue life of aircraft fuselage longitudinal LJs.

(3) Develop different LP strategies adopting a generic approach which includes not only LP process parameters but also different spatial definition of laser-peened areas (LP layout) on the targeted structure to explore an optimised LP treatment by
   a. the development of a crack growth modelling approach for laser-peened aircraft fuselage skin type structures to gain insights on which are the main strategic LP factors to influence fatigue crack growth and
   b. by the performance of an extensive experimental fatigue test program and fractographical post-mortem analyses for aircraft fuselage longitudinal LJs to understand the interacting processes between fatigue initiation locations and fatigue lives with the induced RS field.

1.4 Research Approach

As for the different nature of the two different types of structures (aircraft fuselage skin type structure and the aircraft fuselage longitudinal LJs) two individual research approaches were developed.

The aircraft fuselage skin type structure will be represented by a large (400 mm **x** 800 mm) Centre Crack Tension (CCT-) sample made of 1.6 mm 2524-T3 conventional aerospace aluminium alloy. A schematic view of the research approach adopted to investigate fatigue crack growth laser-peened aircraft fuselage skin type structure hence CCT-samples is sketched in Figure 1-2. It consists of blocks of experimental and modelling efforts. The experimental part will

- firstly, characterise fatigue crack growth of un-peened baseline (BL) 2524-T3 CCT-samples using mechanical testing techniques in order to create the benchmark and further to develop own crack growth data to derive crack growth related material constants (Walker model) which are needed as model inputs.
- secondly, measure RS in laser-peened 2524-T3 1.6 mm CCT-sample using non-destructive diffraction techniques to analyse the results of the LP treatment. Obtained RS field will be also be used as model inputs.
- thirdly, characterise fatigue crack growth of laser-peened CCT-samples to produce empirical evidence of the effect of LP. Laser-peened CCT-samples were also needed to validate modelling results.

Analyses of different strategies of LP and their effects on crack growth in large aluminium panels are performed by modelling efforts which is built together by the following steps:

- development of numerical Finite Element Analyses (FEA) crack model to compute Stress Intensity Factors (SIFs) in RS fields with validation of the SIF model by analytical solution (BL).
- performance of crack growth prediction using the numerically determined SIF results and experimentally derived material constants.
- analyses of a LP parameters study using the modelling approach to explore an optimised LP treatment of CCT-samples.

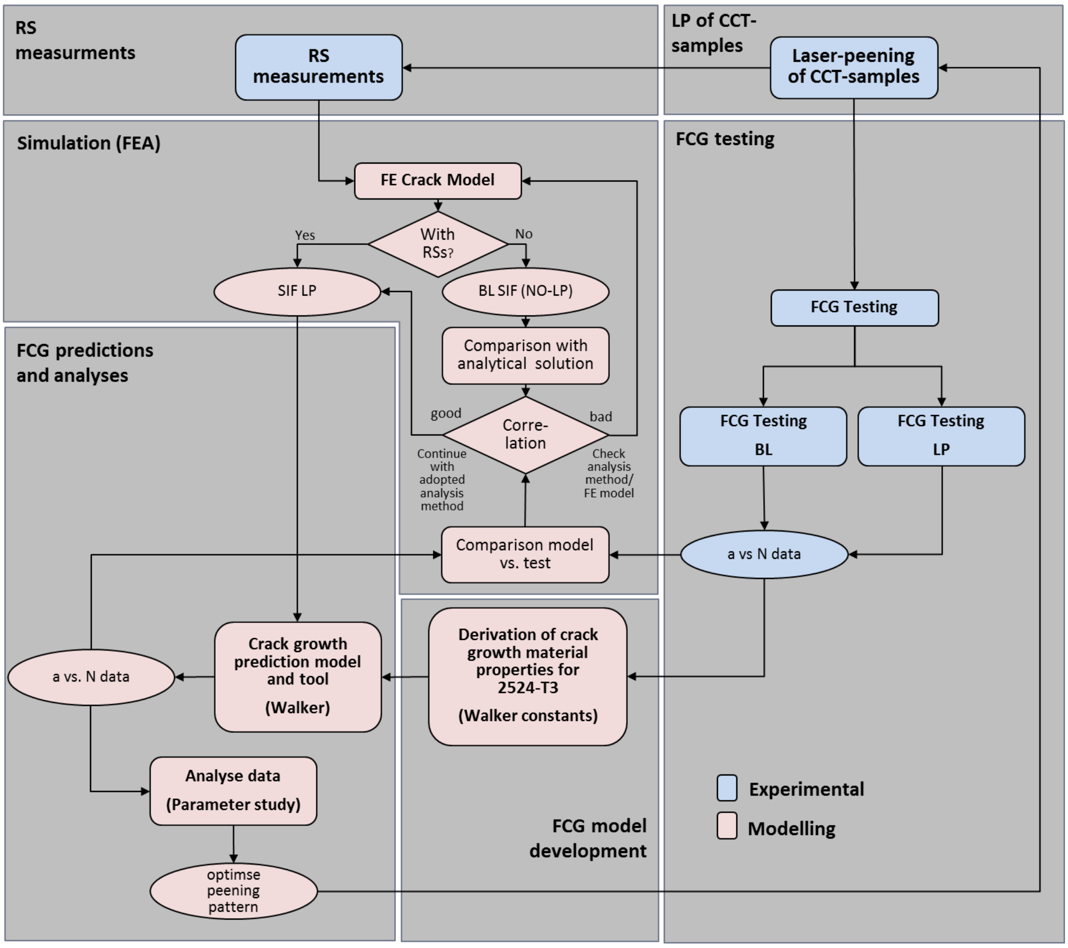

Figure 1-2: Schematic view of approach for aircraft fuselage skin type structure (CCT-samples).

The aircraft fuselage longitudinal LJ will be represented by an industrial standard[2] 3 fastener row and 5 fastener per row LJ coupon (110 mm **x** 250 mm per sheet) made of 2.5 mm thin 2024-T3 conventional aerospace aluminium alloy. Figure 1-3 shows the schematic which will

---

[2] Airbus standard LJ coupon

be followed to examine the application of LP on LJ samples. The experimental approach will compromise:

- Derivation of definition of LP strategies from the literature describing fatigue in longitudinal LJs and obtained mechanical fatigue test results of un-peened BL LJ samples.
- Measurements of RSs in laser-peened LJs using ICHD and diffraction techniques.
- Fatigue testing of laser-peened LJs using different LP strategies.
- Fractographical analyses correlating RS field, determined fatigue lives and features of fracture to derive new optimised LP strategies.

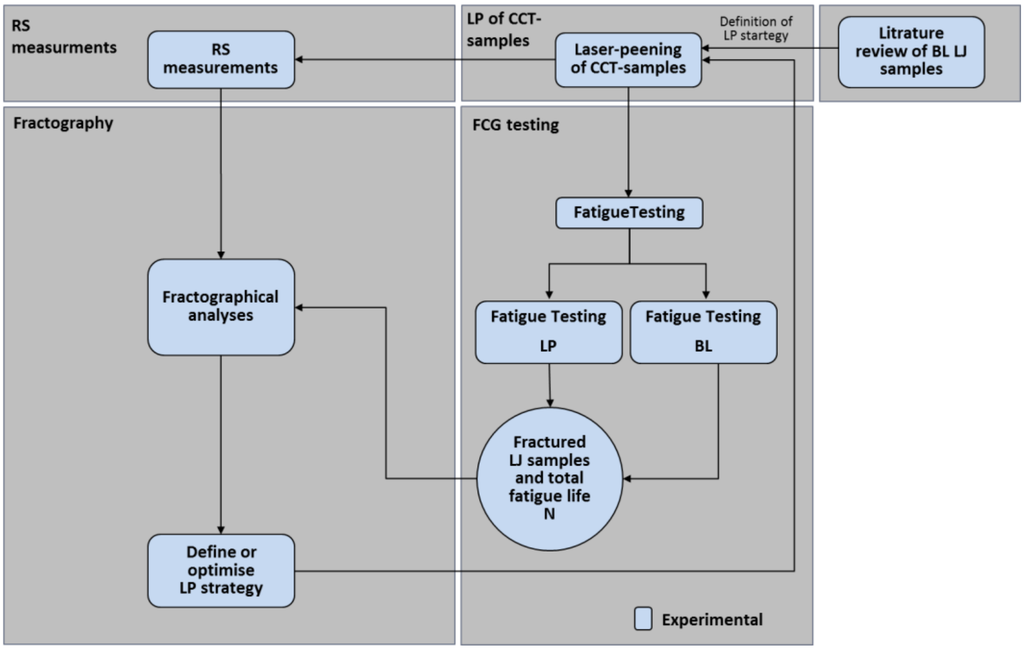

Figure 1-3: Schematic view of approach for aircraft fuselage longitudinal LJ samples.

1.5 Structure of Thesis

This thesis is organised in 10 chapters.

Chapters 1 presents an overview of the historical context of developments which occurred in the broader field of aircraft fuselage fatigue, the research motivation and subsequent research objectives. Finally, the structure of the thesis is outlined.

Chapter 2 opens up by summarising the relevant theoretical framework of fatigue and fracture mechanics. Then the established research of fatigue in pressurised aircraft fuselage structures is reviewed focusing on empirical crack growth data of conventional fuselage aluminium alloys and the multiple degradation factors regarding fatigue which occur in longitudinal fuselage LJ. Before the chapter close with a summary and concluding remark, the current understanding of role of residual stresses in fatigue and fracture mechanics will be reviewed. In this course the LP process and other standard process to introduce RSs will be introduced.

In **Chapter 3** the applied experimental procedures are described. Initially, the geometries, materials and LP treatments of the two different test specimen types (aircraft fuselage skin type sample – CCT-sample and the longitudinal LJ sample) are characterised and presented. Then the experimental protocols of conducted RS measurements of semi-destructive Incremental Centre Hole Drilling Method (ICHD) and non-destructive diffraction techniques are detailed. Mechanical crack growth and fatigue testing techniques are outlined and the experimental test matrices for the two specimen types are given before the last section provides details about the procedure which were followed for the fractographical investigation.

Chapter 4, **5, 6** and **7** frame the central focus of the research results generated by experimental and numerical efforts. It starts by presenting the empirical obtained RS field which are analysed and discussed in **chapter 4**.

Empirical derived fatigue crack growth data of laser-peened CCT-samples are analysed in **chapter 5**. This chapter provides the experimental evidence of the effects of laser-peened induced RSs on crack growth in large aluminium panels which are similar to aircraft skin fields.

Chapter 6 ties on to the preceding chapter 5 and describes firstly the applied modelling approach which was then further utilised to conduct a parameters study investigating different LP treatments and their subsequent effect on crack growth retardations. Secondly, the outcoming results are presented, analysed and discussed.

The fatigue and fracture behaviour of the different applied strategies on laser-peened LJ samples will be analysed in **chapter 7**. Results will be also discussed in the light of measured RS fields.

Chapter 8 and **chapter 9** will close by drawing conclusions and outlining recommendation of potential future research.

References and **Appendices** will be finally attached to the thesis.

2 Theoretical Framework and Literature Review

In this chapter, a literature review is presented. After a short introduction into the theoretical background of fatigue and fracture mechanics, two main sections summarise the research conclusions of fatigue of aircraft aluminium alloys and fastened Lap-Joints (LJs). After that, research which investigated the role of Residual Stresses (RS) in Fatigue behaviours will be reviewed. This review will put a focus on Laser-Peening (LP) induced RS fields, and therefore the LP process will be introduced and subsequent research on measured RS fields will be reviewed.

2.1 Theoretical Framework of Fatigue and Fracture Mechanics

2.1.1 Introduction to Fatigue of Material

A. Wöhler described the fatigue phenomenon as:

“Material can be induced to fail by many repetitions of stresses, all of which are lower than the static strength. The stress amplitudes are decisive for the destruction of the cohesion of the material. The maximum stress is of influence only in so far as the higher it is, the lower are the stress amplitudes which lead to failure.”

This is a fundamental difference to static analysis which examines failures in structures depending on the maximum value of force which is applied to the structure irrespective of time-related parameters. Fatigue analysis is used to predict the service-life of a structure under cyclic loading. This is in contrast to static analysis which aims to define the maximum monotonic load a structure can sustain before failure.

However, the fatigue phenomenon is well known today, and there is a broad range of textbooks available discussing all relevant concepts and equations to understand, assess and predict fatigue and fracture [32–35]. Most affected industries also developed their guidelines and software to ensure the integrity of their products. This section will be limited to a brief introduction of concept and equations relevant to further discussions in the main chapters and is abstracted for the most part from J. Schijve’s textbook *“Fatigue of Structures and Material”* [32].

Fatigue analysis is indispensable for engineers and researchers who analyse metallic components of machines that are in-service and subjected to cyclic loadings, such as aircraft and trains, to ensure a reliable and safe operation of such machinery throughout their service-life. In the aerospace industry, fatigue analysis by analytical, modelling and testing approach is applied to justify safe operation of aircraft towards airworthiness authorities. Moreover, it used to define inspection intervals to ensure continued airworthiness of aircraft damage-tolerant structures.

For predictions of the fatigue life, it is important to understand the fatigue mechanism in detail. The fatigue mechanism, caused by cyclic loading, can be divided into three stages: initiation of small cracks, followed by macro crack growth and finally the complete failure. The actual fatigue life is split into a crack initiation period and a crack growth period, see Figure 2-1.

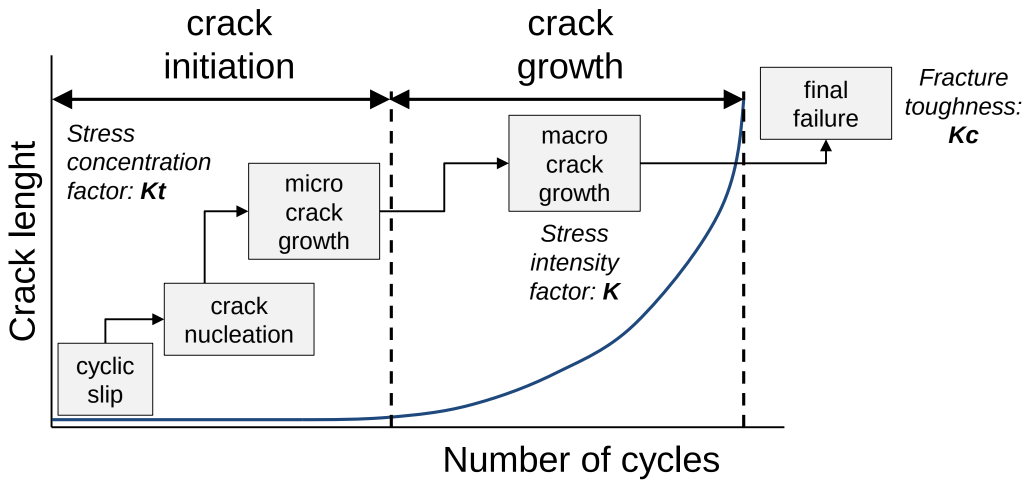

Figure 2-1: Three stage of fatigue life

The separation of the two periods of the fatigue life is of great importance as the mechanics are very different. The crack initiation period consists of cyclic slip, crack nucleation and micro-cracking, so that is characterised by local microscopic processes which are mainly influenced by material free surface conditions and a heterogeneous stress distribution around the grain boundaries of the material. Local stresses can be very different from global stresses in case of stress concentration by geometric conditions such as holes or fillets which are then described by the stress concentration factor Kt or microscopic flaws in the material such as void or pores. The crack growth period is predicted by means of fracture mechanics. The stress intensity factor K (which will be outlined in chapter 2.1.2.1) is the most important parameter which is used for crack growth prediction. The final failure is described by the fracture toughness factors $K1_C$ and K_C. According to Schijve [32], the difference between crack initiation phase and crack growth phase is:

"The initiation period is supposed to be completed when micro-crack growth is no longer depending on the free surface conditions."

and respectively Schijve [32] defined the crack growth period as:

"Crack growth resistance, when the crack penetrates into the material, depends on the material as a bulk property. It is no longer a surface phenomenon."

However, it should be noted that in different contexts crack initiation can have a very different definition. In the aerospace industry, for instance, crack initiation can consider the complete fatigue life which was evaluated by fatigue endurance tests with negligible crack growth periods or the crack growth periods which grow cracks that cannot be detected with respective non-destructive testing methods. In contrast to Schijve's definition, those practical approaches, however, are not based on the different mechanics which determined the micro and macro crack so that in the following Schijve's definition of crack initiation will be taken as reference since the mechanical view point of Schijve will help to understand the role of RSs for both periods.

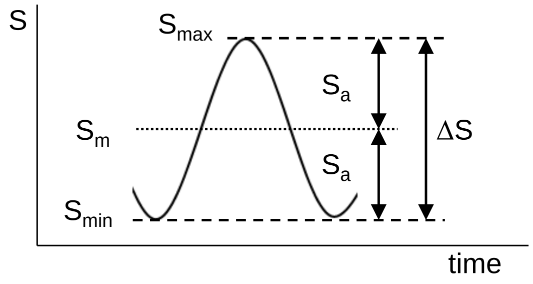

Figure 2-2: Fatigue stress cycle definition

As mentioned, the fatigue life of a structure includes both a crack initiation and a crack growth period. The fatigue life approach describes both periods by the same concepts and parameters. This is favourable for a structure where the macro crack growth period is negligible in comparison to the crack initiation period, or where the macro crack growth is small because of the absence of bulky material where the cracks are able to propagate. A tensile test specimen with a relatively small cross section represents such a structure. Macro crack growth is evaluated by means of fracture mechanics which are explained in chapter 2.1.2. Incremental fatigue damage is caused by cyclic loading, see Figure 2-2, which in its simplest form is a stress cycle with constant amplitudes. This can be described by the stress amplitude S_a and the mean stress S_m. Similarly, it can be characterised by the parameters S_{max} and S_{min} in the stress ratio:

$$R = \frac{S_{min}}{S_{max}} \; (Equation\ 2.1)$$

ΔS is the stress range and is either defined by the difference of S_{max}- S_{min} or by twice the stress amplitude S_a.

The S-N curve also called a Wöhler or stress-life curve, is the result of several fatigue test samples fatigue cycled under constant amplitude. Those collected data are then processed using statistics in which for each S_a, the number of load cycles N until final failure of the structures occurred were determined. The fatigue life N depends therefore on the value of the stress amplitude of the stress cycle under cyclic loading. Basically, there are two statistical methods to determine the S-N curve:

1. **by linear-regression analysis:** Testing a number of test samples with different stress amplitudes S_a. The resultant sets of points of the fatigue endurance tests are usually plotted on a log-log scale to achieve a linear relationship by linear regression analysis between S_a and N, Figure 2-3a.
2. **by normal-distribution analysis:** Testing a number of test samples on the same horizon of stress amplitudes S_a. Assuming Gaussian distribution, the 90 % survival line can be determined for each horizon. Linear-interpolation between those different horizons can be used to form S-N curves, see Figure 2-3b.

The slope of the linear curve described by Basquin is defined with -1/k. However, the S-N curve is a material specific value which must be established experimentally for fatigue analysis of materials. S-N curves are obtained for different stress concentration factors (K_t) values which are experimentally established to take into account different geometrical properties.

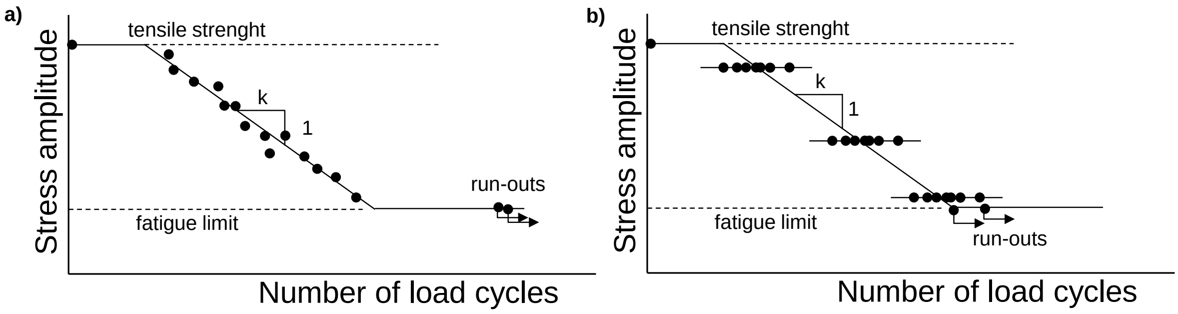

Figure 2-3: Examples of S-N curves. a) approach by linear-regression b) approach by normal-distribution

An example of S-N data for un-notched (K_t = 1.0) 2024-T3 sheet and multiple R-ratios is shown in Figure 2-4. In this example the number of cycles is plotted against the maximum stress S_{max} which is given on a linear scale. It can be noticed that different R-ratios result in different fatigue lives. This so called mean stress effect will be described in chapter 2.1.2.3.

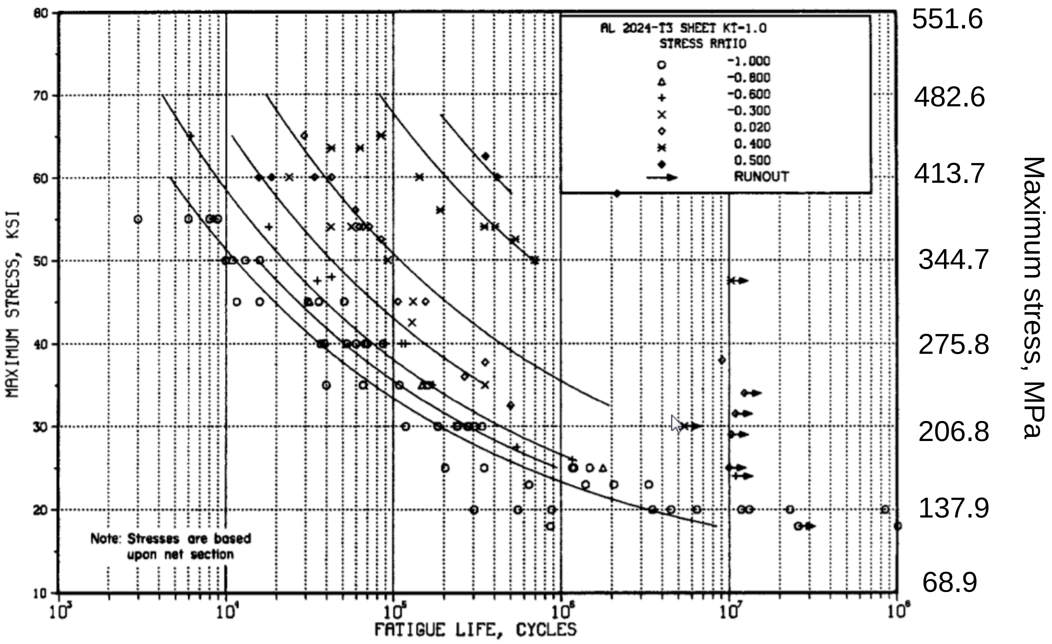

Figure 2-4: Example of S-N data for a 2024-T3 bare sheet of 2.286 mm thickness and multiple R-ratios. (data was taken from [36] **and edited by author)**

2.1.2 Introduction to Linear-Elastic Fracture Mechanics

The theory of fracture mechanics enables engineers to assess existing cracks or other flaws and their propagations in structures. This consist of crack growth (crack propagation), the static strength of a damaged structure (residual strength) and the maximum crack length (critical crack length) analyses. In the aerospace context, this maximum static load typically referred to limit load which is the highest anticipated load an aircraft will experience throughout its service life. Fracture mechanics can be applied if crack or flaws are already assumed to be in a structure. Hence, crack initiation processes took already place and cannot be studied by means of LEFM.

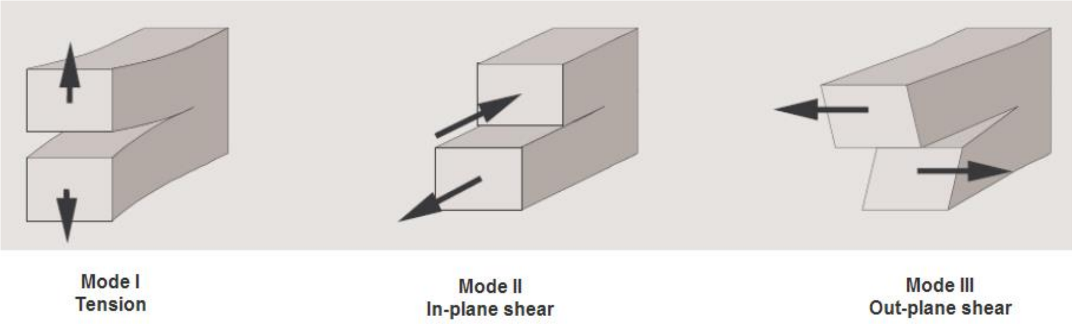

Figure 2-5: Crack modes

Crack growth depends besides the material properties on the type of loading. Figure 2-5 shows three different modes of loading under which a crack propagates. Conventionally the stress intensity factor for crack mode I is written as K_I. All further explanations refer to the mode I only. A crack in Mode I propagates perpendicular to the external applied tensile stress direction which is the case for all test sample geometries in this work. The tensile loading opens the crack in every cycle. Mode II and mode III are shear modes under which fatigue cracks could propagate.

2.1.2.1 Stress Intensity Factor

The stress intensity factor K is the fracture mechanics concept for the crack growth period and describes the stress distribution around crack tips. Figure 2-6 illustrates an infinite sheet containing a through-the thickness crack of a length of 2a, which is loaded in tension (crack mode I). For this case, with σ as the remote loading and a as the crack length, the elastic stress field near (r<<a) the crack tip in a polar coordinate system is defined by following equations:

$$\sigma_x = \frac{\sigma\sqrt{\pi a}}{\sqrt{2\pi r}} \cdot \cos\frac{\theta}{2}\left(1 - \sin\frac{\theta}{2}\sin\frac{3\theta}{2}\right) - \sigma \ (Equation\ 2.2a)$$

$$\sigma_y = \frac{\sigma\sqrt{\pi a}}{\sqrt{2\pi r}} \cdot \cos\frac{\theta}{2}\left(1 + \sin\frac{\theta}{2}\sin\frac{3\theta}{2}\right) \ (Equation\ 2.2b)$$

$$\tau_{xy} = \frac{\sigma\sqrt{\pi a}}{\sqrt{2\pi r}} \cdot \cos\frac{\theta}{2}\sin\frac{\theta}{2}\cos\frac{3\theta}{2} \ (Equation\ 2.2c)$$

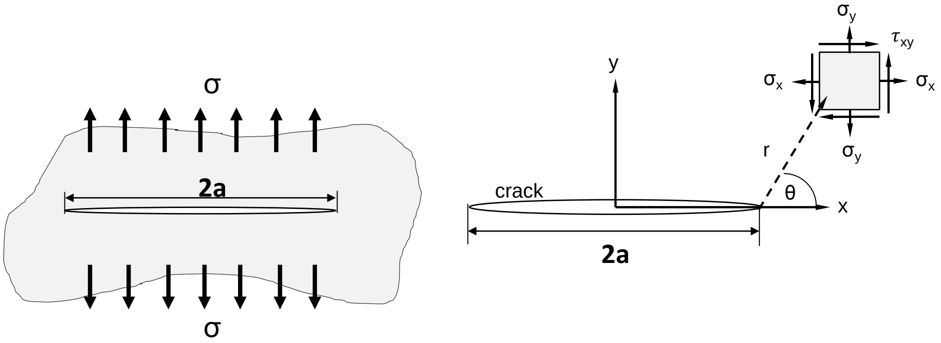

Figure 2-6: Infinite sheet with a mode I crack and definition of stress field around the crack tip

Those three before mentioned equations can be summarised and formulated as:

$$\sigma_{i,j} = \frac{K}{\sqrt{2\pi r}} f_{i,j}(\theta) \ (Equation\ 2.3)$$

The stress intensity factor K can be described as:

$$K = \beta\sigma\sqrt{\pi a} \ (Equation\ 2.4)$$

The dimensionless factor β in the equation or also beta correction factor can be found in the literature for various geometries and loading conditions [37], as shown in Figure 2-7. To derive such beta correction factors, various approaches have been applied by many researchers and engineers. Among these approaches, some are of analytical nature, such as the weight functions method [38] and others use numerical approaches via Finite Element Method (FEM) [39], see chapter 6.1. Many times closed-form solutions are derived by means of FEM but result in analytical function [40]. SIF´s beta correction factors are calibration factors accounting for finite geometries as the mathematical derivation relates to an infinite plate as indicated in Figure 2-7. Most of standard crack growth cases are already covered in the specific literature so that engineers and researchers also linearly superimpose SIF solutions when applicable.

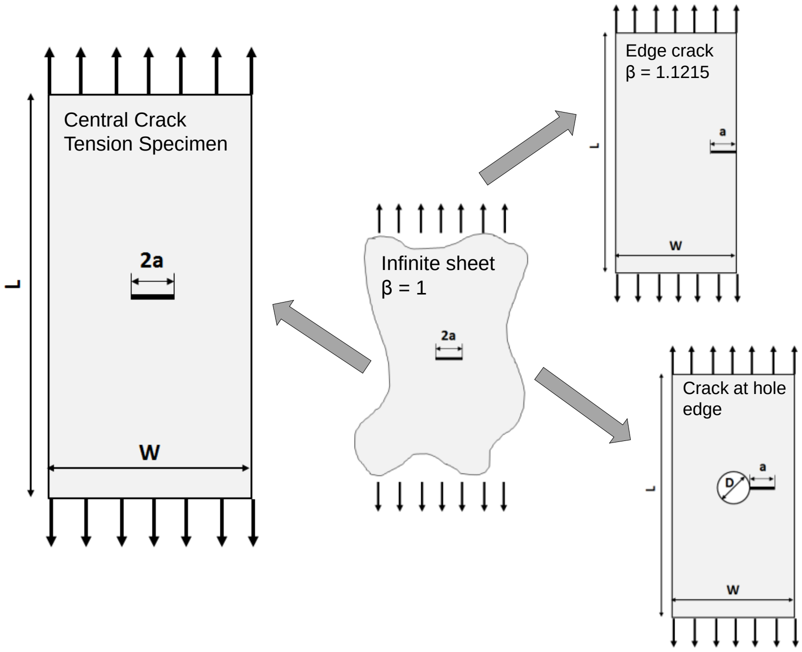

Figure 2-7: Beta correction factors - Infinite sheet vs engineering structures.

For an infinite sheet, β takes the value 1 and *K* can be described as:

$$K = \sigma\sqrt{\pi a} \ (Equation\ 2.5)$$

For a central crack tension (CCT) specimen *K*, as illustrated in Figure 2-7 is formulated as:

$$K = \sigma\sqrt{\pi a}\sqrt{\sec\left(\frac{\pi a}{W}\right)} \ (Equation\ 2.6)$$

according to Feddersen [32] and in line with the ASTM standard [41]. After substitution of the beta correction factor, K derives into:

$$K = \sigma\sqrt{\frac{\pi a}{\cos\frac{\pi a}{W}}}\ (Equation\ 2.7)$$

The stress intensity factor range for cyclic loading, see Figure 2-8, is formulated by the following equation:

$$\Delta K = \beta\Delta\sigma\sqrt{\pi a}\ (Equation\ 2.8)$$

By applying the cyclic loading with a stress range of $\Delta\sigma = \sigma_{max} - \sigma_{min}$, the stress intensity factor range ΔK can be written as $\Delta K = K_{max} - K_{min}$.

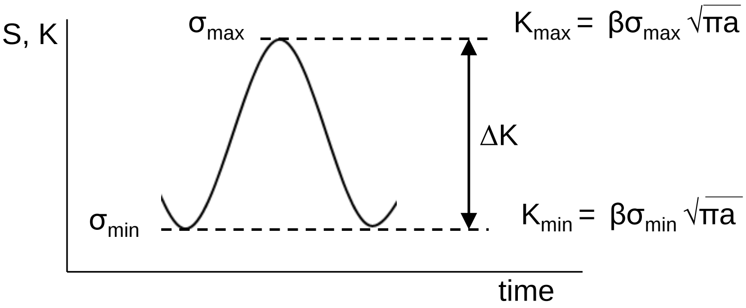

Figure 2-8: Stress intensity factor under cyclic loading

2.1.2.2 Fatigue Crack Growth Characterisation Models

Fatigue crack growth predictions are very complex in nature because of the vast amount of effects on the crack life by different factors. However, any prediction model must be based on the assumption that flaws or small cracks are already present in the structure, as the crack initiation period is governed by different mechanics and theories. Therefore, crack growth predictions represent only the crack propagation period, recall Figure 2-1. The main factors for the crack propagation period are the SIF and the SIF range, as discussed before. There are several crack growth prediction models established by researchers and engineers to accurately model crack growth for a specific configuration. The crack growth prediction models relevant to this work are described below.

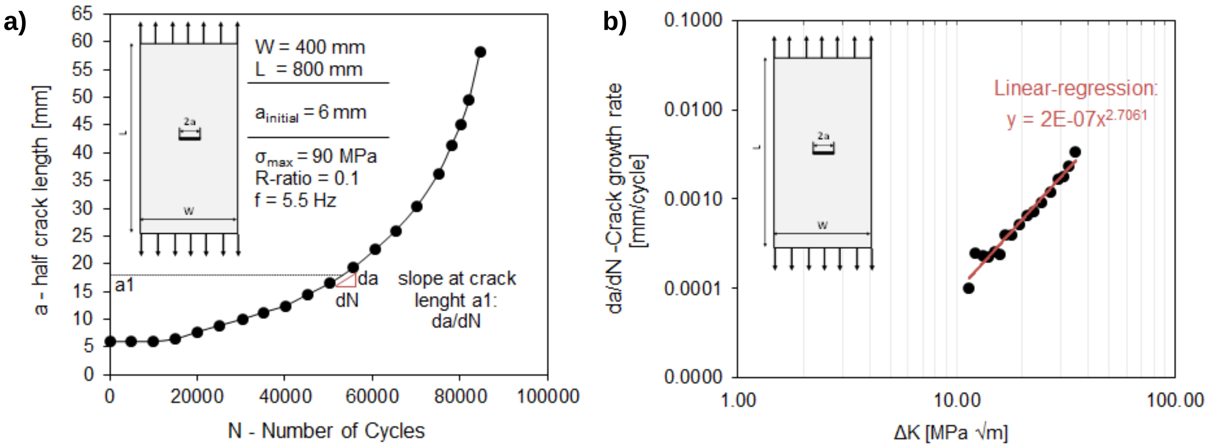

Figure 2-9: Crack growth data. a) crack length versus N and b) crack growth rate versus ΔK

The foundation of any crack growth prediction model is characteristic material data of crack propagation which are typically evaluated from fatigue crack growth tests with constant amplitudes applied on test specimens with specific geometrical conditions (beta-correction factors). Figure 2-9a represents an example of obtained crack growth test result for a central cracked tension (CCT) specimen. It shows the crack length *a* as a function of accumulated load cycles *N*. The slope of the crack growth curve, which is defined by da/dN, is the crack growth rate. The growth is nonlinear as a function of the crack length *a*.

The crack growth curve can be described as follows;

$$a(n) = a_0 + \int (da/dN)dN \ (Equation\ 2.9)$$

where a_0 is the initial crack length which is assumed to be in the structure for crack propagation analysis. The integral is solved from the initial crack length to final crack length to determine the complete crack growth period. The crack growth rate da/dN can be plotted on a double log scale versus the stress intensity factor range ΔK, as shown in Figure 2-9b. In contrast to of crack growth which depends on cyclic loading, characterised by Δσ, the stress intensity factor rate ΔK increases because of ΔK's dependence on the crack length (recall equation 2.5). Crack growth rates from test data can be processed with ASTM standard E647 [41] secant method which is formulated as:

$$\left(\frac{da}{dN}\right)_{\bar{a}} = \frac{(a_{i+1} - a_i)}{(N_{i+1} - N_i)} \ (Equation\ 2.10)$$

in which ā is the average crack lengths over the increment expresses as:

$$\bar{a} = 0.5\ (a_{i+1} - a_i)\ (Equation\ 2.11)$$

This resulting graph as shown in Figure 2-9b represents the crack growth resistance of materials. The practical application, and thus the importance of the data (da/dN vs ΔK-curve) in any crack growth predicting model is mainly based on the similarity concept or similitude principle. The similarity concept says that:

"Similar cyclic conditions (ΔK and R) applied to fatigue cracks in different specimens or structures of the same material should have similar consequences, i.e. similar crack extensions per cycle, thus the same da/dN." [32]

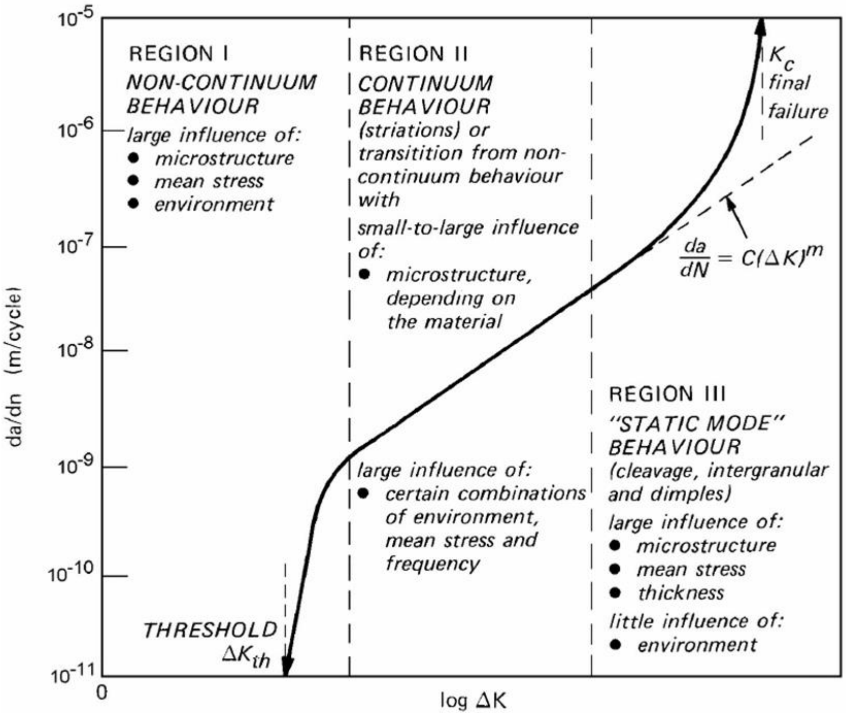

Figure 2-10: Characteristic crack growth resistance curve. Crack growth versus ΔK (Graphic was taken from [42]**)**

Although the similarity concept is the most important concept to determine crack growth rates by calculating the SIF range, it does not say anything about the amount of crack extension per cycle. This must be determined by test results as described before. Figure 2-10 illustrates a complete da/dN vs ΔK-curve. The curve can be separated into three regions, region I, II and III. It is further characterised by two asymptotes: One on the left hand to the curve, which remarks the threshold region (region I) from where crack growth can be expected to start. The relevant factor for the threshold region is K_{th} and in this region I, the crack growth behaviour is mainly influenced by the material microstructure and applied mean stresses. And the asymptote on the right hand to the curve, where the stress intensity K reaches its critical limit K_c. It can be noticed that for such a case the crack growth rate becomes infinitely high so that an abrupt failure of the specimen has to be assumed. Region II, also called Paris region is characterised by a steady constant slope. Crack growth rates in region II can be described by following, known as the famous Paris equation:

$$\frac{da}{dN} = C\ \Delta \mathrm{K}^m\ (Equation\ 2.12)$$

C and m are the so-called Paris constants and are derived by linear-regression analysis in the double log scales as shown in Figure 2-9b. Paris was the first in 1961 [43] to find the linear relationship between da/dN and ΔK in a log-log plot for the stable crack growth of region II. The Paris model is now generally accepted for a wide range of different materials, and it is used by many researcher and engineers for practical applications. However, the physical meaning is limited, and other characterisation models were established which offer improvements. Those will be described in the next section. The major shortcoming of the Paris formulation is that it can only model fatigue crack growth accurately in region II and it does not account for mean stress effects.

In region III, K_C is the important parameter, as the failure of any structure occurs at:

$$K_I \geq K_C \ (Equation\ 2.13)$$

where K_c is the fracture toughness which is a material property depending additionally on the thickness by:

$$t \geq 2.5 \left(\frac{K_C}{\sigma_y}\right)^2 \ (Equation\ 2.14)$$

in which σ_y the tensile yield stress of the material. The fracture toughness K_{Ic} is valid for plane strain conditions. For plane stress conditions, hence for decreased sample thickness, the fracture toughness K_c increases, as shown in the schematic in Figure 2-11.

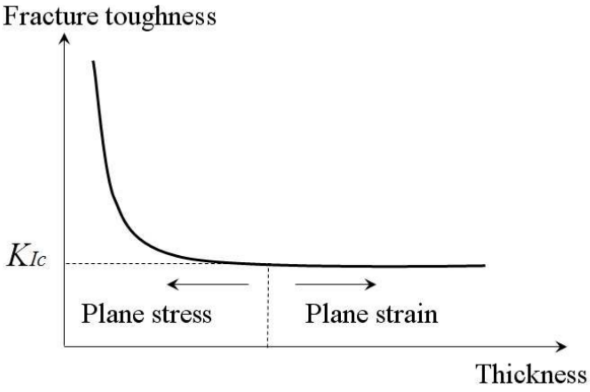

Figure 2-11: Effects of sample thickness on fracture toughness. (Graphic was taken from [44]**)**

2.1.2.3 The Mean Stress Effect

A model to characterise crack growth in the Paris region (region II) taking into consideration the mean stress effect is Walker's empirical crack growth model [45] which is formulated as:

$$\frac{da}{dN} = \frac{C_0 \cdot (\Delta K)^m}{(1-R)^{m(1-n)}} (Equation\ 2.15)$$

in which C_0, m and n are material constants which are determined by a fitting procedure [45]. The R ratio accounts for the changes of mean stresses. It can significantly alter the FCGRs so that for increased R-ratio values the FCGR becomes greater and vice-versa. As the Walker model can describe the behaviour of FCGR with respect to different mean stresses, it does not provide a physical explanation of the mean stress effect. Further, equally to the Paris model, the Walker model can only approximate the FCGR behaviour accurately in the region II.

For that reason, Forman came up with his equation. It is commonly being used in the aerospace sector, as it can accurately model region II and III by the describing the behaviour of FCGR using the following equation:

$$\frac{da}{dN} = \frac{C\ \Delta \mathrm{K}^{\mathrm{m}}}{(1-R)\ K_c - \Delta \mathrm{K}}\ (Equation\ 2.16)$$

However, Elber offered a physical reasoning for the mean stress effect in the paper “Fatigue Crack Closure under Cyclic Tension” [46]. He assumed that crack closure was the cause of mean stress effects. Elber thought that there is an effective cyclic stress intensity range ΔK_{eff} which is the part ΔK cycle during which the crack is open. As illustrated in Figure 2-12, the ΔK_{eff} is defined by $\Delta K_{eff} = K_{max} - K_{open}$. That means that FCGR is longer a result of the complete ΔK cycle if $K_{min} \leq K_{open}$. In simple words, a crack does not grow if it is closed.

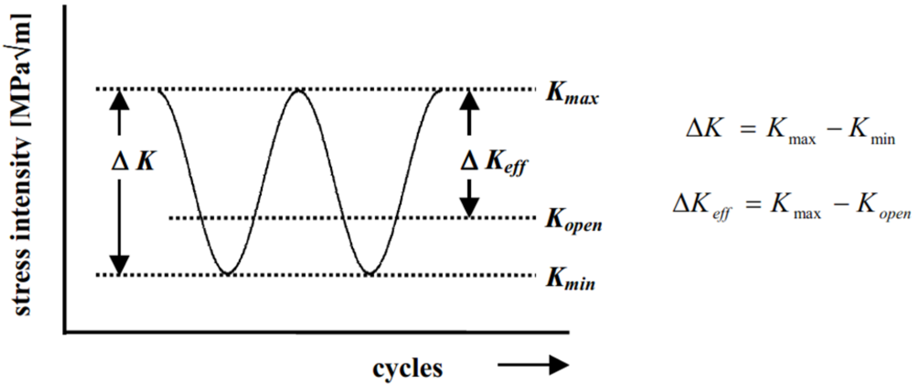

Figure 2-12: Schematics of Elber’s crack closure model. (Graphic was taken from [42]**).**

T. Mann [47] who reviewed mean stress effect models, including Walker’s and Elber’s model. He concluded that the Walker model can accurately predict the mean stress effect for 2024-T3 and 7075-T6.

2.2 Fatigue in Pressurized Aircraft Fuselages

Pressurised aircraft fuselage structure, in particular, the fastened Lap-Joint, as drawn in Figure 2-13 was the focus of many researchers in the field of aeronautical fatigue and structural integrity (a comprehensive review is given in the book by A. Skorupa and M. Skorupa: [48]). As illustrated in the drawing of the longitudinal LJ splices the upper fuselage shell is joined to the bottom shell by mechanical fasteners, e.g. solid rivets or Hi-Lok bolts in contemporary metallic fuselages.

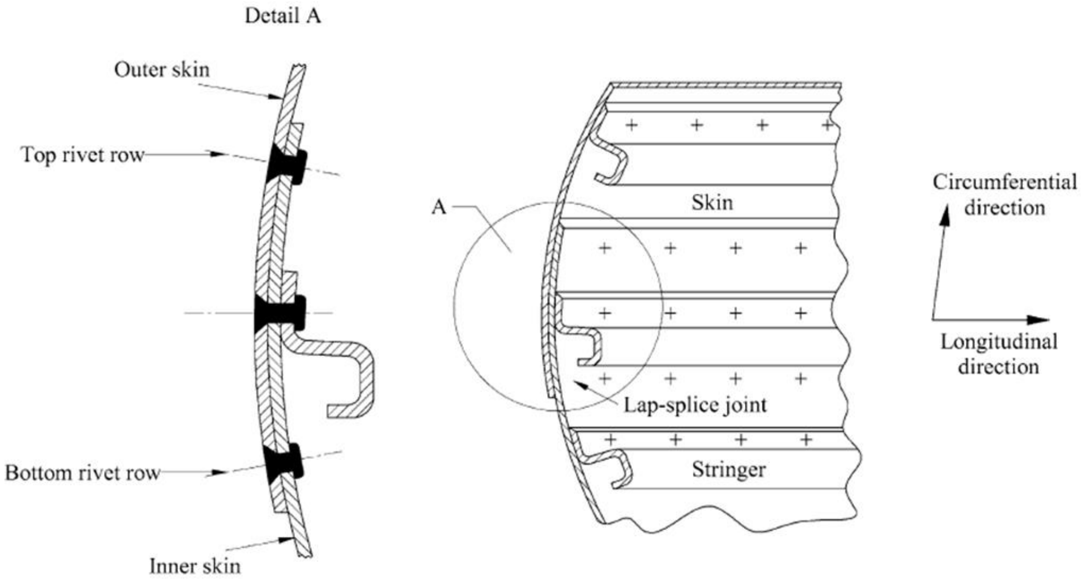

Figure 2-13: Longitudinal LJ of pressurised aircraft fuselages. (Illustration was taken from [48]**).**

The primary load of aircraft fuselages act as applied membrane stress on the fuselage skin. It is a result of the pressurisation of the cabin although other flight carrying loads e.g. manoeuvre or air gust loads also act on the structure. The differential pressure between the fuselage cabin and the atmospheric pressure at high altitudes, however, dominates in the equation [49]. Maximum membrane circumferential stresses, therefore, depend on the flight altitude and aircraft type (skin thickness and radius of the fuselage) and can range from 80 MPa to 120 MPa [49]. According to the theory of thin-walled pressure cylinders, the circumferential stress can be estimated from equation 2.17 in which σ_C is the circumferential stress in the skin, p_i is the internal cabin pressure, r_F is the radius of the fuselage and t_F is the thickness of the fuselage skin:

$$\sigma_C = p_i * \frac{r_F}{t_F} \ (Equation\ 2.17)$$

As an example in Figure 2-14 the circumferential membrane stress has been calculated using equation 2.17 for different aircraft types and skin thicknesses which can vary along the fuselage for a cruise altitude of 45,000 feet. Repetitive ground-air-ground (GAG) flight cycles of those loads eventually initiate fatigue in LJ.

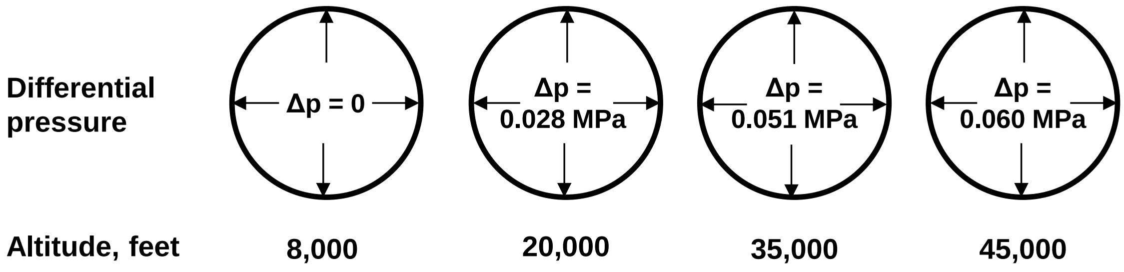

A320: r = 1.975 m, t = 2.5 mm -- 47.4 MPa
A320: r = 1.975 m, t = 1.6 mm -- 74.1 MPa

A330: r = 2.820 m, t = 2.5 mm -- 67.7 MPa
A330: r = 2.820 m, t = 1.6 mm -- 105.8 MPa

B737: r = 1.880 m, t = 2.5 mm -- 45.1 MPa
B737: r = 1.880 m, t = 1.6 mm -- 70.5 MPa

Figure 2-14: Pressure and resulting circumferential stresses of different aircraft types and skin thicknesses

2.2.1 Crack Growth in Aircraft Fuselage Aluminium Alloys

Two of the most common aluminium alloys used for today’s airframes are 2024-T3 and 7075-T6. 2024-T3 and 7075-T6 are conventionally used for aircraft fuselage skin panels which are mainly dominated by tensile pressurisation loads. 7075-T6 is also largely used in compression dominated structures, e.g. the upper wing skins where damage tolerance considerations are secondary [50]. T. Dursun and C. Soutis [50] give a review of recent developments in advanced aircraft aluminium alloys which include 2024-T3 and 7075-T6. They concluded that those two aluminium alloys are important today and will play a crucial part of future metallic aircraft fuselage structures. However, future research activities must be focused on sustained and improved structural integrity in fastened structures. Especially, fretting fatigue which occurs typically in aircraft fuselage joints must be enhanced in order to use the advantage of those recent improvements in fatigue and fracture mechanical properties of advanced aluminium alloys.

However, the crack growth resistance of 2024-T3 and 7075-T6 was analysed by many previous researchers. A summary of this research and experimentally derived Paris constants for various R-ratios was compiled by T. Mann [47]. He also gathered *C* and *m* data for multiple R-ratios, which was originally determined by C. M. Hudson [51] for 2024-T3 and 7075-T6. A reconstruction of FCGR using the provided *C* and *m* values, da/dN vs ΔK for the range of ΔK of 6 MPa√m – 40 MPa√m was realised, as shown in Figure 2-15a for 2024-T3 and in Figure 2-15b for 7075-T6. It can be noticed for both alloys that FCGR alters significantly between the different values of R-ratio. The lower the R-ratio becomes, the slower the crack grows, consequently. This mechanism can be explained by previously described by Elber's physical crack closure model and the assumption that the effective ΔK_{eff} which takes into account only the period of the stress cycle during which the crack is open significantly changes with the mean stress. A comparison of FCGR for the two aluminium alloys is given in Figure 2-16. FCGRs of 2024-T3 are lower than those for 7075-T6 so that by implication 2024-T3 provides a better crack growth resistance than 7075-T6.

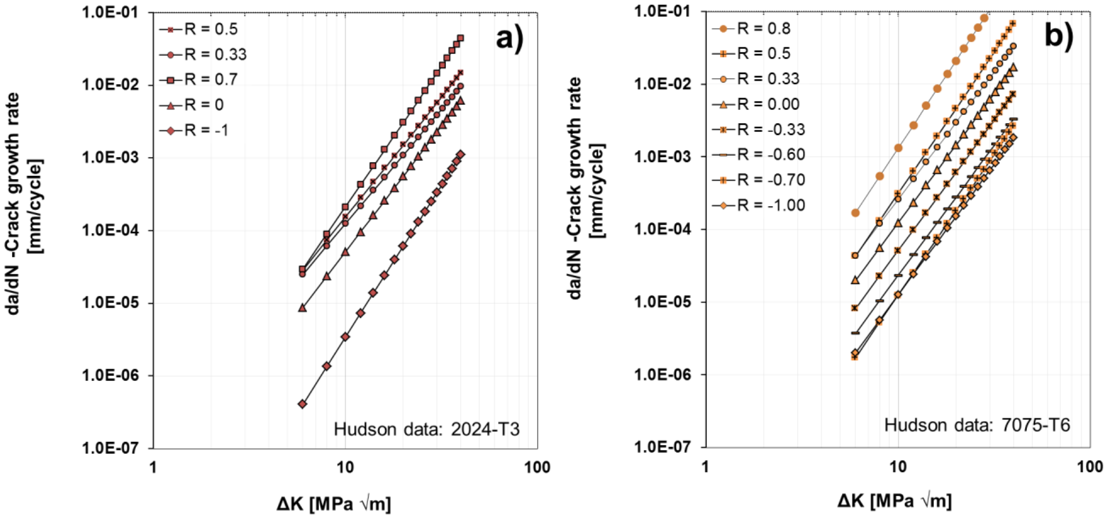

Figure 2-15: FCGR for two conventional aircraft aluminium alloys and multiple R-ratios. a) FCGR for 2024-T3 and b) FCGR for 7075-T6.

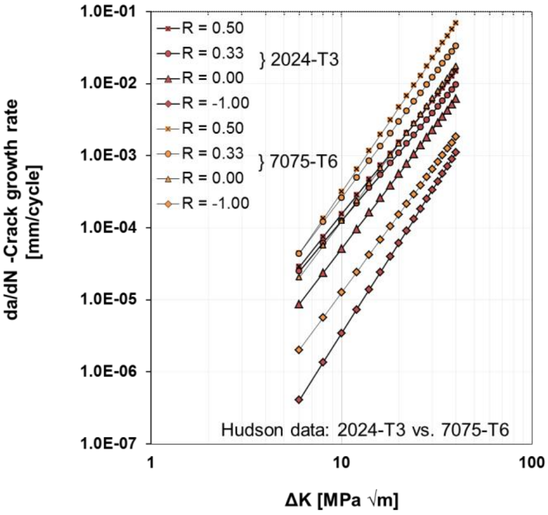

Figure 2-16: Comparison of FCGR for 2024-T3 and 7075-T6 aircraft aluminium alloys and multiple R-ratios.

Fracture toughness (K_{Ic}) and static yield strength were compared by Verma *et al.* [52] for 2024-T3 and 7075-T6. It was concluded that 2024–T3 alloy has high ductility and good fracture toughness (K_{Ic} = 37 MPa√m) but has relatively low yield strength (σ_y = 324 MPa). In contrast, 7075 alloy under T651 temper condition has yield strength more than 500 MPa. The reported fracture toughness is on the other hand only 24 MPa√m. This makes 2024-T3 to be used for structure which are moderately loaded but need high resistance to fatigue cracking. 7075-T6 on the other hand is applicable for highly loaded structures.

2.2.2 Fatigue in Aircraft Fuselage Longitudinal Fastened Lap-Joint

There is a vast amount of work found in the literature [48] which not only emphasises the complexity but also offers explanations for various effects of multiple factors which in combination determine the fatigue performance of the aircraft fuselage longitudinally fastened LJ. It is a crucial element of modern aircraft architecture. To understand the role of acting stresses in LJs a detailed knowledge of specific loading distribution as described in Figure 2-17 and their subsequent effects is necessary. The main contributing load distribution components are:

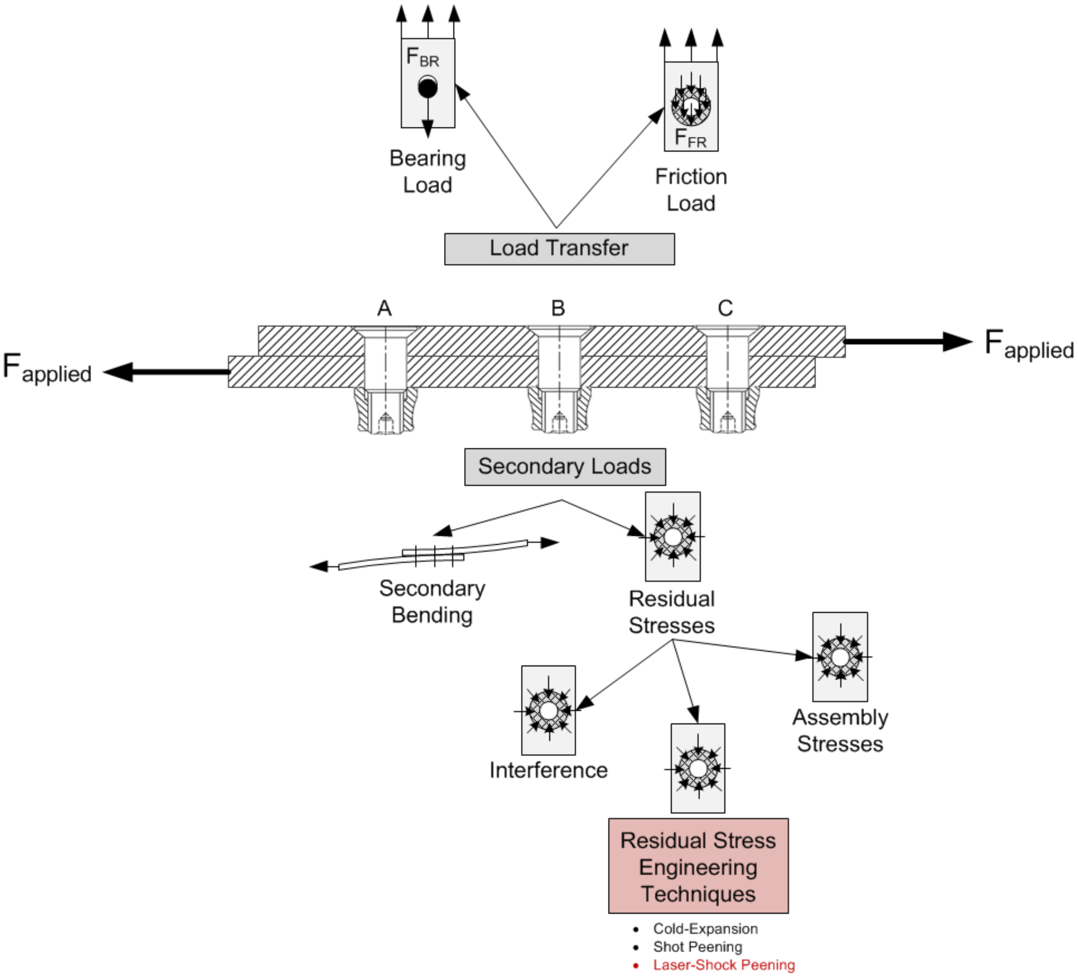

Figure 2-17: Schematic view of principal loading components on fastened lap-joint samples.

- **Nominal applied tensile membrane stresses** and subsequently stress concentration at fastener-hole due to by-pass loads.

- **Load transfer** (see chapter 2.2.2.1)mechanisms distributing the load by:
    - ***Bearing loads*** of the fastener on the fastener-hole
    - ***Frictional loads*** on faying surfaces and subsequent fretting damage

- **Secondary loads** effects which arise from the LJ configuration such as:
    - ***Secondary bending*** (see chapter 2.2.2.2) coming from eccentricities or misalignments
    - ***Residual stresses*** (see chapter 2.2.2.3) resulting from fastener fitting, assembly stresses or residual stress engineering technologies, e.g. cold-expansion or LP.

Before those mechanisms are explained in detail in their respective individual section, a review of published fatigue response data will be given. Experimental results for constant amplitude fatigue endurance tests using 2024-T3 Alclad and 7075-T6 Clad LJ samples are presented in Figure 2-18. LJ samples used by Hartmann [53] were two-row LJ with a sheet thickness of 0.8 mm and snap rivets with diameters of 3.2 mm. The S-N data shows that the 2024-T3 fatigue properties are better than those of 7075-T6 which confirms the picture which was drawn by the FCGR data for 2024-T3 and 7075-T6, as presented in the previous chapter.

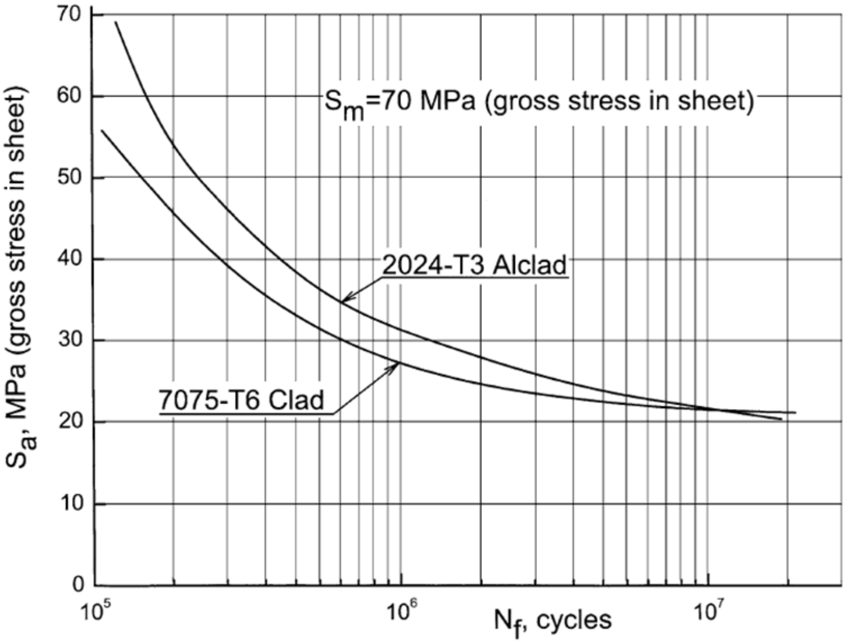

Figure 2-18: Fatigue response in the form of mean S-N curves for LJ in 2024-T3 Alclad and 7075-T6 Clad, as experimentally determined by Hartmann [53] **and review by Skorupa and Skorupa** [48]**. (Data plot was taken from** [48]**)**

According to that data, an applied nominal stress amplitude of 50 MPa and corresponding maximum stress of 120 MPa considering a mean stress of 70 MPA would provide ~220,000 load cycles until failure for a 2024-T3 LJ and ~140,000 fatigue cycles for a 7075-T6 made LJs.

The fatigue resistance of a bare sheet of 2024-T3, as shown by the S-N curve in Figure 2-4, would result not fail under fatigue loading for a maximum applied stress of 120 MPa and an R-ratio of 0.02. This outcome indicates the detrimental effect on the fatigue life induced by the previous mentioned mechanisms which occur in a cyclic loaded LJ as illustrated in Figure 2-17. A good overview of fatigue strength reduction factors at rivet holes for aircraft fuselage lap joints is given by M. Skorupa *et al.* [54]. The current understanding of the degrading mechanism will be described in the following taking into account the most prominent studies.

2.2.2.1 Load Transfer

The principal purpose of LJs is the transmission of loads from one sheet to the other. This task results in a complex local stress field around each fastener-hole which depends on the role of various loading components (as it is broken down in Figure 2-17) which are themselves a product of different design and manufacturing specifications. Understanding this system of driving variables is essential in order to comprehend the mechanics of fatigue and fracture of LJ structures.

The main external loading is coming from the pressurisation load case of aircraft fuselages which results in effect as in plane ($F_{applied}$) and out of plane bending stresses (*secondary bending* stresses) on LJs. The transmission of loads from sheet to sheet can either be through the fastener as *bearing load* (F_{BR}) or through the mating surfaces as *friction load* (F_{FR}).

The proportion of each load component during load transmission has a significant effect on the fatigue performance of LJ samples [48]. Unlike the bearing load which appears to occur by design as bearing pressure from the fastener on the hole shank, frictional forces also can significantly contribute to the load transfer in LJ structures [55,56]. Besides frictional coefficients of respective materials, the installation process of the fastener drives the amount of load transferred by friction by two main considerations: Fastener fitting and clamping forces.

For solid rivets, both the fore mentioned parameters are decided by the rivet installation process specification. Specifically the squeezing force of solid rivet installation produces the final geometry of rivets, and in consequence, the rivet fitting and clamping forces are determined. Mueller [55] has investigated in detail the effect of different squeezing forces during the solid rivet installation process on the load transmission of 2024-T3 clad LJ. He conducted a series of friction tests of LJ samples in which translational and rotational forces were put in contrast to resulting displacement collecting data of all frictional forces occurring in a LJ. From this data, it can be concluded that higher squeezing forces result in higher load transfer through friction. Mueller found that the frictional load transmission could be up to 50% of the external applied load for solid rivets, as further analysed by means of detailed three-dimensional FEA by Mueller [55]. This is not true only because of resulting higher clamping pressure but also because of the increased interference fitting of rivets as a consequence of increased squeezing forces. Rans [57] confirms the conclusions by his FEA efforts. Brown and Straznicky [58] further validated FEA results of the relationship between squeezing force and clamping pressure experimentally by using a pressure sensitive film between sheets during the rivet installation process. Their data, as presented in Figure 2-19, also illustrates the extent of the clamping pressure around the fastener-hole which also offered an explanation of failure mechanism and locations, as described later in section 2.2.2.4. According to Mueller's [55] and Brown and Straznicky's [58] FEA and experimental data, the clamping pressure contributes to load transmission by friction. The clamping pressure exists locally around the fastener-holes underneath the rivet-head [55] and slightly beyond [58] with the peak pressure at the hole edge rapidly decaying in the radial direction away from the hole. This pressure distribution was measured by Brown and Straznicky [58] for different levels of squeezing force.

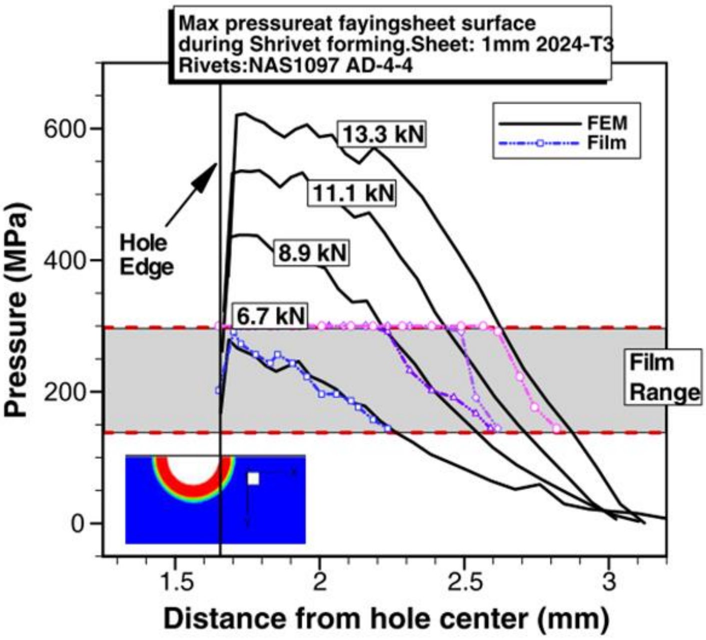

Figure 2-19: Max pressure distribution around fastener holes predicted by FEM simulation and that measured by a pressure sensitive film for different squeezing forces, as performed by Brown and Straznicky [58]**.**

Fretting-fatigue around those fastener holes was then identified and correlated with their results by all investigators [55,58,59] as one of the dominant processes of the failure mechanism in high load transfer LJ samples. Fretting-Fatigue will be described in detail later in next chapters.

However, as Mueller [55] determined the role of friction solely on quasi-static friction tests, Starikov [56] found that the effect of transient cyclic loading needs to be considered when analysing frictional forces in LJs. Starikov who used strain gauge rosette equipped fasteners to derive the proportion of bearing and friction load in AA7475-T761 LJs found that after fatigue cycling eventually 80-90% of the external applied load could be carried by frictional forces and the remaining by bearing forces carried by the fastener. Further, the experimental results showed that after a certain amount of transient load cycles the frictional forces become stable. Szolwinski *et al.* [60] explained the dominance of friction in cyclic loading conditions by an increase in coefficient of friction due to fretting wear debris occurring on the faying surface. Fretting wear occurs on the faying surface due to relative motions of the sheets and consequently removes the first layer of cladding. As a result, the underneath located bulk material start to adhere with each other and increased frictional coefficients can be expected. Further detailed implications of high load transfer via friction are explained in section 2.2.2.5.

2.2.2.2 Secondary Bending

In order to explain the crack nucleation sites in LJ structures a full understanding of the local stress field in LJ structures is required. For that secondary loads need to be taken into account besides the above mentioned mechanism dealing with load transmission. The major mechanism of so called secondary loads (see Figure 2-17) is *secondary bending* which occurs in LJs due to inherent eccentricities of LJ's design. As aircraft fuselage LJ structures are not loaded with external bending moments but solely with external tensile loads, bending moments occur from out-of-plane displacement due to eccentricities which are then called *secondary bending*. Stresses resulting from *secondary bending* superimpose with stresses coming from the external tensile loads and therefore increase the peak tensile stress in LJs. As illustrated in Figure 2-20, peak secondary bending stresses occur at the faying surface at the outer rivet rows A and C. The increase in peak stress is detrimental to the fatigue performance of LJ structures and is another major contributor to the poor fatigue performance of LJ structure in comparison with the base sheet fatigue properties.

Schijve *et al.* [61] describes those secondary bending characteristics in detail for LJ samples and offers a one-dimensional analytical methodology to quantify resulting stresses and displacement. Consequently, a bending factor was defined as the ratio of bending stress and the nominal tensile stress coming from LJ eccentricities or misalignments of LJ's clamped ends. The so called neutral line method by Schijve *et al.* is in good agreement with their FE analysis and showed that the amount of secondary bending can be controlled by several geometric variables of LJ. Increasing the distance between the rivet rows or increasing the overlap region reduces the amount of secondary bending in aircraft fuselage LJs. Subsequently, the fatigue performance increased as bending factors decrease. Both conclusions could be derived from Schijve *et al.* neutral line model [61] and were confirmed by experimental data [53], which was referred to.

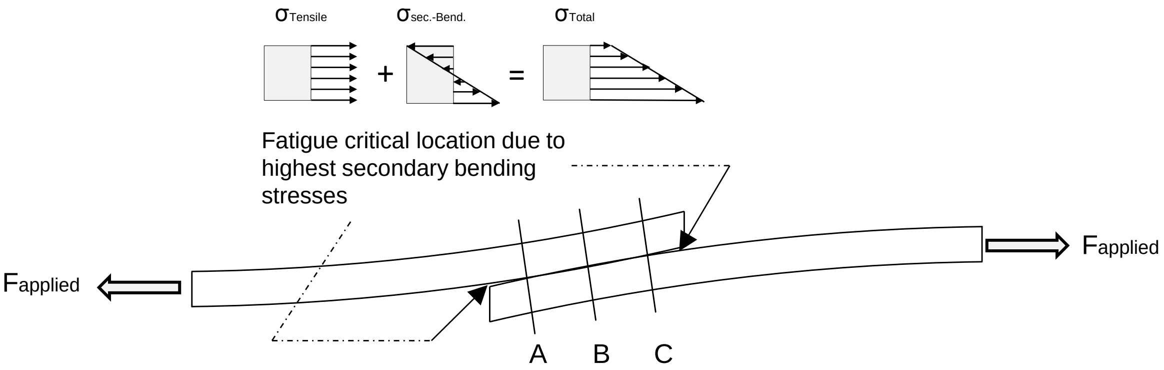

Figure 2-20: Secondary bending in LJs.

Despite the sophistication of the neutral line model, it failed to predict stress fields to explain the experimental observation made by Mueller [55] who reported crack nucleation remote from the fastener-hole. In response to that, Rans *et al.* [57,62] identified two major shortcomings of Schijve's neutral line model originating from its one-dimensional nature. Firstly, it cannot take into account variation of secondary bending along the fastener-row and secondly, it fails to model the effects of secondary bending variation deriving from the dimensions of the fastener head.

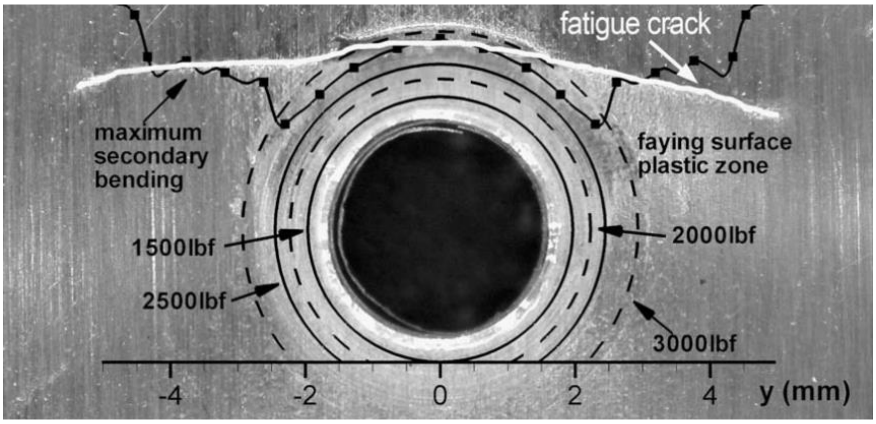

Figure 2-21: Correlation of typical location of fatigue cracking observed in universal rivet joint and FE results showing outer sheet faying surface region of maximum bending, as investigated by Rans *et al.* [59].

A three-dimensional FE study was then conducted by Rans *et al.* [57,62] which showed the effects of solid rivet installation specifications (squeezing force and rivet type) on the secondary bending variation of LJ. The FE model which showed good agreement with neutron diffraction measurements of residual strain disclosed significant variations of secondary bending along the width direction of LJs. The variation of secondary bending could be correlated with the fastener-head size, and it was revealed that the highest secondary bending stresses occur remotely from the fastener-hole following the projected fastener-head edge on the faying surface. The variation was due to the constraint of out-of-plane rotation resulting into secondary bending by the clamped fastener-heads underneath the fastener-head. Beyond this constraint secondary bending could occur. Those results could not only explain the before mentioned fractographical data from Mueller. Supplementary, Rans *et al.* [57,59] correlated with good agreement the fracture line and location of crack nucleation remote from the hole edge observed in their own LJ fatigue test samples with the position of maximum secondary bending coming from their FE study, as demonstrated by Figure 2-21.

Lastly, it could be concluded that the rivet manufacturing process represented by the squeezing force did not significantly affect the secondary bending behaviours but nevertheless the type of rivet did depending on whether if it was a universal or countersunk type. This geometrical condition changed the constraint of out-of-plane rotation and shifted the location of maximum secondary bending. It shifted from a position remote from the centre of the fastener-hole in the longitudinal direction for universal rivet to a position at the fastener-hole in the transverse direction for countersunk rivets. This shift was only observed on the faying surface of the outer sheets. The inner sheet’s secondary bending behaviour is dominated by the driven head geometry.

2.2.2.3 Residual Stresses

RSs can have significant effects on initiation and growth of fatigue cracks in LJ structures. Three sources of RSs in LJs can be principally identified as shown in Figure 2-17:

(1) RSs coming from oversized fastener in relation to the fastener-hole known as Interference.
(2) RSs as a result of assembly procedures, e.g. clamping of the two sheets and resulting contact stresses.
(3) Designed RSs which are induced into structures by usage of RS engineering techniques, e.g. Cx or LP, which will be described separately in chapter2.3.

The assembly of LJ with either solid rivets or Hi-Lok bolts potentially introduces RSs into the structure. For solid rivets, the final geometry of the rivet and the fastener-hole is determined after the completion of the manufacturing (squeezing-) process and therefore, depends on manufacturing process specification parameter, namely the squeezing force. Those RSs are a result of interference and clamping of the sheets, as was extensively studied by Rans *et al.* [57,63] by means of three-dimensional FE analysis. The investigators simulated the rivet forming process for universal and countersunk rivets using different squeezing forces to analyse the impact on the resulting RS field on 2024-T3 clad LJs. It could be concluded that higher squeezing force translated into higher radial expansion hence interference which in turn increased the magnitude and regions of compressive RSs around the rivet-hole. A comparison of RSs with a pure radial expansion model highlighted that for the rivet installation process a significant portion of the resulting RS field originates from the clamping of the two sheets. The rivet type was found to have no significant influence on the RS field. The benefits regarding the overall fatigue performance and crack growth of those numerically determined compressive

RSs near the rivet-hole that depend on the squeezing force were reported by Rans *et al.* [57,63] in a follow-up experimental study using LJ fatigue test samples altering the squeezing force [57,59]. From this investigation, it could be concluded that increasing the squeezing force and consequently the compressive RS characteristics around the rivet-hole result into an overall increase in fatigue life of LJ samples with universal and countersunk rivets, as demonstrated by Figure 2-22.

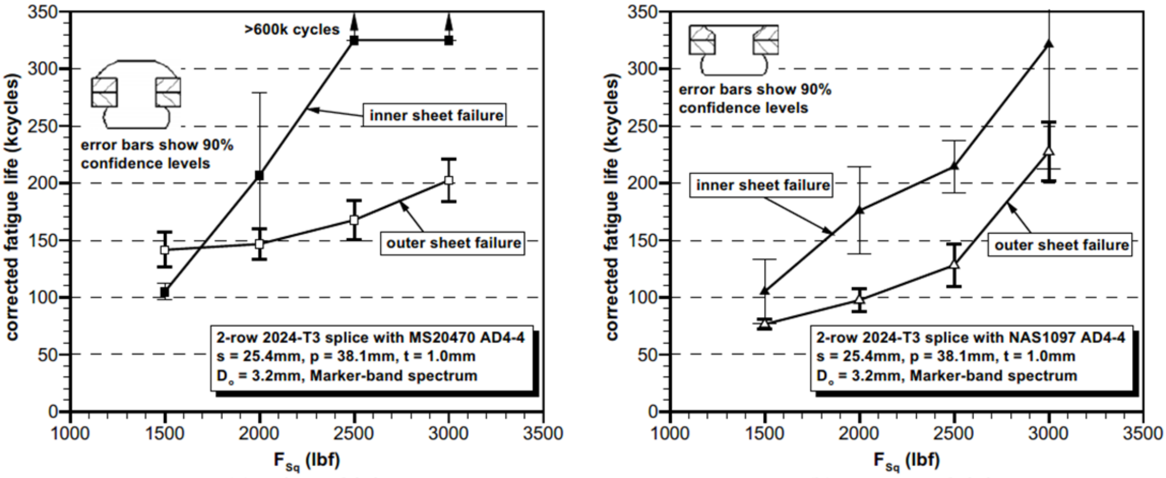

(a) universal joint (b) countersunk joint

Figure 2-22: Overall fatigue lives for inner and outer sheet failure for different squeezing forces and consequent different RS fields, as determined by Rans *et al.* [59]**. (Data plot was taken from** [59]**).**

Crack growth analysis of LJ was conducted by fractographical methods using SEM investigation and a marker band technique. Results underlined the benefits of increased compressive stresses as a result of higher squeezing forces on crack growth rates which could repeatedly be measured.

For Hi-Lok bolts, the final geometry of the bolt and the fastener-hole can be pre-defined as the manufacturing process does not involve any shape altering of the bolt, as is the case for solid rivets. This gives the designer a choice to define interference so that RSs are always the product of clamping but do not necessarily originate from interference. To the best knowledge of the author, there is no published study investigating the RS field resulting from the manufacturing process of LJs using Hi-Lok bolts. And further, the clamping forces which are produced by Hi-Lok bolts are not found in the literature. However, the mechanism and principles of interference and clamping which are involved in the formation of RS using squeezing rivet can be derived from previously summarised studies.

2.2.2.4 Failure Mechanism and Crack Initiation Location

As mentioned before the GAG load cycles of pressurised fuselage cabin incrementally induces fatigue damage in the LJ element. The most fatigue critical locations were found to be the skin at the upper and bottom fastener-rows (refer to Figure 2-13) due to secondary bending effects as described earlier. Principally, fatigue cracks initiate and emanate from three different locations as shown in Figure 2-23 at fastener-holes or in their near vicinity depending on the complex interaction of load transfer, secondary bending and residual stress conditions:

- Cracks at the net cross-section of the sheet in the fastener-row (Figure 2-23a).
- Cracks above the fastener-hole at the edge of the fastener
  (bolt circle in Figure 2-23b).
- Cracks above the fastener-hole at the edge of the clamped area (dashed circle in Figure 2-23c).

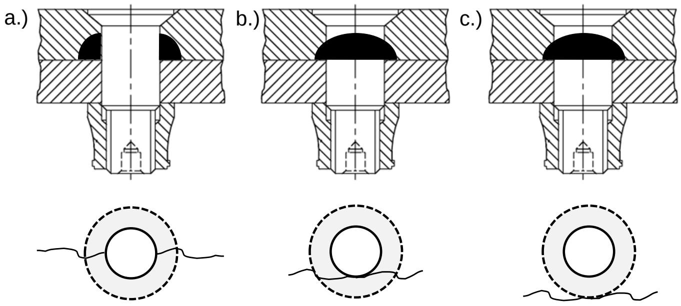

Figure 2-23: Most common fatigue crack initiation location in LJ samples.

Mueller systematically analysed the shift of the initiation location in dependence of the squeezing force and applied net-section stress [55]. His results are shown in Figure 2-24. Also Skorupa *et al.* [64] report data on fatigue crack location. Both studies concluded that initiation at the minimum cross-section is found when only a minor part of the load is transferred by surface friction. In consequence the fastener carries the bulk of the load and subsequently pressure is applied on the hole shaft which creates the stress conditions at the fastener-hole to initiate fatigue cracking (Figure 2-23a). Low-load transmission in Mueller’s work as shown in Figure 2-24 was a result of modest squeezing forces which in turn controlled the clamping force and the clamping pressure on the faying surfaces of the fasteners, as described in section 2.1. For higher clamping pressures which would result in increased load transfer in friction, however, the failure location moved away from the hole edge (Figure 2-23b). For a high clamped fastener condition the nucleation of cracks occurs above the hole at the boundary of the clamped area (Figure 2-23c). As described earlier in section 2.1 for high load transmissions in transient cyclic loading the load can be carried up to 90% by the faying surfaces. This growth leads to fretting-fatigue which is discussed separately in the next section.

Lastly, the applied maximum stress also influenced the failure initiation location for the same described reasons. For higher applied external loads the initiation moves back to the fastener-hole as for high loads more of the load is carried in a loaded pin-hole manner rather than surface friction. This is because higher loads can overcome the frictional forces executed by the clamping and move the sheets so that the fastener can carry the load. For lower applied stresses frictional forces may dominate the force equilibrium and no relative movements can be induced, so that surface friction and subsequent fretting-fatigue prevail.

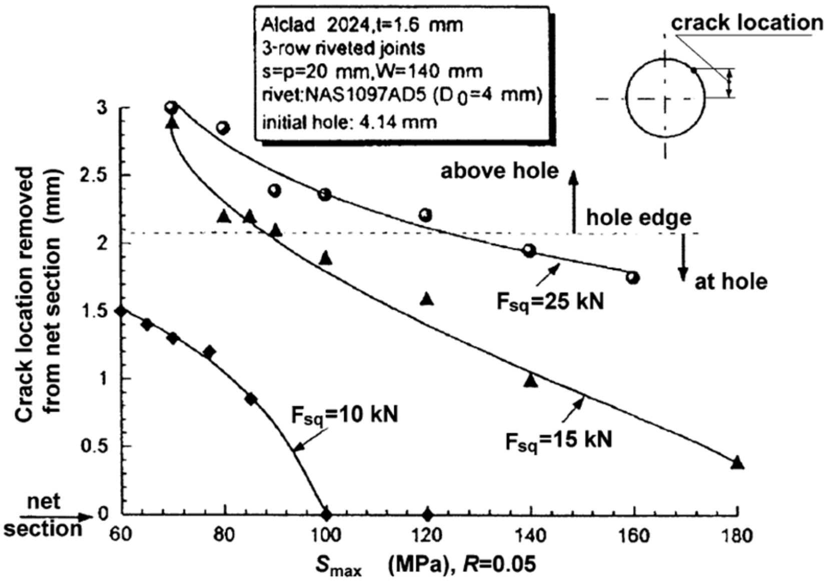

Figure 2-24: Dependence of the fatigue crack initiation locations in LJ samples on the applied maximum stress for different rivet squeeze forces, as investigated by Mueller [55]**. (Data plot was taken from** [55]**).**

2.2.2.5 Fretting-Fatigue in Lap-Joints

Fretting-fatigue describes the fatigue crack initiation and subsequent growth as a result of fretting. According to Hills and Nowell [65], Fretting is a synergy of wear, fatigue and corrosion. It occurs if two clamped bodies in contact move locally relative tangential to each other which could be caused by oscillatory motions such as fatigue cycling or vibrations. Szolwinski *et al.* [60] referred to a general three stage model of the fretting-fatigue process. In the first stage, local relative motion causes wear on the mating surfaces which typically remove the clad layer for clad aluminium alloys. After the oxide surface layer is worn away the underlying bulk material can begin to adhere to each other. "Cold-welds" are formed which accumulate wear debris between the contact surfaces. This is turn will increase the frictional forces as the coefficient of friction is increased by this wear debris. Recall the experimental results from Starikov [56] described in section 2.2.2.1 who could confirm the concept of this the second stage. Further cyclic motion increases the wear debris and induces plastic deformation on the contact surfaces which initiate multiple embryo fatigue cracks along the contact surface. If wear rates are high, those embryo cracks are again worn away. Instead, they propagate into the bulk material where they become stage II fatigue cracks governed by bulk far-field stresses and the laws of fracture mechanics.

The role of frictional forces as previously mentioned in section 2.2.2.1 was explained by Szolwinski *et al.* [66] and as shown Figure 2-25. With increasing clamping forces, frictional forces can resist any relative movements of the sheets which will stick the two sheets together. As the load is increased, those frictional forces may be overcome depending on the coefficient of friction and clamping force. This would lead to relative movement of the sheets thus slipping, and the load can be consequently transferred on to the fastener. On unloading, this slipping is reversed and frictional forces again become dominant in the load transmission. It is this stick-slip mechanics on the faying surface which cause wear. For high slip amplitudes and high clamping forces resulting in high contact stresses in the near surface region fretting damage is exerted. The complete theory of mechanics of fretting-fatigue can be found here [60,65,67].

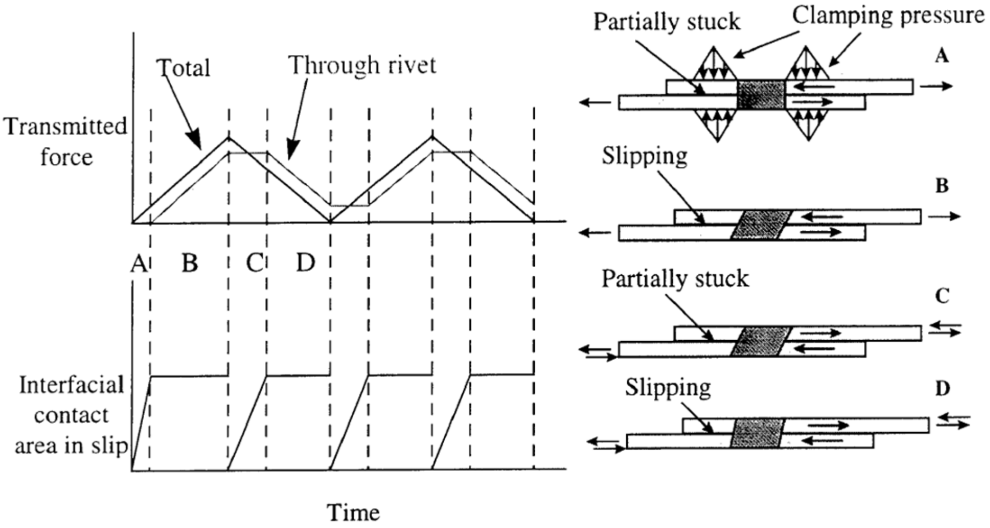

Figure 2-25: Schematic view of the load transfer in LJs inducing fretting-damage by Szolwinski *et al.* [66].

A few researchers studied the fretting-fatigue mechanics in LJ samples by FE analysis [58,68]. A detailed examination of surface contact stresses around the clamped region in the vicinity of the fastener-hole in LJs, and their relationship with subsequent fretting was conducted by Brown and Straznicky [58]. They correlated FE results of the distribution of contact surface stresses on the faying surface around the fastener-hole with to observed fretting-damage of 2024-T3 LJ test samples. They concluded that the peak maximum principal stress which is a result of the applied squeezing force responded well with the location of fretting-fatigue cracks.

Fretting-fatigue is a known issue, and it is recognised as the crucial fatigue initiation mechanism of LJ in aircraft fuselages which ultimately results into WFD [48]. The North American Space Agency (NASA) examined and catalogued in detail an extensively fretting-fatigue damaged 2024-T3 Alclad fuselage full-scale fatigue test barrel after 60,000 simulated flights [69]. Tear-down inspection showed that fatigue cracks initiated by fretting at the faying surface and grew along the faying surface up to three skin thicknesses before they broke through to the outer surface. At the outer skin, fretting-fatigue cracks occurred under all rivets. WFD and MSD were also found in the test article as cracks linked-up proving that fretting-fatigue is a major issue of ageing aircraft fleets.

A complete review of fretting and fretting-fatigue literature from 1960 to mid-1996 with a major focus on aircraft joints was compiled and summarised by the U.S. Department of Transportation [70] showing again the appreciation by major stakeholders in the field of aircraft structural integrity of the wide-spread issues of fretting-fatigue in aircraft LJ.

2.2.2.6 Growth of Fretting-Fatigue Cracks

Analysing the growth of fretting-fatigue cracks in LJ samples is often an experimentally challenging exercise, as those cracks initiate on the faying surface where they cannot be observed in-situ or non-destructively. For that reason, fractographic post-mortem analysis techniques were often used by researchers [57,59,71,72] to investigate the development of the shape of fatigue cracks in LJs.

Fretting-fatigue cracks can be divided into two separate phases which lead to their distinguishable fracture surfaces on the sample. The first phase is dominated by the fretting process and local contact forces besides the overall global loading. The left behind fracture of this phase does not exhibit classical features of a fatigue crack such as radial marking emanating from the initiation location. The second phase is only controlled by classical fatigue theory and depends on global loading only. Features of the fracture can be easily identified and compared to standard fatigue theory. Gracia and Grandt [72] studied fracture surfaces of fretted fatigue samples and formulated a criterion to distinguish the two phases on a fracture surface of fretted samples:

"*A fretting crack fracture surface […] can be observed by locating the remaining fracture surface that does not resemble or is not indicative of a fatigue crack surface*" [72].

With this criterion, the researchers found that for fretted fatigue samples those two regions can be conveniently identified during fractographic investigations for their test samples. It could be concluded that fretting-fatigue cracks start from multiple fretted initiation locations which then coalesced into one larger fatigue crack and that the fretted region penetrating from the faying surface can be as deep as 750 µm for their test samples.

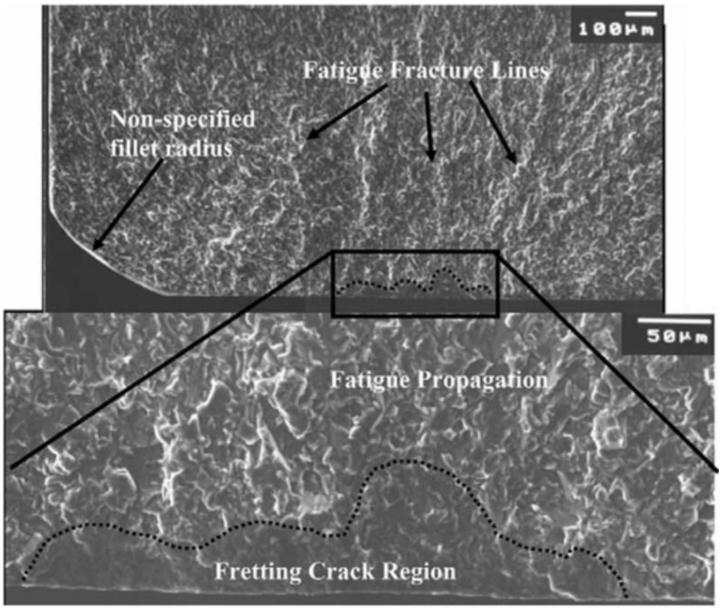

Figure 2-26: Fracture surface showing typical fretting cracks, as found by Gracia and Grandt [72]**.**

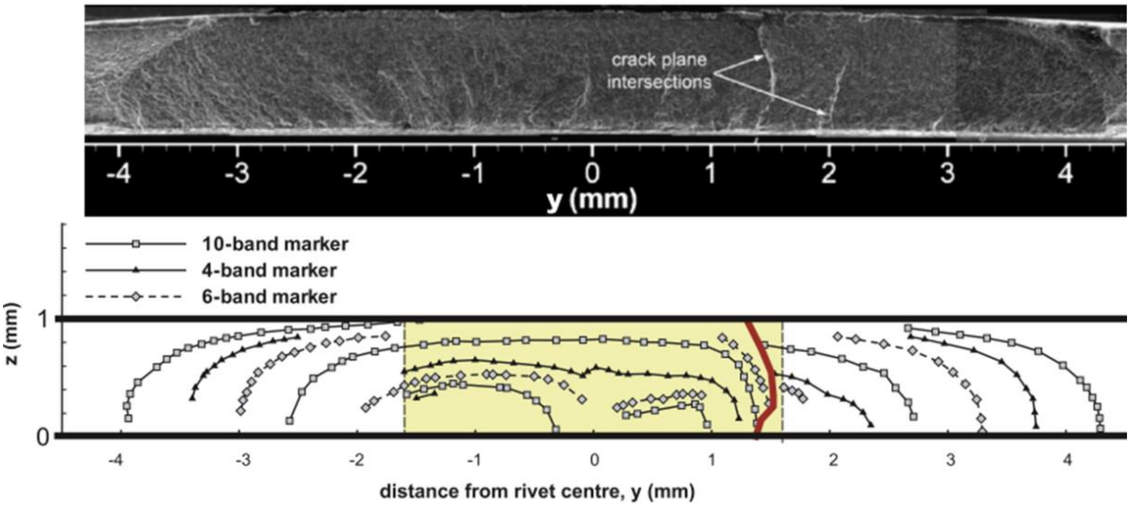

Figure 2-27: Fretting fatigue crack front reconstruction for 2024-T3 LJ samples, as observed by Rans *et al.* [59]**.**

Fatigue cracks in LJ samples exhibit the same two distinguishable features as described by Gracia and Grandt [72] who used uniaxial dog-bone test samples in a standard fretting-fatigue test rig. However, the development of the fatigue crack which will eventually form as fretted initiated multiple cracks coalesced with each other were studied by Rans *et al.* [59]. In Figure 2-27 fretting-fatigue crack of 2024-T3 Alclad LJ samples are illustrated as obtained by Rans *et al.* [59]. Using an extreme time consuming fractographic marker band technique Rans *et al.* [59] found that multiple crack initiation location eventually forms a semi-elliptical crack shape which propagates through the thickness as well as along the faying surface (compare with Figure 2-23). Multiple crack planes were found on the fracture surface indicating multiple origins. The semi-elliptical shape was attributed to high secondary bending stresses. This shape development of semi-elliptical fatigue cracks derived from secondary bending was initially studied by Fawaz [71] who concluded from his work that the crack advance along the faying surface significantly exceeded than that in the thickness direction. This effect was especially true for a higher sheet thickness. However, there was no effect on the total fatigue life observed.

2.3 The Role of Residual Stresses and Laser-Peening in Fatigue

The role of RS in fatigue and fracture mechanics is significant. RS can have both detrimental and beneficial effects on the fatigue performance depending on the algebraic sign and location in the component so that knowing the RS state in any structure which is subjected to external cyclic loading and therefore is susceptible to fatigue damage needs to be carefully assessed. RS denotes a mechanical stress state within a structure or component without the presence of any external load (mechanical or thermal). RS are mostly locked in from previously applied mechanical or thermal processes to any structure or component. A RS field always consist of compressive and tensile stresses as the mechanical stress equilibrium condition must be fulfilled in a body as formulated by the following equations assuming a three-dimension infinitesimal cube as shown in Figure 2-28:

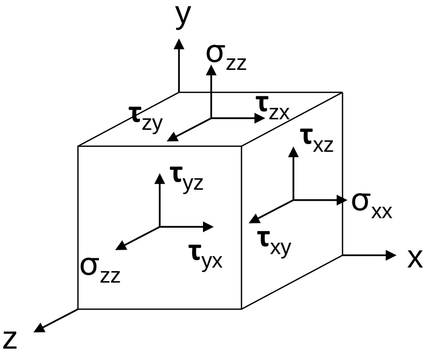

Figure 2-28: Infinitesimal three-dimensional cube and all relevant stress components

$$\frac{\partial \sigma_{xx}}{\partial x}+\frac{\partial \sigma_{xy}}{\partial y}+\frac{\partial \sigma_{xz}}{\partial z}=0\ \ (Equation\ 2.18a)$$

$$\frac{\partial \sigma_{xy}}{\partial x}+\frac{\partial \sigma_{yy}}{\partial y}+\frac{\partial \sigma_{xz}}{\partial z}=0\ (Equation\ 2.18b)$$

$$\frac{\partial \sigma_{xy}}{\partial x}+\frac{\partial \sigma_{yy}}{\partial y}+\frac{\partial \sigma_{zz}}{\partial z}=0\ (Equation\ 2.18c)$$

An illustrative example of a RS field thought the thickness (σ_{res}) of a sheet with the thickness *t* is shown in Figure 2-29. Near surface compressive RS (-) with high-stress gradients are balanced out with tensile RS (+) in the core of the sheet. Respectively, in this example, the one-dimensional equilibrium conditions is fulfilled if the following equation

$$\int_{-t/2}^{t/2} \sigma_{x,res}\, dx=0\ (Equation\ 2.19)$$

is satisfied. Equally, the same condition must be satisfied for moment and thermal formulations. For 2D plane stress condition ($\sigma_z = 0$), RS (σ_{res}) can be described expressed as:

$$\frac{\partial \sigma_{xx}}{\partial x} + \frac{\partial \sigma_{xy}}{\partial y} = 0 \quad and \quad \frac{\partial \sigma_{xy}}{\partial x} + \frac{\partial \sigma_{yy}}{\partial y} = 0 \; (Equation\ 2.20a\ and\ 2.20b)$$

Stress components can be calculated using Hooke’s law (plane stress):

$$\sigma_{xx} = \frac{E}{1-\nu^2}\left(\varepsilon_{xx+}\nu\varepsilon_{yy}\right) \quad and \quad \sigma_{yy} = \frac{E}{1-\nu^2}\left(\varepsilon_{yy+}\nu\varepsilon_{xx}\right) \; (Equation\ 2.21a\ and\ 2.21b)$$

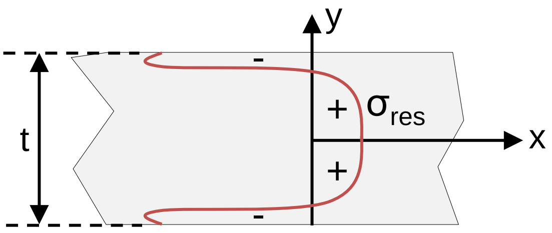

Figure 2-29: Example of residual stress field (Illustration according to [32]**)**

A comprehensive overview of the role of RSs in the degrading processes during material fatigue can be found in the textbook by Withers [73].

2.3.1 Origins of Residual Stress

The origins or causes of RS within a component are multiple. RSs can be introduced into a part unintentionally as it is the case in welding or casting processes for instance. This process is caused by different thermal behaviours of different areas of the component. During casting different areas of the casting material have dissimilar cooling rates and grains are formed inhomogeneous so that misfits of the various grains are locked in, and RS are caused. Those RS are unwanted but come as a by-product of the manufacturing process.

RS can be introduced by cold worked processes, rather than previous mentioned thermal induced RS. In contrast to previously described unintended RS, there are RS which are introduced into the structure by design using processes such as cold-expansion (Cx), shot-peening (SP), deep surface rolling, pneumatic hammer peening or laser-peening (LP). Those RS are a product of introduced irreversible inhomogeneous plasticity (permanent deformation) and a correspondent elastic response by the respective surrounding material. In the following, the Cx, SP and LP process will be introduced and compared as those methods find extensive conventional applications in the aerospace industry.

2.3.1.1 Cold-expansion Process

The FTI split sleeve cold-expansion technique [8] is described since this is the most relevant to the aerospace sector to enhance the fatigue life of fastener holes. In fact, it is commonly used by aircraft manufacturers since it was developed by Boeing in the early 70s. During the FTI cold expansion process an oversized tapered mandrel, pre-fitted with the lubricated steel split sleeve, is pulled through a pre-drilled hole as shown in Figure 2-30a. The mandrel and the sleeve are designed to result in prescribed plastic deformation of the hole shank, which in turn outcomes in a RS field around the hole as illustrated in Figure 2-30b and Figure 2-30c. In fact, these RS are the result of an elastic region which surrounds the plastic region around the hole. This elastic region is pushing back on the plastically deformed region near the hole, and therefore compressive stresses are induced. Tensile RSs are formed to satisfy the stress equilibrium condition.

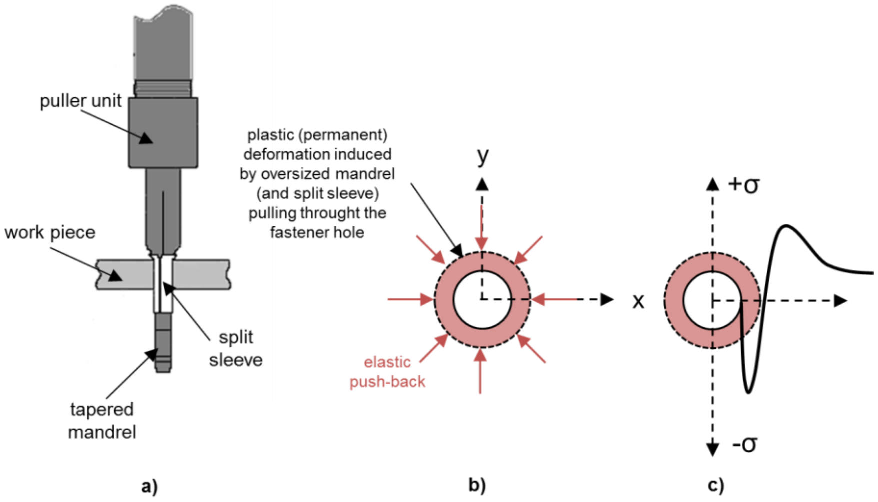

Figure 2-30: Cold-expansion process. a) FTI split sleeve cold-expansion tooling b) Mechanism of RS generation c) Example of typical RS by cold-expansion.

Although the split sleeve cold-expansion technique is commercially used since 1969, literature presenting the beneficial results on crack initiation and growth is mainly limited to no transfer open-hole samples [9,20,74,75] rather than more complex structural joint specimens [76–78].

2.3.1.2 Shot-Peening

Similar to the Cx process, shot-peening is also a cold-worked process in which a work piece is bombarded with spherical particles. Those particles can be made of glass, ceramic or metal and cause when impacted on the surface of the work piece a local permanent deformation (dimple), as illustrated in Figure 2-31. Those permanent deformations, in turn, lead to the reaction of the surrounding material which elastically push back onto the deformed region and therefore produce compressive RS at the surface and sub-surface region. A typical RS profile is given in Figure 2-31c. RS profiles induced by SP are limited (< 1 mm) regarding the penetration of compressive RS [28] so that SP can only be considered for application regarding the near surface region, e.g. surface cracks [30].

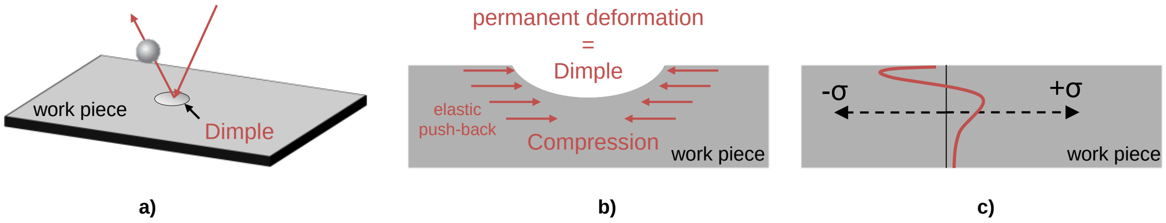

Figure 2-31: Illustration of Shot-Peening Process (Illustration according to [28]**). a) Principle of the SP process b) Mechanism of RS generation c) Typical RS profile induced by SP.**

Metal Improvement Company (MIC) which is a major vendor of SP services uses SP for a number of industrial applications such as SP of gears to improve the performance of the root section of the tooth profile which is intensely loaded by bending loads. Other applications include fatigue improvements of crack shafts, compression springs and turbomachinery blades and buckets [19].

2.3.2 Laser-Peening

Laser-peening, often also referred as Laser Shock Peening (LSP) is in relation to the previously introduced processes a “new” technique to induce RS states into metallic components. It is new in the sense of conventional prevalence and applications in relevant industries which are up till today not as wide spread as Cx or SP for a number of diverse reasons. Today commercial applications of LP to improve fatigue properties are known for improvement of fretting of titanium fan blade dovetails of Rolls Royce engines [31]. LP is provided by MIC for fan blade application with its only own plant site in Derby, UK besides its Headquarters in the US [79]. FAA and CAA have certified the laser peening treatment [79]. Other applications of LP are limited to military projects, such as LP of wing attachment lugs of F22 Raptor aircraft [80] to increase inspection intervals to reduce operational costs.

However for the research community LP is known since the early 1970s where LP as a process to induce RS into metals was researched and developed with great effort by the Battelle Memorial Institute in Columbus, Ohio in the US [81–85]. This basic research focused on the understanding of critical process parameter and configurations [81,82,85] and first attempts to enhance the fatigue performance of fatigue test samples [84] using a high energy (200 J) neodymium glass pulsed laser.

Subsequent research was performed in France by Fabbro and Peyre *et al.* at the Laboratoire d’Application de Lasers de Puissance-Arcueil Cedex (LALP) [86–88] which lead to one of the most acknowledged publication in the field [86] with almost 500 citations. Both the US American and French work is based on a LP process variant referred as “confined ablation mode” (CAM) in which a metallic work piece is irradiated with a short (in the scale of nanoseconds), intense (greater than 1 GW/cm^2) high energy laser pulse (>10 J) and rather large spot sizes (diameter: 3 – 5 mm) which generate high-pressure shock waves travelling into the work piece. The high-pressure shock wave is a result of the interaction of the focused laser beam with the sacrificial opaque overlay, most commonly black paint or metallic foil, which covers the sample, and the confining medium, most commonly water.

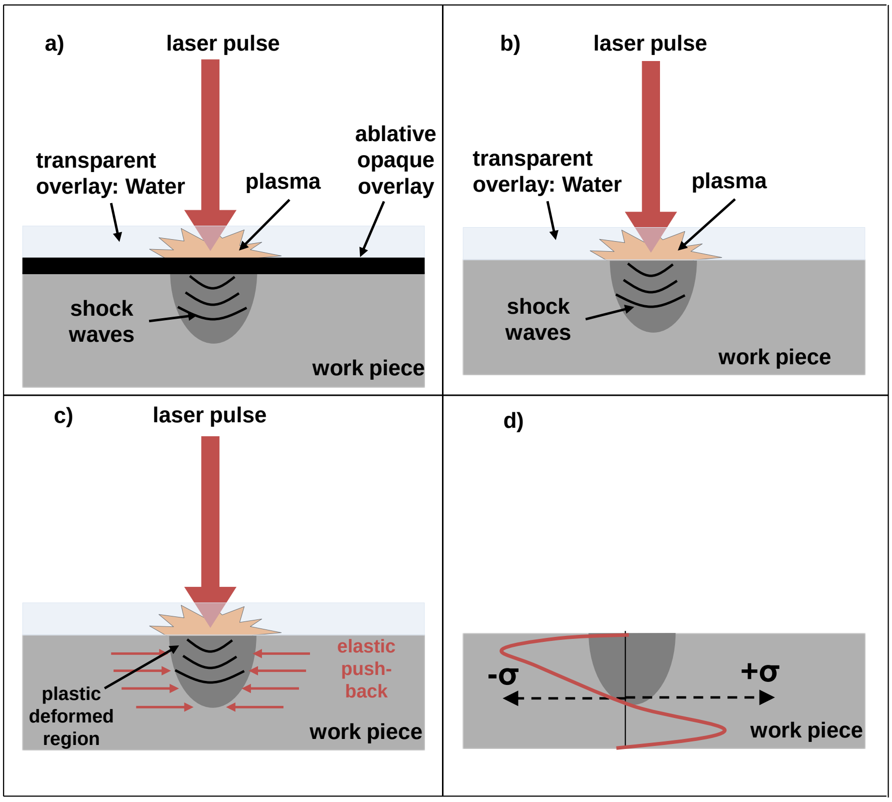

Figure 2-32: Illustration of Laser-peening Process. a) Principle of LP in confined ablation mode b) Principle of LP without Coating (LPwC) c) Mechanism of RS generation d) Typical RS profile induced by LP.

The confined ablation mode LP set-up is illustrated in Figure 2-32a. The sacrificial opaque overlay prevents any thermal effects on the surface of the target by protecting the material surface from any ablation. Hence, LP can be considered an exclusively mechanical treatment. However, when the laser beam, characterised by the spot size (d), the frequency (f), the wave length (nm), the pulse duration (ns) and energy (J), hits the opaque overlay, this thin layer of sacrificial overlay of which only a very thin portion (less than 10µm) is ablated, absorbs the laser energy, and is being vaporised. This vapour further absorbs the laser energy and is steadily heated and ionised into plasma. The plasma expands but is constrained by the confining medium (water) which results in a generation of shock waves which propagate into the material. This wave causes permanent plastic deformation to a depth at which the peak stress no longer exceeds the Hugoniot elastic limit (equivalent to yield strength under shock conditions) of the metal. This plasticisation, in turn, induces residual stresses in the affected region, as shown in Figure 2-32c. A typical RS profile can be characterised by a compressive region underneath the treated surface with a peak value of compressive stress near the surface and a tensile region surrounding the compressive region to balance the stress state [86], see Figure 2-32d.

Recently, much LP research is performed by academia such as the Universidad Politécnica de Madrid [10,89–96] or in Johannesburg at the University of the Witwatersrand, South Africa [10,22,23,97]. Those research groups use another variant known as LP without Coating (LPwC) in which the basic principles of LP as just described are applied but no sacrificial opaque coating is utilised in the LP process set-up, see Figure 2-32b. This set-up additionally is characterised by lower laser energies (100 mJ – 2.5 J), higher overlapping of single laser spots and smaller laser spot sizes (diameter: 0.4 – 1.5 mm) than what is used in the "confined ablation mode". The decrease in laser energies in LPwC set-ups is applied to minimise thermal effects on the surface of the work piece. Originally this approach was used by Toshiba Corporation [98,99] to LP nuclear power reactors as the accessibility of the boiling water reactor was a problem due to radio activity and the location of the boiler under water so that since then LPwC has established its place as a flexible LP variant. However, studies using medium energy lasers investigating the effect of the sacrificial coating have shown that the peak compressive RS is higher for the "confined ablation mode" [90].

Further details on LP can be found in review papers [100,101] which give insight into the effects of LP on mechanical properties such as micro-structure and hardness or on LP process parameters on resulting RS fields. Specific discussions on those results are described later if necessary. In the following, only LP process parameters and their effect on RS are introduced.

2.3.2.1 Laser-Peening Parameters

LP process parameters which need to be considered in defining any LP treatment are: (1) Wave length of the laser beam [nm], (2) Laser energy [J] (3) Laser frequency [Hz], (4) Pulse duration (FWHM) [ns], (5) Laser spot geometry and size/ Laser spot area [mm^2] – which can be derived into a significant LP performance indicator: The **Power Density** which is defined as:

$$\boldsymbol{Power\ density}\ [GW/cm^2] = \frac{Laser\ energy\ [J]}{Pulse\ duration\ [ns] \cdot Laser\ spot\ area\ [cm^2]}$$

The power density represents the performance of a single pulse and in realistic LP applications an array of laser pulses which is needed to cover a designated area on the target component. This designated area is referred to as the **LP layout**. In that context two more parameters can be defined to form a complete LP strategy:

The **pulse density (or coverage)** which is defined as:

$$\boldsymbol{Pulse\ density}\ [pulses/cm^2] = \frac{number\ of\ laser\ pulses\ [\#]}{LP\ layout\ area\ [cm^2]}$$

and the **LP pattern** which is the definition of a sequence of laser spots to LP the LP layout.

A commonly applied LP pattern [10,91–96,98,102] is shown in Figure 2-33. This LP pattern is a raster zig-zag pattern in which two directions can be differentiated. The **scanning**

direction, as indicated in Figure 2-33, defines the advancing directions to form a row of laser pulses. The **stepping direction** consequently is referred to the advancing direction of multiples rows of laser pulses. However, other investigators used different LP patterns [24,103,104] especially for the “confined ablation mode” LP set-up. The raster zig-zag pattern is commonly for LPwC.

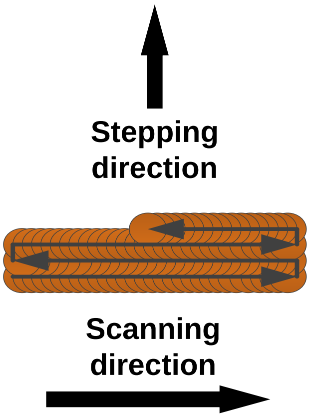

Figure 2-33: LP raster zig-zag pattern.

2.3.2.2 Effect of Laser-Peening Parameters on Residual Stresses

Investigations of the impact of LP process parameters on RS profile are a central objective to optimise LP strategies on different materials and geometries. A typical RS profile through the thickness is shown in Figure 2-34. There can be six parameters declared to describe a RS profile:

(1) penetration depth which defines the depth measured from the surface up to which compressive RS are present
(2) maximum or peak compressive RS magnitude
(3) depth of maximum compressive RS magnitude
(4) maximum or peak tensile RS magnitude
(5) depth of maximum tensile RS magnitude
(6) surface RS

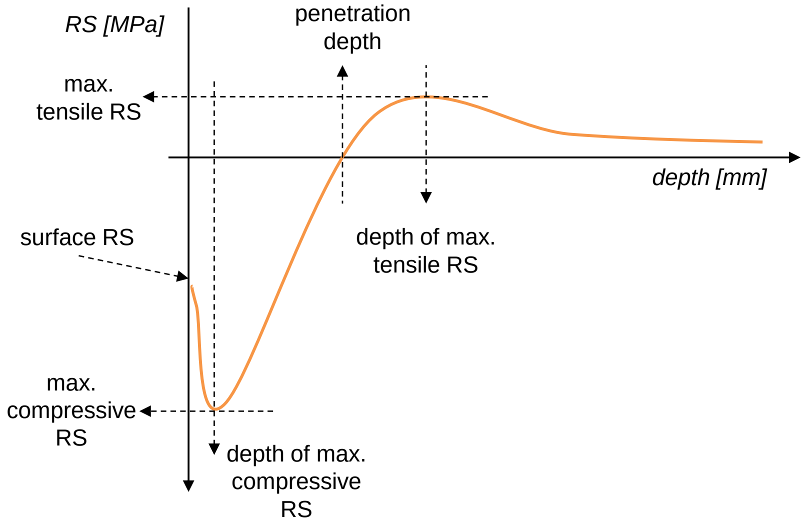

Figure 2-34: Example of a typical Residual Stress Profile through the thickness and describing characteristics.

Typical values of RS profiles depending on LP process parameters and processed material are summarised in Table 2-1. It can be abstracted from this review that LP induced RS profiles show:

- peak compressive RS of 75 MPa – 410 MPa for 7000 series aluminium alloys
- penetration depth greater than 2.5 mm for 7000 series aluminium alloys
- peak compressive RS of 600 MPa – 1200 MPa for stainless steel
- penetration depth greater than 4 mm for stainless steel
- peak compressive RS of 180 MPa – 200 MPa for 2000 series aluminium alloys
- penetration depth of 0.9 mm for 2000 series aluminium alloys

Table 2-1: Overview of published RS profiles and applied LP process parameters

Researchers Ref.	material	LP variant	LP process parameters:						LP pattern	resulting RS profile characteristics:					
			power density	pulse density	pulse repitition	spot geometry and size	laser energy	pulse duration FWHM		penetration depth	max. compressive RS	depth of max. compressive RS	max. tensile RS	depth of max. tensile RS	surface RS
			[GW/cm2]	[pulse/cm2]		[mm]	[J]	[ns]		[mm]	[MPa]	[mm]	[MPa]	[mm]	[MPa]
Peyre [86]	7075-T7351 t = 40 mm	CAM	1		1	circular diameter: 5-12		15-30		>2.5	surface value				-75
			2		1										-150
			2		2										-175
			3		1										-160
			3		3										-300
			4		3										-350
Rubio-González, et al. [92]	duplex stainless steel t= 9.5 mm	CAM		900		circular diameter: 1.5	2.5	8	rzz	>4	-600	surface 0.0			-600
				1600						4	-800	surface 0.0			-800
				2500						>4	-1200	surface 0.0			-1200
Ocaña,J.L et al. [95]	2024-T351 t = 8 mm	LPwC		900		circular diamter: 1.5	2	9.4	rzz	0.9	-180	sub-surface: 0.1			
				1600						0.9	-200	sub-surface: 0.1			
				2500						0.9	-180	sub-surface: 0.1			
Luong,H. Hill,M.R. [104]	7075-T7451 t=19mm	CAM	3		3	square		18		2.19	-311	sub-surface: 0.121			
			4							2.44	-339	sub-surface: 0.101			
			5							2.42	-411	sub-surface: 0.05			
P.R. Smith et al [81]	Ti-6Al-4V	CAM	5.5		3	circular diameter: 5.6				>0.5	-650	surface 0.0			
			7								-600				
			9								-600				
			5.5		1					>0.5	-500	surface 0.0			
			7								-550				
			9								-450				

The effects of pulse density on the RS profile as studied by Peyre *et al.* [86], Rubio-González *et al.* [92] and Ocaña *et al.* [95] and the effect of pulse repetition, which describes the repetition of multiple laser pulses at the same location, as studied by Peyre *et al* [86] and P.R. Smith *et al.* [81] for aluminium[86,92,95] and titanium alloys [81,95] on the RS profile have shown that:

- All materials have their optimum shock conditions [86,95] regarding the pulse density. A general trend, however, is that with increasing pulse density the peak compressive RS increases but after exceeding a certain value, RS increases in depth but the peak compressive stress near the surface decreases [86]. For AA 2024-T351 plate with a thickness of 8 mm, for instance, a maximum of compressive peak stress can be found between the pulse densities of 1500 pulses/cm^2 and 2000 pulses/cm^2 for an applied laser energy of 2 J, a laser beam spot size of 1.5 mm and no use of opaque sacrificial layer in the set-up [95].
- Increasing the pulse repetitions, the peak compressive RS increases. This relationship was found for aluminium [86,95] and titanium alloys [81]. For cast alloys, an increase in the number of impacts of the laser beam would enhance the affected depth of the material but would not further increase the maximum compressive RS magnitude near the surface [86].
- The power density can increase the peak compressive stress, but saturation will be achieved individually for every material. Pulse repetition can overcome this saturation so that the peak compressive RS can be further increased [86]. In general, it can be summarised that power density is not as effective as pulse density or pulse repetition in alter the RS profile.

The effect of wave lengths on the RS field has been analysed by G.Gomez-Rosas *et al.* on Al.6061-T6 alloy [93]. They found that for wave lengths of 1064 nm and 532 nm the RS profile is similar in shape and with increasing pulse density, the maximum stress increases respectively. For 1064 nm wave length and 1.2 J energy, the maximum compressive stress has been found greater than for 532 nm wave length and a pulse energy of 0.9 J.

Recently, the research investigated the effect of LP parameters beyond LP process parameters themelves. The effect of the LP raster zig-zag pattern for instance has been studied by Correa *et al.* [102] by means of FEA suggesting that RS anisotropy can be manipulated using the LP pattern orientation. They conclude that for a raster pattern where the LP layout dimension in the stepping direction is longer than the dimension in the scanning direction, the stress component in the stepping direction will become dominant. Conclusively, the orientation of the raster pattern needs to be carefully chosen depending on the component and loading conditions.

Despite these efforts of investigating effects of LP raster pattern, no analyses were found to the best knowledge of the author, which engages with the effect of different proportions of a laser-peened and un-peened region in a test sample. As known from Peyre *et al.* [86] the remaining elastic material generates compressive RSs. Limiting space in which material can remain elastic would have effects on the generation of compressive RS, but no systematic obtained experimental nor theoretical data is available.

2.3.2.3 Laser-Peening versus Shot-Peening

As SP is currently the most conventional technique to induced RS into metallic materials, LP must offer significant unique features in order to justify its place in further research and eventually application in industry. Although, LP is similar to SP as both processes are applied to engineer RS fields and are based on principles of cold-working targeting the surface. However in terms of resulting RS field some distinct differences can be found in published research.

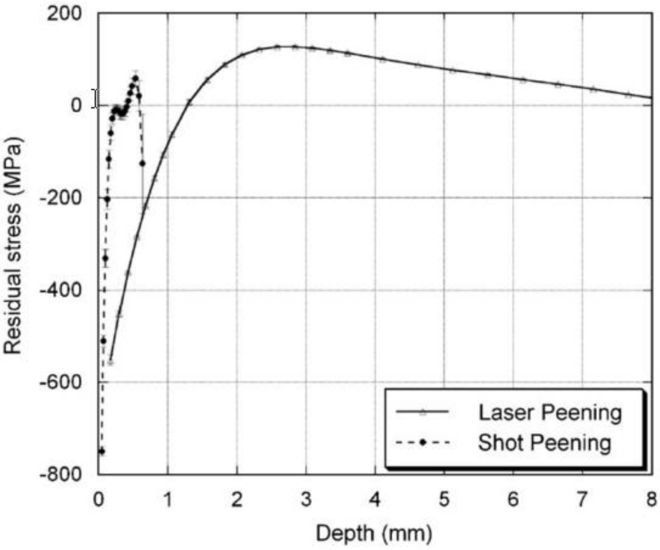

Figure 2-35: One-dimensional RS profile for LP and SP titanium (Ti–6Al–4V) measured by slitting method by K. Liu and M. R. Hill (Data plot taken from [105]**).**

Comparing LP with SP as done by C.A. Rodopoulos *et al.* [106] and K. Liu and M. R. Hill [105] the general picture arises that SP has the potential to induce larger peak compressive stresses into the material than LP. However, for SP samples, penetration depths were observed significant smaller than for LP. C.A. Rodopoulos *et al.* [106] peened a 30.0 mm thick rolled 2024-T351 plate with LP and SP. LP was performed using 10 GW/cm^2 and 2 and 3 passes and was contrasted with SP samples peened with 4A intensity [106]. For LP the peak compressive RS was measured by the hole-drilling technique for the sample having 3 LP passes to be -230 MPa in the near surface region. SP provided a peak compressive stress of -350 MPa. The penetration depth for SP could not be measured but from the collected data it can be noticed that for LP samples significant more thickness is covered in compressive stresses than for SP samples. This trend was also found by K. Liu and M. R. Hill who used a rolled milled and annealed Ti–6Al–4V plate of final sample thickness of 6.35 mm during their peening procedures. Their LP treatment was defined as power density of 10 GW/cm^2, a pulse duration of 18 ns, and a 3.0 mm spot size whereas the SP treatment used an intensity of 8A on the Almen strip. Figure 2-35 shows their RS result for LP and SP samples and it can be seen that SP induces greater compressive SR of 750 MPa at a sub-surface location of 0.05 mm while LP generates a compressive RS of 552 MPa at a depth of 0.17 mm. Penetration depths of the LP samples is clearly larger than for SP [105].

In addition to the differing RS field, another major distinction can be made when LP is compared with SP. Surface roughness measurements showed that SP produces higher surface roughness than LP which if applied in confined ablation mode as done by K. Liu and M. R. Hill [105] leaves waviness on the surface rather than altering the roughness. Peyre *et al.* provided however R_a values of LP (R_a = 1.3 μm) and SP samples (R_a = 5.7 μm) which underline this observation. The un-peened samples had a Ra value of 0.6 μm. However, for LPwC this trend could be different. No direct comparison could be found but Sánchez-Santana *et al.* [94] reported for their LP experiments without the use of protective coating, a surface roughness value (R_c) of 12.166 μm. This was an increase by a factor of 2.85 in comparison to the un-peened surface (R_c = 4.226 μm). As fatigue initiation is mainly a surface phenomenon as described earlier the implications of those observations can be significant. The the effects of different RS profiles and surface conditions produced by LP and SP will be discussed in course of the next section.

A relative recent review paper from 2014 by Sticchi *et al.* [25] compares several RS engineering techniques and discusses processes beyond Cx, SP and LP and their resulting RS field and their impact on the fatigue life. The paper concludes that LP is a very flexible technique compared to other processes to enhance the fatigue life by engineered RS fields. However, it was found that although LP is already applied at maintenance and production of aircraft engine parts for its merits, the application on airframe components is still more an academic activity rather than industrial.

2.3.3 Effects of Residual Stress on Fatigue and Crack Growth Performance

The beneficial or detrimental effects of RSs on fatigue and crack growth are widely researched today for a diverse range of RS origins. The causes of RSs can be manifold, e.g. thermally induced due to welding processes [44,107,108] or Laser-Heating (LH) [12,17,18] or cold-worked induced by SP [30,104–106], Cx [9,20] or LP [27,86,89,92,109–117]. Fatigue and crack growth of LP induced RSs in various sample geometries were mainly investigated for aluminium alloys [27,86,92,109,110,114–116], titanium [113] and steels [86,89,117]. In the following a review related to mainly LP induced RSs will be made to address the effects of RS on fatigue, fretting-fatigue and macro crack growth.

Published research on the fatigue performance in laser-peened induced RS fields suggests that the fatigue resistance and the fatigue initiation location are significantly affected. Peyre *et al.* [86] conducted fatigue experiments using a three-point bending test (stress ratio R = 0.1; test frequency f = 40-50 Hz) and untreated, shot-peened and laser-peened 7075-T6 test samples. Crack initiation and crack growth stages were detected by using a potential drop method. From this research, as shown in Figure 2-36, two major conclusions can be made. Firstly, LP has the potential to improve the fatigue performance by a significant factor and is superior in that attempt to SP. Secondly, the improvements are mainly based on the crack initiation stage rather than the crack growth stage, as analysed by Peyre *et al.* [86].

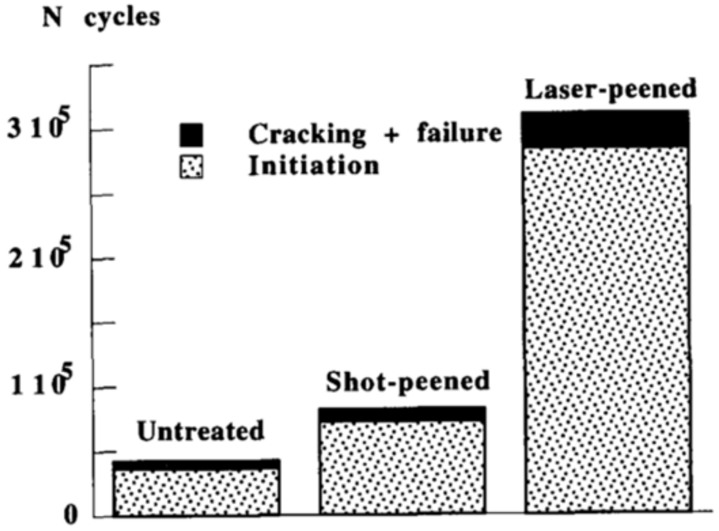

Figure 2-36: Fatigue response for untreated, SP and LP 7075 alloy. Comparison of initiation and crack growth stages at σ_{max} = 260 MPa as experimentally determined by Peyre *et al.* [86]**.**

As per the fatigue initiation location, it was found by several researchers including G. Ivetic *et al.* [10] who analysed the fatigue performance of laser-peened AA 6082-T6 open-hole fatigue samples, X.Q. Zhang *et al.* [118] who used AA 7075-T6 aluminium alloy to investigate the fatigue failure of laser-peened CT-samples, L. Zhang *et al.* [119] who investigated different shocked paths on fatigue property of AA 7050-T7451 dog-bone samples and Liu and Hill [105] who examined laser-peened fretting-fatigue test samples that the failure initiation were transferred to sub-surface locations underneath the LP region. This shift of failure location was correlated with regions of significant balancing tensile RSs for all studies which came as a by-product of the LP process to equilibrate the induced compressive RS field. In Ivetic *et al.* [10] samples a maximum tensile RS of 50 MPa was reckoned from FE predictions whereas Liu and Hill [105] provided RS measurements of up to 200 MPa tensile RS in their titanium samples underneath the surface. It was concluded that those significant tensile RSs promoted fatigue initiation caused the change in location while the targeted area which was filled with compressive RSs was “healed” from fatigue failure initiation mechanisms. In contrast to the studies by G. Ivetic *et al.* [10], L. Zhang *et al.* [119] and X.Q. Zhang *et al.* [118] whom all reported a beneficial effect as an overall fatigue life improvement, are the experiments conducted by Liu and Hill [105] on laser-peened fretting-fatigue samples. Their results exposed failure which occurred outside the fretted zone and provided no fatigue life enhancement marking ambiguous fatigue behaviour for LP samples. No overall benefit of compressive RS was also found by A. Chahardehi *et al.* [117] as high balancing tensile RSs of approximately 150 MPa in the core of the steel test samples overwhelmed all potential benefits of the compressive stress field of -550 MPa underneath the penned surface.

This inconclusive effect on the fatigue performance of LP samples clearly arises from the LP literature. Although the majority of scientists report on a range of beneficial effect of life improvements on the overall fatigue performance of usually factors of 3 - 4 [26,86,102,104,118] compared to untreated samples, other studies also created awareness that LP could also result in no or even negative fatigue life extensions [10,24,117] due to unwanted sub-surface cracking caused by high tensile RSs or due to internal cracking induced by hard LP treatments [120].

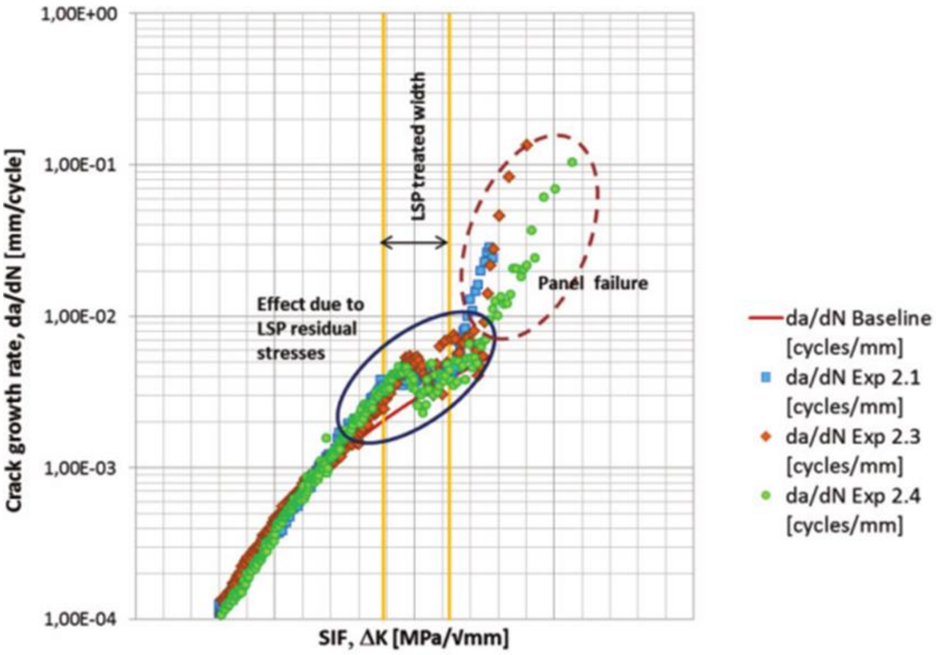

Figure 2-37: FCGR (da/dN) vs SIF range (ΔK) for laser-peened aluminium CCT-sample (160 mm by 400 mm by 2.0 mm) as studied by S. Taddia and E. Troiani [27].

The effects of LP induced RSs on macro crack growth characteristics were also investigated by various research groups using typical CT samples [89,92,112–116], but also efforts on CCT-samples were outlined in a conference paper by S. Taddia and E. Troiani [27]. They described the effect of LP on crack growth behaviour of 2 mm thin aluminium sheets with a centre starter notch. In the paper, the authors laser-peened a stripe on a 160 mm by 400 mm CCT-sample left and right to the centre notch. The consequent *da/dN* vs *ΔK* data, as shown in Figure 2-37, revealed that retardation of crack growth rate within the LP stripe (LPS) occurs but there was no overall life extension observed on the crack life. This reduction was explained by an acceleration of cracks due to balancing tensile RSs outside the peening stripe. As the peening stripe was placed with a distance (no quantifying data provided) to the centre notch, the crack travelled through the balancing tensile RS field and accelerated which in turn resulted in a detrimental crack life reduction.

Other studies on the crack growth period in LP CT-samples showed that if the peening area is designed in a manner so that the compressive RS is maximised and is placed near to the crack tip an overall benefit can be observed in test samples [92,113]. To that end, J.Z. Zhou *et al.* [113] conducted LP experiments varying the dimension of the LP area adjoining the crack tip in a Ti–6Al–4V CT-sample. It was shown that if the LP area is elongated in the longitudinal direction, the compressive RS is maximised which results in a doubling of the crack growth life in comparison with un-peened samples. The effect of the compressive RS field could also be observed when striations on the fracture surface were analysed under a SEM.

2.3.3.1 Cold-Expansion of Fastener Holes

The effect of RS induced by the Cx process as described earlier in chapter 2.3.1.1 on the crack growth performance was investigated by Buxbaum and Huth [76] using 2024-T3 open-hole, single LJ and LJ samples assembled with Hi-Lok fasteners. Buxbaum and Huth [76] defined life ratios to quantify the fatigue life improvement of Cx and they found that for their open-hole, single LJ and LJ samples, double sided Cx and constant amplitude loading, life ratios of 20.9, 9.9 and 1.8 can be achieved respectively. This trend showed that with increasing complexity of the sample, fatigue life improvement becomes more difficult to obtain. Also, laboratory results and achievements on simple geometries cannot be straight forwardly translated into more practical structures of similar type.

In order to analyse the crack growth behaviour test samples were pre-cracked with different initial crack sizes using small saw-cuts. All test results exhibited crack growth life benefits deriving from the expansion process with significant difference depending on the initial pre-crack size. For increased initial crack sizes the beneficial effect decreased so that for pre-crack sizes larger than the fastener-hole radius Cx was found to have no significant effect anymore. Zhang and Wang [77] followed-up this analysis with a more practical investigation by applying cold-expansion on low-load transfer lap-joints at different stages of their baseline fatigue life irrespective of existing (pre-)cracks in the sample to establish data for aircraft in-service applications of Cx. The compiled fatigue data revealed that part-life cold-expansion could offer significant fatigue life improvements. It was shown for LJ samples which were cold-expanded at 25% of the baseline fatigue life the improvement exceeded even the production case which defines cold-expansion before fatigue cycling. For cases at 50% and 75% of the BL fatigue life, the improvements of Cx incrementally dropped down and were for both cases under the improvement of the at production case. Despite the beneficial fracture mechanical effects of compressive RSs, this trend was explained by the inability of the Cx process which included reaming of the fastener-hole to remove rather larger existing crack as a result of previous fatigue cycling. For the 25% case, the crack size which was accumulated however could have been removed by the reaming process leaving behind a pristine condition which explains the optimised conditions regarding life improvements.

Yanishevsky *et al.* [78] experimentally examined the fracture characteristics of cold-expanded 7075-T73 high-load transfer fastened double strap butt-joints. Fatigue cycling under spectrum load of test samples revealed that cold-expanded holes with interference fitted Hi-Lok bolts exhibited no failure with the test stopped after the cycle count was three to five times greater than the number of cycles which was compiled for non-Cx test samples depending on the relative position of the fastener-hole in relation to the edge (edge margin). Fractographical analyses also showed that the failure location potentially moves in cold-expanded samples to secondary locations where high RS gradients are expected in the transition region of the introduced RS field where compression changes into tension. This outcome is particularly important when considering new inspection requirements.

2.3.3.2 Laser-Peening of Fastened Lap-Joints

As LP is a relatively industrially immature technique to engineer RS in metallic structures, there is no abundance of publications which refers to a specific application of LP on LJ structures. However, LP efforts were conducted on open-hole samples [10,24,84,103,121–123] to investigate the effects on potential life improvements by reducing the severity of the stress concentration caused by the fastener-hole.

Achintha *et al.* [24] investigated laser-peened 2024-T351 open-hole samples of 5 mm and 15 mm thickness using two different LP approaches (LP layouts) and analysed the subsequent fatigue behaviour. Samples were laser-peened by MIC using a squared laser-spot varying the LP process parameters depending on the thickness of the sample. For 5 mm thick plates a laser power density of 3 GW/cm^2, pulse width of 1 ns and 3 layers of laser-spot were applied, while the 15 mm thick plates were irradiated with 4 GW/cm^2 with keeping the remaining parameters constant from the 5 mm plates. The two different approaches of LP which were applied to 5 mm thick samples consisted of laser-peening globally the full-face of the net-section where the fastener-hole is located on the one hand and local introduction of RS around the fastener-hole within a square of 20 x 20 mm with leaving un-peened material on the net-section on the other hand. For the thick (15 mm) samples only the global full-face LP approach was applied. Anyhow, a fastener-hole of 8 mm in diameter was machined after LP. For comparison, conventional shot-peening (SP) was applied to an additional set of test samples with 15 mm thickness globally to the full-face. Fatigue cycling of test samples was performed using relatively high loads of 145 MPa and 220 MPa as maximum nominal net-section stresses. Fatigue strength test results exhibited for 15 mm thick samples that LP could not increase the fatigue endurance whereas SP, however, provided little life improvements on the lower applied stress level only. Those results emphasised the importance of resulting tensile residual stresses as they through-the-thickness which occurred after the compressive stress state in the near surface region needed to be equalised increasing the maximum net-section stress particularly in the bore of the fastener-hole where crack initiation was found. RS prediction by the Eigenstrain method confirmed this trend and predicted up to 150 MPa balancing residual tensile stress. For 5 mm thick laser-peened open-hole samples the fatigue performance of the different two LP approaches were analysed, and it was found that the local approach of laser-peening a region in the vicinity of the fastener-hole leads to a noteworthy fatigue strength increase. Again, the finding could be explained by adducing RS predictions which concluded that local LP produced higher compressive RS (350 MPa) in comparison to the global LP approach (200 MPa). The un-peened region in the local LP approach gave space to accommodate tensile residual stresses outside the LP region where as in the global approach balancing tensile RSs were forced to form through-the-thickness near to the bore of the fastener-hole. This mechanism increased crack initiation in comparison to the local LP approach which could produce a through-the-thickness compressive stress state especially near to the bore of the hole which retarded early fatigue failure. The conclusion from Achintha *et al.* [24] work indicated the crucial role of balancing tensile RSs which occur either through-the-thickness or outside the treated area depending on the area which is designated for LP and the effect it has on the formation of compressive RSs consequently.

The optimal manufacturing sequence of operations namely the LP step and drilling of the fastener-hole step were studied on LP open-hole samples by Zhang *et al.*[123] and Ivetic *et al.* [10]. Both studies came to the same conclusion that the most beneficial sequence of operations is that LP is applied before the drilling of the fastener-hole. Although both studies found that some decreasing re-distribution of initial LP introduced RSs occurs after drilling, the results in terms of compressive RSs are still superior to the reverse sequence of operations, which was not able “lock” enough RSs, especially near the free surface at the bore of the hole.

On LP of LJ samples, Giummarra and Zonker [124] reported solely to the best of the author’s knowledge fatigue test results. In their experimental study, they used low-load transfer LJ made of 7085-T7651 aluminium plates of 6.35 mm thickness comparing LP with various other surface treatments. LP was performed by MIC using laser strength of 4 GW/cm2, 18 ns pulse width and 3 laser pulses over the area on both faces over the complete reduced gauge area of the test sample. The results exhibited that LP is a process which could improve the fatigue resistance of low-transfer LJ samples by a factor of 2.16.

2.3.4 Residual Stresses and Predicting Crack Growth

The effects of residual stresses on crack growth have been under investigation for many years for several different backgrounds. As discussed earlier RS present in metallic structures can be induced, either purposely to enhance the crack growth life or RSs can be a result of manufacturing processes, as is most commonly discussed for welding applications, such as for friction stir welding (FSW) [107] for instance.

There have been several approaches published which describe methodologies of calculating crack growth in the presence of residual stresses in order to define an effective SIF (K_{eff}). Basically, two different approaches can be identified:

(1) The K_{res} (or K_{resid}) approach with the application of the linear superposition principle [11,125–127], as defined, as:

$$K_{eff} = K_{res} + K_{app} (Equation\ 2.22)$$

where K_{res} is the SIF caused by the residual stress field without loading and K_{app} is the SIF resulting from external loading systems,

(2) And the crack closure approach of defining a crack opening SIF (K_{open}) [20,46,128,129], as defined, as

$$\Delta K_{eff} = K_{max} - K_{open} \quad (Equation\ 2.23)$$

where K_{max} is the maximum applied stress in the stress cycle of the external loading and K_{open} is the corresponding opening stress, as defined by Elber [46].

The K_{res} approach has the advantage that K_{res} can be calculated separately and then superimposed with familiar analysis of SIF calculation. This approach reduces work effort and simplifies the analyses, on the one hand. However, it neglects the non-linearity of contact condition, occurring between the crack flanks, and further, it does not take into account the non-linear relationship between external load and K_{eff}. Both non-linarites invalidate the linear superposition principle. However, there are two conventional techniques, which can be found in current research papers, to compute K_{res} to follow this approach; the weight function method (WFM) [125–127] and the FEM [11,20,107]. The research by Y.C Lam and K.S. Lian [130] compared the WFM and the FEM using the K_{res} approach. It was found that the approach using the WFM will result in overly conservative numbers. This is because the WFM method does not account for any redistribution of RSs as the crack grows, in contrast to the FEM, which incorporates this capability by balancing the RSs for every crack length. To account for redistribution of stresses while applying the WFM, complementary data are necessary, which give information about redistribution patterns of RSs during crack growth. However, this research proves that the redistribution of stresses during crack growth is an essential factor, in order to develop an accurate prediction model. Although the WFM is promising in terms of reducing the work effort by generalising the formulas once established for any geometry, loading system and crack profile, this method needs more additional data, to be collected, as one will initially expect.

The second approach, crack closure involved calculation of the crack opening stress. According to Elber (refer to section 2.1.2.3), crack growth can only occur when the crack is open, and the relating crack opening stress was found to be greater than zero experimentally by Elber [46]. This research has found wide consequences in the science of fracture (e.g. retardation effect, mean stress effects). Most of the time, crack opening stresses are determined experimentally [20,46,128], but also numerical investigations have been published [129,131]. M.H. Gozin *et al.* [129] have shown a process where crack growth is calculated in the presence of RSs by determining crack closure using FEM. The final crack growth results in the light of test evidence are good. However, the very high modelling effort required, especially for 3D problems is an issue, and the benefits of the technique may be questioned for the accuracy achieved [129].

A third approach can be mentioned and may be described as an improvement of the K_{res} approach [132], where the K_{eff}, as a total K, is directly calculated by means of FEM while considering RSs in the model. This operation may be done for several reasons, e.g. invalidity of the superposition principle, caused by non-linear contact conditions between the crack flanks during due to internal compressive stress fields and further by non-linear relations of K_{eff} depending on external loads, as discussed previously for the K_{res} approach. Disadvantages of this approach are the increased work effort since SIFs have to be determined for every single load level, which is applied to the structure. This is in contrast to the traditional K_{res} approach, where only the K_{res} as a constant value has to be determined, and the variable K_{extL} is known from analytical linear solutions. D. Schnubel *et al.* [132] have followed such a process. Also, contact constraints between the crack flanks were also modelled in the SIF simulation. This was done for laser heated induced RSs. The developed model demonstrated very high accuracy in the light of experimental data [132].

2.3.5 Residual Stress Measurements

Techniques of RS measurement can be categorised into destructive, semi-destructive and non-destructive methods. Typical examples of each category are given in Table 2-2[3]. In general, destructive methods of RS measurements are based on elastic strain relaxation records after material is removed from the sample whereas non-destructive procedures use radiation (X-rays) or sub-atomic particles (neutrons) to measure atomic d-spacing (interplanar lattice spacing) which can be further processed into strain without the need of any damage on the measured component. The Incremental Centre Hole Drilling (ICHD) [133,134] method is

---

[3] Italic and bold techniques are used in this work.

considered a sub-category of destructive methods. It is categorised as semi-destructive since the damage (a small hole) induced during the measurement is rather local than it is the case for contour [135,136] or slitting method [137] in which the complete sample is destroyed. The principles of ICHD (stress relaxation) and diffraction techniques are reviewed in the next chapter.

All of these RS measurement techniques shown in Table 2-2 are well established and standard procedures in current research and industrial practice. This appreciation is reflected by several standards available in the literature for ICHD [133,134] or any X-ray diffraction (XRD) [138] technique for instance. Extensive textbooks about XRD and Neutron diffraction techniques [139,140] are also published for profound insights into the details of each diffraction technique.

Table 2-2: Typical examples of RS measurement techniques are categorised into destructive, semi-destructive and non-destructive methods and related references of standards guides and applied research (mostly LP related). Further advantages and disadvantages are listed for all listed techniques.

Category	RS measurement Technique	Advantages	Disadvantages	Measurement depth[4]	Ref.
Destructive	Slitting method	-applicable for thin sheets	-only through the thickness average RS values can be measured	0.1 mm-100 mm	[105, 137]
	Contour method	-stress distribution over thickness and lateral direction in one measurement	-FE post-processing requires extensive resources e.g. time and expertise -surface RS not reliable	1.0 mm-100 mm	[51,54][135,136]
Semi-destructive	***ICHD***	-stress distribution over thickness -relatively quick and cost-effective	-no strain/ stress mapping possible -measuring depth is limited	0.1 mm-10 mm	[133, 134, 141, 142]
Non-destructive	Laboratory XRD	-relatively quick and can be performed in own Lab.	-only surface RS values can be measured.	0.001 mm-0.02 mm	[118, 138, 142]
	Synchrotron XRD	-stress mapping possible -deep penetration	-extensive resources required e.g. access to equipment, time and expertise	0.1 mm-20 mm	[69,72, 73,75, 76]
	Neutron diffraction	-stress mapping possible -very deep penetration	-extensive resources required e.g. access to equipment, time and expertise	1.0 mm-30 mm	[75, 80–82]

It is favourable to gather RS information from more than one technique as every technique has its advantages and disadvantages as listed in Table 2-2. S. Coratella *et al.* [142] successfully performed RS measurements using multiple methods (Contour, Neutron diffraction, Hole Drilling, Laboratory XRD and Synchrotron XRD) to compensate each of its weak points in order to come to a complete RS picture in a laser-peened aerospace component. RS

---

[4] Values taken from [175]

measurements were further compared with RS predictions using the Eigenstrain method. From the published data, it can be concluded that the contour method is unreliable on the surface but laboratory XRD therefore will provide accurate results for the surface but cannot be used for measurement in the bulk material. Neutron and Synchrotron diffraction techniques showed good agreement with the FE predictions away from the surface.

2.4 Summary and Concluding Remarks

Fatigue and crack growth in conventional aircraft fuselage aluminium alloys and fuselage fastened LJ samples were reviewed. It was found that the literature provides a detailed picture of why and how aircraft fuselage structures fail under fatigue loading conditions. The LEFM theory, as it was developed since the 1960’s, especially by researchers in the field of structural integrity of lightweight aerospace structures, offered sufficient methodologies and understandings to analyse fatigue failure mechanisms in metallic aircraft structures, taking into account various effects, such as the mean stress, crack closure effect and effects from fretting-fatigue. The main failure mechanism in LJ structures was identified as fretting-fatigue which depends on a complex interaction of load transfer, secondary bending and RSs which in effect significantly reduces the fatigue performance of LJs compared to the base sheet material. Improvements in chemical composition and consequent damage-tolerant capabilities of aircraft aluminium alloys could do its part, but new ways must be found to further extend the fatigue resistance, especially for aircraft fastened LJ. Therefore, techniques which induce engineered compressive RS fields were applied by engineers to enhance the crack resistance of aluminium aircraft structures further. The role and effect of RS in that process are subject to many publications. According to those publications, compressive RSs have the potential to further improve the fatigue response of metallic structures. The effect of RSs on the crack growth period is understood well. This fact is also manifested by the presence of several crack growth modelling approaches which were applied successfully to predict crack growth in the presence of RSs. On the other hand, effects on the crack initiation period are still unclear in the sense of the underlying mechanisms which delay nucleation of cracks. Therefore, initiation was mainly analysed using empirical S-N data.

However, the RS state depends to a great extent on the specific technique which is applied to induce a RS state. There are two widely accepted RS inducing methods which are currently applied by the aerospace industry; the SP and Cx process. However, both techniques are limited and have their individual shortcomings. Cx can induce compressive RSs only around fastener holes with RS fields of limited radii. SP, on the other hand, is flexible in the sense of where RS can be introduced but it induces RS profiles which are very shallow. Further, it produces rough surfaces which can have a detrimental effect on the fatigue performance. A promising and relatively new technique is LP, which is a flexible and highly controllable process which can produce deeper compressive RS profiles than SP. This circumstance, in turn, results in superior fatigue improvements when compared to SP applications. However, the literature indicates that a specific LP treatment must be thoughtfully managed so that tensile RS which occur along with induced compressive RS as a consequence of the process of equalisation of the stress state do not produce premature crack initiation which can have detrimental effects on the fatigue performance. A large amount of the LP literature discusses the effect of LP process parameters on resulting RS field using a range of metals including aircraft aluminium alloys and titanium alloys for fan blade applications. Although, general trends of different effects of LP process parameters, such as the sample thickness or the material on peak compressive RS or penetration depth can be now outlined, the role of other contributors to the formation of RS fields such as the LP layout or LP pattern is not well researched yet.

First attempts were published [27,97] to improve the crack growth capabilities in aircraft aluminium using large CCT-panels (160 mm by 400 mm) which are used to represent aircraft fuselage skin fields. Those experimental efforts were, however, not successful in that endeavour. Moreover, they failed to systematically analyse different LP treatments, not only in the light of different used LP process parameters and subsequent RS profiles but also by defining different positions and dimensions of the LP area (LP layout) on the sample. Therefore, there is no understanding of what would be the optimised engineered RS using LP in order to define an effective treatment.

As per the application of LP to aircraft fuselage fastened LJ structures to improve this crucial and fatigue susceptible component, there is currently no publication available discussing this subject in detail. However, open-hole samples, which can be regarded as forerunners of the LJ sample in a test sample maturity hierarchy, have been subject of the LP research. The most significant conclusion from those scientific results is that is more advantageous to first laser-peen the sample and then drill a fastener hole into the laser-peened area. There is one paper discussing the application to a single low-load transfer LJ sample for wing applications which indicate that there is enormous potential to extend fatigue and crack growth performance of aircraft fuselage LJs.

3 Experimental Procedures

This chapter introduces and describes the material, sample specification, LP treatments and manufacturing processes which were applied to three types of test samples:

(1) *LP parameter study sample* (1.6 mm) which were used to study the effect of LP process parameters.
(2) *CCT sample* used for fatigue crack growth tests to analyse the effect of different LP strategies on macro crack growth.
(3) *Fastened Lap-Joints (LJ)* used for fatigue endurance tests to analyse the effects of different LP strategies on the fatigue overall fatigue life.

After that, descriptions of RS measurements experiments using ICHD and diffraction techniques give details about the instrumentation and methodologies which were used. This section is then followed by details about the mechanical fatigue and crack growth testing, such as load conditions and test matrices. Lastly, fractographic procedures will be outlined which were performed to analysed fractured test samples.

3.1 Laser-Peening, Material and Samples

3.1.1 Laser-Peening Process at the CSIR

Laser-peening of all test samples analysed in this work were performed at the Council for Scientific and Industrial Research (CSIR) National Laser Centre in Johannesburg in South Africa. This was done in collaboration with the University of Witwatersrand (Wits) which was initiated by Airbus (project sponsor).

The CSIR‘s LP set-up consists of a Quanta-Ray Pro Q-switched Nd: YAG laser with a maximum energy capability of 1.0 J. The laser emits laser light with a wavelength of 1064 nm and operated for this study at a pulse repetition rate of 20 Hz. For the work presented in this thesis, LP was performed in the LPwC configuration so that besides the laser, a confining medium and an XYZ stage was necessary to realise the complete LP set-up.

For the confining medium distilled water was delivered to the surface of the work piece by a water jet, as shown in Figure 3-1. The movement of test samples was realised by XYZ Aerotech Pro165 high precision positioning stage (accuracy of +/-8 microns, bi-directional repeatability of 1 micron, and encoder feedback of 0.1 microns), with a movable range of 150 x 150 mm in continuous motion.

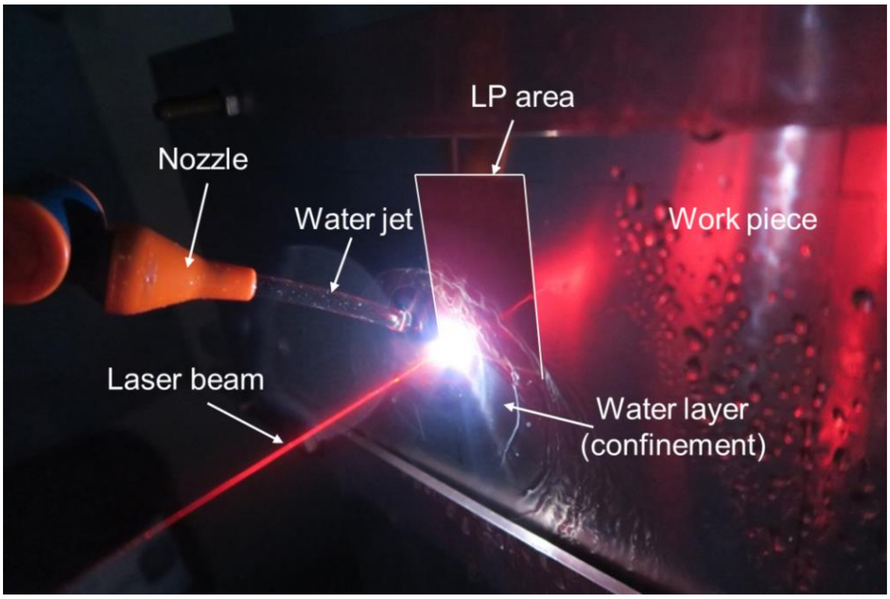

Figure 3-1: Delivery of confining medium (deionized water) during the laser-peening process (Photograph: courtesy by Wits, edited by author).

Since the peak power intensity, which depends on the laser pulse energy, the pulse width and the spot size, is crucial in the LP process, these processing parameters were constantly measured in order to achieve robust LP results. The laser energy was adjusted in the laser setting to realise different power densities. The defined energy level is observed by splitting off 2% of the beam. The width of the laser pulse is measured using a fast photo-diode and oscilloscope. Pulse widths at 1064 nm wave length were in the range of 8-9 ns with 8.6 ns representative at Full Width Half Maximum (FWHM). The laser spot size is adjustable and the defined spot size is verified using a charge-coupled device (CCD) beam profiler.

3.1.2 Laser-Peening of Aircraft Fuselage Skin Aluminium Alloy

Before CCT-samples as a representative fuselage skin structure were laser-peened, a LP process parametric study was performed on the designated aluminium alloy 2525-T3 using a simpler sample type (*LP parameter study sample*). Two sample types are therefore introduced in the following. The first one is used in a fundamental study of the interaction of the material and the laser using various different process parameters and the second one was designed to study the effect of RS (induced by LP) on the crack growth resistance (*CCT-sample*).

3.1.2.1 Aircraft Fuselage Skin Aluminium Alloy 2524-T3 clad

Alclad aluminium-copper alloy 2524 was used for the experimental study which investigates the effect of LP on crack growth in fuselage skins. 2525-T3 sheets of 1.6 mm thickness were supplied in sheets of 800 mm x 400 mm by Airbus (sponsor). Material and thickness selection was decided to simulate the reality on modern aircraft fuselage skins. 2524-T3 was developed during the design of the Boeing 777 aircraft to possess higher damage-tolerance capabilities and therefore was designated to substitute 2024-T3 which was the standard material for fuselage skin structures [50]. T. Dursun and C. Soutis [50] concluded in their relatively recent (2013) review of aircraft aluminium alloys that 2524-T3 has 15-20% increased fracture toughness and a fatigue strength of 70% of the yield strength whereas the 2024-T3 only comes to 45% of the yield strength for similar fatigue property.

The nominal chemical composition of 2524-T3 is given in Table 3-1.

Table 3-1: Chemical composition of 2524 (values given in weight in percentage, remainder aluminium) [50]

Si	Fe	Cu	Mn	Mg	Cr	Zn	Ti
0.06	0.12	4.0-4.5	0.45-0.7	1.2-1.6	0.05	0.15	0.10

The T3 treatment of the material consists of solution heat treatment, cold working and natural ageing. The clad layer on both surfaces of the aluminium alloy substrate consisting of unalloyed aluminium is specified for this sheet thickness to be less than 5 % of the total thickness [148].

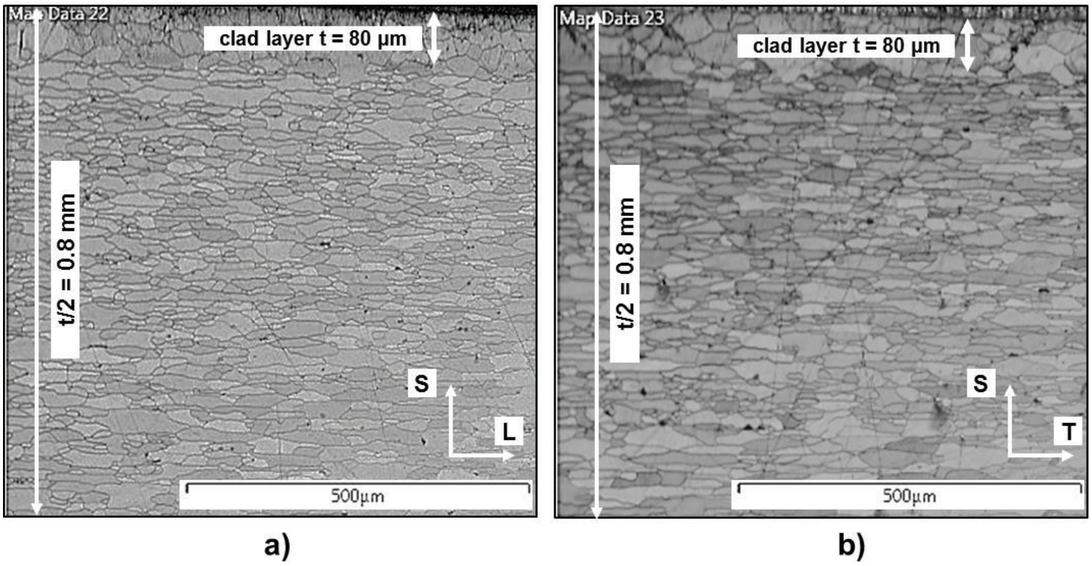

Figure 3-2: Back scatter images of 2524-T3 grain structure. a) L-S plane and b) T-S plane.

A piece of 2524-T3 was prepared by mechanical grinding (1200g, 2500g, 4000g and 3 µm diamond compound),final polishing (colloidal silica suspension – OP-S Suspension) and chemical etching using a chemical solution of 95% distilled water, 2.5% nitric acid, 1.5%

hydrochloric acid and1% of hydrofluoric acid. A resulting image showing the grain structure of 2524-T3 taken by Backscattered Electrons (BSE) technique for L-S and T-S planes is presented in Figure 3-2.

The dimension of grains was determined according to ASTM standard E112-12 [149] and are reported in Table 3-2.

Table 3-2: Dimension of grains

Material	(L)]	(T)	(S)
2524-T3	48 µm	50 µm	11 µm

The grain structure is typical for cold rolled sheets and consist of pancake shaped grains in the substrate, as it was also found by Shou *et al.* [150] for 2524-T3 which is associated with a rolling reduction of 5% to a final thickness of 1.65 mm. Also, the distinctive fine grains as described are in line with data given by Shou *et al.* [150] who analysed the grain size of different 2524 samples in which the rolling reduction of the final thickness during the T3 treatment was varied. They concluded that for lower rolling reductions insufficient energy is stored by the deformation to support the occurrence of recrystallization during rolling and annealing. The clad layers on both surfaces are 80 µm thick (2.5 % of sheet thickness) as specified by Alcoa [148] and consist of larger uniform grains of 60 µm in L, T and S direction.

Mechanical properties were measured perpendicular to the longitudinal rolling direction (T-S) according to ASTM standard E8/ E8M [151] using a load controlled INSTRON servo-hydraulic test machine with a maximum load capacity of 100 kN and a loading accuracy of 0.5%. Displacements were measured by an INSTRON extensometer with a gauge length of 50 mm with a range of ± 2.5 mm. Results, as reported in Table 3-3 (first row), are the arithmetic average of three test samples.

Table 3-3: Mechanical properties for 2524-T3

Material	Yield stress YTS [MPa]	Ultimate tensile stress UTS [MPa]	Elongation at fracture [%]	Grain direction
2524-T3 test	290	413	7	T-L
2524-T3 [50]	306	434	24	L-T

Comparing the obtained values with the data compiled by T. Dursun and C. Soutis [50] (row two in Table 3-3), it strikes that the measured properties are slightly lower for YTS and UTS.

The elongation at fracture is almost reduced by a third of the values given by T. Dursun and C. Soutis [50]. This could be reasoned by the fact that the grain orientation differs for the two values. As the tensile tests were performed in T-L direction, values from the literature were obtained for the L-T direction.

3.1.2.2 The Laser-Peening Parameter Study Sample

In order to analyse effects of power density and pulse density on the formation of RS in 1.6 mm thin 2524-T3 aluminium, a test sample was designed as shown in Figure 3-3. In total 9 samples were cut out from an 800 mm by 400 mm sheet using a guillotine. The sample was then irradiated on <u>both surfaces</u> using the LP process as described in section 3.1.1. The designated LP area was defined in the centre of the sheet (30 mm by 30 mm) as illustrated in Figure 3-3 with the rolling direction of the material parallel to the stepping direction of the applied LP raster zig-zag pattern.

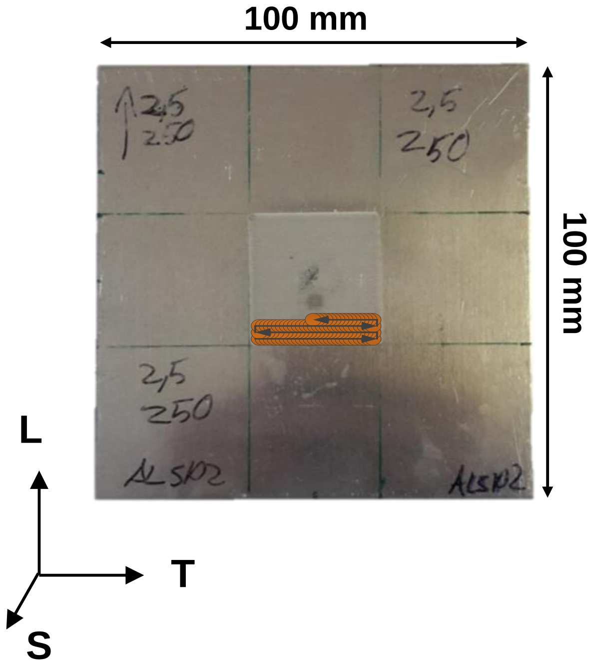

Figure 3-3: Photograph of test sample design used in the LP process parameter study: A 100 mm by 100 mm sheet of 1.6 mm thickness made of 2524-T3 aluminium-copper alloy. LP was conducted on a patch of 30 mm by 30 mm in the centre of the sample with the LP raster zig-zag pattern's stepping direction parallel with the rolling direction of the sheet (L-T). Illustration of the zig-zag pattern was superimposed (out of proportion) to the photograph.

The circular laser spot size diameter was set to 1.5 mm and respective power densities were enabled by varying the laser energy. Pulse densities were managed by controlling the overlapping of single laser spots in the LP raster zig-zag pattern. The complete LP process matrix and respective sample ID are shown in Table 3-4.

Table 3-4: LP treatment matrix used in LP process parameter study.

Sample ID	Power density [GW/cm^2]	Pulse density [pulses/cm^2]
#1	2.5	750
#2	2.5	500
#3	2.5	250
#4	2.0	750
#5	2.0	500
#6	2.0	250
#7	1.5	750
#8	1.5	500
#9	1.5	250

3.1.2.3 Laser-Peening of CCT-Samples

CCT-samples for fatigue crack growth tests were then manufactured from 2524-T3 of 1.6 mm thickness representing the typical aircraft condition. The overall dimension of the test samples was 400 mm in width and 800 mm in length. A centre notch of 12 mm length and 0.1 mm width was introduced using an EDM process to seamlessly initiate fatigue cracks. In order to investigate the effect of LP on fatigue crack growth, CCT-samples were then laser-peened on both faces, according to the two LP layouts as drawn in Figure 3-4. In Figure 3-4a one single peening stripe was applied to the centre of the sheets. After LP, the EDM notch was introduced on top of the peening stripe. The dimension of the laser-peening stripe (LPS) was 30 mm in width (w_{LP}) and 50 mm in length (L_{LP}). In Figure 3-4b two single stripes right and left of the centre notch were introduced 25 mm from the samples centre symmetry line (d_{LP}). The width of the peening (w_{LP}) stripe was set to 30 mm and the length (L_{LP}) was 50 mm.

In total one sample was processed by the laser to produce the LP layout with a single LPS and two replicate samples were irradiated according to the LP layout is shown in Figure 3-4b. LP process parameters were applied to the samples according to Table 3-5. Samples designated by *1-A* refer to single LPS samples whereas *2-A* and *2-B* samples refer to two LPS samples. The stepping direction of the raster zig-zag pattern was parallel with the longitudinal direction of the CCT-sample, as indicated in Figure 3-4.

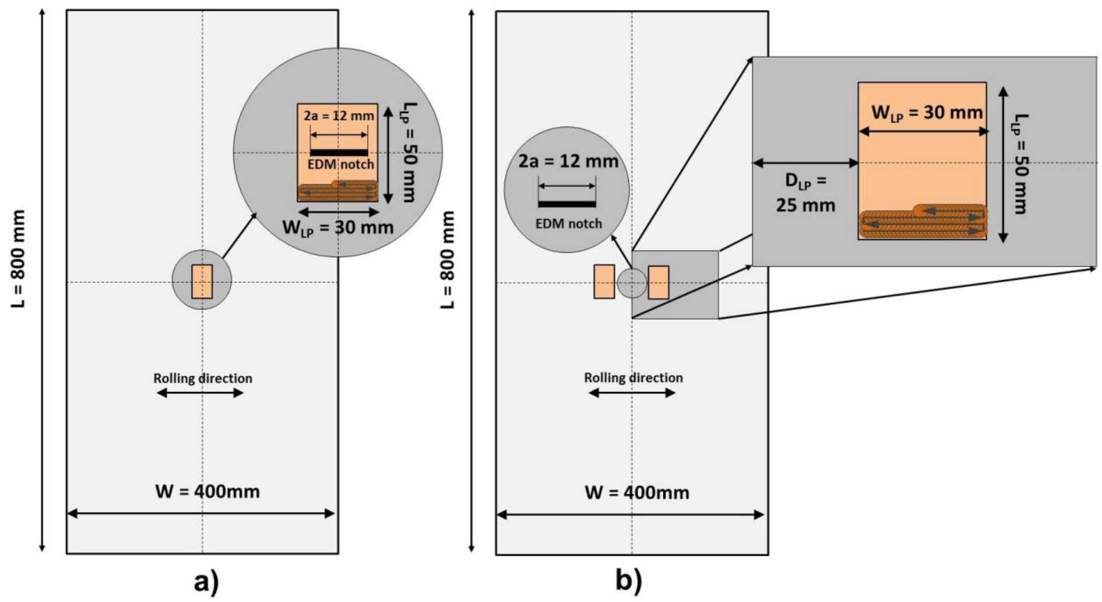

Figure 3-4: Illustration of laser-peened CCT-crack growth samples defining two LP layouts. a) Single laser-peening stripe at the centre of the samples and b) Two laser-peening stripes left and right from the centre notch.

Table 3-5: LP process parameters applied on CCT-crack growth samples.

Case	dLP [mm]	wLP [mm]	Power density [GW/cm2]	Pulse density LP Face 1 [Pulses/cm2]	Pulse density LP Face 2 [pulses/cm2]
1-A	0	30	2.5	750	750
2-A	25	30	1.5	250	250
2-B	25	30	2.5	750	500

3.1.3 Laser-Peening of Fastened Lap-Joint

3.1.3.1 Lap-Joint Test Sample and Material

The fastened LJ test sample used for the experimental fatigue test program was designed according to the geometry as shown in Figure 3-5. Test samples were made from aerospace typical cladded aluminium-copper (Al-Cu) alloy 2024-T3 2.5 mm thick sheets which were provided by Airbus in single sheets of 110 mm x 55 mm. The sheet rolling direction was perpendicular to the longitudinal axis (y-direction) of the specimen, representing together with the material selection the aircraft fuselage situation.

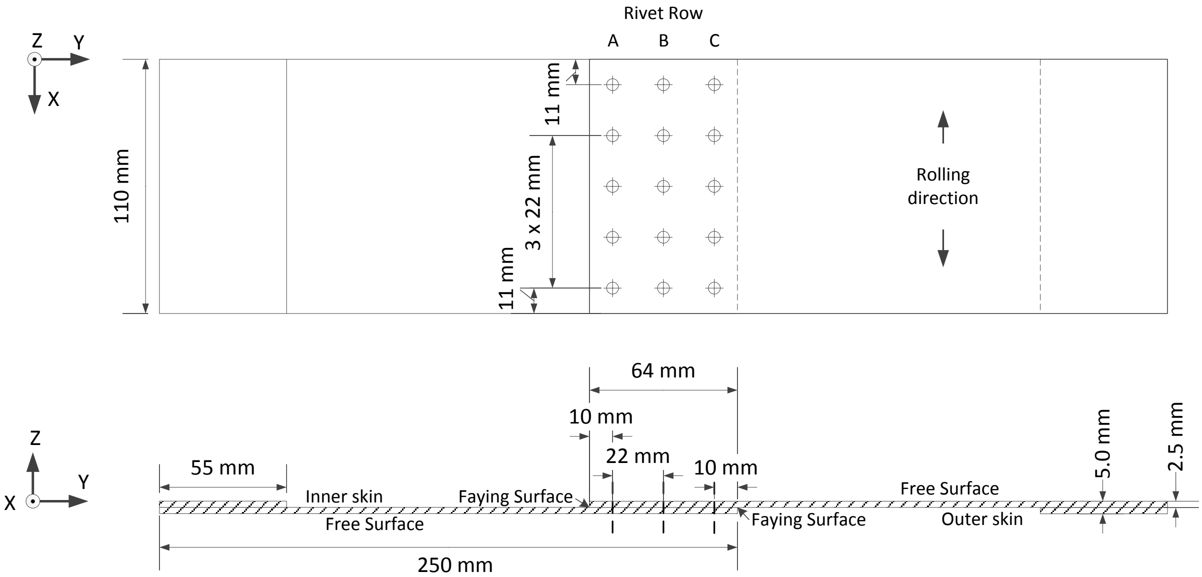

Figure 3-5: Drawing of the fastened Lap-Joint fatigue test sample, the defined coordinate system and the definition of fastener rows A, B and C.

Alcoa provides a detailed chemical composition for the 2024 alloy series [148] which is shown in Table 3-6. The T3 treatment of the material consists of solution heat treatment, cold working and natural ageing. The clad layer on both surfaces of the aluminium alloy substrate consisting of unalloyed aluminium is specified for this sheet thickness to be less than 2.5 % of the total thickness [148].

Table 3-6: Chemical composition limits of 2024 (values given in weight in percentage, remainder aluminium). [148]

Si	Fe	Cu	Mn	Mg	Cr	Zn	Ti	others, each	others, total
0.50	0.50	3.8-4.9	0.30-0.9	1.2-1.8	0.10	0.25	0.15	0.05	0.15

The grain structure of the material was analysed after a piece of the material was mounted, ground (1200g, 2500g, 4000g and 3 µm diamond compound), polished (colloidal silica suspension – OP-S Suspension) and chemically etched using a chemical solution of 95% distilled water, 2.5% nitric acid, 1.5% hydrochloric acid and1% of hydrofluoric acid. The microscopic photograph of the grain structure is shown in Figure 3-6.

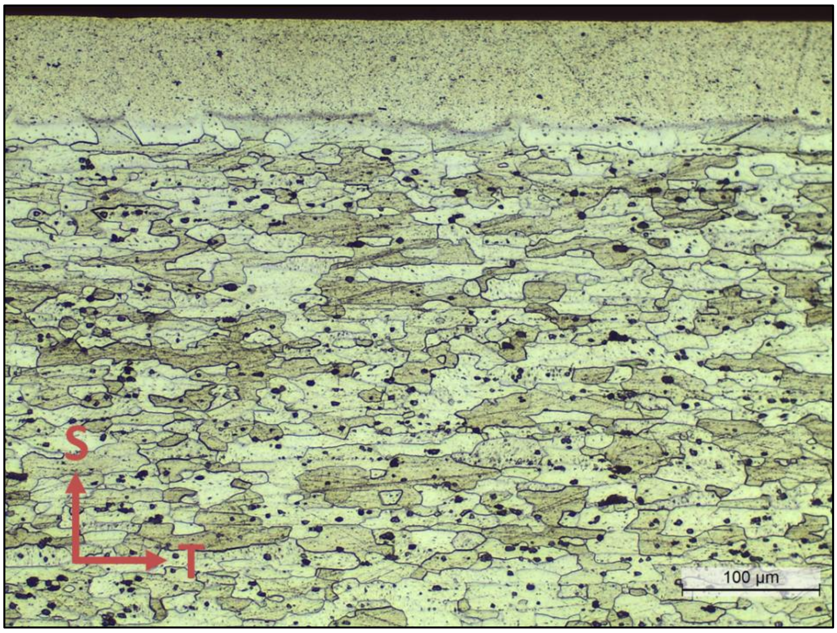

Figure 3-6: Optical micrograph of 2024-T3 grain structure.

Mechanical properties were determined by tensile tests which were conducted perpendicular to the longitudinal rolling direction according to ASTM standard E8/ E8M [151] using a load controlled INSTRON servo-hydraulic test machine with a maximum load capacity of 100 kN and a loading accuracy of 0.5%. Displacements were measured by an INSTRON extensometer with a gauge length of 50 mm with a range of ± 2.5 mm. Results, as reported in Table 3-7, are the arithmetic average of three test samples.

Table 3-7: Mechanical properties for 2024-T3

Material	Yield stress YTS [MPa]	Ultimate tensile stress UTS [MPa]	Elongation at fracture [%]	Grain direction
2024-T3 test	317	461	7	T-L
2024-T3 Spec. [148]	289	434-441	10-15	L-T

Similar to the comment made for the 2524-T alloy, the obtained values show that the elongation at fracture is reduced in comparison to values given the Alcoa specification. Again, this deviation could be reasoned by the fact that the grain orientation differs for the two values.

The fastener array of the fatigue sample consisted of 3 rows of 5 rivets. The fasteners were titanium (Ti-6Al-4V) countersunk (100° flush shear) HI-LOK™ bolts, as shown in Figure 3-7 and further specified by the dimensions given in Table 3-8.

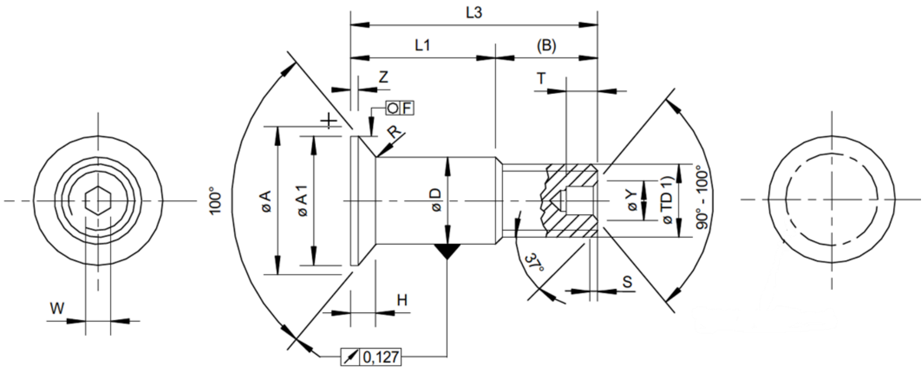

Figure 3-7: Sketch of HI-LOK™ fastener and definition of all geometric dimensions

As the HI- LOK™ fastener system consists of two parts, the threaded HI-LOK™ bolt and a HI-LOK™ collar, matching collars used for the manufacturing of the LJ sample were selected. Collars were made of 2024-T6 aluminium and had a minimum axial static load limit of 7110 N and a minimum and maximum locking torque of 0.2 mN and 1.4 mN respectively. The geometry of the collar is shown in Figure 3-8.

Table 3-8: Dimension of HI-LOK™ fastener with a nominal shaft diameter of 4.8 mm (HL11 V6) [152]

Nominal diameter	ØA		ØA1	B	ØD			ØTD		F	H		R		Z	S	Thread	W		T		ØY	
	min	max	min	ref	min	min	max	min	max		min	max	min	max				min	max	min	max	min	max
4.8 (3/16)	7.534	7.661	6.858	8.255	4.788	4.801	4.813	4.597	4.674	0.127	1.143	1.194	0.508	0.762	0.381	0.79	UNJF-3A	2.009	2.047	2.921	3.429	2.642	3.023

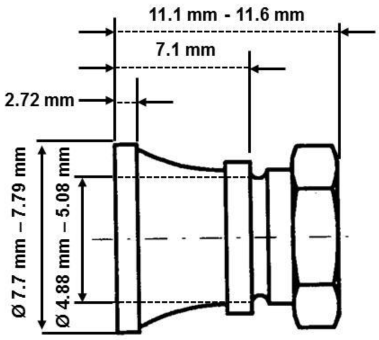

Figure 3-8: Sketch and dimension of HI-LOK™ collar.

In order to reduce anticipated secondary bending stresses (refer to chapter 2.2.2.2), a symmetrical design of the LJ was chosen. For that reason, extra tabs of aluminium 2024-T3 with a thickness of 2.5 mm were bonded to the end of sheets. Additional aluminium tab was bonded to the clamping area of the assembled LJ in order to protect the LJ from damage caused by the clamping (or gripping) system of the test machine.

3.1.3.2 Laser-Peening Strategies

The LP strategies for LJ samples consist of the definition of LP layout; LP pattern and LP process parameters. As described earlier in chapter 2.2, the most critical fastener row in which fatigue failure can be confidently anticipated are row A and C, as defined in Figure 3-5. Therefore, LP strategies were designed to target those fatigue critical locations. In this course, four different LP layouts have been defined as illustrated in Figure 3-9 (*S-A*, *S-B*, *P-A*, *P-B*). Figure 3-9 exhibits the LP layout on single un-assembled aluminium sheets. In principle, two samples had a single LP "*Stripe*"(*S*), and two samples had multiple LP "*Patches"* (*P*). The Stripe LP layout attempts to "engineer" residual stress globally across the fatigue sensitive rivet-rows A or C respectively, whereas the Patch LP layout is designed to locally enforce the fatigue resistance by compressive RS around anticipated fastener-holes and leaves an un-peened area between the *Patches*. In *B* samples the respective LP layout (*S* and *P*) has been elongated in y-(longitudinal) direction of the sheet if *A* sample is taken as a reference point.

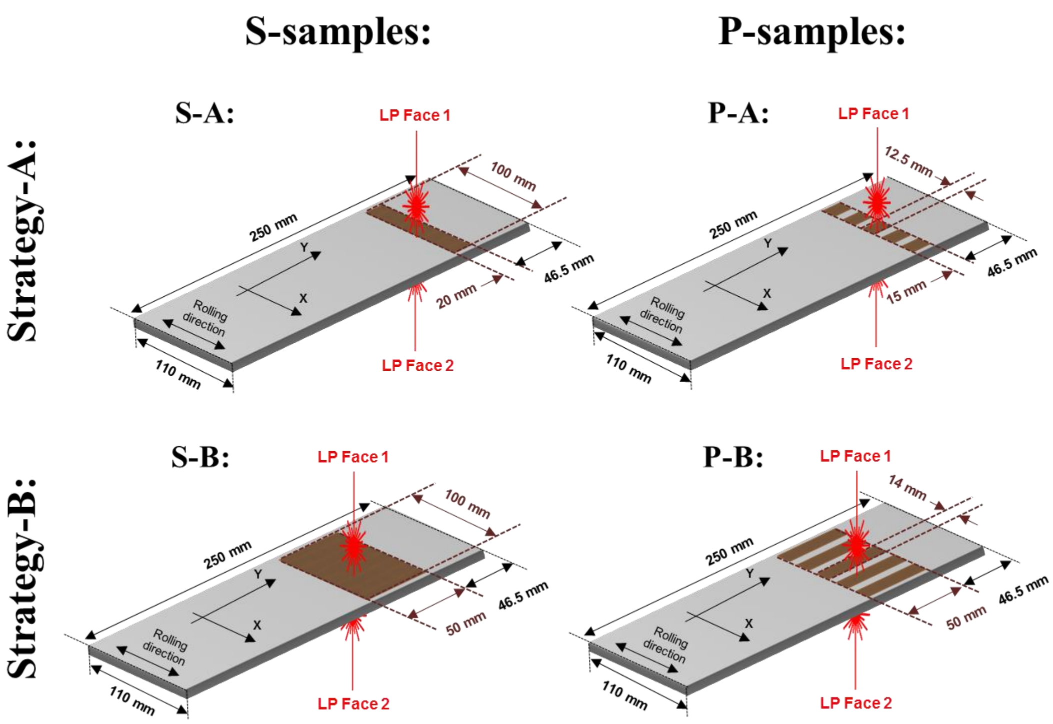

Figure 3-9: Illustration of definition of four LP layouts of unfastened LJ sheets: (1) left upper corner *S-A*, (2) left lower corner *S-B*, (3) right upper corner *P-A*, (4) right lower corner *P-B*.

The LP layout was laser-peened using the raster zig-zag pattern so that the stepping direction was aligned with the longitudinal direction (y-direction) of the sample. Figure 3-10 shows an example photograph of the LP area on a *P-A* sample. A sketch of the LP raster pattern is put over the photo to indicate the realisation of the LP layout by the laser. A study of the effects of the LP raster zig-zag pattern on the RS component in stepping and scanning direction by C. Correa *et al.* [96] indicated that a zig-zag pattern has the potential to introduce a non-biaxial stress field in which the stepping direction was coincidence with the most compressive RS direction. In order to use this effect to counteract the external loading which is coincident with the longitudinal direction, the orientation of the LP pattern was selected.

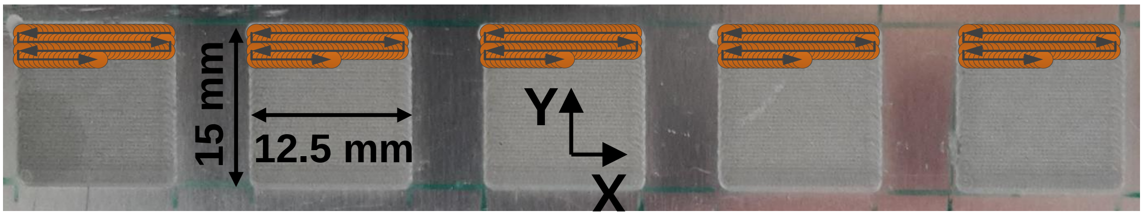

Figure 3-10: Example of LP raster zig-zag pattern as applied to realise the LP layout (*P-A*). Stepping direction in longitudinal (y-direction) of the sheet. Illustration of the zig-zag pattern was superimposed (out of proportion) to the photograph.

Two sets of LP process parameters were applied to *A* and *B* sample respectively as specified in Table 3-9. Strategy A uses more intense LP process parameters than strategy B. It can be noted that in strategy *B* the LP process parameters vary between the *LP Face 1* and *LP Face 2* (recall Figure 3-9). *LP Face 1* refers to the sheet surface which was irradiated *before LP Face 2* so that finally both sheet surfaces were laser-peened accordingly.

Table 3-9: LP process parameters used for LJ *A* and *B* samples.

Strategy	Power Density [GW/cm^2]	Coverage LP Face 1 [pulses/cm^2]	Coverage LP Face 2 [pulses/cm^2]	Laser Energy [mJ]
A	2.5	750	750	380
B	2.0	500	350	300

3.1.3.3 Manufacturing Sequence of Laser-Peened Fastened Lap-Joints

As earlier reviewed in chapter 2.3.3.2, two studies by Zhang *et al.* [123] and Ivetic *et al.* [10] on laser-peened open-hole samples revealed that the manufacturing sequence of LP and drilling of rivets-hole have significant impacts on the subsequent fatigue performance. Both studies conclude that the most beneficial sequence of operation in terms of consequent fatigue life improvement is that LP is applied before the drilling of the fastener-hole. This practice was adopted in this study, as illustrated in Figure 3-11, so that before drilling of the fastener hole and assembly of the complete LJ specimen, LP was applied on both surface of the bare aluminium sheets. After the drilling process, no final reaming of the hole was performed.

Hi-LOK bolts were installed to fasten the two sheets using spanner and Allen key. Clearance fit tolerance rivet installation was ensured for all LJ samples in which the average hole diameter of 4.87 mm was consistently measured 0.06 mm larger than the measured bolt shaft diameter. In order, to reduce expected high secondary bending stresses, as described by Schijve *et al.* [61] and Rans *et al.* [62] (recall chapter 2.2.2.2), and furthermore reduce local stresses at the zone where LJ samples are clamped into the fatigue testing machine at the end of the sample, LJs were reinforced by 2.5 mm thick bonded aluminium sheets, using a two component adhesive (Aerospace adhesive: Araldite® 420 A/B [153]). Laser-peened LJ samples were additionally reinforced with 0.7 mm thick aluminium sheets on top of the previously described reinforcements and their opposite surface. This was necessary after initial LP LJ sample fractured at the clamped zone due to high stress concentrations from clamping's "spiky" grips. Additionally, a commercial two component sealant (Naftoseal MC-630 C-2 [154,155]) was applied to the sheet-sheet and bolt-sheet interfaces during assembly of the LJ, as it is common practice in the manufacturing process of large aircraft fuselages.

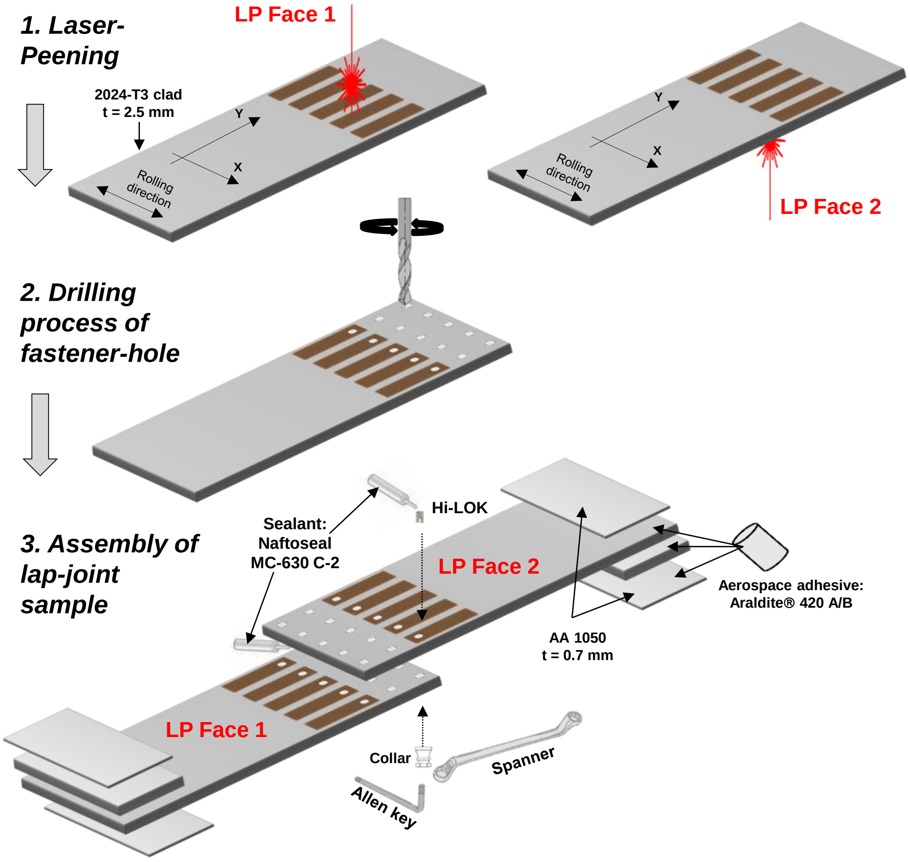

Figure 3-11: Manufacturing process of LJ fatigue test samples. 1. Laser-Peening 2. Drilling of fastener hole 3. Assembly of LJ sample which includes the application of aerospace sealant and extra tabs at sample end (gripping area) are bonded to the LJ sample to reduce secondary bending and to protect the area from gripping devices.

As concluded from data reviewed in chapter 2.2, fatigue failure can be assumed to initiate at the faying surface. For that reason, in *B samples* the surface which was laser-peened according to the pulse density as defined in Table 3-9 the *LP Face 1* was specified to be the faying surface. Higher compressive RS were anticipated at the *LP Face 1* surface as a result of greater pulse densities as Peyre *et al.* [86] and Rubio-González *et al.* [92] observed in their studies (recall chapter 2.3.2.2).

3.2 Residual Stress Measurements of Laser-peened Test Samples

Two different types of RS measurements were performed to analyse the effect of LP and various process parameters on the formation and variation of RS of AA2524-T3 sheets of 1.6 mm thickness. ICHD experiments were performed on the test samples (*LP parameter study sample*) as shown in Figure 3-3 and AA2524-T3 *CCT-samples* as earlier presented in Figure 3-4 were used during Neutron diffraction experiments.

For *LJ samples*, RS field were determined in sheets using ICHD and synchrotron XRD measurements. ICHD measurements were taken on single un-assembled LJ sheets before the fastener hole was drilled. Two synchrotron-XRD techniques were used on single un-assembled LJ sheets after the fastener hole was drilled:

- **energy-dispersive (ED-) XRD technique;** which uses a polychromatic beam (multiple photon energies) and relates the detected shift in the energy spectra of the diffracted beam to mechanical strain.
- **angle-dispersive (AD-) XRD technique;** which is a uses straightforward implementation of Bragg’s law by using a monochromatic X-ray beam and detects the shift in the diffraction angle to relate this information to mechanical strain.

Using ED- and AD-XRD technique, 1D and 2D stress maps could be created which is useful to assess the RS condition beyond a single location.

3.2.1 Incremental Centre Hole Drilling

The Incremental Centre Hole Drilling method (ICHD) is in contrast to other techniques the most straightforward, cost-effective and reliable method for RS determination. It is common practice in the field by researcher and engineers in academia and industry. This is manifested in two major standards describing the ICHD method. Both standards can be consulted for all necessary details of the method and implementation of it:

(1) ASTM Standard E837 [133]
(2) NPL Measurement Good Practice Guide No. 53[5] [134]

The basic principle of strain measurements during ICHD is simple and follows as:

- Drilling (milling[6]) a small hole in the sample or component by multiple increments of depth.

---

[5] Consulted and followed for ICHD measurement within the framework of this dissertation.

[6] It was concluded by Nau *et al.* [176] that less heat was generated by orbital milling which resulted in more accurate strain readings than it was the case for simple drilling.

- Recording the elastic strain relaxation for every depth increment by e.g. pre-installed strain gauge rosette.
- Computing the RS state which was situated in the sample before the drilling of the hole for each depth increment.

For computing RS especially if the RS distribution is non-uniform, Schajer [156] proposed the integral method which was adopted by the two above mentioned standards [133,134]. The integral method accounts for the change in stiffness which is needed in calculating stresses as the hole depth increases. Therefore, coefficients were derived for each increment of depth by means of FEA for multiple hole diameters and strain gauge types [133]. It is illustrated in Figure 3-12 that if for the first depth increment a coefficient a_{11} is used, the coefficient changes for the second increment to a_{21} (former a_{11}) and a_{22} as the second increment also changes the first increment. Recorded elastic strain relaxation can then be explicitly assigned to RS valued and pseudo-effects of RS reading, produced by merely stiffness changes can be avoided.

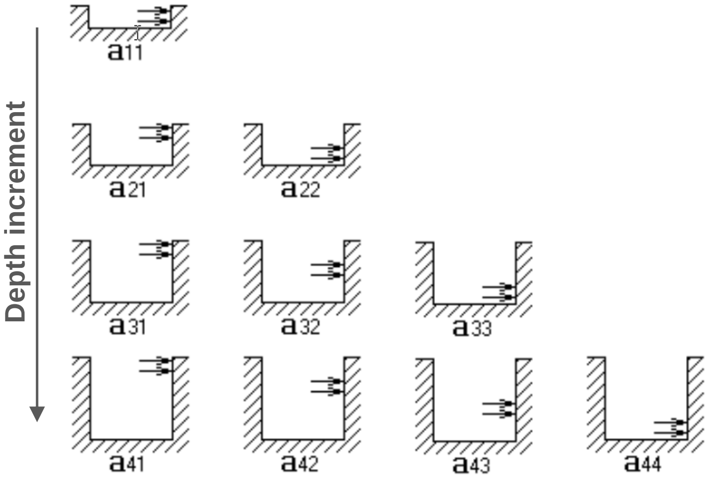

Figure 3-12: Principle of the integral method and coefficients used for RS computing during ICHD measurements (Graphic was taken and edited from [134]**).**

3.2.1.1 *Aircraft Fuselage Aluminium Alloy 2524-T3 sheets*

Semi-destructive RS measurements were taken using the ICHD method in accordance to the Measurement Good Practice Guide No. 53 [134] at the centre of the sample as indicated in Figure 3-13a. ICHD measurements were taken using Stresscraft's hole-drilling equipment and Vishay's strain gauge rosettes CEA-09-062UL-120 as shown in Figure 3-13b, analysing the RS distribution through the thickness produced by LP. Test samples exhibited distortion after LP so that either the concave or convex surface could be measured as only one replicate samples were designated for ICHD measurements. For this study the concave surface was chosen for measurements which correspond to the surface (*LP Face 2/ concave*) which was laser-peened after the opposite surface (*LP Face 1/ convex*) surface was processed.

Sample surfaces were prepared before strain gauge installation as instructed in [134]. In order to avoid RS pseudo-effect as a consequence of the drilling process on a delicate (low stiffness) thin sheet of 1.6 mm thickness, the back surfaces were reinforced using an epoxy resin of 5 mm thickness providing more stiffness to the measurement location. As the drilling process consists of a downward motion on a limp structure the sheet could be affected and bend which would cause unintended stresses which will be recorded during the ICHD measurement. The method of epoxy resin reinforcements was successfully applied by Toparli [13] during ICHD measurements on thin aluminium sheets. Toparli's dissertation also exhibited that with the usage of reinforcing the back surfaces no correction needed to be performed to account for thin structures during the computation of RS using the integral method as integrated in Stresscraft's RS INT software version 5.1.2 and 5.1.3 which is based on the integral method of Schajer [156] and respective FE determined coefficients.

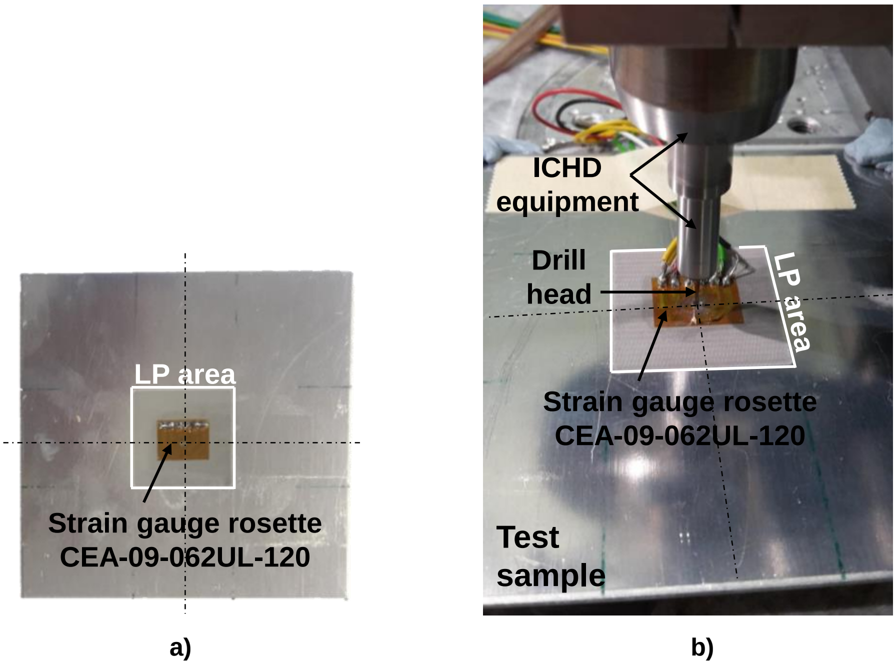

Figure 3-13: RS measurement by ICHD method on laser-peened AA 2524-T3 samples of 1.6 mm thickness. a) Position of CEA-09-062UL-120 strain gauge at the centre of the samples b) ICHD test set-up.

The drilling increments were defined as 4 steps of 32 µm each, 8 steps of 64 µm each and 8 steps of 128 µm so that a nominal measuring depth resulted in 1408 µm. Recorded strains as a result of elastic relaxation as the drilling process removes material were then used in RS calculations via INT software version 5.1.2 as provided by Stresscraft.

3.2.1.2 Fastened Lap-Joints

ICHD measurements of RS changes with depth into the sheet were performed on un-assembled laser-peened single 2024-T3 clad sheets, before drilling of the fastener holes (recall manufacturing sequence of Figure 3-11), according to guidelines given in Measurement Good Practice Guide No. 53 [134]. Same conditions and procedure as described in section 3.2.1.1 for AA2524-T3 clad samples were applied during ICHD experiments with the exception that for LJ samples no epoxy resin reinforcement was attached to the back surface. This measure was avoided to ensure further usage of LJ samples in mechanical fatigue testing. Also, a slight stronger sheet thickness of 2.5 mm was judged by engineering judgement to be sufficient in order to prevent any induction of pseudo-stress during the drilling process. The centre of the ICHD hole was made coincident with the centre of the designated fastener-hole at positions of the edge *Hole 1* (H1) and at middle *Hole 3* (H3) on *LP Face 1* and *LP Face 2* as defined in the sketch given in Figure 3-14. The small hole produced during the ICHD process is subsequently removed by the drilling process for the production of the fastener-hole, as the diameter is far greater than the small hole introduced by the ICHD process. This approach allowed further usage of LJ samples during succeeding fatigue testing. ICHD measurements were performed on *S-A*, *S-B*, *P-A* and *P-B* samples.

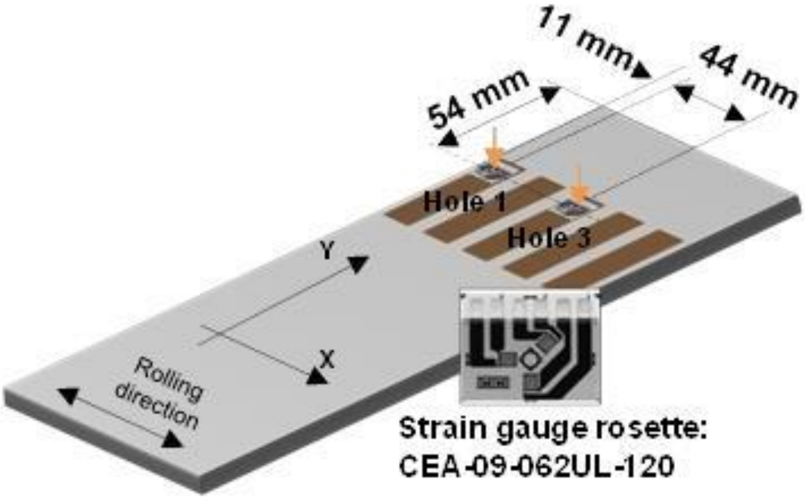

Figure 3-14: Sketch of the position of ICHD measurements using strain gauges of CEA-09-062UL-120. Two measurement locations were defined: Edge hole (*Hole 1*) and centre hole (*Hole 3*).

3.2.2 Diffraction Techniques

Diffraction techniques to measure RSs are fundamentally based on the interaction between electro-magnetic (X-rays) or corpuscular (Neutrons) radiation and the lattice of polycrystalline materials. The idea of stress measurement as graphically conceptualised in Figure 3-15 was formulated by Sir William Lawrence Bragg in the law of X-ray diffraction. The corresponding mathematical equation which is derived by means of trigonometric relationships of wave length, interplanar spacing and reflection angles [138] is written as:

$$\lambda = 2d(hkl)\sin\theta(hkl) \quad (Equation\ 2.24)$$

in which λ is the wave length of any incoming beam (X-ray or Neutron), d the spacing between two lattices in a crystalline material, θ the glancing or reflection angle and hkl are Miller indices which describe and define the orientation of lattice planes in polycrystalline materials [138,139].

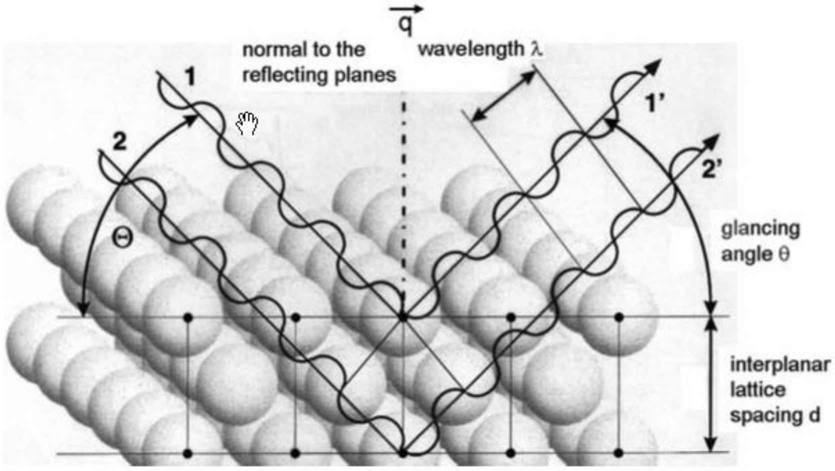

Figure 3-15: Schematic view of Bragg's law (Graphic was taken from [139]**).**

By determining a spectrum of a diffracted beam characterised by the intensity and the angle of that intensity, as shown in Figure 3-16, the lattice spacing d can be calculated for a specific crystallographic plane, knowing the X-ray wave properties using Bragg's law. The exact angular position of the intensity peak is found by a fitting procedure [139]. Any difference in the lattice spacing from the measured component and a stress-free sample gives the measured strain as given by:

$$\varepsilon = \frac{d - d_0}{d_0} \quad (Equation\ 2.25)$$

in which *d* is the measured lattice interplanar spacing and d_0 the lattice interplanar spacing for a corresponding stress-free condition.

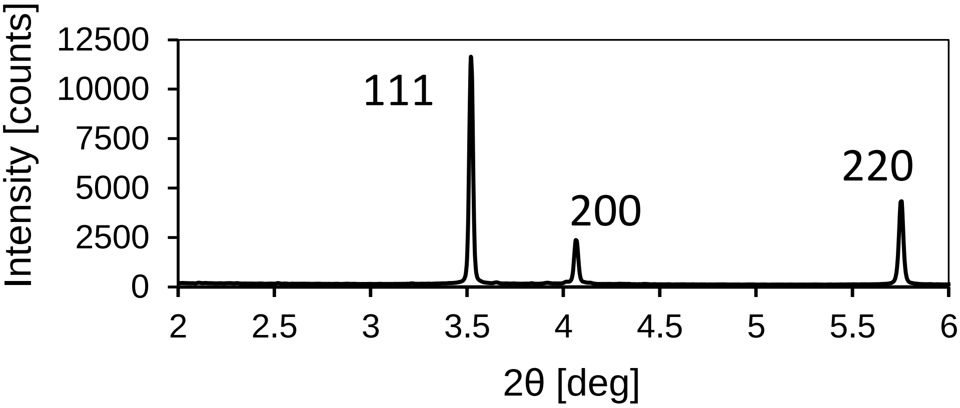

Figure 3-16: Example of measured spectra of diffracted X-ray beam (diffractogram) of an XRD experiment. The spectra show diffraction peaks for three different crystallographic planes: 111, 200 and 220.

3.2.2.1 Neutron Diffraction at SALSA/ ILL on Laser-Peened CCT-samples

One AA 2524-T3 laser-peened CCT-sample (laser-peened according to LP treatment 2-B as defined in section 3.1.2.3) was analysed for RSs by neutron diffraction technique using the Strain Analyser for Large and Small scale engineering Applications (SALSA) instrument [147] at the Institut Laue-Langevin (ILL) in Grenoble, France. All three orthogonal stress components were measured using the reflection of the {311} lattice plane as suggested by the textbook on "Neutrons and Synchrotron Radiation in Engineering Materials Science" [139] since this plane orientation provides a good representation of the macro elastic strain. The distance between the lattice planes was determined using a monochromatic neutron beam with a wave length of 1.61 Å and measuring diffracted neutrons under an angle (2θ) of 82° plus considering ± 3°- 4° detector range. The experimental set up as presented in Figure 3-17 shows the configuration of d-spacing measurement in the longitudinal direction of the CCT-sample in the SALSA beamline. The nominal gauge volume of the incoming beam was set to 0.6 mm by 0.6 mm in horizontal directions as illustrated in Figure 3-17 and the gauge dimension in the vertical direction was 2 mm.

The principal sample arrangements used in this study for measuring the transverse and normal stress component are illustrated in Figure 3-18. There were in total six measuring points on the sample surface selected for RS evaluations. In Figure 3-19 the half laser-peened CCT-samples is shown and the designated measurement points are marked (red points) and further given in the table next to the figure. Measurements were only taken on one-half of the sample taking the vertical symmetry into account so that only one of the two peening stripes was covered in this study. For RS evaluation through the thickness, three positions of the gauge volume were defined through the normal direction of the 1.6 mm thin sheet as further illustrated in Figure 3-19.

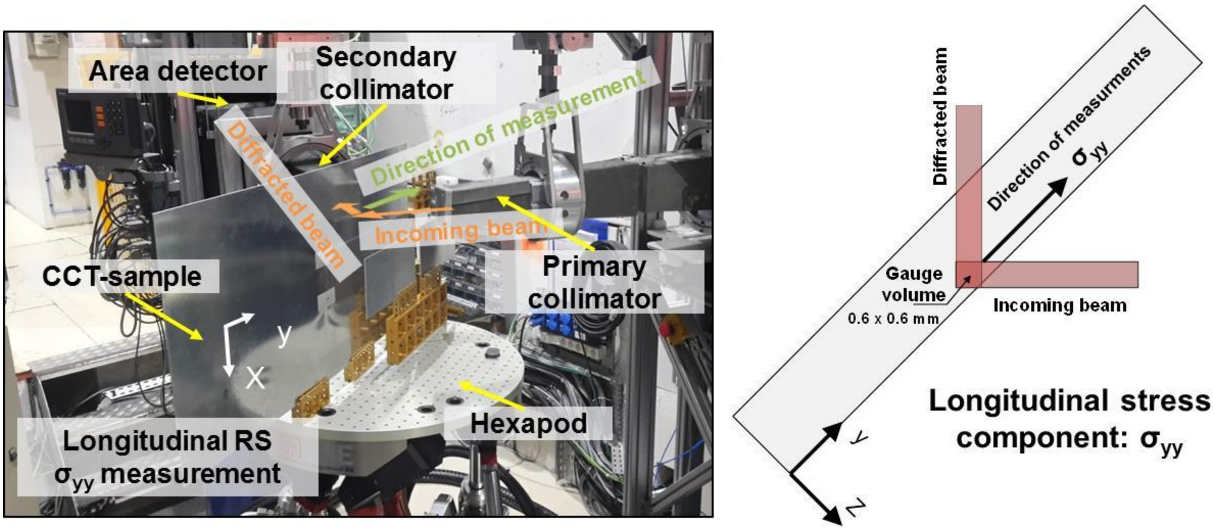

Figure 3-17: Photograph of the experimental set-up at the SALSA beamline at the ILL (left figure) and illustration of the top view of the set-up (right figure) showing the incoming beam and diffracted beam and the gauge volume in the sample.

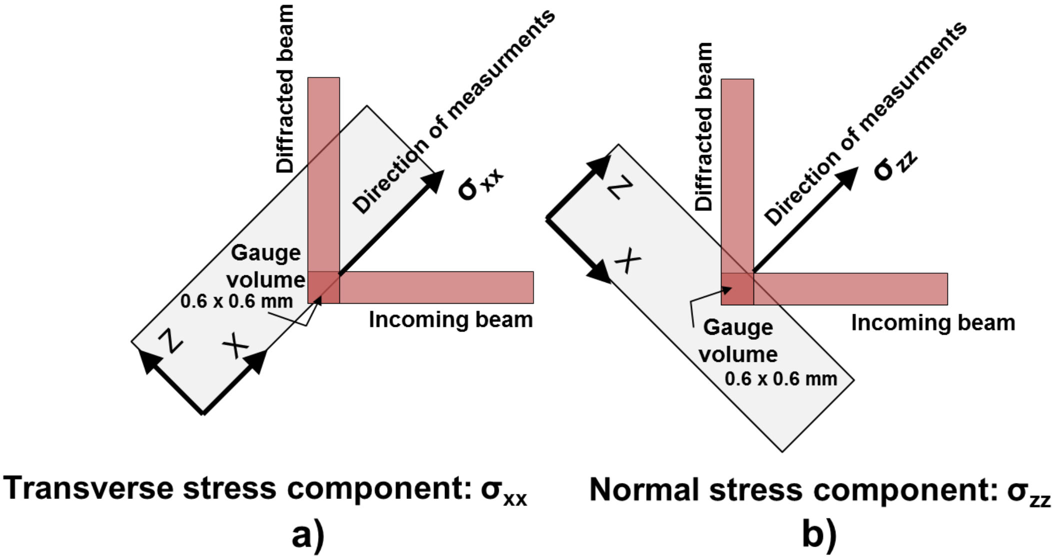

Transverse stress component: σ_{xx}
a)

Normal stress component: σ_{zz}
b)

Figure 3-18: Illustration of the sample configuration for measuring the transverse and the normal stress component at the SALSA beamline.

For every measuring position, 300 neutron counts were captured. Recorded spectra, as shown for one example in Figure 3-20, were then further post-processed using the Lamp tool provided by the SALSA beamline. Fitting procedures were based on Gaussian distribution and a fitting range of 79° to 85° was selected.

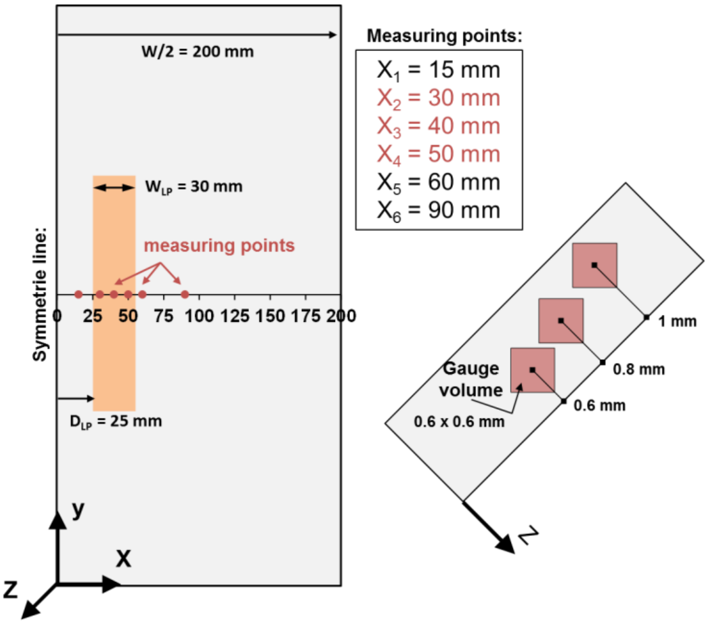

Figure 3-19: Graphic of neutron diffraction measurement locations on laser-peened CCT-sample in the transverse (x-direction) and through the thickness direction (z-direction).

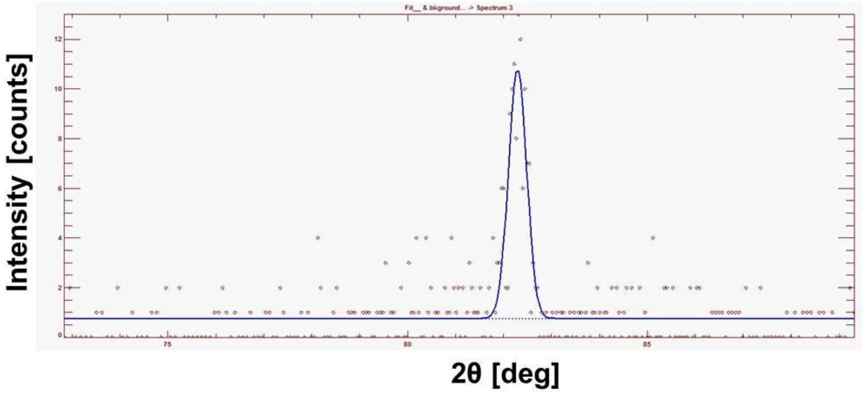

Figure 3-20: Example of measured diffraction spectra showing one diffraction peak corresponding to the 311 plane.

Despite that tri-axial measurements were taken, plane stress condition can be assumed to the CCT-sample due to the thin nature of the 2524-T3 sheet. Following the methodology as outlined by Albertini *et al.* [157], this state can then be exploited to calculate a value of the unstrained lattice parameter a_0 by the application of the condition $\sigma_z = 0$ to the stress tri-axial formula:

$$\sigma_{zz} = \frac{(1-\nu)E}{(1+\nu)(1-2\nu)} \cdot \varepsilon_{zz} + \frac{\nu E}{(1+\nu)(1-2\nu)} \cdot (\varepsilon_{xx} + \varepsilon_{yy}) \quad (Equation\ 2.26)$$

in which E refers to the macroscopic elastic modulus (E = 70,500 MPa) and ν is the Poisson’s ratio (0.33). It can then be further formulated that:

$$a_0 = \frac{1-\nu}{1+\nu}\, a_z + \frac{\nu}{1+\nu}\left(a_{xx} + a_{yy}\right) \ (Equation\ 2.27)$$

since it can be referred to an isotropic behaviour of the cell, as the lattice parameter does [158]. This concept must be applied point by point. The average values can be taken over regions which can be assumed to be homogeneous in composition and structure.

Finally, strain values were determined by:

$$\varepsilon_i = \frac{a_i - a_0}{a_0} \quad (Equation\ 2.28)$$

Stresses then could be calculated by applying the equation for a bi-axial stress state for σ_{xx} and σ_{yy}:

$$\sigma_{xx} = \frac{E}{1-\nu^2}\left(\varepsilon_{xx+}\nu\varepsilon_{yy}\right) \quad and \quad \sigma_{yy} = \frac{E}{1-\nu^2}\left(\varepsilon_{yy+}\nu\varepsilon_{xx}\right) \ (Equation\ 2.29a\ amd\ 2.29b)$$

3.2.2.2 Energy-Dispersive Synchrotron XRD at Bessy-II on Laser-Peened LJs

RSs between fastener-holes on un-assembled but already drilled LJ sheets were studied using a non-destructive XRD technique at BESSY-II’s EDDI beamline in Berlin, Germany. The EDDI beamline provides an efficient method to evaluate the high stress gradient of near-surface RS fields [159]. It is, therefore, optimal for this study as high stress gradients are anticipated in the near surface region. The schematic EDDI beamline layout is given in Figure 3-21.

This beamline layout is designed to take RS measurements in energy-dispersive XRD mode [139,159] using a polychromatic beam produced by the wiggler with an energy range of 10-80 keV. Diffracted beam spectra were recorded by the detector under a fixed angle of $2\theta = 16°$ in symmetrical ψ-mode by tilting the sample stepwise in 10 steps from $\psi = 0°$ up to $\psi = 71.57°$. The gauge volume of the incoming beam was set to 1000 µm by 1000 µm by slit systems S1/ S2. The angular divergence of the diffracted beam was limited to $\Delta 2\theta \leq 0.01°$ by the double slit system S3/ S4 which was fixed to 30 µm by 1000 µm (S1/ S2 and S3/ S4 as given in the description of beamline layout in Figure 3-21). In this configuration 12 reflections E(hkl) {111/

200/ 220/ 311/ 222/ 400/ 331/ 420/ 422/ 511/ 440/ 531} were identified in the energy diffraction spectra which were then correlated to depth information.

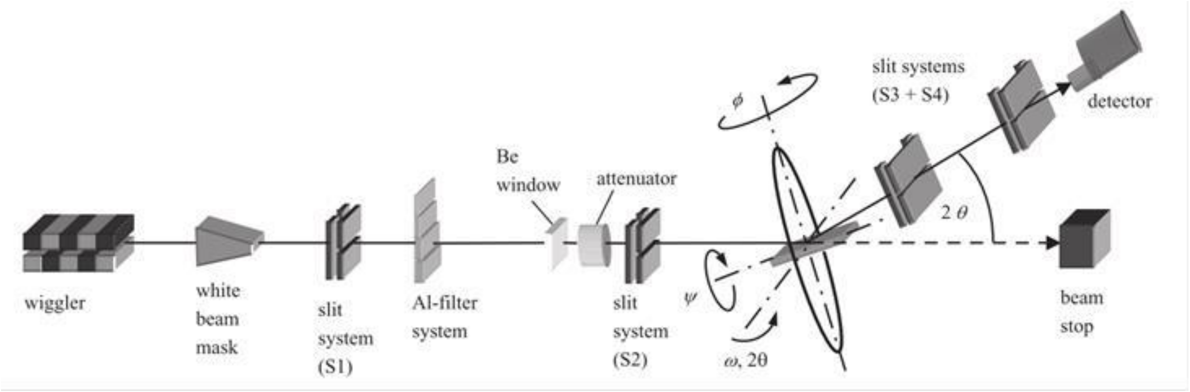

Figure 3-21: Schematic view of the EDDI beamline layout at BESSY-II in Berlin, Germany (Illustration was taken from [159]**)**

The relationship of photon energy and mechanical strain which is the fundament of the energy-dispersive mode of RS XRD measurements is described by the Einstein-Planck relation which is given as:

$$E = \frac{hc}{\lambda} \ (Equation\ 2.30)$$

in which *E* stands for energy, *h* is Planck's constant, *c* the velocity of light in vacuum and *λ* for the wave length must be inserted into Bragg's law as given in equation 2.24. This will result into:

$$d(hkl) = \frac{hc}{2\sin\theta}\frac{1}{E(hkl)} = const.\frac{1}{E(hkl)} \ (Equation\ 2.31)$$

relating lattice d(hkl) spacing to energy E(hkl). And with respect to the sample system as defined in Figure 3-21, the strain can directly be calculated for all diffraction peaks and tilt angles by:

$$\varepsilon_{\phi\psi} = \frac{E_0(hkl)}{E_{\phi\psi}(hkl)} - 1 \ (Equation\ 2.32)$$

where E_0 is the energy that refers to the strain-free lattice parameter.

Average depth information τ of measured strain is derived from each reflection E(hkl) on the energy scale. According to Ch. Genzel *et al.* [159], a general formulation of the 1/*e* penetration depth τ is defined by the depth where 63% of the total detected radiation intensity *I* come from. It can be formulated as:

$$\tau = \frac{sin^2\theta - sin^2\psi + cos^2\theta\ sin^2\psi\ sin^2\eta}{2\mu(E)\ sin\theta\ cos\psi} \ (Equation\ 2.33)$$

in which $\mu(E)$ is the linear absorption coefficient depending on the energy E and η is the sample rotation around the diffraction vector.

Table 3-10: Example of depth resolution of energy-dispersive XRD measurements in respect to the corresponding reflection plane (hkl) as determined by equation 2.33.

Reflection plane (hkl)	Depth [µm]
111	42.45
200	63.41
220	165.04
311	243.51
222	267.66
400	362.57
331	428.34
420	446.55
422	519.26
511	566.64
531	672.24

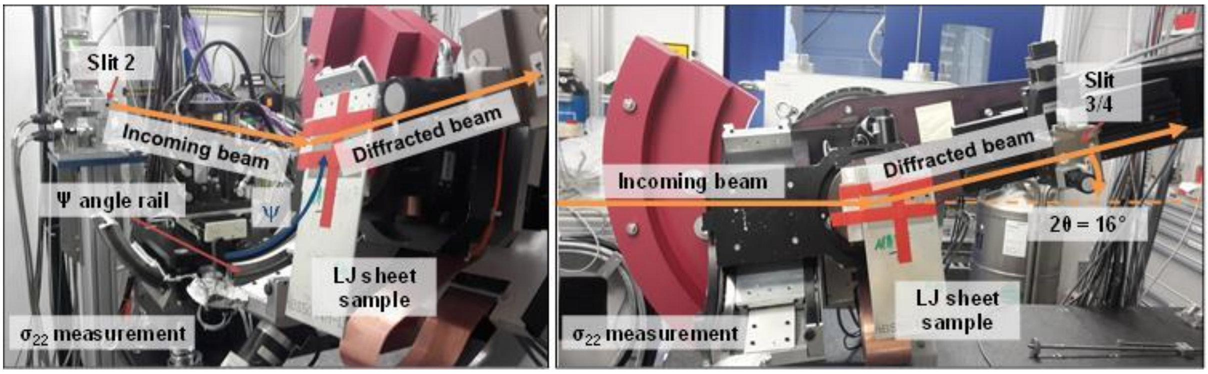

Figure 3-22: Photograph of the experimental set-up and the analysed LJ sheet at the EDDI beamline using the energy-dispersive mode for XRD RS measurements under a fixed diffraction angle of 2θ = 16°. RS measurements of longitudinal (y-direction) S_{22} stress component at ϕ = 0°/180° is shown here.

Figure 3-22 shows the experimental set-up which was used during the RS measurements of LJ sheets. The LJ sheet was fixed to the experimental table with duct tape (in red). An example of a measured diffraction spectrum is given in Figure 3-23. In this example all 12 reflections E(hkl) {111/ 200/ 220/ 311/ 222/ 400/ 331/ 420/ 422/ 511/ 440/ 531} are indicated in the spectra which was detected for a tilt angle of ψ = 14.314° and ϕ = 0°/180° (longitudinal y-direction). The intensity versus energy spectra were fitted using the Pseudo-Voigt function. Fitted peaks $E_{\phi\psi}$(hkl) for all measured tilt angles, were then further derived in stress information by applying the $\sin^2\psi$-method as described in detail here [139]. For further computation of RS values, the reflection plane 440 was not considered as the diffraction peak, as seen in Figure 3-23, was not sound and RS resulted in inconsistent data.

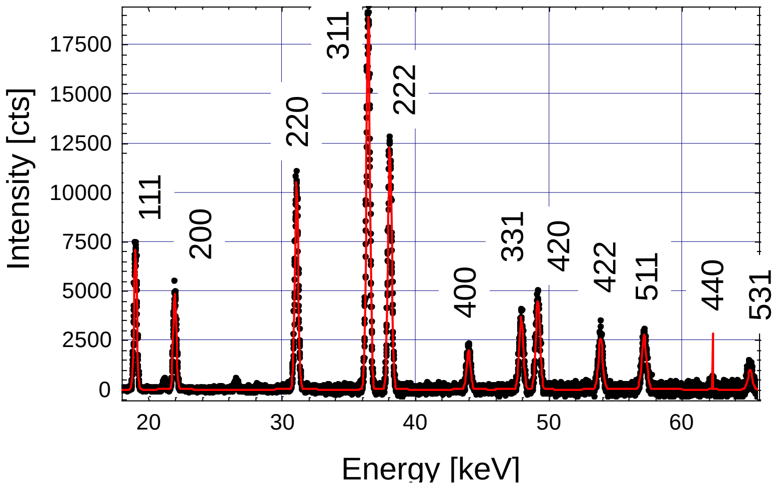

Figure 3-23: Example of measured diffraction spectra showing 12 diffraction peaks for a tilt angle ψ = 14.314°.

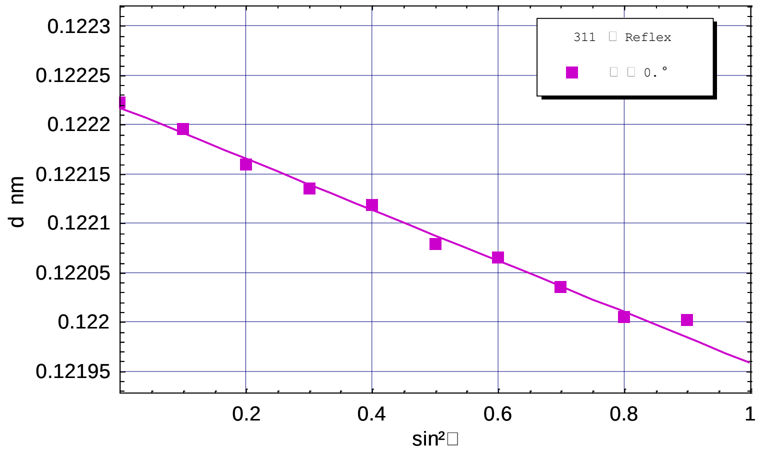

Figure 3-24: Example of d vs sin^{2}ψ plot for the 311 plane.

A typical plot of converted $E_{\phi\psi}$(hkl) data for the 311 plane is given in Figure 3-24. Applying the sin^{2}ψ-method the slope (*m*) of the curve which is determined by linear-regression analysis was used to calculate stresses by equation 2.34 assuming plane stress conditions [139]. Stresses were calculated using diffraction elastic constants $S^7{}_2$ (DEC) for high strength aluminium alloys.

$$\sigma_\phi = \frac{m}{\frac{1}{2}s_2(hkl)} \quad (Equation\ 2.34)$$

Both drilled *S-B* and *P-B* samples (B-samples) were radiated with synchrotron X-ray beams on both surfaces (corresponding to *LP Face 1* and *LP Face 2*) with a distance between the single measuring point of Δ = 1 mm in order to determine RS maps across the LP fastener hole row, as illustrated in Figure 3-25. As shown, measurements were taken from the edge of the sheet across two fastener holes on a line which was coincident with the centre line of the

---

[7] as provided by EDDI beamline MATHEMATICA® post-processing tool

fastener row. With the applied experimental set-up XRD measurements could be made up to depths of 670 – 740 µm. Because of the non-destructive nature of XRD measurements, LJ samples could be used further for fatigue testing.

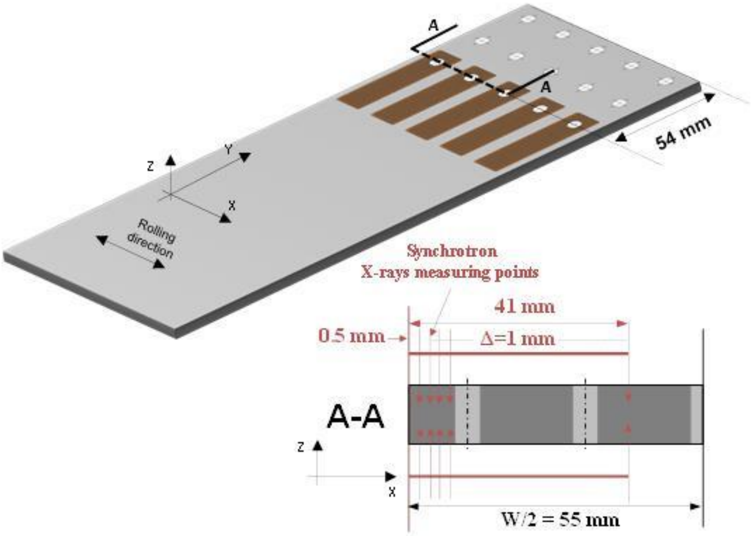

Figure 3-25: Graphic of XRD measurement locations on LJ sheet. XRD measurements location on both surfaces across fastener holes with an equidistant between measurement points of Δ1 mm.

3.2.2.3 Angle-Dispersive Synchrotron XRD at Petra-III on Laser-Peened LJs

Another XRD experiment to determine LP induced RS on single drilled (step 2 of Figure 3-11) LJ sheets was performed at the High Energy Materials Science (HEMS) P07B beamline of Petra III/DESY facility in Hamburg, Germany. In contrast to the previously explained XRD measurements at BESSY-II’s beamline using the energy-dispersive technique, P07B beamline as outline by N. Schell *et al.* [160] uses the angle-dispersive measurement technique. Moreover, it was possible to perform RS measurements through the complete thickness (average RS values) of LJ sample (t = 2.5 mm) using the P07B beamline. However, no depth resolution could be achieved using the experimental set-up as shown in Figure 3-26 so that merely an average through the sheet thickness value was measured.

In this set-up an X-ray beam with a wave length of $\lambda = 0.14235$ Å carrying a photon energy of E = 87.1 keV and a beam gauge volume of 0.1 mm by 0.1 mm was used. The incoming beam was diffracted by the crystalline structure of the samples and the diffracted beam was captured by a 2D XRD 1622 Digital X-ray Flat Panel Detector. The pixel pitch of the detector was 200 µm. The distance between test samples and the detector was adjusted to 1720 mm so that three full Debye-Scherrer rings corresponding to three crystallographic reflection planes {111/200/220} could be captured on the detector.

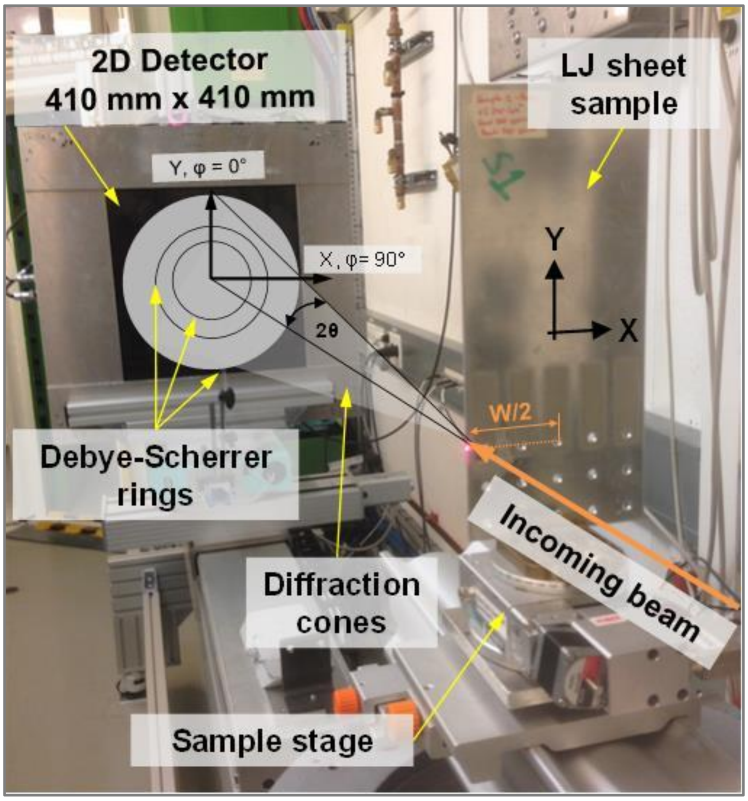

Figure 3-26: Photograph of the experimental set-up at the HEMS P07B beamline using angle-dispersive mode for XRD RS measurements. Superimposed sketch of diffraction cones and detected Debye-Scherrer ring on the 2D area detector.

An example of an image captured by the area detector showing the diffracted X-ray impacts as intensities are presented in Figure 3-27. Three reflection planes could be measured {111/ 200/ 220} and were identified by using equation 2.35 and a lattice parameter a = 4.05 Å respectively.

$$d(hkl) = \frac{a}{\sqrt{h^2 + k^2 + l^2}} \quad (Equation\ 2.35)$$

Table 3-11: Reflection planes and corresponding 2θ values determined by using equation 2.35 and Bragg's law (equation 2.24)

Reflection plane (hkl)	2θ
111	3.489
200	4.029
220	5.698

The data inherent in the image was the converted into diffractograms (Figure 3-28) using the a2tool by feeding the necessary data to calculate 2θ values by means of trigonometry such as the distance of the sample to the detector and wave length into it. An example of a diffractogram for φ = 0° is given in Figure 3-28 and all three reflection peaks can be seen. For φ = 0° data was integrated from φ = -5° to φ = 5° and for φ = 90° from φ = -85° to φ = 95° respectively. Diffractograms were compiled and processed into RS values for *S-B* and *P-B* (B-samples) on the centre line of the laser-peened fastener row as indicated in Figure 3-26. Measurement points had an equidistance of 1 mm over half the width of the LJ sheet (55 mm).

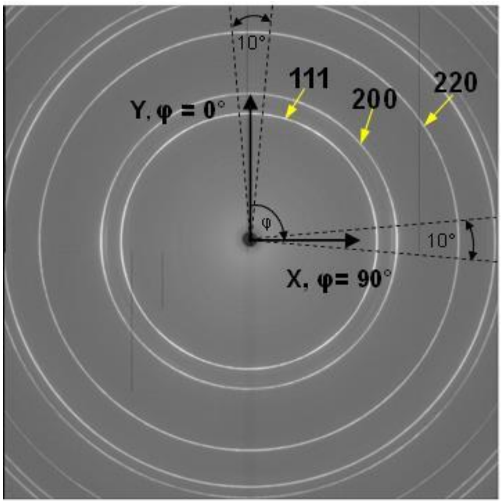

Figure 3-27: An example of photo-image captured by the 2D area detector showing the intensities of diffracted X-rays. Three full Debye-Scherrer rings were identified corresponding to reflection planes: {111/200/220}. φ = 0° corresponds to σ_{yy} (longitudinal) and φ = 90° (transverse) corresponds to σ_{xx} respectively. Intensities were integrated over an angle of 10°.

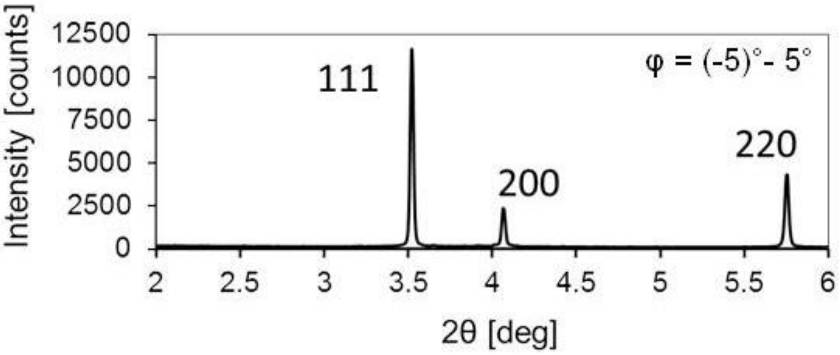

Figure 3-28: Example of measured diffractogram showing three reflection peaks {111/ 200/ 220} for φ = 0° (longitudinal) y-direction of LJ sample.

2θ values were processed into strain by using Bragg's law (equation 2.24) and assuming plane stress conditions d_0 values were determined by further assuming equilibrium condition [139]. Only the {111} reflection plane was processed into strain and a DEC (E_{111}=73.3 GPa) value for were taken from Clausen *et al.*[158]. Diffraction peaks were fitted using Origin®8 software's Gaussian distribution fitting function. Stresses were finally calculated using equation 2.21.

3.3 Crack Growth and Fatigue Testing

In order to analyse the effect of LP on the fatigue crack growth performance of laser-peened CCT-samples and laser-peened fastened LJ samples mechanical tension-tension endurance tests have been performed and the followed procedure will be described in this section.

3.3.1 Crack Growth Testing of Laser-Peened CCT-Samples

Fatigue crack growth tests of CCT-samples were performed using a load controlled INSTRON servo-hydraulic fatigue test machine with a maximum load capacity of 100 kN. A series of CCT-samples were constant amplitude tested in Baseline (BL) configuration for three different R-ratios of R = 0.1 (*CCT-BL-1 to CCT-BL-3*), R = 0.3 (*CCT-BL-4 and CCT-BL-5*) and R = 0.5 (*CCT-BL-6 to CCT-BL-7*) to derive Walker’s crack growth model constants for AA2524-T3 1.6 mm thin sheets. Samples in LP configuration were tested applying R = 0.1. All loads and LP parameters of BL and LP test samples are outlined in Table 3-12. Three different LP configurations (*1-A*, *2-A* and *2-B*) were analysed corresponding to the LP treatments as described in chapter 3.1.2.3.

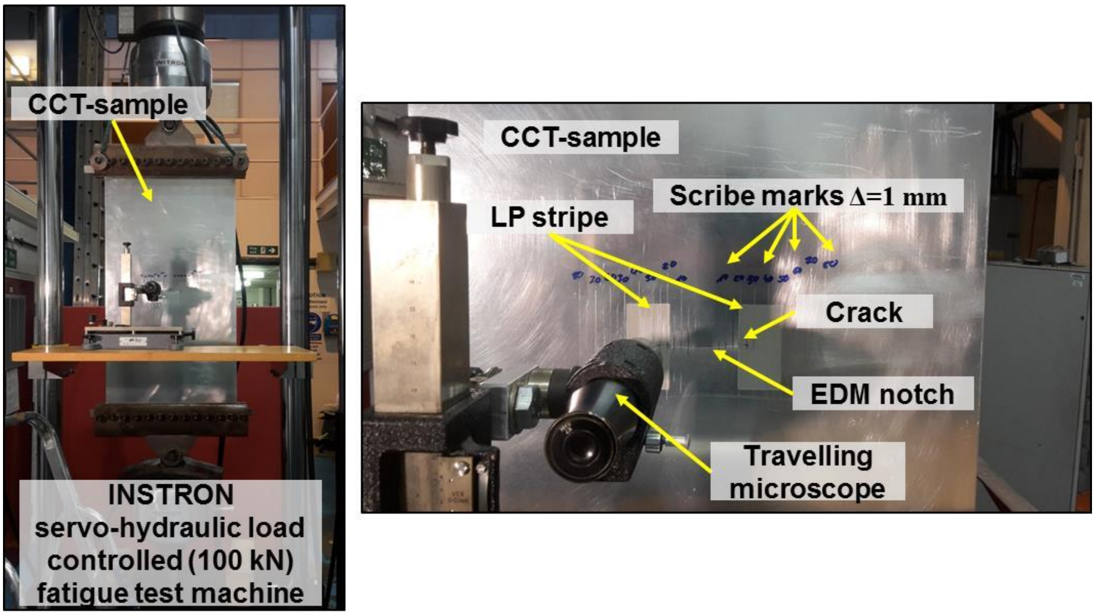

Figure 3-29: Photographs of the experimental set-up in Cranfield’s structural integrity test lab. CCT-samples in load controlled INSTRON servo-hydraulic fatigue test machine with a maximum load capacity of 100 kN (left figure) and optical travelling microscope and assisting scribe marks (equidistance of 1 mm) during crack growth testing (right figure).

A single CCT-sample was tested treated in *1-A* configuration (*CCT-LP1-1*), and two samples were mechanically cycled to failure in each 2-A (*CCT-LP2A-1*and *CCT-LP2A-2*) and 2-B (*CCT-LP2B-1* and *CCT-LP2B-2*) LP configuration respectively. All CCT-samples were orientated in the T-L direction.

Crack lengths were measured, as shown in Figure 3-29, via an optical travelling microscope and assisting scribe marks which were processed to the sample's surfaces prior to testing with an equidistance of 1 mm using a height gauge. Crack length measurement were taken on the front face only as no obvious deviation between front and back face were observed. Test samples were aligned to the hydraulic test machines and gripped by self-aligning grips. All tests were performed at room temperature and applying a constant amplitude load cycle frequency of 5.5 Hz. Crack growth rates were calculated by ASTM E647-00 [41] proposed secant method (ASTM E647-00 Appendix X1.1).

Table 3-12: Test matrix of CCT-crack growth samples.

Sample ID	Nominal applied Stress, max [MPa]	R-ratio	Laser-Peening (as defined in chapter 3.1.2.3)
CCT-BL-1	90	0.1	NO LP
CCT-BL-2	90	0.1	NO LP
CCT-BL-3	90	0.1	NO LP
CCT-BL-4	110	0.3	NO LP
CCT-BL-5	110	0.3	NO LP
CCT-BL-6	120	0.5	NO LP
CCT-BL-7	120	0.5	NO LP
CCT-LP1-1	90	0.1	1-A
CCT-LP2A-1	90	0.1	2-A
CCT-LP2A-2	90	0.1	2-A
CCT-LP2B-1	90	0.1	2-B
CCT-LP2B-2	90	0.1	2-B

3.3.2 Fatigue Testing of Fastened Lap-Joints

Fatigue endurance tests at constant amplitude were performed using an INSTRON 8031 servo-hydraulic load controlled fatigue test machine with maximum fatigue load capacity of 50 kN on baseline (*LJ-BL*) un-peened LJs and laser-peened LJ samples. Both *S-samples* (*LJ-S-A* and *LJ-S-B*) and *P-samples* (*LJ-P-A* and *LJ-P-B*) were examined in order to determine the effect of the different LP strategies and their corresponding measured RS fields on the fatigue performance. Fatigue testing was carried out in cyclic tension-tension condition using an R-ratio of 0.1, a frequency of 8 Hz and loading conditions, as described in Table 3-13. All tests were performed at room temperature (18°-20°C). From Table 3-13, it can be noticed that for *BL* and *strategy-B* samples testing were conducted at two load levels (stress amplitudes: σ_{amp} = 49.5 MPa and σ_{amp} = 72.0 MPa) and three replicate LJ samples were completely fractured per load level and per LP layout to assess the scatter of the LP process and its resulting RS field. For *strategy-A* samples, only two replicate samples per LP layout were fatigued until rupture for one load level (σ_{amp} = 49.5 MPa).

Table 3-13: Test matrix of LJ sample fatigue endurance testing.

		Sample ID	Nominal applied Stress,max [MPa]	Cross-section Area [mm^2]	Applied Load, max [N]	Applied Load, min [N]	Applied Load, amp. [N]	Applied Stress, amp. [MPa]
Baseline No LP		**LJ-BL-1**	110	275	30.3	3.0	13.6	**49.5**
		LJ-BL-2	110	275	30.3	3.0	13.6	**49.5**
		LJ-BL-3	110	275	30.3	3.0	13.6	**49.5**
		LJ-BL-4	160	275	44.0	4.4	19.8	**72.0**
		LJ-BL-5	160	275	44.0	4.4	19.8	**72.0**
		LJ-BL-6	160	275	44.0	4.4	19.8	**72.0**
LP Strategy-A		**LJ-S-A-1**	110	275	30.3	3.0	13.6	**49.5**
		LJ-S-A-2	110	275	30.3	3.0	13.6	**49.5**
		LJ-P-A-1	110	275	30.3	3.0	13.6	**49.5**
		LJ-P-A-2	110	275	30.3	3.0	13.6	**49.5**
LP Strategy-B	**S-samples**	**LJ-S-B-1**	110	275	30.3	3.0	13.6	**49.5**
		LJ-S-B-2	110	275	30.3	3.0	13.6	**49.5**
		LJ-S-B-3	110	275	30.3	3.0	13.6	**49.5**
		LJ-S-B-4	160	275	44.0	4.4	19.8	**72.0**
		LJ-S-B-5	160	275	44.0	4.4	19.8	**72.0**
		LJ-S-B-6	160	275	44.0	4.4	19.8	**72.0**
	P-samples	**LJ-P-B-1**	110	275	30.3	3.0	13.6	**49.5**
		LJ-P-B-2	110	275	30.3	3.0	13.6	**49.5**
		LJ-P-B-3	110	275	30.3	3.0	13.6	**49.5**
		LJ-P-B-4	160	275	44.0	4.4	19.8	**72.0**
		LJ-P-B-5	160	275	44.0	4.4	19.8	**72.0**
		LJ-P-B-6	160	275	44.0	4.4	19.8	**72.0**

3.3.3 In-situ Stress Analysis of Fastened Lap Joints Using Strain Gauges

Out of plane or secondary bending occurring in the LJ samples on an application of cyclic tensile loading was quantified using uniaxial strain gauges located as shown in Figure 3-30. Consequent stresses were calculated assuming uniaxial Hook’s law.

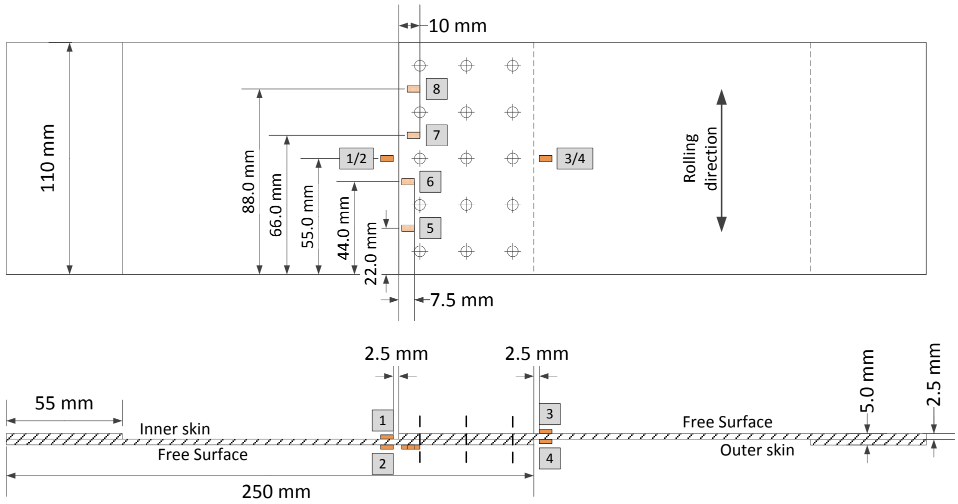

Figure 3-30: Drawing of strain gauge map on LJ sample.

3.4 Fractography

For further in-depth analyses to understand the underlying mechanism of beneficial or detrimental effects of LP on LJ samples in order to customise the LP strategy in the pursuit of maximising the benefits of LP, post-mortem fractorgraphic methods were conducted as described in the following section. Those analyses were exclusively performed on LJ samples since the observation of fatigue damage evolution during testing could be performed straight forwardly as cracking occurs typically hidden away between the two sheets of the LJ sample.

3.4.1 Post-mortem Fracture Surface Examination Using Microscopy

Fracture surfaces were analysed after breakage of LJ samples in order to characterise the fracture of BL and laser-peened samples and to deduce the fracture progression sequence. To begin, micrographs were taken of identified fretting-fatigue and fatigue cracks using a microscope equipped with a Leica EC3 digital camera in order to identify failure initiation location and propagation paths. Also SEM images were taken using a Philips XL30 SFEG SEM machine. Multiple pictures were taken and stitched together in order to show representative cracks in test samples. Obtained micrographs were then further processed by scaling and editing, so that illustrations of maps describing the complete fracture surfaces could be created.

3.4.2 Striation Counting on Fractured Lap-Joints

Further efforts consisted of analysing fracture surfaces using a Phillips XL30 SFEG SEM for post-mortem crack growth analyses by quantifying the crack growth progression marks known as striations. Fatigue striations can be related to crack growth rate by assuming that the spacing between striations are the result of the crack advancement from one applied load cycle [161]. Spacing between fatigue striations as exhibited in Figure 3-31 were quantified by averaging measurements of the distance of bands of 4 – 20 striations and counting the number of striation within this distance at multiple locations at the same overall crack length. The overall crack length was determined by considering the distance of a particular measurement location relative to the pre-identified initiation location. All measurements were performed along the sheet thickness direction, as this was found to be the dominant propagation direction of cracks. Overall guidelines as summarised from research of fatigue striations conducted by E. Hershko *et al.* [162] were considered during striation measurements.

Since enormous time efforts are needed to examine fracture surfaces by striation counting only fractured *LJ-BL* and *LJ-P-B* samples were considered in order to analyse the effect of laser-peened induced RSs on the fatigue crack growth rate of LJ samples.

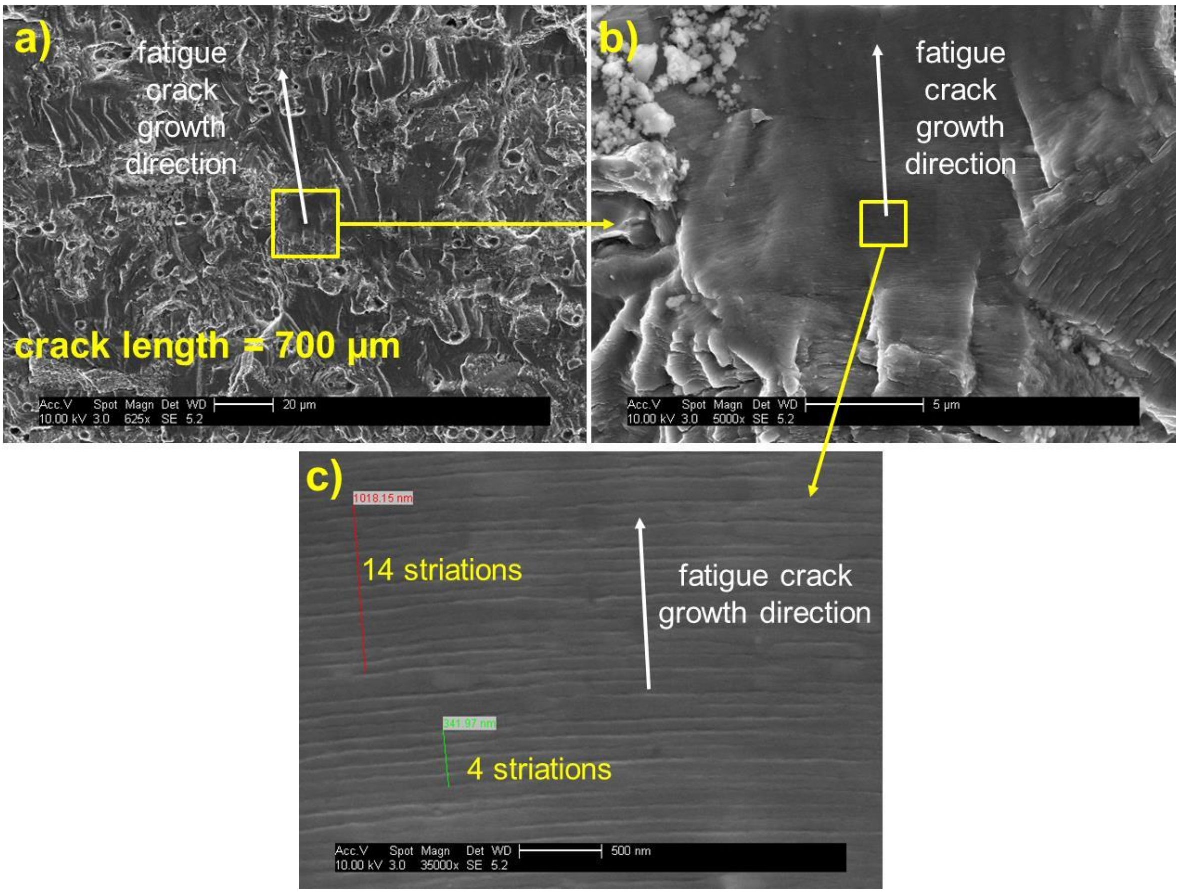

Figure 3-31: SEM images of fatigue striation at different magnifications. a) Fatigue crack growth fracture surface at 625x magnification, b) Fatigue crack growth striation at 5,000x magnification and c) Fatigue crack growth striation at 35,000x magnification.

4 Residual Stresses in Laser-Peened Aircraft Aluminium and Lap-Joints

This chapter presents the results of RS measurements which were obtained by the experimental procedures and techniques as described in the preceding section. Initially, RS results for laser-peened 1.6 mm 2524-T3 samples will be described. Then RSs for laser-peened LJ samples made of 2.5 mm 2024-T3, are presented, before the obtained results are discussed and compared to RS result which were found in the literature. Further, discussions will reflect on the results in the light of the used measurement procedures. Lastly, the effects of different parameters of the LP treatment are discussed.

4.1 Residual Stresses in Laser-Peening Parameter Study Sample and CCT-Samples

The following two separate sections present RS results determined by ICHD and neutron diffraction. ICHD measurements were taken from the simple test samples (*LP parameter study sample*) as shown in Figure 3-3. Recall that nine different sets of LP process parameters were applied to these test specimens, as shown in Table 3-4: LP treatment matrix used in LP process parameter study. Neutron diffraction experiments were performed on 2524-T3 CCT-samples as described in section 3.1.2.3.

4.1.1 Laser-Peening Process Parameters Study

Figure 4-1 presents RS profiles for nine different sets of LP process parameters through the sheet thickness determined by ICHD. Only the stress component which is parallel to the stepping direction of the applied LP raster zig-zag pattern is plotted in the diagrams as all of the data showed a bi-axial stress field. The RS data for a constant power density of 2.5, 2.0 and 1.5 GW per cm^2 are shown in Figure 3-17a to Figure 3-17c to compare different pulse densities (250, 500 and 750 spots per cm^2) respectively. In Figure 3-17d to Figure 3-17f the RS data presents RS profiles for a constant power density so that varying power densities (2.5, 2.0 and 1.5 GW per cm^2) can be compared.

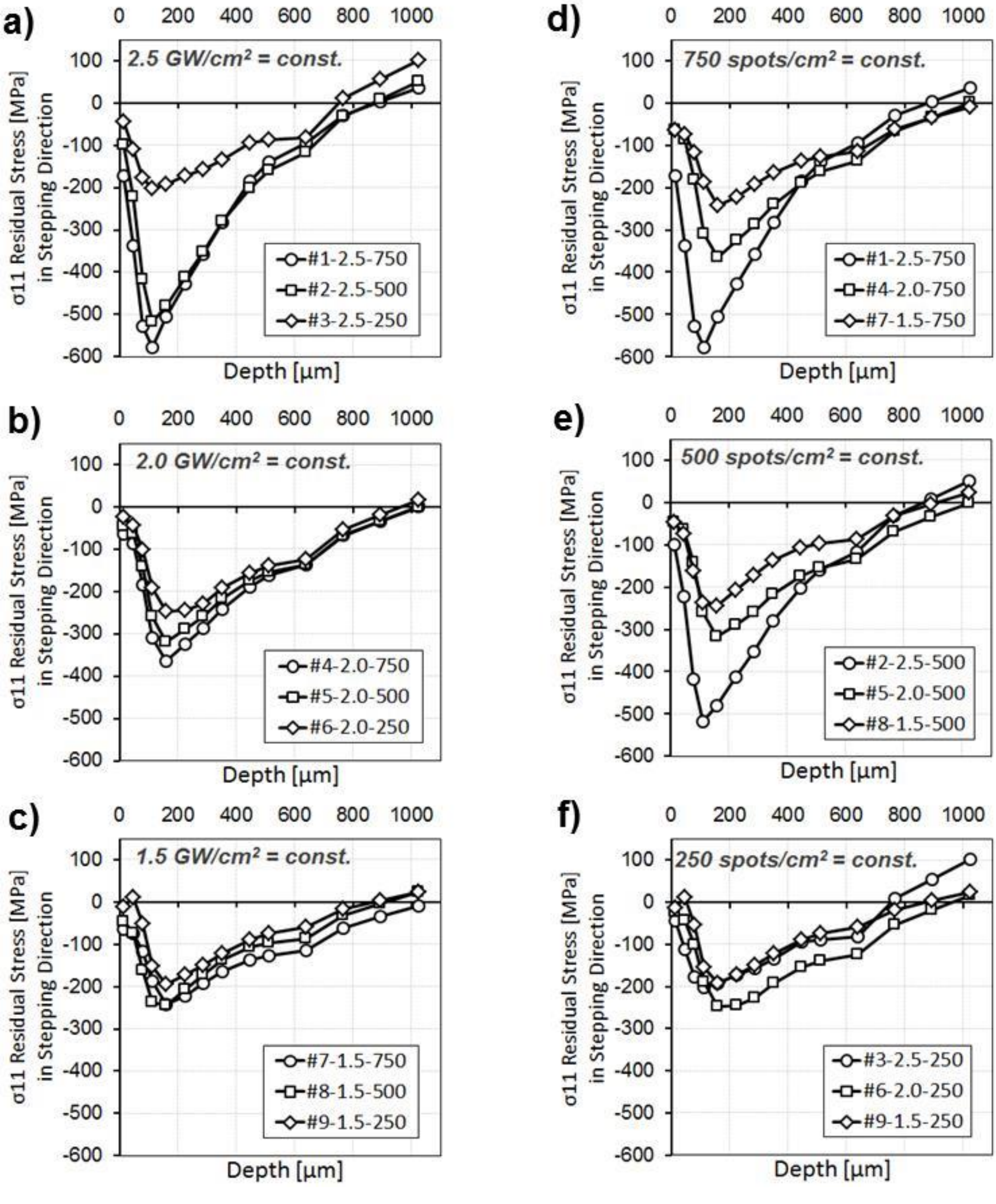

Figure 4-1: Plots of RS profiles through 1.6 mm sheet thickness for varying power densities and pulse densities. a), b) and c) Comparisons of three different pulse densities of 250, 500 and 750 spots per cm^2 for constant power densities of 2.5, 2.0 and 1.5 GW per cm^2. d), e) and f) Comparisons of three different power densities of 750, 500 and 250 spots per cm^2 for constant power densities of 2.5, 2.0 and 1.5 GW per cm^2.

Different near surface RSs (at 16 µm depth) were observed for all test samples. A summary of obtained near surface RSs, as shown in Figure 4-1, concerning different LP process parameters is given in a contour map as presented in Figure 4-2. The contour lines in the data plot differentiate three different ranges of stress magnitudes (green = 0 MPa to -50 MPa; red = -50 MPa to -100 MPa; blue = -100 MPa to -150 MPa). The white arrow indicates the trend of increased values, and consequently, the numbers between data points give the growths in percentage. From this map which put into relation the LP process parameters and surface RS values, it can be noticed that with increasing pulse density the near surface RSs become larger. For a power density of 2.5 GW per cm^2 this trend becomes evident as with increasing the pulse density from 250, 500 to 750 pulses per cm^2 the surface RS result into -45 MPa, -100 MPa and -173 MPa respectively. This is an increase of 285 % from 250 to 750 pulses per cm^2. Analogously for a power density of 2.0 and 1.5 GW per cm^2 and an increase in surface RS of 167 % and 392 % can be abstracted from the map. Power density when decreased generally exhibited larger surface RS but, the same impact is not observed for all comparisons as is the case for increased pulse densities. For instance, increasing power density from 1.5 to 2.0 GW/cm^2 no increase in near surface RS was observed for 500 and 750 pulses per cm^2.

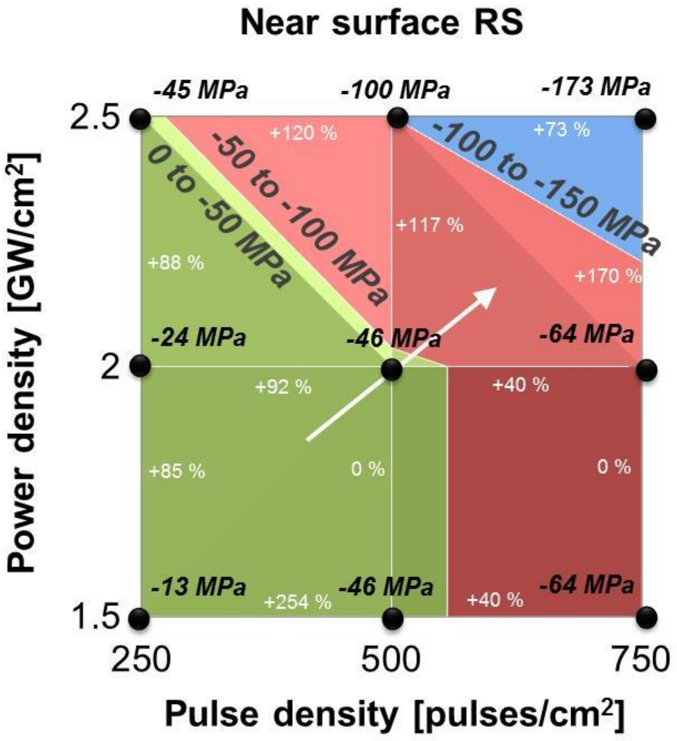

Figure 4-2: Contour map of surface RSs in relation to power density and pulse density.

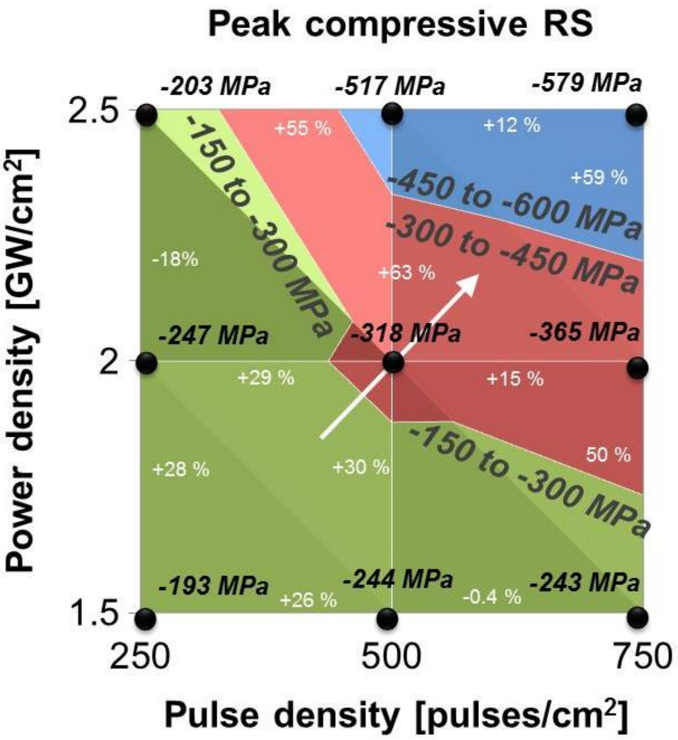

Figure 4-3: Contour map of peak compressive RSs in relation to power density and pulse density.

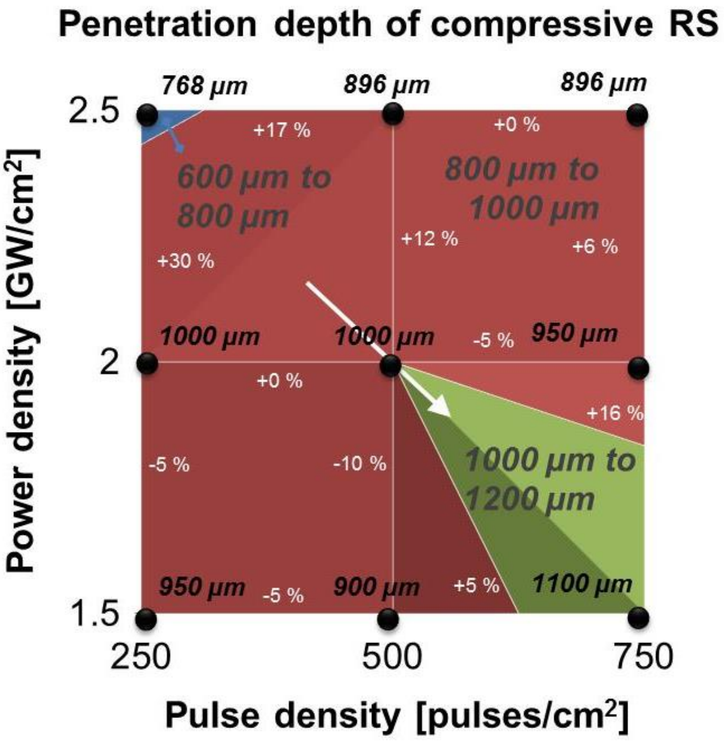

Figure 4-4: Contour map of penetration depths of compressive RSs in relation to power density and pulse density.

Regarding the peak compressive RS, as analysed from the ICHD measurements as shown in Figure 4-1, the effect of power density and pulse density can be explained by the help of the contour map as shown in Figure 4-3. The plot is similar to the map described for near surface RSs. In this plot the contour lines differentiate three different ranges of stress magnitudes (green = -150 MPa to -300 MPa; red = -300 MPa to -450 MPa; blue = -450 MPa to -600 MPa). From this data plot, the general observation is that the power density and pulse density have similar weights on the impact on the peak compressive RS values. As an example for constant held pulse density of 750 pulses per cm^2 and increasing the power density from 1.5 to 2.0 and 2.5 GW per cm^2 peak compressive RS also increase by 50% and 138% respectively. In contrast, increasing the pulse density from 250 to 500 and then to 750 pulses per cm^2 for a constant power density of 2.5 GW per cm^2 an increase in peak compressive RS of 55 % and 185 % can be calculated.

The penetration depth of the compressive RS field was also studied using the RS profile of Figure 4-1 and is given as a contour plot. In this plot, as shown in Figure 4-4, the three different areas define three ranges of penetration depth (green = 1000 μm to 1200 μm; red = 800 μm to 1000 μm; blue = 600 μm to 800 μm). The arrow which points towards the trend is reversed in this plot which indicates a dissimilar behaviour exhibited by the data. It seems that the penetration depth increases if power density is decreased and pulse density is increased. The overall trend is measured taking the penetration depth as a result of 2.5 GW per cm^2 and pulse density of 250 pulses per cm^2 (768 μm) and comparing it with penetration depth as a result of 1.5 GW per cm^2 and pulse density of 750 pulses per cm^2 (1100 μm). This is a rise in penetration depth of 43 %. The described trend, however, is inconclusive taking into account all LP process parameter configurations.

4.1.2 Residual Stresses in Laser-Peened CCT-Samples

Neutron diffraction (ND) measurement values of RS determined for laser-peened 2524-T3 CCT-samples (*LP-2-B*) are shown in Figure 4-5. Three measurements which vary in the thickness direction and the respective average value are plotted in the diagram for six measurement points across the width of a CCT-sample. The RS is given for the longitudinal (y-) direction. For the average RS, the data values are given next to the data point.

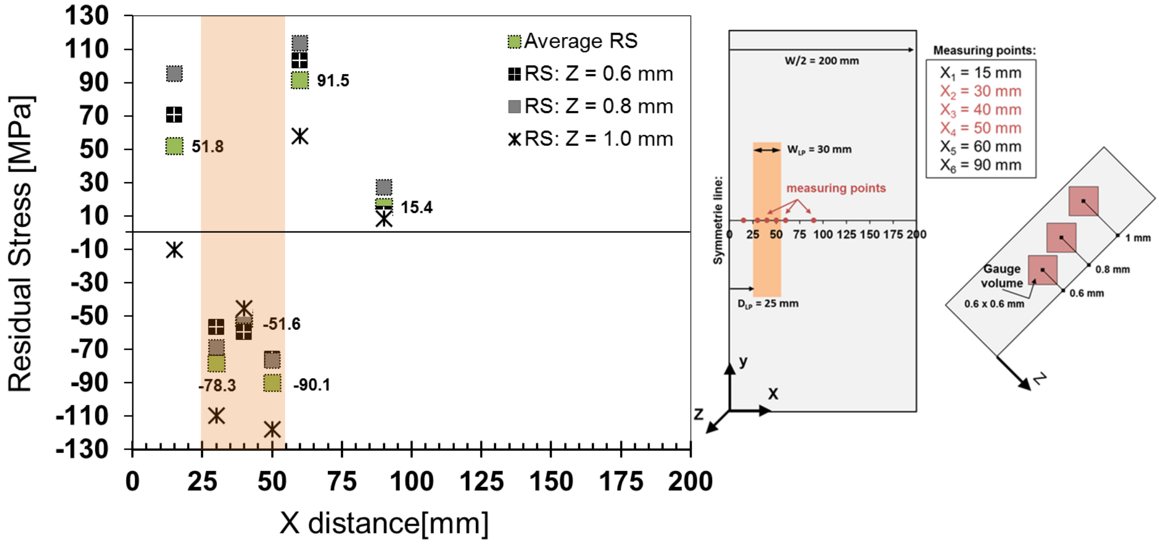

Figure 4-5: Neutron diffraction RS measurement result for a laser-peened 2524-T3 CCT-sample. Residual stress is given for the longitudinal (y-) direction.

In brief, the obtained ND data indicate two general observations. Firstly, RS in the LPS (light orange area) are compressive and tensile outside the LPS. This is expected since LP introduced plastic deformation and provokes an elastic push back by the surrounding un-peened material. Moreover, RS result measured on 2524-T3 samples exhibited strong RS profile, as described in chapter 3.2.1.1. Secondly, RS values decrease with increased penetration of the gauge volume into the sheet normal direction indicating a high gradient of RS.

The compressive RS within the LPS ranges from $\sigma_{RS,yy}$ = -45.2 MPa (x_3 = 40 mm/ z = 1.0 mm) and $\sigma_{RS,yy}$ = -118.0 MPa (x_4 = 50 mm/ z = 1.0 mm). Between the centre line (x = 0 mm) and the LPS, an average tensile RS of $\sigma_{RS,yy}$ = 51.8 MPa was measured. The region after the LPS, in between the LPS and the edge of the sample (x = 200 mm), accommodates an average tensile RS of $\sigma_{RS,yy}$ = -91.5 MPa immediately outside the peened area and rapidly drops to $\sigma_{RS,yy}$ = 15.4 MPa with a distance of 35 mm away from the LPS.

4.2 Residual Stresses in Fastened Lap-Joints

RS measurement results on laser-peened LJ samples are presented in individual sections according to the applied measurement technique. Those RS results coming from those different methods will be contrasted and compared. The longitudinal stress component σ_{yy} will be highlighted during the presentation, and subsequent conclusion of results, as this is the most crucial component for further analysis of following fatigue performances because of the coincidence direction with the external loading direction.

4.2.1 Residual Stresses Measured Using ICHD - Strategy-A vs Strategy-B

ICHD measurement results are given in Figure 4-6 comparing RS profiles through the LJ sheet thickness for all investigated LP strategies. Those values were taken from *LP Face 1* and *Hole 1* to compare the different LP strategies only.

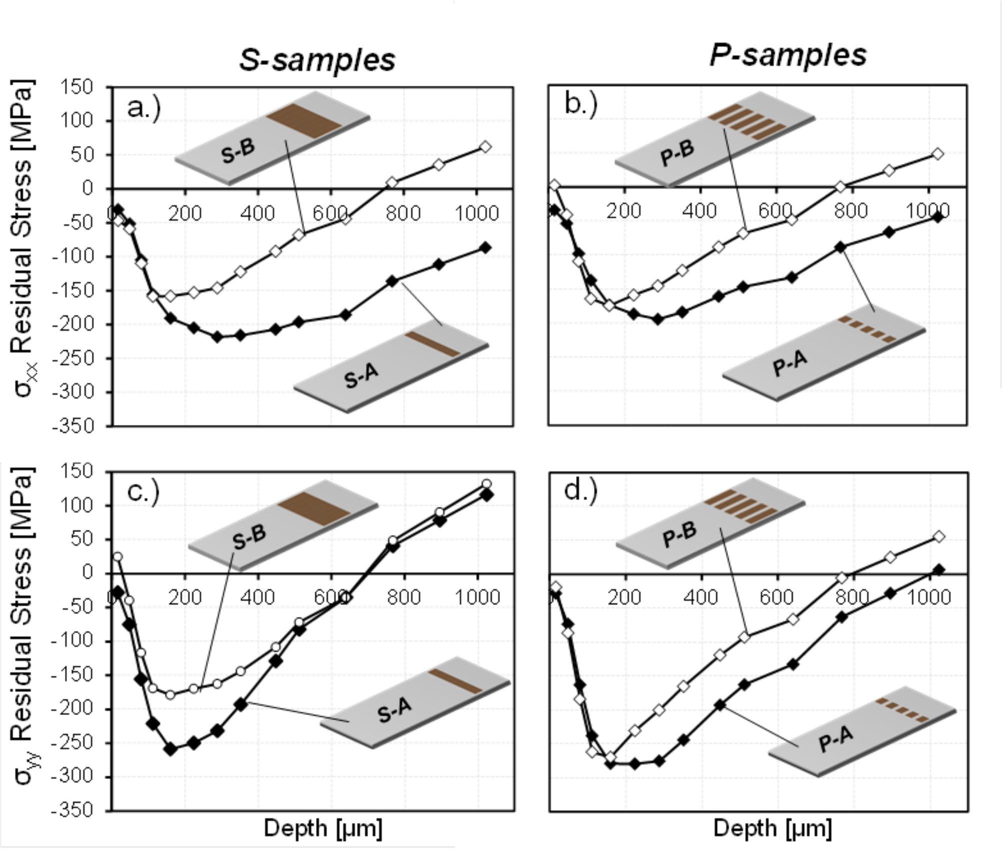

Figure 4-6: ICHD determined RS profiles through the thickness of LJ sheets. a.) σ_{xx} *S-A* vs *S-B*, b.) σ_{xx} *P-A* vs *P-B*, c.) σ_{yy} *S-A* vs *S-B*, d.) σ_{yy} *P-A* vs *P-B*,

For presented results, σ_{yy} refers to stresses in longitudinal and σ_{xx} for the transverse direction of the sheet receptively (compare with Figure 3-14). All LP strategies produced compressive stresses. Near surface (up to 48 µm deep) RS were similar and near zero for all LP strategies. The effects of different LP strategies became more evident analysing the maximum RS value.

For the designated loading direction (y-direction) of assembled LJ samples, (Figure 4-6c. and Figure 4-6d.) RS for *P-samples* (P-A: σ_{yy} =-280 MPa, P-B: σ_{yy} = -270 MPa) generally show greater compressive RS than their laser-peened *S-sample* counterparts (*S-A*: σ_{yy} =-256 MPa, *S-B*: σ_{yy} = -178 MPa). The difference between *A* and *B* samples is significant for *S-samples* but not for *P-samples*. The *P-B sample* (*P-B*: σ_{yy} = -270 MPa) maintained almost the same compressive stress maximum as *P-A samples*. (*P-A*: σ_{yy} =-280 MPa). This was despite LP parameters such as the Power Density and Pulse Density being decreased in Strategy B peening process.

In terms of depth of generated compressive RS in loading direction, the P-layout produces deeper compressive stress than S-layouts. The S-layouts show identical penetration depths of ~ 700 microns for both *A* and *B* samples, whereas in *P-samples* depths of compressive stress are different in *A* and *B* strategies (P-A: depth ~ 1000 microns, P-B: depth ~ 800 microns).

Table 4-1: Summary of compressive RS profiles for LP strategies.

Strategy	Power Density [GW/cm^2]	Pulse density LP Face 1 [spots/cm^2]	Max. Compr. RS σ_{xx} [MPa]	Depth of Compr. RS σ_{xx} [µm]	Max. Compr. RS σ_{yy} [MPa]	Depth of Compr. RS σ_{yy} [µm]
S-A	2.5	750	-218	>1100	-256	~700
S-B	2.0	500	-158	~750	-178	~700
P-A	2.5	750	-194	>1100	-280	~1000
P-B	2.0	500	-174	~770	-270	~800

A summary of laser-peened induced RS profiles is given in Table 4-1 to contrast LP process parameters with maximum compressive RS and penetration depth of measured RS profiles. Taking the maximum compressive RS in both transverse and longitudinal direction into account irrespective of identical location in depth the bi-axiality of the RS profile can be assessed. A summary of bi-axiality which is defined by the ratio of σ_{xx} and σ_{yy} which was produced by the different LP strategies is given in Table 4-2. From this data, it can be concluded that *P-samples* produce higher bi-axiality or anisotropy favouring the longitudinal stress component than *S-samples* regardless of applied LP process parameters.

Table 4-2: Summary of bi-axiality of RS profiles

Strategy	Max. Compr. RS σ_{xx} [MPa]	Max. Compr. RS σ_{yy} [MPa]	Bi-axiality σ_{xx}/σ_{yy}
S-A	-218	-256	0.85
S-B	-158	-178	0.89
P-A	-194	-280	0.69
P-B	-174	-270	0.64

A summary of tensile RS values is given in Table 4-3. Tensile RSs are produced to achieve and satisfy the equilibrium condition. Comparing *S*- and *P-sample*'s maximal tensile RS y-directional component significant differences can be noticed. Namely, *S-samples* show tensile RS values 2.4 – 16.7 times higher than *P-samples* for both *A*- and *B-samples*.

Table 4-3: Summary of tensile RS profiles for LP strategies.

Strategy	Power Density [GW/cm^2]	Pulse Density LP Face 1 [spots/cm^2]	Max. Tensile RS σ_{xx} [MPa]	Max. Tensile RS σ_{yy} [MPa]
S-A	2.5	750	n/a	117
S-B	2.0	500	62	132
P-A	2.5	750	n/a	7
P-B	2.0	500	49	55

4.2.2 Residual Stresses Study Measured Using ICHD - Strategy-B

A more comprehensive RS study using ICHD measurement was performed on strategy *B-samples* only. Preliminary fatigue test results which will be described in later chapters (chapter 7.2.1) have shown superiority on the fatigue performance by *B-samples* so that *A*-samples were excluded for further investigations. RS profiles of *P-B* and *S-B* were further studied to analyse the variation of RS in different locations on the LJ sheet. This included both LP layout: *P-samples* with *S-samples*:

- *LP Face 1* vs *LP Face 2*
- *Hole 1* (edge hole) vs *Hole 3* (centre hole)

4.2.2.1 LP Layout - P-samples vs S-samples

As earlier mentioned measured RS profiles comparing *P-B* and *S-B samples* are exhibited in Figure 4-7. *P-samples* produce higher compressive RS values than *S-samples* (*P-B*: σ_{yy} = -270 MPa vs *S-B*: σ_{yy} = -178 MPa) in the longitudinal y-direction of the LJ sheet. The penetration depth varies slightly and is also deeper for *P-B samples* at almost 800 microns versus approximately 700 microns for *S-B samples*. For the transverse direction, both RS profiles are similar.

Near surface RSs vary for both measured stress directions, but those RS are not regarded as highly diagnostic as the first increment of ICHD measurement is averaged over the top 32 μm which are located in the clad layer (refer to the discussions in section 4.3.1).

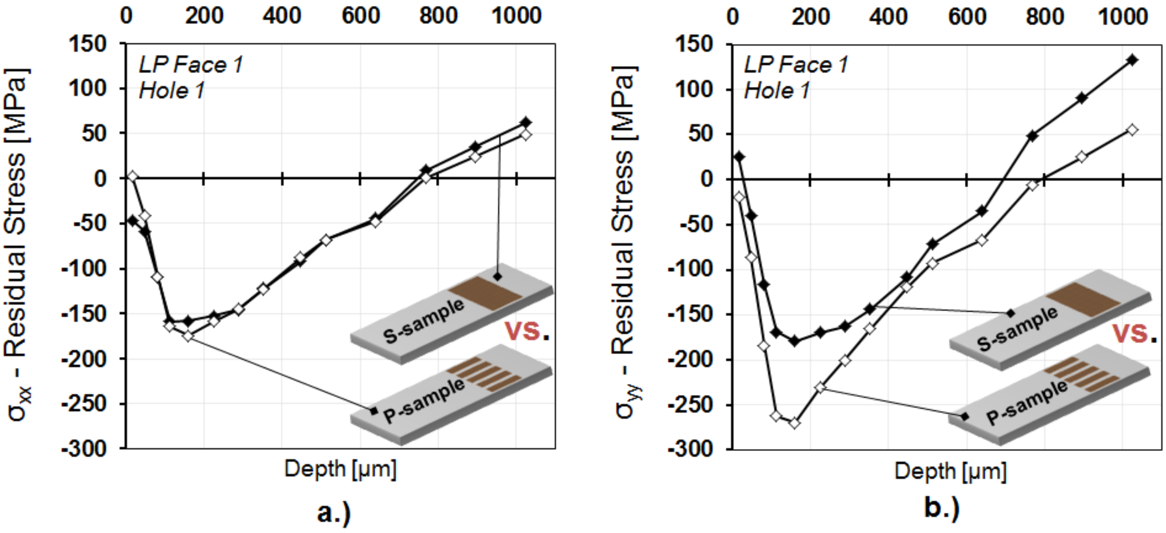

Figure 4-7: Comparison of RS profiles through the thickness of LJ sheets of *P-samples* vs *S-samples*. ICHD measurements were taken at LP Face 1 and Hole 1 location on the single LJ sheet. a.) σ_{xx} *P-B* vs *S-B* and b.) σ_{yy} *P-B* vs *S-B*

4.2.2.2 LP Surfaces - LP Face 1 vs LP Face 2

Figure 4-8 shows RS profile comparing *LP Face 1* and *LP Face 2*. Recall that *LP Face 1* corresponds to the surface of the LJ sheet which was laser-peened before *LP Face 2* and that for strategy *B-samples* a different pulse density was used for *LP Face 1* (500 spots/cm^2) and *LP Face 2* (350 spots/cm^2).

For *P-samples* as presented in Figure 4-8a and Figure 4-8b, the ICHD data shows that the effect of different applied pulse densities and also the sequence of peening the two surfaces result in small but observable differences. For the longitudinal y-direction, the maximum RS values are slightly more compressive for *LP Face 1* (LP Face 1: σ_{yy} = -270 MPa) than for *LP Face 2* (LP Face 2: σ_{yy} = -236 MPa) taking the maximum RS values into account. For the transverse direction, the difference in maximum compressive RS value is more evident and substantial, and a difference of $\Delta\sigma_{xx}$ = 70 MPa can be calculated.

Comparisons of RS profiles for *LP Face 1* and *LP Face 2* on *S-samples* are given in Figure 4-8c and Figure 4-8d. A similar trend as described before for *P-samples* can be noticed for *S-sample*'s transverse RS profile with differences of $\Delta\sigma_{xx}$ = 64 MPa. The longitudinal RS profiles are similar with a minor difference of $\Delta\sigma_{yy}$ = 6 MPa.

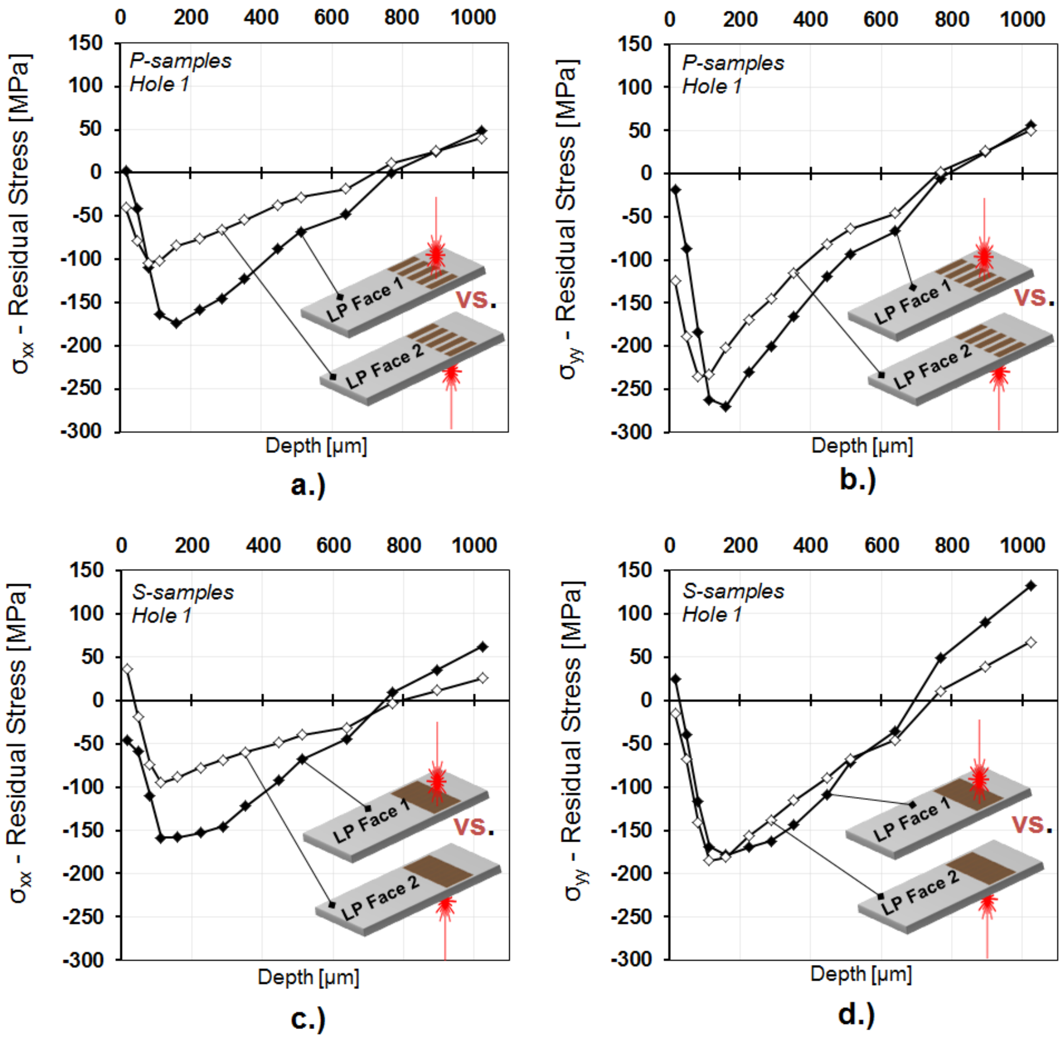

Figure 4-8: Comparison of RS profiles through the thickness of LP Face 1 vs LP Face 2 ICHD measurements were taken at Hole 1 location on the single LJ sheet. a.) *P-samples*: σ_{xx} Face 1 vs Face 2; b.) *P-samples*: σ_{yy} Face 1 vs Face 2; c.) *S-samples*: σ_{xx} Face 1 vs Face 2 and d.) *S-samples*: σ_{yy} Face 1 vs Face 2

4.2.2.3 Location - Hole 1 vs Hole 3

In order to analyse the variation of RS along the width of LJ sheets, ICHD measurements were taken at the location of designated *Hole 1* which corresponds to fastener hole near to the edge of the LJ sheet and *Hole 3* which is the centre fastener hole of a five fastener row.

The ICHD data comparing *Hole 1* and *Hole 3* for *P-samples* are shown in Figure 4-9a Figure 4-9b and for *S-samples* in Figure 4-9c and Figure 4-9d. The variation of RS profiles for the two locations across the width of laser-peened LJ sheets and along the centre line of the designated fastener row is insignificant for both investigated LP layouts. Minor differences, however, could be mentioned. For the y-directional of stress component in *P-sample*, for instance, a difference of $\Delta\sigma_{yy}$ = 16 MPa. However, considering the uncertainties of the measurements and the LP process, it could be concluded that variation of RSs are stable across the width of LJ sheets (refer to discussion about the Errors and LP Consistency in section 4.3.1).

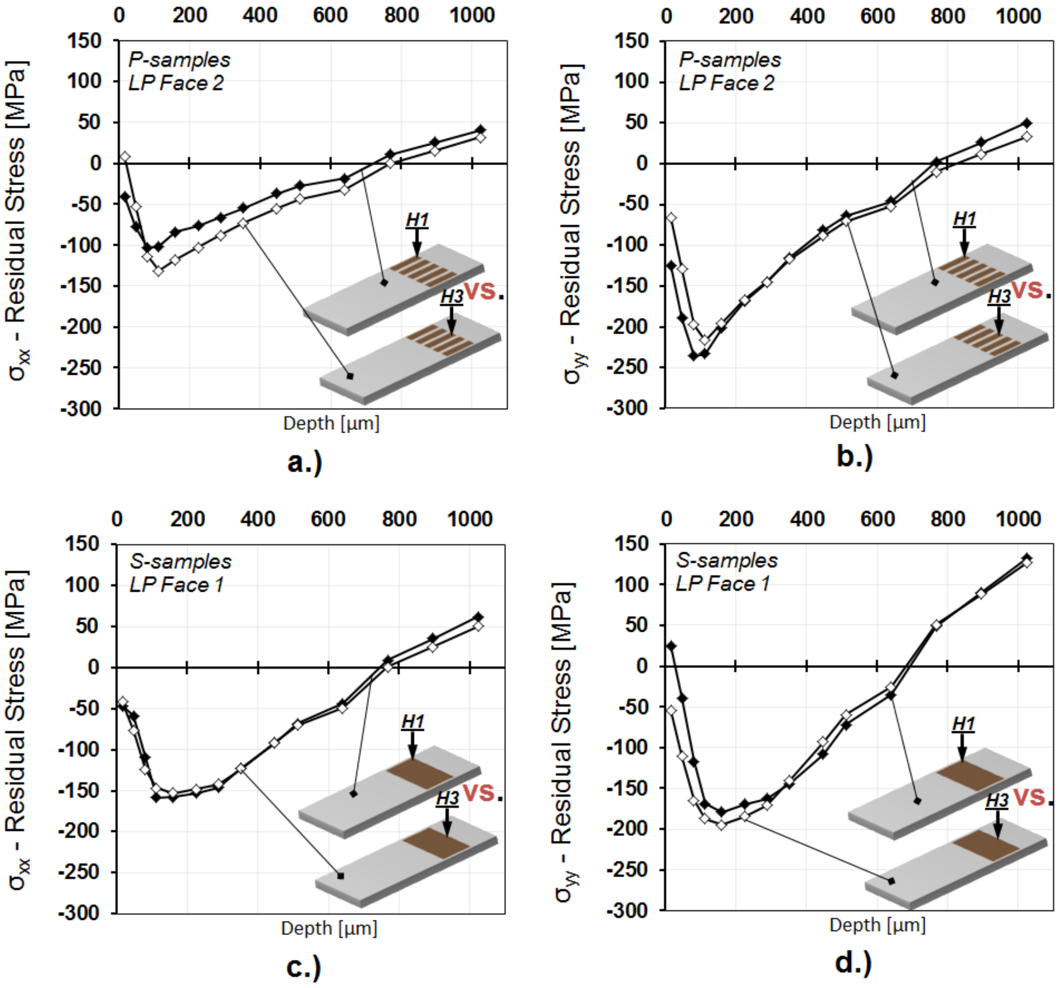

Figure 4-9: Comparison of RS profiles through the thickness of Hole 1 (edge hole) vs Hole 3 (centre hole). ICHD measurements were taken at LP Face 2 for *P-samples* and LP Face 1 for *S-samples*. a.) *P-samples*: σ_{xx} Hole 1 vs Hole 3; b.) *P-samples*: σ_{yy} Hole 1 vs Hole 3, c.) *S-samples*: σ_{xx} Hole 1 vs Hole 3 and d.) *S-samples*: σ_{yy} Hole 1 vs Hole 3

4.2.3 Synchrotron X-Ray Diffraction Results: Strategy-B

Synchrotron XRD measurements were only taken for *B-samples* (*S-B* and *P-B*) and will be presented in two sections divided by the XRD mode used to obtain RS data. Therefore for following presentations of XRD results *S-* and *P-samples* refer to *S-B* and *P-B samples* only.

4.2.3.1 BESSY-II Results: 2D Stress Maps

XRD measurement results of RS using the energy-dispersive (ED-XRD) mode at BESSY-II's EDDI beamline for *S-* and *P-samples* are presented in Figure 4-10. The 2D contour plots show the XRD measurements in relation to the position of fastener holes (Hole-1 and Hole-2). Un-measured depths (light grey area), hence the core of the LJ sheet across the width of the LJ sheet are left blank. The depth is measured from the top surface which also represents *LP Face 1*. Locations of maximum and minimum RS values are also indicated in the contour plots.

Contour plots representing the RS condition in *S-samples* can be seen in Figure 4-10a (transverse-σ_{xx}) and Figure 4-10b (longitudinal-σ_{yy}). For both stress direction, the LP layout *S-B* correlates with the 2D stress map in terms of anticipated compressive and tensile RS regions. Considering the crucial longitudinal stress component, the un-peened area at the edge of the LJ sheet (0 mm -5 mm) show significant tensile RS values up to a maximum value of σ_{yy} = 172 MPa at a depth of 645 µm. This was expected as equilibrium state must be achieved by the structure after LP induced compressive RS fields. In the laser-peened region (≥5 mm) RSs transit into compressive RSs at the LP Boundary Region (LPBR) and remain compressive throughout the LP region as defined by the LP layout. A maximal compressive RS value of σ_{yy} = -194 MPa was measured at the centre of the LJ sheets between Hole 2 and Hole 3 at a depth of 363 µm. Maximum compressive and tensile stresses correlate with LP Face 1 at the top surface.

RS contour plots for *P-samples* are shown in Figure 4-10c (transverse-σ_{xx}) and Figure 4-10d (longitudinal-σ_{yy}). As already observed for *S-samples*, the contours of RS values shadow the LP layout in the sense that compressive RSs in the laser-peened region and tensile RSs in the un-peened region match. Maximum tensile RSs in the longitudinal direction at the edge of the LJ sheet were measured up to values of σ_{yy} = 162 MPa which were slightly lower ($\Delta\sigma_{yy}$ = 10 MPa) than for *S-samples*. Maximum compressive RSs had a maximum value of σ_{yy} = -215 MPa which was also a minor decrease of $\Delta\sigma_{yy}$ = 21 MPa. Between the LP Patches of *P-samples* around fastener *Hole 1* and fastener *Hole 2* tensile RSs are observed with a maximum value of σ_{yy} = 89 MPa but those tensile RS magnitudes were not as severe as at the edge of the sheet.

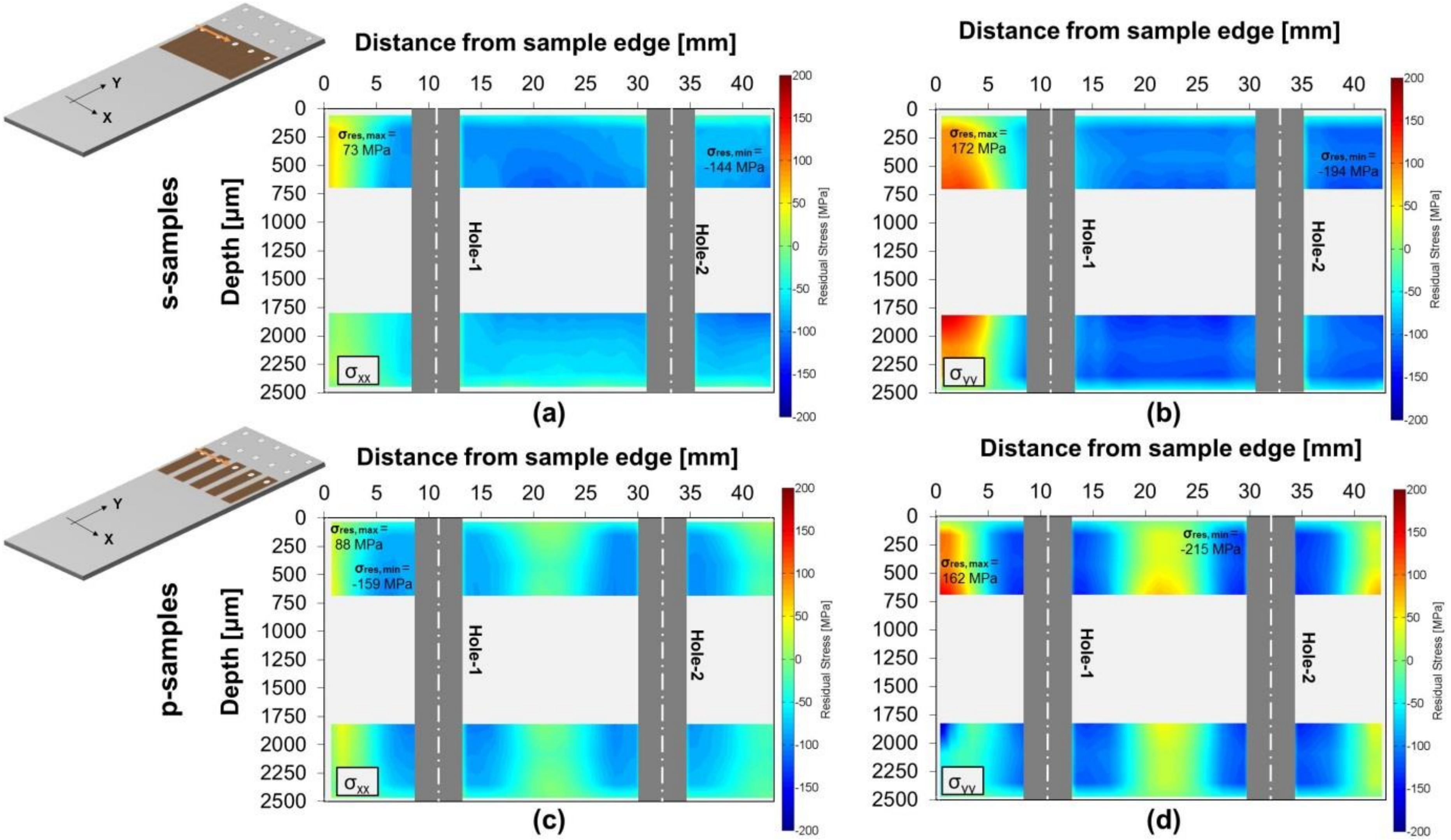

Figure 4-10: RS results of energy-dispersive XRD measurements. Contour plots show 2D stress maps across two fastener holes at near surface region (both surfaces). No measurements (light grey area) could be taken in the core of the 2024-T3 LJ sheet of 2.5 mm thickness. Maximum and minimum and their location of measured values are indicated in contour plots. a) *S-B samples*: σ_{xx} plot; b) *S-B samples*: σ_{yy} plot; c) *P-B samples*: σ_{xx} plot and d) *P-B samples*: σ_{yy} plot;

Studying RSs at the vicinity of the fastener hole edge synchrotron XRD measurement through the thickness are plotted in Figure 4-11. The RS data obtained adjacent to *Hole 1* (H1) for *S-samples* (a) and *P-samples* (b). Three measurements left side and right side of H1 with an equidistance of Δ = 1 mm to each other are plotted in the diagram. Designated LP regions are sketched in light red in the legend attached to the chart. Error bars on XRD data represent the uncertainty coming from the fitting process during the RSs computation. Also previously presented ICHD data measured at the centre of the fastener hole (H1) is added in the plots for comparisons.

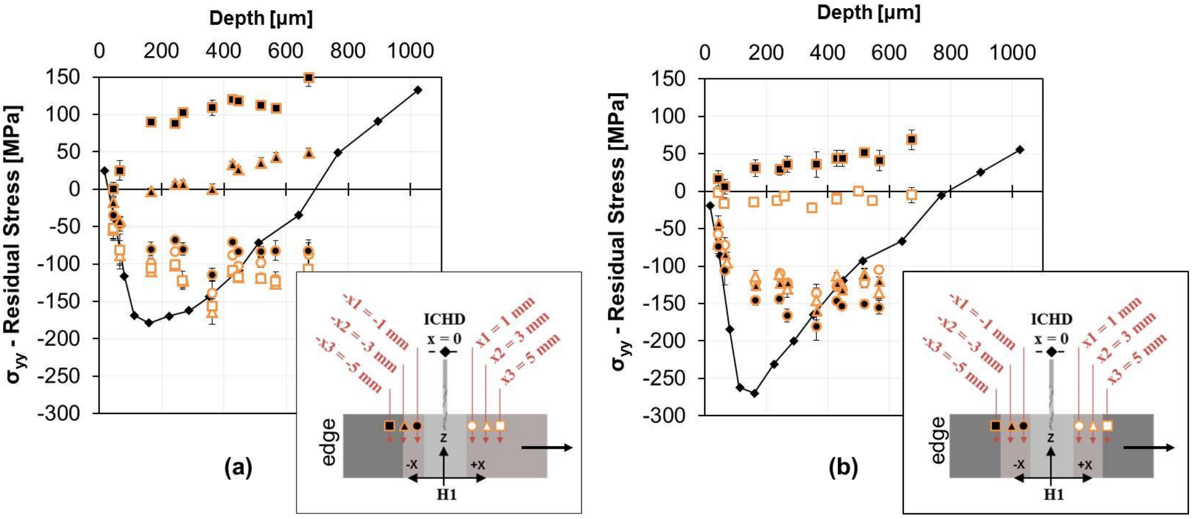

Figure 4-11: Comparison of XRD and ICHD RS measurements at the centre and vicinity of Hole 1 (H1). Depth profiles were measured from LP Face 1. a) *S-B-samples* and b) *P-B-samples*

According to XRD measurements no variation of RSs neither in *S-samples* or in *P-samples* at 1 mm distance to the fastener hole edge compared with measurement to more remote but still within the laser-peened region can be noted indicating that the drilling process of fastener hole leaves the initial RS field unaffected. Error bars for all measurement are small which indicates good correlations during fitting procedures. Also, measurement taken outside the peening region show tensile RSs which are higher in *S-samples* than in *P-samples* confirming the finding of the 2D contour plots.

Figure 4-11a the comparing of XRD measurements with ICHD data is presented for *S-samples* and in Figure 4-11b for *P-samples*. Significant deviations can be noticed taking into consideration only XRD measurements taken in the laser-peened region. Those variations in measurement data are associated with three measurement point of the depths of 165 µm, 244 µm and 268 µm. In that depth, maximum deviation in RS are $\Delta\sigma_{yy} = 73$ MPa for *S-samples* and $\Delta\sigma_{yy} = 124$ MPa for *P-samples*. For depth smaller and larger than those mentioned the agreement of XRD and ICHD data is good for both LP layouts.

4.2.3.2 Petra-III/ DESY Results: 1D Stress Maps

Average RSs through the entire thickness of 2.5 mm thick LJ sheets determined by angle-dispersive XRD (AD-XRD) measurements at Petra-III/ DESY synchrotrons facilities are shown in Figure 4-12 for *S*- and *P-samples*. The crucial longitudinal stress component is displayed only. RS are plotted as 1D line plots mapping the average RS across the centre of the fastener row beginning at the edge of the sample and ending at the half width of the sheet (W/2 = 55 mm).

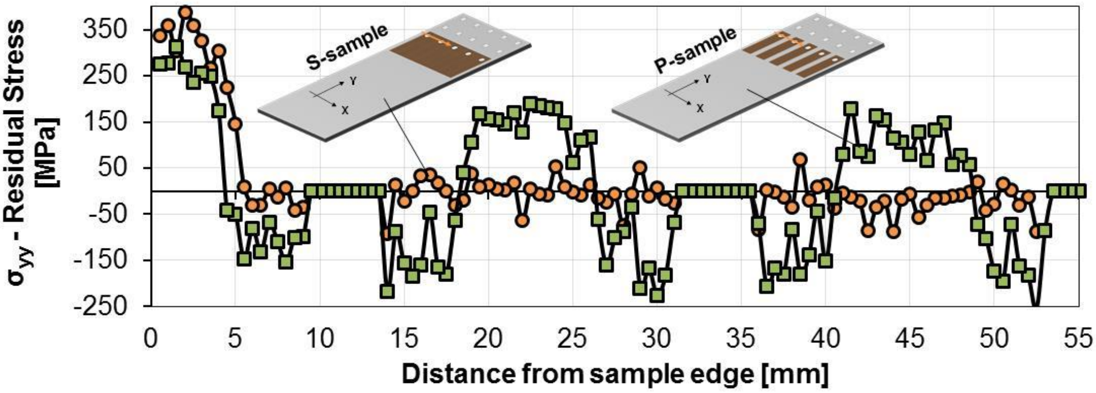

Figure 4-12: Average through the thickness RS results of angle-dispersive XRD measurements for *S-B samples* (green filled squares) and *P-B samples* (orange filled circles) along the width of LJ sheet at a line coincidence with the fastener hole row centre line.

As observed earlier for 2D stress maps (BESSY-II results), the 1D stress maps across LJ width correlate well with the LP layout regarding compressive RS in the peened region and tensile RS in the un-peened region. For *S-samples* the peened area start at 5 mm distance measured from the sample edge whereas *P-sample*'s laser-peened region begins at 4 mm distance. This feature is observed as the shift in the drop of tensile RSs to compressive RS in the LPBR. Tensile RS were higher for *S-samples* at the edge of the sample with average values in the un-peened region of σ_{yy} = 319 MPa in comparison with *P-samples* with an average RS tensile values of σ_{yy} = 268 MPa. *P-samples* show tensile RS between LP patches with lower magnitudes of σ_{yy} = 123 MPa as found at the edge of the sheet. This trend is also in line with observing the BESSY-II 2D stress maps. As fastener holes did not have RS measurements, the line plot was set to zero at those positions.

4.3 Discussion of Results

Processing of test samples and measurements of RSs by the techniques followed specific procedures and characteristics which had effects on obtained RS results. Those effects arising from the interaction of distortion on the delicate 1.6 mm 2524 samples and consequences of the LP treatments for all test samples will be discussed below to explain the measured RS profiles and maps.

4.3.1 Residual Stress Measurement Errors and LP Consistency

Four different techniques of RS determination were applied to develop a comprehensive understanding of the effects of LP on 1.6 mm 2524-T3 specimens and 2.5 mm 2024-T3 LJ samples. Extensive ICHD measurements were performed according to the guideline formulated in Measurement Good Practice Guide No. 53 [134], and the obtained data reasonable fits the picture drawn by relevant publications [95] (recall Table 2-1: Overview of published RS profiles and applied LP process parameters). For 2524-T3 1.6 mm samples, the ICHD measurements show RS values which need more discussion, as distortion was identified as an issue. Section 4.3.2 addresses the issue of distortions and the obtained RS values in contrast to published RS data. However, for ICHD measurements, no error bars could be attached to the RS values, as each data point derives essentially from a single measurement. Multiple repetitive RS measurements could provide a better understanding of uncertainties coming from the LP process and measurement procedures. The ASTM standard E837-13a [133] points out the difficulty to manage the production of non-bias measurement since the operator’s skill and expertise is among the most important factor to obtain accurate results. Goudar and Smith [163] conclude from their analyses of the accuracy of the ICHD method that uncertainties of ±100 MPa can be expected for near surface RSs (less than depth of 200 μm) and for RS measurements deeper in the thickness of test samples uncertainties between ±15-30 MPa were established.

Taking into account the scope of this project and resources such as material, LP supply and time, a detailed uncertainty analysis was not performed. Nevertheless, the obtained ICHD data for laser-peened LJs, measured at different locations (H1 and H3), refer to Figure 4-9, have the potential to demonstrate and analyse uncertainties. An example (*S-B-sample*) of two ICHD profiles and their deviations to each other are shown in Figure 4-13a. Due to the good agreement of the through the thickness profiles of RS, except for the near surface RS values, the measurement data could arguably be used as a piece of evidence to make a statement about the reproducibility of the LP process and the accuracy of the ICHD measurement. If there are no differences in compressive RS values between the two locations (H1 and H3), the comparison is valid. To that end, XRD measurements, as described in section 4.2.3.1 (BESSY-II Results: 2D Stress Maps) and 4.2.3.2 (Petra-III/ DESY Results: 1D Stress Maps), can be consulted. Those obtained RS fields exhibited no major differences of RS across the width of the LJ sample, which makes a case for a valid statement of reproducibility of the LP process and the accuracy of the ICHD measurement. The deviations are shown in Figure 4-13b for relative deviation and in Figure 4-13c for absolute deviations. As mentioned, except to the near surface, the deviations show very close agreement for ≤ 110 µm, indicating a very accurate RS measurement technique. In absolute terms, the deviations away from the near surface region are maximum ± 20 MPa. Furthermore, the values of penetration depths of the two RS profiles are in very close agreement. This data shows that the consistency and stability of the LP process within that limit. Surface RS values of ICHD are notorious for inaccuracies. This is because of the challenge procedure during the ICHD measurement to accurately find the sample surface with the drill bit. The deviation on the surface could also be a result of the LP process and subsequent variabilities. In order to achieve a more accurate picture about surface RSs, techniques such a laboratory XRD could be applied.

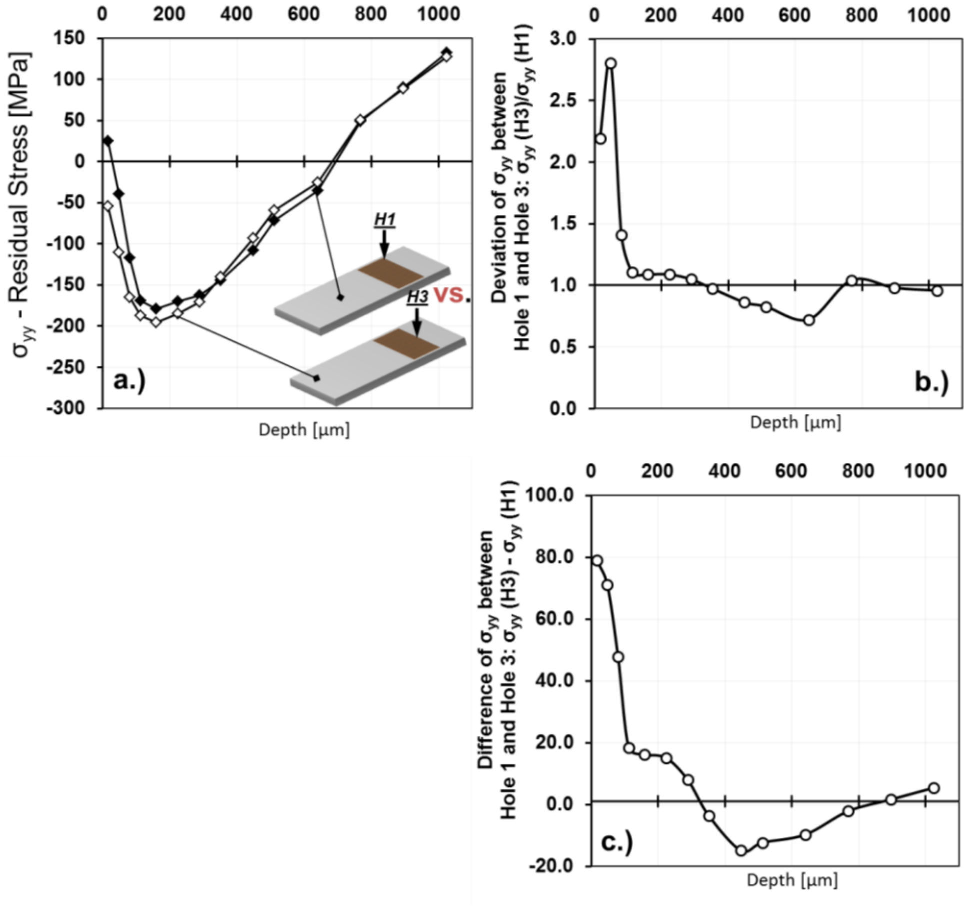

Figure 4-13: ICHD measured RS profiles for two different locations on a LJ *S-B-sample* and their deviation. a) *S-samples*: σ_{yy} Hole 1 vs Hole 3, b) Relative deviation of σ_{yy} measured between H1 and H3 and c) Absolute deviation of σ_{yy} measured between H1 and H3.

In summary, the obtained ICHD measurements can be considered as very accurate (± 20 MPa) and reliable technique to measure consistent RS values deeper in the material (≤ 110 µm). Those determined uncertainty values are in line with the range of uncertainties reported by Goudar and Smith [163]. Although, measurement uncertainties and LP inconsistencies cannot be strictly separated from each other from the final measurement result, it could be justified that LP of test samples by the process applied by the CSIR National Laser Centre in Johannesburg in South Africa induces consistent RS profiles. This can be rationalised by considering that the measurement uncertainties as previously reported and the uncertainties by Goudar and Smith [163] derived for un-peened samples match with each other. As for the low uncertainty of ± 20 MPa for depth of ≤ 110 µm, ICHD measurement can be used as a good reference to assess RS obtained by other techniques such as synchrotron XRD methods consequently. Therefore, in the following ICHD data will be compared to other performed RS measurement experiments.

4.3.1.1 Synchrotron ED XRD and ICHD RS Measurements on LJs

XRD energy-dispersive measurements of RS at BESSY-II were compared to ICHD data, and significant deviations of measured data sets were observed for measurement representative depths of 165 µm, 244 µm and 268 µm corresponding to 220, 331 and 222 reflection planes respectively. Good agreement was found for measurements recorded before and after those three depths (recall Figure 4-11: Comparison of XRD and ICHD RS measurements at the centre and vicinity of Hole 1 (H1). Depth profiles were measured from LP Face 1. a) *S-B-samples* and b) *P-B-samples*). Comparable mismatches regarding location of depths and magnitudes of RS were also observed by M. Toparli [13] and S. Coratella [21] who compared XRD data obtained by BESSY-II facilities and experimental set ups and ICHD measurement experiment procedures as applied to the data presented in this work.

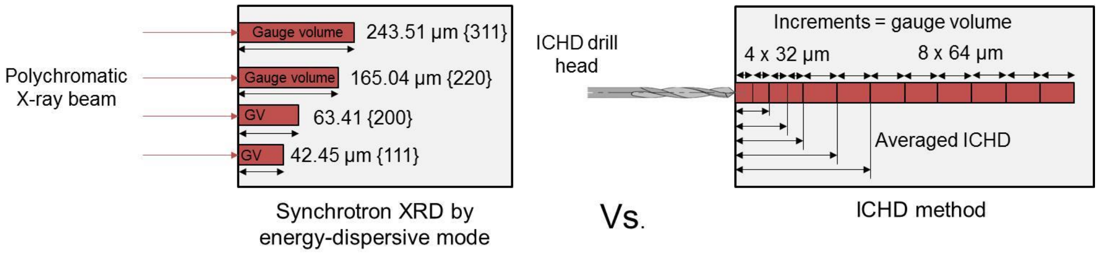

Figure 4-14: Illustration of gauge volumes for different reflections and corresponding depths during energy-dispersive XRD measurement in comparison with increments of ICHD measurements.

The deviations in measurements can be explained by the various principles of RS determinations regarding the depth resolution which is inherently applied during energy-dispersive XRD and ICHD to average RSs within a pre-defined gauge volume. The mechanism of RS determination using energy-dispersive XRD as illustrated in Figure 4-14 (left figure) includes that the gauge volume in depth direction determined by the reflection plane and photon energy begins at the surface for all depths. Despite that exponential weighted averaging (exponential damping) [159] within the gauge volume is performed, averaged RSs consist of all RS counted from the depth until the depth of the measurement. On the contrary, ICHD measurements, as schematically shown in Figure 4-14 (right figure) shift a defined gauge volume, e.g. 32 µm deeper into the test sample so that measurement results only represent arithmetic averaged RSs within the gauge volume without considering RSs of the depths measured before.

In order to compare RS results, ICHD values were averaged over the complete depth of the measurement taking into account RS from previous measuring increments (gauge volumes) as it shown in Figure 4-14 (right figure). Following the logic of ED-XRD measurements, linear arithmetic average values were calculated for the RS data. Although linear averaging is a variation to ED-XRD procedure which uses exponentially weighted average values, this approach prepares the data for a valid comparison. Error bars represent an uncertainty of ±20 MPa, as determined in the section above. In Figure 4-15 the comparison of the data exhibits for *S*-and *P-samples* that the averaged ICHD data shows good correlations on the overall trend of the thickness distribution of RS. The followed procedure reveals the effects of different RS calculation principles as explained earlier.

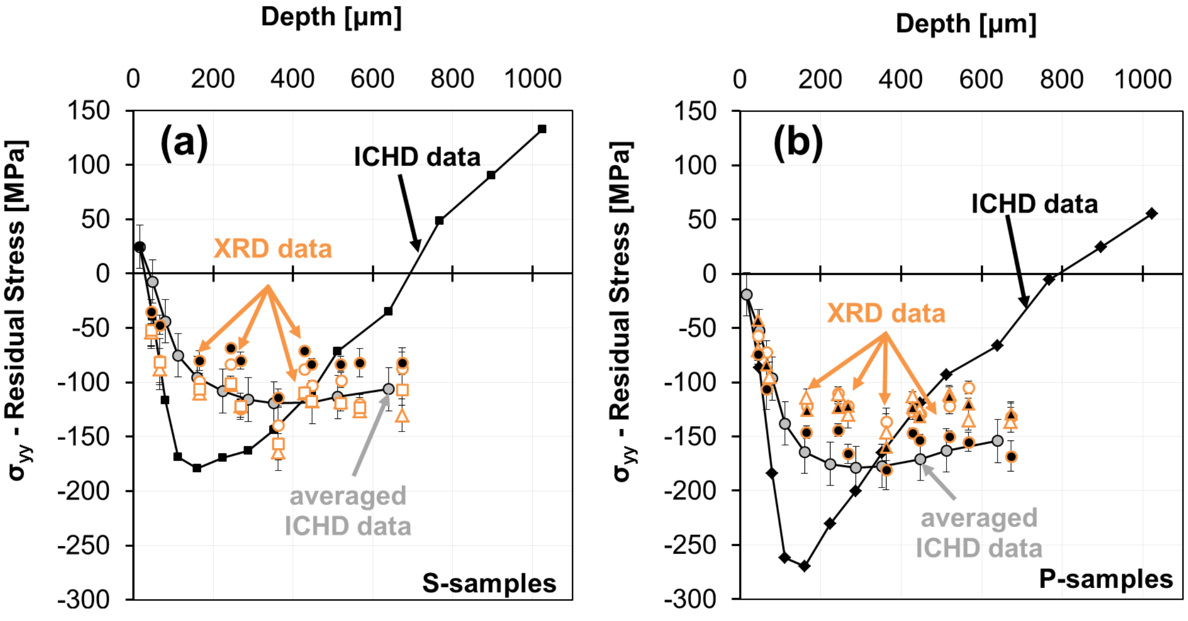

Figure 4-15: Comparison of energy-dispersive XRD, ICDH measurements and averaged ICHD data. a) Comparison for *S-samples* and b) a) Comparison for *P-samples*

4.3.1.2 Synchrotron AD XRD and ICHD RS Measurements on LJs

A major distinction between *S-samples* and *P-samples* can be noticed in the laser-peened region by analysing the average through the thickness results measured by AD-XRD at Petra-III/ DESY. As *P-B samples* exhibit significant compressive RS magnitudes with a mean arithmetic RS value in all laser-peened regions of σ_{yy} = -111 MPa, laser treatments of *S-B samples* only generated an average RS value of σ_{yy} = -10 MPa within the peened region considering the half LJ sample excluding the non-laser-peened regions.

In order to understand those average RS results and in particular the low compressive RS magnitudes within the LP region of *S-samples*, a comparison with through the depth profiles of RS as obtained by ICHD measurement is performed. For that ICHD profiles through the entire thickness were plotted as shown in Figure 4-16. As ICHD measurement only reached a maximum depth of 1408 µm relating the average RS to the centre of the increment at 1024 µm, a complete RS profile through the LJ sheet of 2500 µm could not be obtained even if measurements were taken from both surfaces. Therefore, the graphs showed in Figure 4-16 which assume symmetrical RS profiles (taking LP Face 1 data) were completed in the core where no information is available to calculate an average value which then can be compared with the XRD measurements. Those added RS values have the same magnitude as the last measured data in depth. Average values were weighted taken into account different proportions of increment during the ICHD process and are given in Figure 4-16's bottom box.

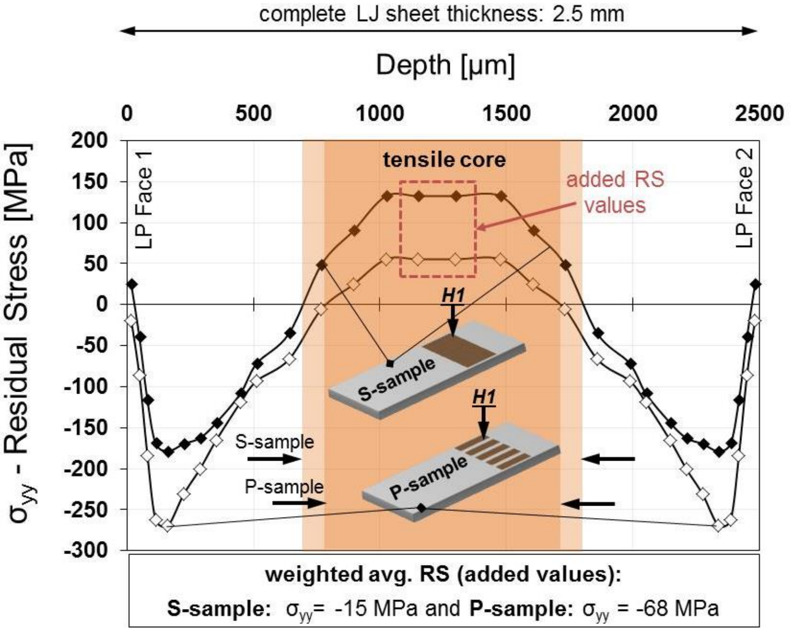

Figure 4-16: Symmetrical RS profile through the complete thickness of LJ sheet (σ_{yy}-longitudinal) comparing *S-* and *P-samples*. Tensile core for both LP layouts indicated in orange. Bottom box gives weighted average values calculated for the complete RS profile of *S-* and *P-samples* taking into account the added values.

It becomes evident by analysing the graphs in Figure 4-16, that a significant portion of the thickness is filled with tensile RSs. For *S-samples* a length of ~1100 µm and for *P-samples* ~900 µm tensile RSs occupy the core of the sheet. This difference in the area of tensile RS can be regarded as relatively minor in comparison to the maximum tensile RS values in the tensile core which were measured for *S-samples* as σ_{yy} = 132 MPa and for *P-samples* as σ_{yy} = 55 MPa.

This is a significant difference of $\Delta\sigma_{yy} = 77$ MPa. Weighted average values for the entire thickness profile result in $\sigma_{yy,av}$ = -15 MPa for *S-samples* and $\sigma_{yy,av}$ = -68 MPa for *P-samples*. Table 4-4 gives a summary of average RS values by angle-dispersive XRD and ICDH. Although average RSs match well on *S-sample*, *P-sample* shows significant deviations between the different measurement techniques.

Table 4-4: Comparison of averaged RS data for angle-dispersive XRD and ICHD measurements.

Strategy	Angle-dispersive XRD average RS σ_{yy} [MPa]	ICHD Weighted average RS σ_{yy} [MPa]
S-B	-10	-15
P-B	-111	-68

Those deviations could come from the method strain calculation by using d-spacing which were measured by AD-XRD technique. The method of obtaining strain free lattice (d_0) values is crucial. d_0-values were determined to exploit the fundamentals of continuum mechanical requirement of stress balance as suggested by Withers *et al.* [164]. This method is not recommended as a first choice. It is preferred to measure stress-free lattice spacing or follow other routes to come to reliable values as outlined by Withers *et al.* [164] but for this work, the stress balance method was chosen as measured values of d_0 provided incoherent RS data. In order to apply stress balance to the LJ sheet, the entire width must be measured. However only the half width was measured at the Petra-III beamline at DESY, so that symmetry condition was applied and RSs were computed. The RSs match other results by energy-dispersive measurements regarding qualitative characteristic. They are also in good agreement with averaged RS results derived from through the thickness profiles of RS measurement by ICHD. No error bars were attached as the method of d_0 determination, and its effect on the uncertainty could not be quantified.

Also, the added values to complete the through the thickness RS profiles can explain the deviations. This can be solved by applying the contour RS measurement technique, which is potent to analyse the distribution of RS throughout the thickness of thicker samples for instance.

4.3.2 Interaction of Distortion and Residual Stress

Both sample types made from 1.6 mm thin 2524-T3 aluminium (LP parameter study sample and CCT-sample) exhibited measured RS values and RS distributions which can not only be explained by the LP process. The LP parameter study sample #1 and sample #2, for instance (refer to Table 3-4), which were peened using the most intense LP process parameter of 2.5 GW per cm^2 and 500 and 750 spots per cm^2 respectively, showed some peak compressive RS values of $\sigma_{RS,\ peak}$ = -517 MPa and $\sigma_{RS,\ peak}$ = -579 MPa. This level of compression is unexpected and could not be found in the reviewed literature for similar aluminium alloys. The CCT-sample on the other hand also showed a lateral distribution of RSs within the LPS that are not typical for a laser-peened area that was treated with equal process parameters. The distribution showed (recall Figure 4-5) that the compressive RS is lower in the centre of the LPS than towards the edges of the LPS.

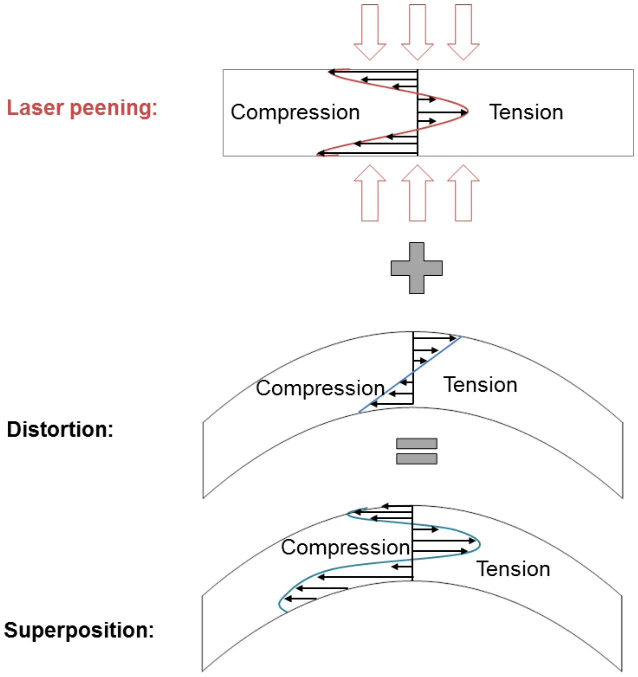

Figure 4-17: Principle of superposition of distortion induced bending stresses and laser-peened introduced RSs.

Obviously visible distortions in the range of 1 – 3 mm were observed for both 1.6 mm thin sample types. No quantification methods were applied to determine the amount of distortion. The issue, mechanics and interaction of distortions and RSs were, however, studied by many researchers in the field of welding and additive layer manufacturing (ALM) and their research conclusions can be consulted to interpret the measured RSs. P.A. Colegrove *et al.* [165] and J. Ding *et al.* [166] studied the relationship between distortions and RSs. In their studies, distortion and RSs were a product of a thermal-mechanical process which included the wire-arc additive manufacturing (WAAM) process and intermediate surface rolling. They concluded that bending stresses coming from distortions superimpose with RSs. The same underlying principle can be applied to the laser-peened LP process parameters study sample, as illustrated in Figure 4-17, in order to explain the atypical results as described above.

As RSs were measured on the concave surface of the LP parameter study sample, compressive bending stresses produced by distortions add to the compressive RS which are a product of plasticisation induced by the LP process. This superposition is the explanation for that overly strong compressive RSs measured for test sample #1 and #2. As the CCT-samples also showed distortions after LP, especially locally at the region of the LPS, it is assumed that the distortion produced bending stresses superimpose with the RS coming according to the same principles as discussed. The complex interaction between distortion and RS is, however, not focus of this study and remains unclear in quantitative terms. Therefore, measured RS on 1.6 mm cannot be quantitatively broken down in the laser-peened RS and bending produced stresses for this study. A typical solution which was applied by researchers to differentiate the two stresses from each other is that the sample is clamped during the processing step which prevents distortions. RS can then be measured in the clamped and unclamped conditions, as done by V. Kostov *et al.* [167], to analyse the superposition of stresses.

4.3.3 Effect of Laser-Peening Process Parameters

4.3.3.1 LP Process Parameter Study Sample

With the insights of the superposition of distortion and LP produced stresses, the LP parameter study which was performed using 1.6 mm 2524-T3 samples, must be interpreted carefully. However, three different products of the LP treatment were analysed: Near surface, peak compressive RS and penetration depth of compressive RSs:

- On the **near surface RS**, the measured data is not sound considering the accuracy of the ICHD measurements for the near surface region as analysed earlier in section 4.3.1. Although, the overall trend of obtained near surface RS data (recall Figure 4-2), which is that with increasing intensity of the process parameters the level of compressive RSs rise consequently fits into the general picture of publications [86,95], no reliable quantitative statements can be made. Additional RS measurement using laboratory XRD techniques can be performed to gain more insights.
- **Peak compressive RSs**, as measured by ICHD (recall Figure 4-1 or Figure 4-3), were found to be in depths in which according to the discussions of ICHD measurement accuracies of section 4.3.1 a reliable and quantitative assessable (±15 MPa). Except from samples #1 ($\sigma_{\text{RS, peak}}$ = -517 MPa) and #2 ($\sigma_{\text{RS, peak}}$ = -579 MPa) which show very strong peak compressive RSs due to the mechanics as previously discussed, all other sample exhibit peak compressive RS result in the range of -193 MPa to -365 MPa. The level of compression increased with intensification of both major LP process parameters. P. Peyre *et al.* [86] explain the effects of power density and pulse repetition on the peak compressive RS. According to Peyre *et al.* [86], the generated pressure of the plasma created by the LP process increases when the power density is amplified. The pulse density can be regarded as a partly pulse repetition and was investigated by Peyre *et al.* [86] and J.L. Ocaña *et al.* [95]. They showed that this effectively enlarges the compression in a sample.

- The reliability of measured **penetration depth** by ICHD can be considered sound following discussions above about the measurement errors. As per the measured depths of compressive RSs, which range from 768 µm to 1100 µm, the trend (recall Figure 4-4) suggests that the compressive RS field becomes deeper when the pulse density is increased, and the power density is decreased. The effect of pulse density to produce deeper compressive RS is well-known [86], and the amount of penetration fits the range of data, as published by other researchers [86,95]. The role of decreased power density in that process to achieve higher penetration depths of compressive RS is on the other hand unclear.

Overall, it can be mentioned that despite the reliability and accuracy of the ICHD method, all presented and discussed results derive from one measurement one single sample. In order to increase the statistical soundness, multiple RS measurements must be applied. This aim was however out of the scope of this work but is regarded essential for LP applications on real-life structures in the framework of quality control.

4.3.3.2 Fastened Lap-Joints

Strategy-A peening treatments (*S-A* and *P-A* samples) show higher compressive stress maxima than samples peened with strategy-B (*S-B* and *P-B* samples) for both stress components. The LP process parameters of power density and pulse density are both larger in strategy-A than in strategy B. It was well established by Peyre *et al.* [86], Rubio-González *et al.* [92] and Ocaña *et al.* [95] that if power density and pulse density (overlapping rate) are increased the compressive RS maxima increases consequently. It becomes more compressive, unless a saturation point is reached. Measured RS profiles confirm this trend in LJ samples. However, analysing longitudinal stress components, *P-B* samples exhibit only a minor reduction of maximum compressive RS value of 24 MPa compared to the respective stronger peening of strategy-A. In contrast, *S-samples* showed a decrease of 92 MPa comparing *S-A*- and *S-B*-samples. In other words, for *B-samples* the same LP process parameters applied on *S*- and *P*-layout result in very different RS profiles where for *A-samples* the RS profiles are similar. This observation indicates that the LP layout is a major driver in the formation of RS in a laser-peened sample and is potent to compensate missing LP forces (pulse density and pulse density) defined by LP process parameters. Hence, coherent comparison of LP process parameters must regard same LP layouts and LP pattern.

4.3.4 Effect of Laser-Peening Layout on LJs

Comparing RS fields as results of LP layout, fair comparisons can only be drawn from strategy *A*- and *B-samples* as for the respective LP strategies LP process parameters were varied. In this light, *P-samples* have higher compressive stresses in the longitudinal direction than *S-samples*. This fact was observed for both *A*- and *B-samples*. It can be explained by the circumstance that in *P-samples* there is more elastic, hence un-peened material present around the LP region which in effect is capable of generating more compressive stress states than it is facilitated in *S-samples*. It is well understood that to produce compressive stress fields, an elastic zone must press back on a plasticised region which is the intrinsic product of the LP process [86]. Although there is no published study showing the effects on generated RS field caused by the different relationships of peened and un-peened region in a test sample, the explanations are in line with the understanding of RS generation as explained by Peyre *et al.* [86].

However, the different LP layouts comparing *S-A* with *P-A* the laser-peening treatments resulted in a minor difference of $\Delta\sigma_{yy} = 24$ MPa taking the maximum compressive RS values into account. For comparison on *S-B* versus *P-B* samples, this trend accummulates into a significant difference of $\Delta\sigma_{yy} = 92$ MPa. *A-samples* have less designated peening area compared with their *B-samples* counterparts which indicate that an increase in peened area amplifies the effect deriving from the relationship of peened and un-peened area. Following this rationale, it could be summarised that with increasing the peened area every unit area which remains unaffected by the LP process hence remains elastic becomes more potent in generating compressive RS and vice-versa.

The LP layout affects the formation of tensile RSs which are a product of the stress equalising process. For *S-samples* which leave only a small ligament on the edge of the LJ sheet higher tensile RSs occur in comparison with *P-samples* which also leave un-peened areas between the patches of laser-peened areas in which balancing tensile RS can be accommodated.

4.3.5 Effects of Laser Raster Pattern Orientation with Respect to Laser-peened Area on LJs

As discussed the LP layout has a significant impact on resulting RS profiles through the thickness which is ingrained in the relationship between plasticised (laser-peened) and elastic (un-peened area). However, research by Correa *et al.* [96] has shown that the raster zig-zag raster pattern (recall Figure 2-33) also affects RS formations. Especially the bi-axiality of RS fields using a raster zig-zag pattern can be explained by their research.

In order to understand Correa *et al.* [96] proposed rationale in the context of RS data of this work, a single laser spot causing elastic push-back by the surrounding area as shown in Figure 4-18. Separating the different main components of stress for a single laser spot into the x- and y- direction will result into the sketch as given in Figure 4-18a. Distribution of compressive (blue arrows) and balancing tensile stresses (red arrows) are specified for σ_{xx} and σ_{yy}. It can be seen that the position of balancing tensile RSs the effective stress direction are located outside a line crossing the laser-peened area (laser spot) whereas the effective stress direction of compressive RSs are located on a coincidence line with the peened area.

Regarding a row of laser pulses arrayed into a line advancing the laser pulses (scanning direction) in the x-direction, as illustrated in Figure 4-18b, the x-component of the stress field (σ_{xx}) coincide with the advancement direction of the laser passes through a field of compressive stresses. This will result in an additive RS forming process. On the contrary, for the y-component of the RS the advancing direction of the laser points towards the tensile RS field. The arithmetic in consequence will produce a subtracting RS forming process. A row of laser pulses will, therefore, result in a bi-axial RS field depending on the dimension of the laser spot row and its relationship with samples geometry and mechanics as discussed for the LP layout. Characterising and quantifying those effects is still an empty field in research and academia so that for this discussion only qualitative analyses can be made.

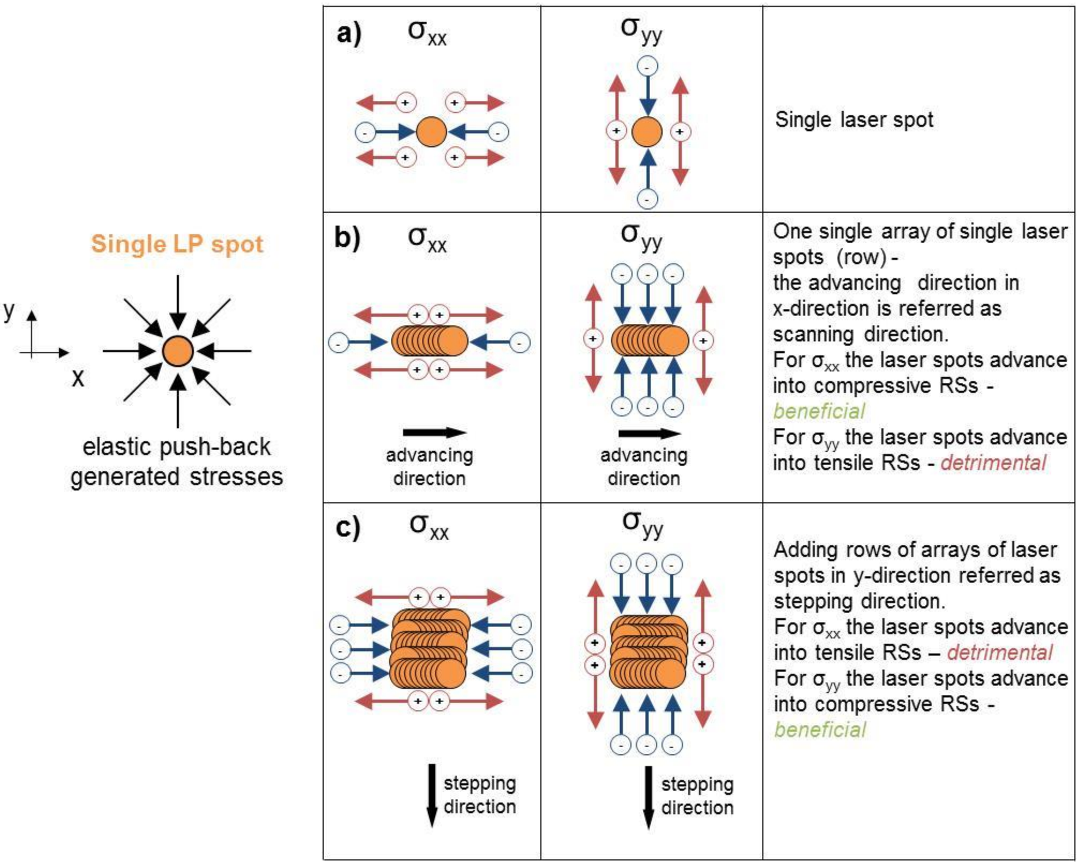

Figure 4-18: RS forming process resulting from the LP raster zig-zag pattern. a) RS forming of single laser spot; b) RS forming of a row of laser spots and c) RS forming of multiple rows of laser spots.

As a complete laser raster zig-zag pattern consists of a second direction which adds multiples rows of laser spots in the stepping direction (y-direction), as given in Figure 4-18c, analogical mechanics to the discussions of single laser spot rows can be applied. The difference, however, is that in this case, the advancing direction is the y-direction (stepping direction). Analysing the generated σ_{yy} for added rows of laser spots in the stepping direction, the complete compressive RS field of the laser spot row is added to each other as the advancement direction points to the compressive RS field. For tensile stresses, the opposite is the case following the same rationale.

Besides the absence of systematic studies that can offer methods to quantify the effect of LP layout and LP raster zig-zag pattern, it can be understood that those two LP parameters are fundamentally entangled with each other so that experimental data of RSs cannot independently be discussed.

In order to examine the effect of the raster pattern on experimental RS results, recall that for *B-samples* the LP process parameters were decreased and the LP layout was altered so that the peened area was elongated in the longitudinal direction coming from the definition in strategy-A. The raster pattern was kept constant with the stepping direction in sheet longitudinal direction.

In this light, the earlier discussion concerning different reductions of peak compressive RS values observed for *S*- and *P-samples* despite identical decreases of LP process parameters, can be explained by the RS formation process as described for Figure 4-18. In particular, for *S-B samples* in contrasts to *P-B samples* (recall Figure 3-9), the decrease of maximum compressive stress can be observed to be much less regarding their respective strategy-A counterparts if longitudinal stress direction is regarded. This was explained by the rationale of favourable relationship of peened and un-peened area applying to *P-samples*. However, this result is also contributed by the LP raster pattern in combination with the LP layout of the *P-B* samples as the elongated direction is also coincidence with the stepping direction and the same argument apply as described for Figure 4-18. In other case *S-A* samples which have a similar LP layout with the main difference that the elongation of the LP area is in x-direction across the width of the sample and in line with the scanning direction of the zig-zag pattern would need to show similar grades of bi-axiality. This is however not the case. In fact, the LP patch around the fastener hole in *P-B* samples is elongated in the longitudinal direction and a non-bi-axial stress field is generated (*P-B*: $\sigma_{xx}/\sigma_{yy} = 0.89$) which reinforces the stress generation in the stepping (longitudinal) direction of the LP zig-zag raster pattern. For *S-B* samples the grade of bi-axiality is not as distinctive although the peening area was also elongated in line with the stepping direction. However the overall LP layout does not support the argument as the LP layout dimension also favours the scanning direction by defining a peening area across the width of the LJ sheet.

4.4 Summary and Conclusion

RS measurement using different techniques have been performed on laser-peened 1.6 mm 2524-T3 and 2.5 mm 2024-T3 LJ samples. Table 4-5 summarises the key result for all measurements taken laser-peened 1.6 mm 2524-T3 and Table 4-6 is showing an equivalent summary for all RS measurement conducted on 2.5 mm 2024-T3 LJ samples.

Table 4-5: Summary of RS measurements taken for samples made of t = 1.6 mm 2524-T3 clad sheets

			ICHD			**Neutron diffraction**
			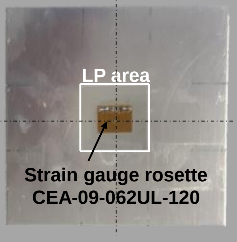			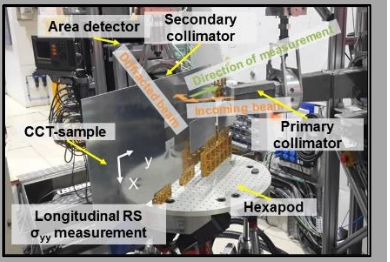
Sample ID	**Power density [GW/cm²]**	**Pulse density [pulses/cm²]**	Near surface RS [MPa]	Max. compr. RS [MPa]	Pene-tration depth of compr. RS [µm]	Max. compr. RS [MPa]
CCT-LP-2-B	2.5	750/ 500	n/a	n/a	n/a	-118
#1	2.5	750	-173	-579	896	n/a
#2	2.5	500	-100	-517	896	n/a
#3	2.5	250	-45	-203	768	n/a
#4	2.0	750	-64	-365	950	n/a
#5	2.0	500	-46	-318	1000	n/a
#6	2.0	250	-24	-247	1000	n/a
#7	1.5	750	-64	-243	1100	n/a
#8	1.5	500	-46	-244	900	n/a
#9	1.5	250	-13	-193	950	n/a

Table 4-6: Summary of RS measurements taken for LJ samples made of t = 2.5 mm 2024-T3 clad sheets

LP Strategy for LJ amples	**Maximum Compressive RS σ_{yy}**		
	ICHD	**ED-XRD**	**AD-XRD**

	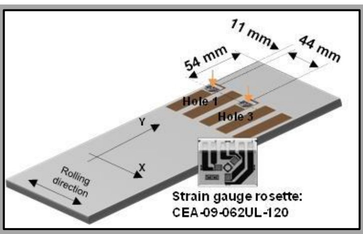	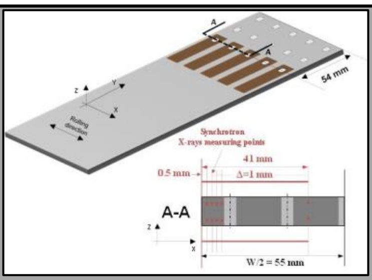	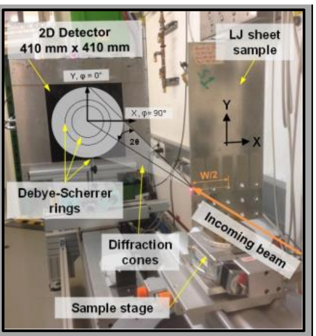
	Through the thickness RS profile	Multiple through the thickness RS profiles = RS field	Multiple average through the thickness RS values = RS field
S-A	-256 MPa	n/a	n/a
P-A	-280 MPa	n/a	n/a
S-B	-178 MPa	-194 MPa	-87 MPa
P-B	-270 MPa	-215 Mpa	-253 MPa

From all obtained RS measurements, the following conclusions can be made:

- Obtained ICHD results confirm that ICHD is a reliable and robust RS measurement technique. This conclusion is, however, not true for near surface RSs. Since ICHD are limited to through the thickness profile of RS, XRD techniques can be applied to complete the image of a specific RS field in lateral directions as those provide efficient tools to create RS maps beyond the through the thickness distribution. Both techniques are complementary to each other in the pursuit of creating a comprehensive understanding of the RS condition within a sample after LP.
- LP conducted by the process at the CSIR is robust, and displays consistent process outputs in the form of induced RS fields.
- LP induces peak compressive RS of $\sigma_{\text{res, compr.}}$ = 200 – 350 MPa in 2000 series aluminium but the exact level of compression depends mainly on applied LP process parameters and the LP layout.
- Deep penetration depths of compressive RSs between 700 μm to 1000 μm were consistently measured showing superior behaviour to SP induced RS profiles which have typical penetration depth of 100 – 200 μm.
- Increasing power density and pulse density will result in higher compressive peak RSs.
- The LP layout has a significant effect on the formation of compressive RSs, as that un-peened material generates compressive stresses by its elastic response to the plasticisation of the laser-peened region. Therefore, the LP layouts need to be carefully chosen definitions in order to outline an effective LP strategy.

- Un-peened areas exhibit significant tensile RSs which need attention when external loads are applied to the structure.
- Laser-peened thin products (1.6 mm) suffered from distortions. The role of distortion induced bending stresses in the measurement process needs addressing in future works. Ways of preventing distortion could be another way to deal with this issue.
- For laser-peened CCT-sample additional RS measurement techniques can be applied in the future in order to develop a sharper image of the RS condition and distribution.

5 Crack Growth in Laser-Peened CCT-Samples

In this chapter crack growth results will be presented for BL and laser-peened CCT-samples which were laser-processed according to the descriptions in chapter 3.1.2. Also, BL crack growth results are used to develop the Walker model for 2524-T3 aluminium alloy.

5.1 Baseline CCT-samples

FCGRs (*da/dN*) were determined from crack length - cycles data by using ASTM E647-00 [41] proposed secant method for all three tested R-ratios. FCGRs are plotted against *ΔK* in the diagram as shown in Figure 5-1. *ΔK* values were calculated using the Feddersen [32] equation applicable for CCT-samples (recall equation 2.6 and section 2.1.2.1).

The log-log diagram exhibits FCGRs for a range of SIF range (*ΔK*) of 8 MPa√m to 37 MPa√m which is typical for a damage-tolerance assessment of aircraft fuselage skin structures. The data further illustrates the effect of R-ratio, and consequently, the effects of applied mean stresses become evident. As reviewed in chapter 2.1.2.2 that crack growth rates increase with increasing R-ratios, the obtained crack growth test data for 2524-T3 CCT-BL-samples confirm this general trend. In detail, the experimental FCGR results can be separated into two regions over the range of compiled ΔK values (8 MPa√m – 37 MPa√m): region II and the beginning of region III.

For all three CCT-BL-samples tested at R = 0.1, it can be seen that the set of data over the range of ΔK is linear and therefore within region II of the *da/dN* vs *ΔK* plot. The data for all three replicated samples were combined and fitted using linear-regression analysis to determine Paris coefficients (recall equation 2.12 in chapter 2.1.2.2).

CCT-BL-samples with higher R-ratios accelerate into region III sooner than BL R = 0.1 test samples. For R-ratio of 0.3, the linear region II was limited to ΔK = 24 MPa√m and subsequently data compiled for R-ratios of 0.5 were trimmed at ΔK = 22 MPa√m before the Paris coefficients were determined by linear-regression for their separate region II summarising the two duplicate test samples respectively.

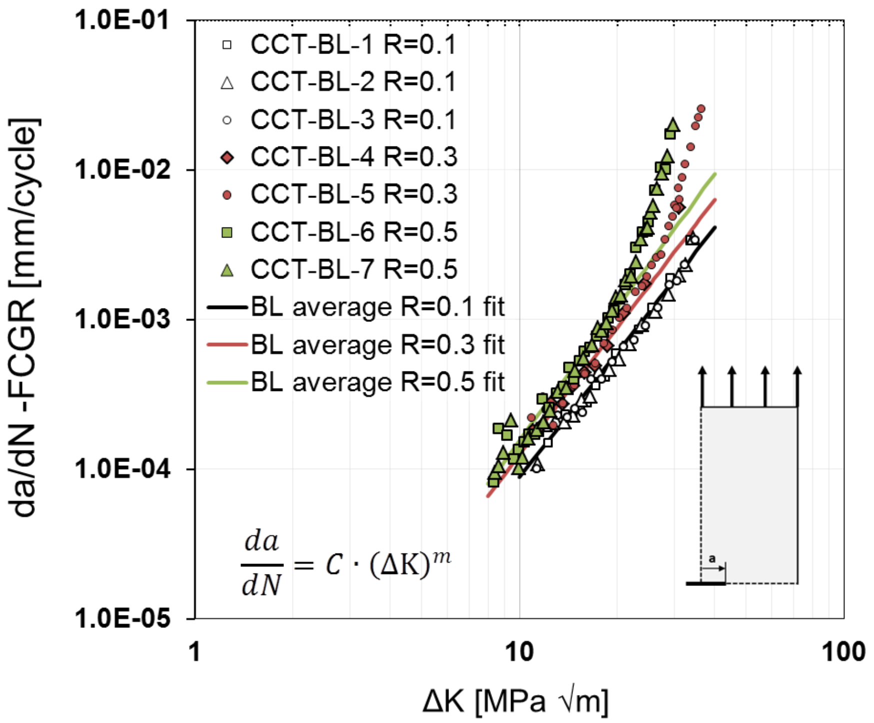

Figure 5-1: CCT-BL-samples crack growth test data for three R-ratios (R = 0.1, R = 0.3 and R = 0.5). Log-log diagram of crack growth rates (*da/dN*) vs *ΔK*.

Table 5-1: Determined Paris coefficients and correlation with test data.

R-ratio	Paris coefficients for trimmed data range (region-II)			R^2 region-II (correlation with trimmed data range)	R^2 (correlation with complete data range)
	C [mm/cycle]	m	upper limit of data trim[8]		
0.1	$1.49*10^{-07}$	2.77	No trim	n/a	0.96
0.3	$1.84*10^{-07}$	2.83	ΔK=24 MPa√m	0.98	0.79
0.5	$1.69*10^{-07}$	2.96	ΔK=22 MPa√m	0.98	0.82

Paris coefficients for three R-ratios are listed in Table 5-1. Besides, the correlation coefficients R^2 were calculated for the trimmed region II and the complete compiled data range representing the quality of the Paris crack growth model with the test data from duplicate test samples. The correlation for the region II is very good for all CCT-BL-samples ($R^2 = 0.96 - 0.98$). For the complete range of ΔKs, the correlation is poorer ($R^2 = 0.79$ for R = 0.3 and $R^2 = 0.82$ for R = 0.5) since the Paris model describes only the linear region II of stable crack growth. The obtained test data, however, extends into region III.

---

[8] Data was trimmed to the linear region II of the da/dN vs ΔK plot.

5.2 Determining Walker's Material Coefficients

To perform accurate crack growth predictions in later chapters that consider mean stress effects, as it is particularly needed if crack growth is predicted in the presence of RSs, the CCT-BL-samples were tested under three different R-ratios to develop an appropriate crack growth characterisation model. The Walker crack growth model, as described before in chapter 2.1.2.2 (refer to equation 2.15), is capable of accounting for mean stress effect and describe crack growth data for different R-ratios.

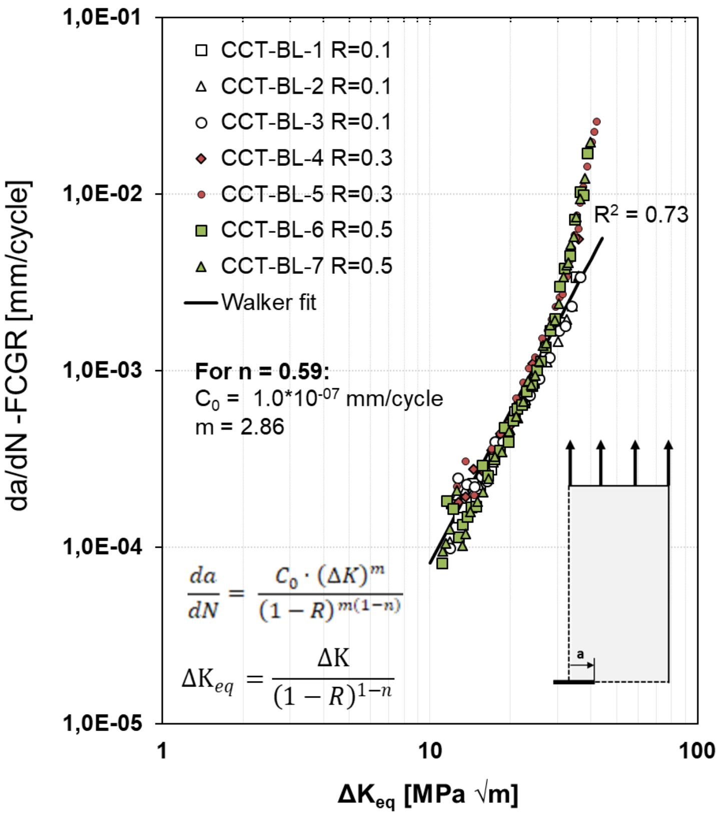

Figure 5-2: Best Walker fit for 2524-T3 t =1.6 mm (T-L) crack growth data obtained for R = 0.1, R = 0.3 and R = 0.5.

To determine the constants for the Walker model a similar approach as followed by J. Melson [168] was adopted. By collapsing all crack growth data from various R-ratios in one single line by plotting da/dN data against an equivalent SIF range (ΔK_{eq} – refer to the equation in Figure 5-2), which is defined as the SIF range (ΔK) at R-ratio of 0.0. A linear regression fit can then be performed for any n value. The linear regression fit of the collapsed data, presented in Figure 5-2, resulted in C_0 and m after an optimisation algorithm determined n (0.59) and consequently, C_0 ($1.0*10^{-07}$ mm/cycle) and m (2.86) which resulted in the **highest correlation coefficient (R^2) value** for the set of data. The correlation (R^2 = 0.73) of the Walker fit is moderate for the range of SIF range. As it can be seen from Figure 5-2 the deviation is mainly located in the region of higher ΔK-values for the data from R-ratios of R = 0.3 and R = 0.5 as those data sets exhibit an earlier departure into region-III then the data obtained for R =0.1. Anyhow, for the most portion of the range of *ΔK*-values, the correlation is reasonable.

A comparison of predicted FCGRs using the developed Walker model and test data of crack growth rate (*da/dN*) vs SIF range (*ΔK*) in log-log diagrams are plotted in Figure 5-3a for R = 0.1, in Figure 5-3b for R = 0.3 and in Figure 5-3c for R = 0.5 in order to cross-check the robustness and accuracy of obtained Walker coefficients. For all three R-ratios, the general agreement between test data and prediction is close. Except from predictions for R = 0.1 which exhibits excellent correlation (R^2 = 0.97), there can be a slightly poorer agreement noticed for R-ratios of 0.3 (R^2 = 0.80) and 0.5 (R^2 = 0.81). Again, as it can be noticed from Figure 5-3, the correlation is much better if the data is trimmed at higher values of *ΔK*.

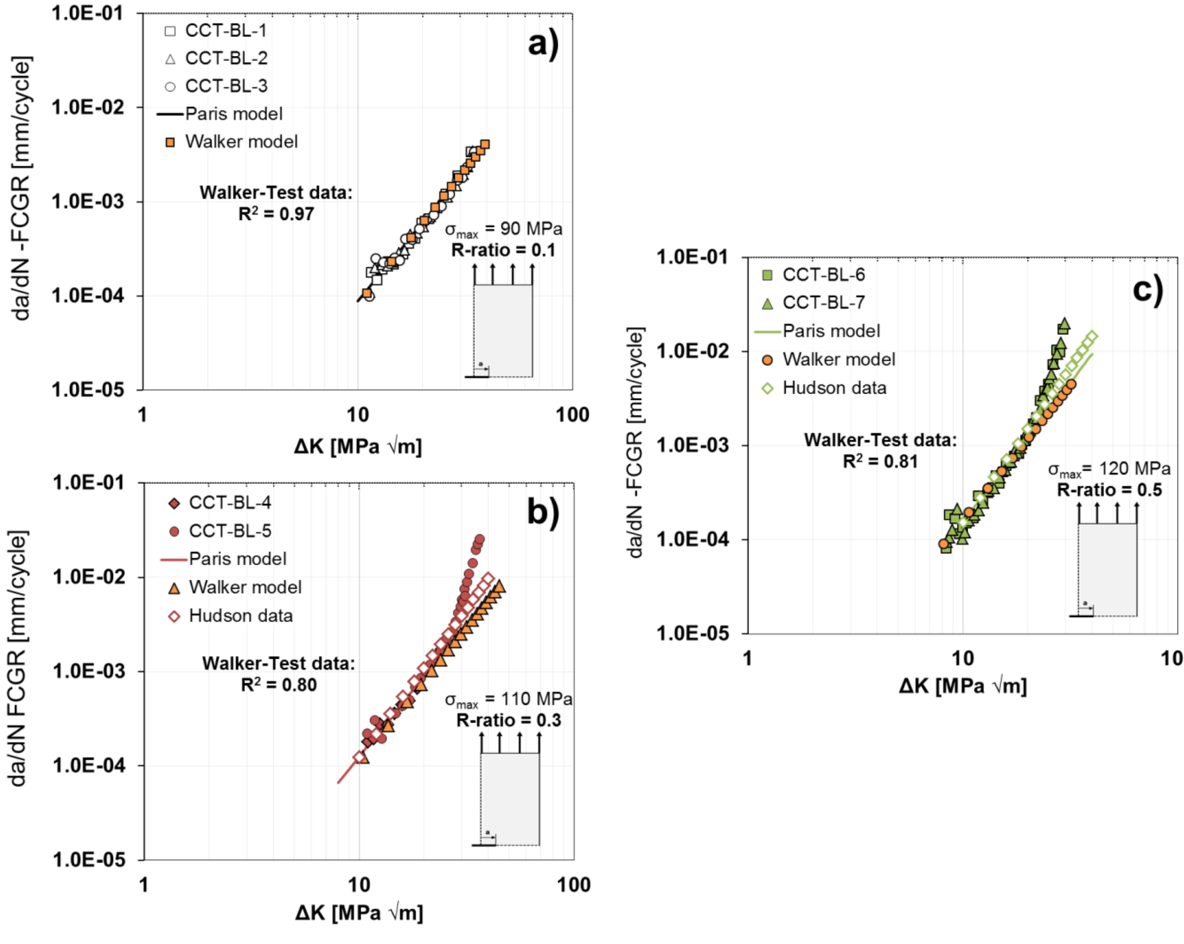

Figure 5-3: Crack growth rate (*da/dN*) vs SIF rang (*ΔK*) in log-log diagrams comparing Walker model prediction against test data. a) R = 0.1, b) R = 0.3 and c) R = 0.5.

In addition in Figure 5-3, FCGRs determined by Hudson [51] for 2024-T3 (R = 0.33 and R =0.5), as reviewed in chapter 2.2.1, are compared to the test results obtained for R = 0.3 and R= 0.5. The agreement of FCGRs displays that firstly, the obtained FCGRs are within expectation as published results and secondly that 2524-T3 exhibit very similar FCGR as 2024-T3.

5.3 Laser-peened CCT-sample – Results and Discussions

Three different LP treatments were applied to CCT-sample, as illustrated in Figure 5-4 and previously defined in chapter 3.1.2.3. *LP 1-A* (Figure 5-4a) had one LP stripe (LPS) across the initial EDM notch and two additional definition of LP treatments *LP 2-A* (Figure 5-4b) and *LP 2-B* (Figure 5-4c) corresponds to two different sets of LP process parameters described by power density (constant) and the variable pulse density (e.g. 200/200 spots/ cm^2) of both surfaces of the sheet (A - Soft LP: Power Density: 1.5GW/cm^2, Pulse Density: 250/250 spots/ cm^2; B - Hard LP: Power Density: 2.5GW/cm^2, Pulse Density: 750/500 spots/ cm^2) in which two (w_{LP} =)30 mm wide peening stripes are placed with a distance of (d_{LP} =) 25 mm away from the centre line in both lateral directions. The RSs in *LP 2-B* CCT-samples were presented in chapter 4.1.2. An average maximum compressive RS within the LPS of $\sigma_{RS,yy}$ = -91.5 MPa and an average tensile RS of $\sigma_{RS,yy}$ = 51.8 MPa between the centre and d_{LP} was measured.

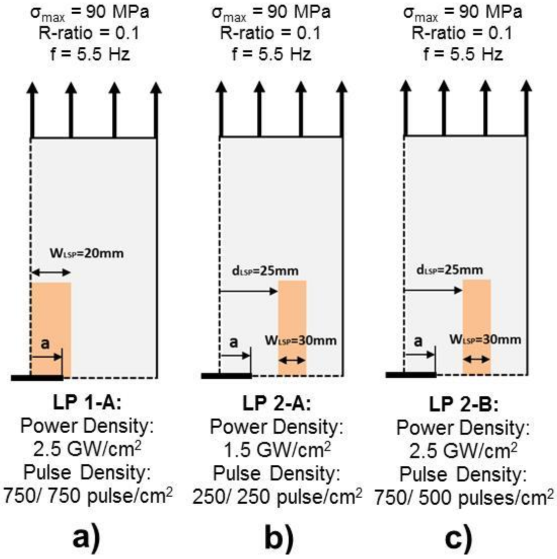

Figure 5-4: Definition of LP treatments for laser-peened CCT-samples. a) *LP 1-A*, b) *LP 2-A* and c) *LP 2-B* (as defined in chapter 3.1.3).

Test results of crack growth lives (*a* vs *N*) obtained from BL samples (*CCT-BL*) and *LP 1-A* CCT-sample (*CCT-LP1A*) are compared in Figure 5-5. For this case, no crack initiated from the sharp EDM notch and the test was stopped at N = 307,000 cycles. For that reason, no crack growth rate can be reported, and further analysis cannot be performed. As *BL* CCT-samples initiated cracks within 5,000 to 10,000 cycles, it can be concluded that the application of LP was effective in stopping any initiation at given test conditions.

A comparison of crack lives (*a* vs *N*) and crack growth rates (*da/dN*) versus average half crack length (*a*) for *BL*, *LP 2-A* and *LP 2-B* CCT-samples are plotted in Figure 5-6a and Figure 5-6b respectively. From Figure 5-6a, the effects of LP on the crack lives can be compared with the BL condition. Comparing the average total crack life (N) of *CCT-LP2A* samples ($N_{CCT\text{-}LP2A}$ = 80,436 cycles) with BL samples (N_{BL} = 84,323 cycles), it can be

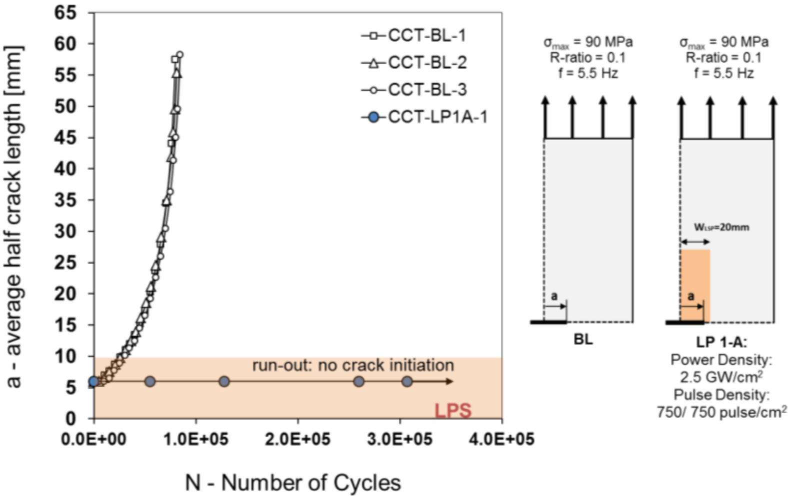

Figure 5-5: Comparison of crack lives (*a* vs *N*) of BL and LP 1-A CCT-samples.

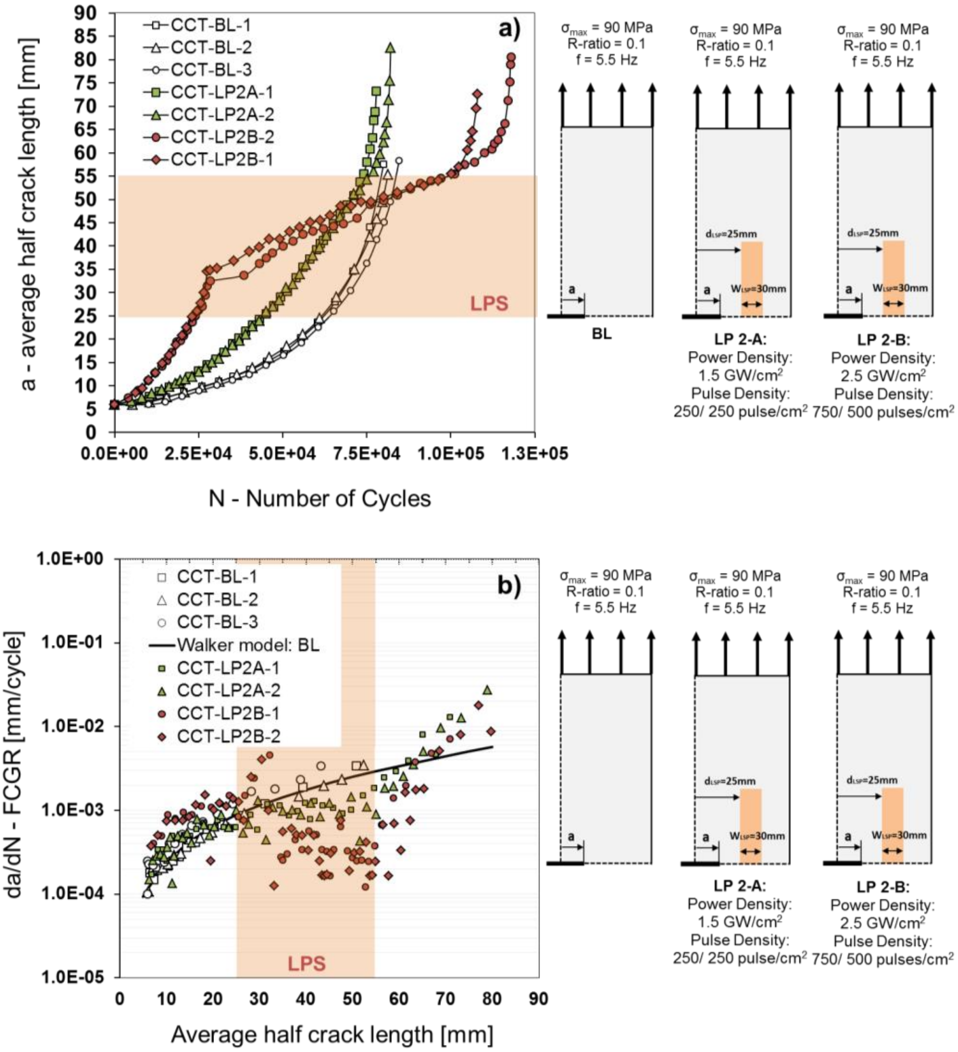

Figure 5-6: Comparison of crack lives (*a* vs *N*) and crack growth rates (*da/dN* vs *a*) of BL and LP 2-A and LP 2-A CCT-sample. a) *a* vs *N* test data and b) *da/dN* vs *a* experimental data

summarised that a minor reduction (LIF = $N_{CCT\text{-}LP2A}$ = 80,436 cycles/ N_{BL} = 84,323 cycles = 0.95) of total crack lives were observed. *CCT-LP2B* samples which were treated with intense LP process parameter exhibited a moderate LIF of 1.35 (LIF = $N_{CCT\text{-}LP2B}$ = 113,610 cycles/ N_{BL} = 84,323 cycles). In contrast to *CCT-LP2A* samples in which no marking point can be identified in which the curves change significantly, the *a* vs *N* plot for *CCT-LP2B* samples reveals the effect of the LP region. For *CCT-LP2B* samples the slope of the curve is abruptly altered after the crack penetrated (*a* =) 8.5 mm (average values of two test samples) into the LP region.

However, the propagation of cracks in both LP configurations ran distinctive from each other and compared with BL samples. This becomes more evident in analysing the plot showing the crack growth rates versus (*da/dN*) the average half crack length (*a*) as presented in (Figure 5-6b). Cracks in LP*CCT-LP2A* samples exhibit a faintly faster growth rate in the region between the initial EDM notch and the peening region and a moderate reduction of FCGR within the LP region. Moreover, the same summary can be drawn for *CCT-LP2B* samples, only that the acceleration outside the LP region and the retardation within the LP region is more evident and substantial than for *CCT-LP2A* samples.

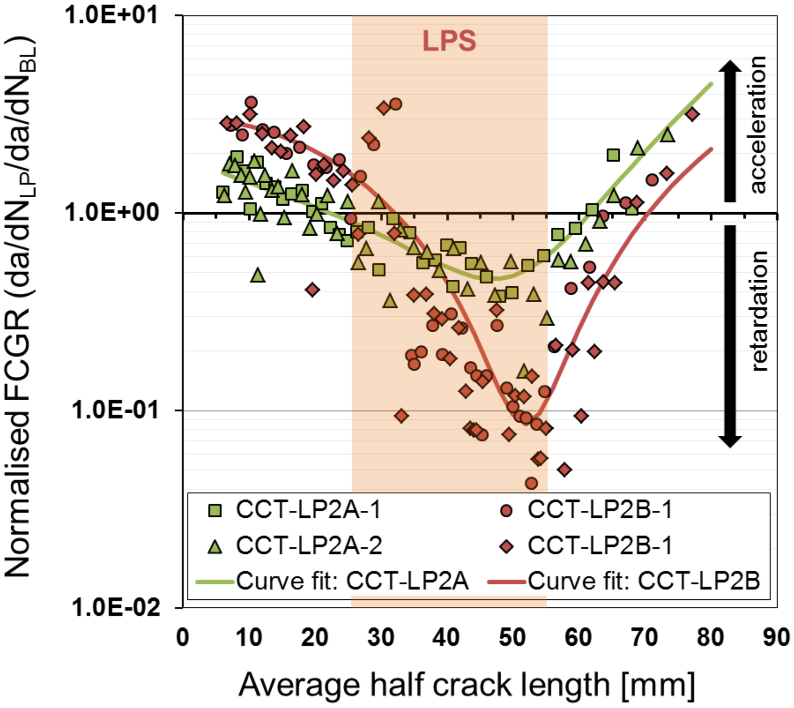

Figure 5-7: Effect of LP on the propagation of cracks in CCT-samples. Normalised crack growth rate versus average crack length.

In order to quantify the effects of laser-peened induced RS field, the FCGRs derived from LP samples, as shown in Figure 5-6b, were normalised by the BL FCGRs, as predicted using the Walker model. The normalised FCGRs are presented in Figure 5-7. Now, the effects of LP show that acceleration of cracks occurs in the range of 1.8 to 1.3 for *CCT-LP2A* samples and of 3.6 to 1.5 for *CCT-LP2B* samples in the area between the initial EDM crack and the peening stripe. Crack retardation within the peening stripe occurs by a factor of 0.8 to 0.3 and 0.4 to 0.06 for *CCT-LP2A* and *CCT-LP2B* respectively. Further the graph demonstrates that crack growth rates for both LP configurations dramatically increase after the crack propagated through the peening stripe.

Different FCGR retardations within the LPS obtained for *CCT-LP2A* and *CCT-LP2B* are evidently the product of different applied LP process parameters and subsequent RS fields. ND RS measurements conducted for *CCT-LP2B* as presented in 4.1.2 exhibited maximum average compressive RS within the LPS of $\sigma_{RS,yy}$ = -91.5 MPa. Following the results obtained during the LP process parameter study performed on the same aluminium alloy and sheet thickness, it can be assumed that RSs in the *CCT-LP2A* are substantially lower, than those samples that were laser-peened with less intense peening parameters (Power density and Pulse density). This outcome causes in consequence less FCGR retardations. As for lack in needed beamtime at the Neutron source at the ILL, no measurements on the *CCT-LP2A* could be performed. Also ICHD measurements could not be applied on the CCT-samples, since no further crack growth testing would have been possible because of the semi-destructive nature of the technique.

5.4 Summary and Conclusions

Fatigue crack growth tests have been performed on BL and laser-peened 1.6 mm 2525-T3 CCT-samples. BL tests were conducted for three different values of R-ratio, and consequently, material coefficients for the Walker crack growth model were determined. The developed model performed accurately to model FCGR in comparison with BL test data. This will serve its purpose in the next chapter when predictions of FCGR in laser-peened CCT-sample will be presented. Also, three different LP treatments were applied to CCT-samples. As a result, fatigue crack growth showed very distinct performances. From those results, the following conclusions can be drawn:

- BL 2524-T3 FCGR exhibit very similar behaviour than 2024-T3 FCGR, as determined by Hudson [51].
- A LPS on top of the EDM starter notch is a very effective way of inhibiting cracks from initiating.
- The investigated LP layout defining two LPS left and right to the EDM notch has the potential to retard FCGRs and moderately improve the crack growth performance by a LIF of 1.35 when an intense LP treatment is chosen (2.5 GW/cm^2, 750/500 spots/cm^2) which correlates to a maximum average RS of $\sigma_{RS,yy}$ = -91.5 MPa within the LPS.
- For an identical LP layout using less intense LP process parameters (1.5 GW/cm^2, 250/250 spots/cm^2), minor detrimental effects on the crack life were determined which resulted in a LIF of 0.95.

- Acceleration of FCGRs was correlated to un-peened regions, whereas retardation of FCGRs was found within the LPS.

Further discussion of the experimental and numerically determined crack growth results will be discussed in the next chapter.

6 Modelling Crack Growth in Laser-Peened CCT- Samples

Modelling crack growth in laser-peened samples is a key enabler for the realisation of LP applications in advanced aircraft fuselage structures. Not only realistic predictions are needed for the implementation of LP applications, but also comprehensive case studies must be performed to develop an understanding of the effects of RSs on fatigue crack growth and further to optimise the LP strategy of any particular sample. Developing a robust prediction model will achieve this without spending too many resources on testing activities.

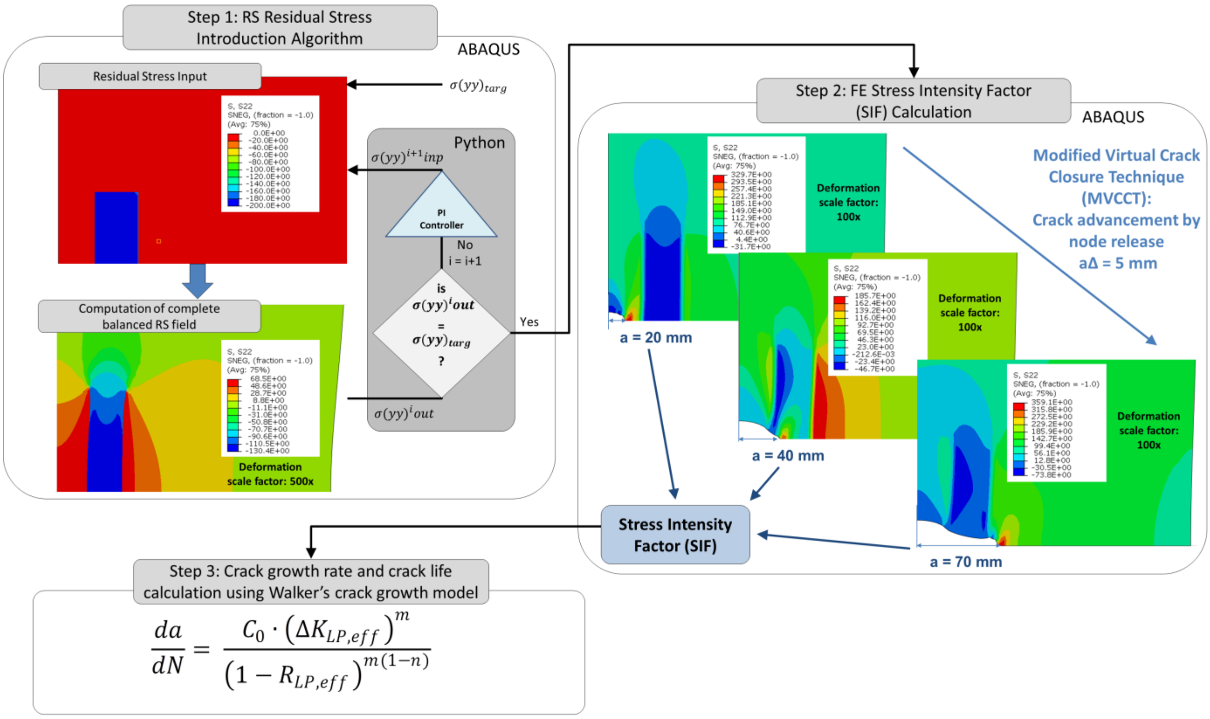

Figure 6-1: Illustration of two step FE modelling process to compute SIFs in laser-peened CCT-samples. Step 1: Introduction of RSs and calculation of the balancing RS field in FE (ABAQUS) iterative PI controller process (Python script). Step 2: Computation of SIFs using prior determined RS fields using MVCCT (ABAQUS). Step 3: Calculation of crack growth rates using Walker's law.

To this end, a three-step modelling approach was developed, as outlined in Figure 6-1, to compute SIFs in the presence of RS and further to predict FCGRs using an empirical crack growth law (Walker) as explained in detail in the following sections.

6.1 Calculation of Stress Intensity Factors using FEM

Finite Element Analysis (FEA) is a useful method for obtaining SIFs for complex geometries and complex loading conditions which cannot be found and composed by standard cases in the literature. There are three approaches:

- **Direct Method:** SIFs are obtained by numerical calculations of stress, displacements or crack-opening displacements.
- **Indirect Method:** The stress intensity is obtained from its relation to other quantities such as elastic energy, work energy for crack closure.
- **Cracked Element:** A cracked element capable of representing stress intensities in the finite-element grid can be used to determine SIFs from nodal displacements along the periphery of the cracked element.

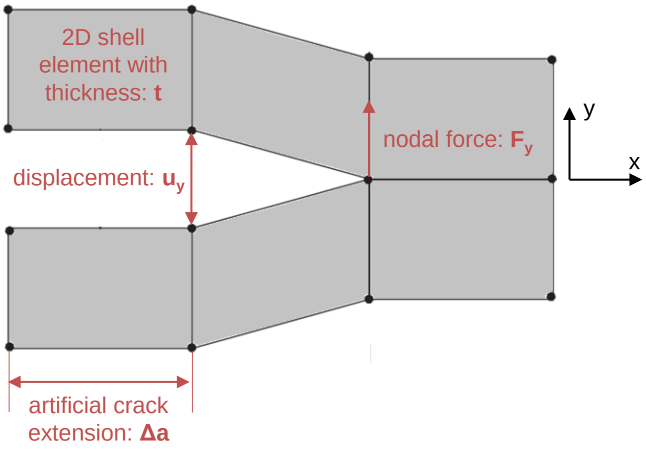

Figure 6-2: Schematic FE mesh for SIF computation via MVCCT (Sketch according to [169]**)**

Among the indirect methods the modified virtual crack closure technique (MVCCT) [39,169,170] is well-established in computing SIFs, especially in RS fields [12,107], and offers a straight forward solution without the need of sophisticated mesh design to determine SIFs by using Irwin's basic energy principle [33]:

$$G = \frac{\sigma^2 \pi\, a}{E} = \frac{K^2}{E} \quad [plane\ stress]\ (Equation\ 6.1)$$

in which *G* is the elastically stored energy release rate (strain energy release rate), *a* is the crack length, *E* the E-modulus and *K* the stress intensity factor. *K* can be calculated by:

$$K = \sqrt{GE} \quad [plane\ stress](Equation\ 6.2)$$

In order to compute the Strain Energy Release Rate (SERR) *G* by means of Finite Element Analysis (FEA) using the MVCCT, a structured FE mesh is necessary, as shown in Figure 6-2. The FE model computes nodal displacements u_y at the node before the crack tip and nodal force *Fy* at the crack tip, irrespective of external or internal loading systems during the same simulation so that *G* can be estimated by:

$$G = \frac{1}{2t\Delta a} \sum F_y u_y \quad (Equation\ 6.3)$$

in which *t* is the thickness of the shell element.

The basic principle of the MVCCT technique becomes evident if the classical VCCT method is understood. During the classical VCCT method, two simulations are performed. During the first run, nodal forces are extracted at the crack tip node. In the second run, the node is released, and the crack can open and extend by one element size. Nodal displacement can be taken at the same node as during the first simulation (former crack tip), and displacement and force can be directly put into energy relationship so that the energy release rate becomes more evident. The MVCCT method assumes that the nodal displacement at the node before the crack tip can be taken as reference for the nodal displacement of the crack tip after node release.

6.2 2D Elastic Finite Element CCT-Model

The basis of the two step FE simulation is a quarter model of the CCT-sample with the identical overall dimensions to the CCT test sample used in the experimental program. This was modelled using ABAQUS 6.13-1, as illustrated in Figure 6-3, in order to reduce computational resources. Two-dimensional quadrilateral finite-membrane-strain elements with reduced integration of the type S4R were used. The element dimensions as shown in Figure 6-3 assume plane stress condition for the 1.6 mm 2524-T3 sheets. Symmetry boundary conditions were applied by rigidly fixing all nodes along the X and Y symmetry line and allowing only movements in the direction of the symmetry line. The material response for 2524-T3 was modelled by a linear-elastic material using Young’s modulus of (E) 70,500 MPa and a Poisson’s ratio (υ) of 0.33.

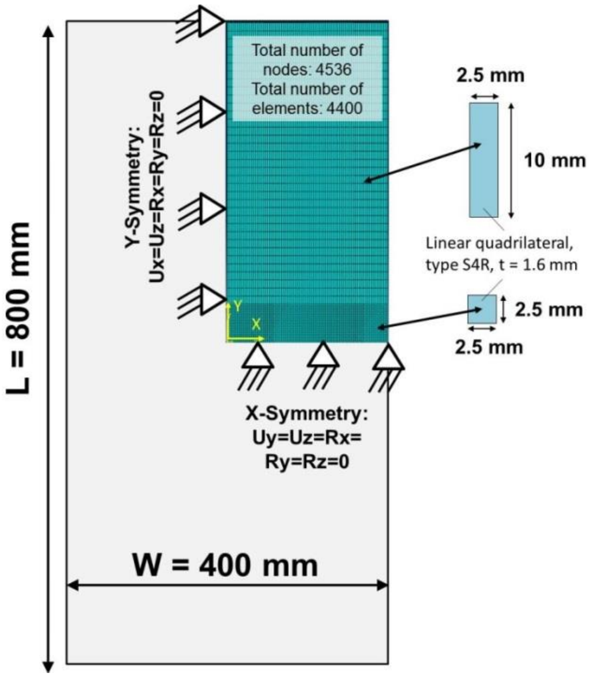

Figure 6-3: Illustration of FE model dimension, mesh and boundary conditions of quarter CCT-sample.

6.2.1 Step 1: Residual Stress Introduction Algorithm

As an alternative to model the LP process itself to compute consequent RS fields for further calculation of SIFs in laser-peened CCT-samples, an iterative algorithm was applied to introduce a designed RS field into the FE model. Introducing pre-defined RS data into any FE code at the location and area of designated LP will ultimately results in a re-balanced stress field, as the FE code finds the equilibrium condition. This results in different stress values to the ones initially introduced. In order to compute a targeted RS field the PI controller process, as shown in Figure 6-4, has been followed as suggested by Y. Lei *et al.* [171]. The process followed consists of five steps as explained in the followings:

1. Definition of a targeted stress state ($\sigma_{yy,targ}$) in the LP region.
2. Introduction of the targeted stress state into the FE model of the sample as the initial stress condition by attaching an ABAQUS user subroutine (SIGINI in Fortran) to the FE model (see Appendix B).
3. Calculation of the balanced RS field as a result of the introduced initial condition in ABAQUS.
4. and 5. Optimisation looping by comparing the balanced RS field calculated by the FE model ($\sigma_{yy,out}$) with the targeted RS at their defined locations ($\sigma_{yy,targ}$) which correspond to the laser-peened area in this work. The procedure starts with i = 0 and $\sigma_{yy,inp} = \sigma_{yy,targ}$ (Step 1) until $\sigma_{yy,out} = \sigma_{yy,targ}$ then the targeted RS field has converged with the predefined targeted RS field and the iterative process can be stopped. If

$\sigma_{yy,out} \neq \sigma_{yy,targ}$ then a proportional integral (PI) controller was used to adapt the initial RS values to produce the targeted RS distribution in the FE model by defining a new input stress ($\sigma_{yy,inp}$). The adjustment equation which was applied to set a new initial condition is formulated as:

$$\sigma^{i+1}_{yy,inp} = \sigma^{i}_{yy,inp} + \beta\left(\sigma_{yy,targ} - \sigma^{i}_{yy,out}\right) \quad \text{(Equation 6.4)}$$

The process was implemented via python scripts (.py) which read ABAQUS output-files (.odb), calculate new initial conditions, then wrote new Fortran script (SIGINI user subroutine) and calculated a new balanced RS field (for an example of the Fortran and python scripts refer to Appendix A).

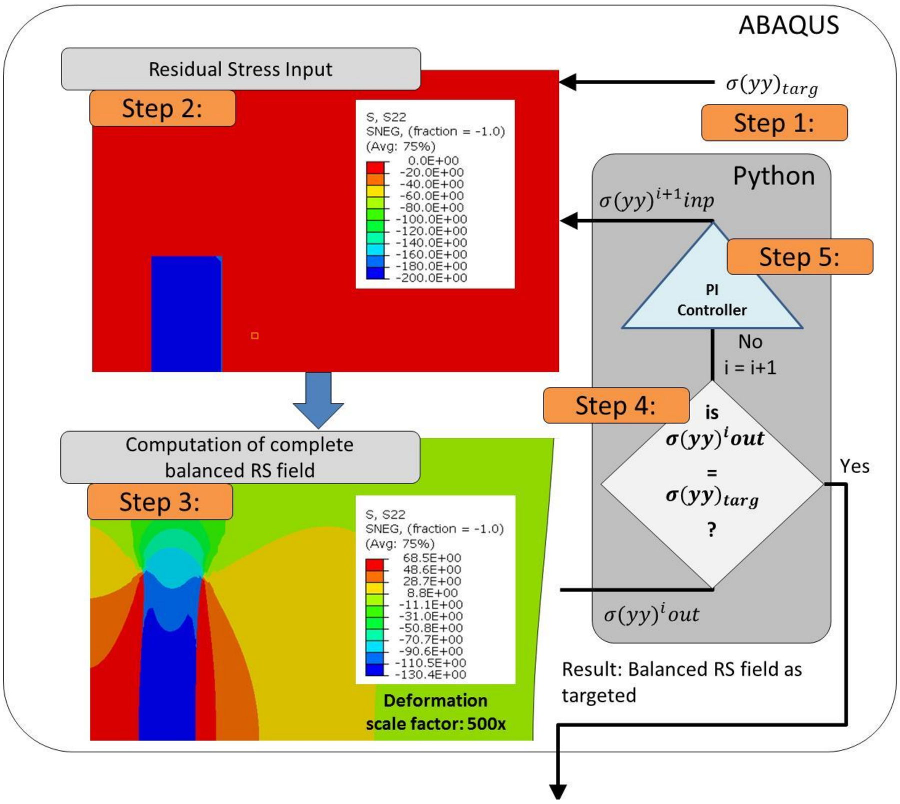

Figure 6-4: Illustration iterative PI controller process in combination with FE model to compute LP induced RS fields.

An example of an initial and a balanced FE calculated RS field is given in Figure 6-4 (Step 2 vs Step 3) which converged after i = 5 iteration loops. The shown stress field is concerning the longitudinal stress component (σ_{yy}) as this is the most important direction for further analyses. All convergences were limited to the longitudinal stress component to save computational resources.

6.2.2 Step 2: FE Stress Intensity Factor Calculation

Total SIFs (K_{tot}) were computed using the MVCCT methodology [39,169,170]. The basic principles of this method are outlined in chapter 6.1 (Calculation of Stress Intensity Factors using FEM). For the simulation of crack advancement in laser-peened CCT-samples an initial RS field, determined as described in the previous chapter, was attached as user-subroutine (SIGINI). The first step of the simulation allowed creation of equilibrium by calculating the balanced RS field.

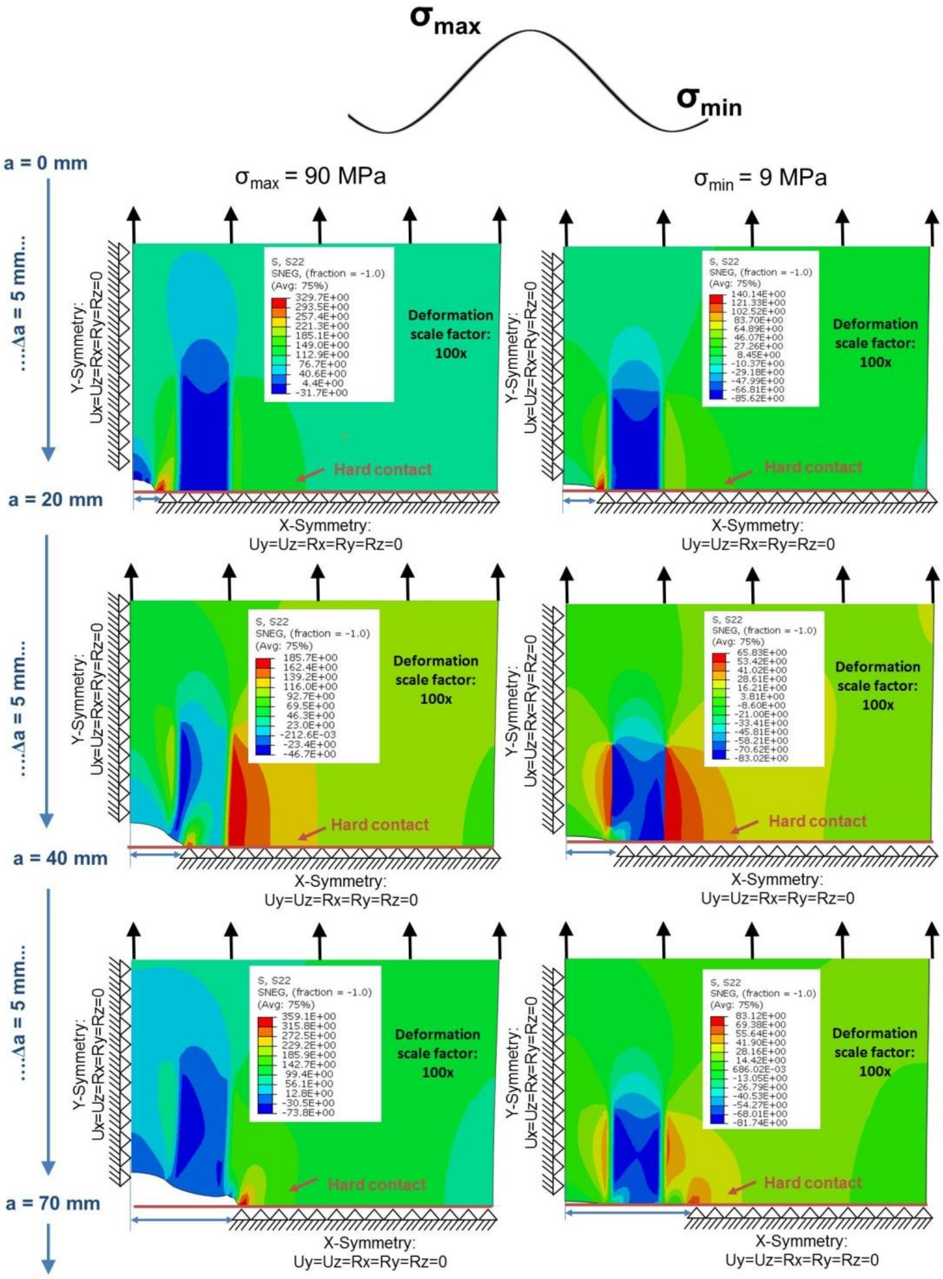

Figure 6-5: Schematic view of the total SIF (K_{tot}) computation and crack advance Δa using MVCCT implemented in FE (ABAQUS) for σ_{max} and σ_{min} taking into account RS (shown by the stress contours) as determined by the PI controller process. LP configuration used for this example is as defined for *LP 2-B* with and maximum compressive RS of -100 MPa in the LPS.

A schematic view of the MVCCT computation process modelling the crack advance which is followed to determine total SIF (K_{tot}) values for the maximum ($K_{tot,max}$) and minimum ($K_{tot,min}$) load of the constant amplitude fatigue load cycle is presented in Figure 6-5. Crack advance Δa was realised by opening the boundary conditions at the X-symmetry line which coincides with the crack growth plane. The mesh size is 2.5 mm in the X-direction but an advance of $\Delta a = 5\ mm$ was chosen so that every two elements the boundary condition was released during the simulation. For each crack length, the nodal force (F_y) at the crack tip and the nodal displacement (u_y) at the element before the crack tip were extracted from the FE model using a python script (.py) to further calculate the SERR as described in chapter 6.1. In order to prevent unrealistic interpenetration of the crack flanks, especially when the crack is advancing through a compressive RS field, hard contact was defined in the FE model. The model also allowed for redistribution of the RS field as the crack advances by calculating a new equilibrium for every new boundary condition.

In Figure 6-6a FE results of computed SIFs with an external stress of 100 MPa are plotted against the half crack length and compared with Feddersen's [32] analytical solution for an un-peened CCT-sample. The deviation ([K_{Fed} - K_{Fe}] / K_{Fed}) between the FE model (K_{Fe}) and the analytical solution (K_{Fed}) is shown in Figure 6-6b. It can be concluded that the FE model delivers accurate SIF results with a maximum deviation of 1.5 % compared with Feddersen's SIF model.

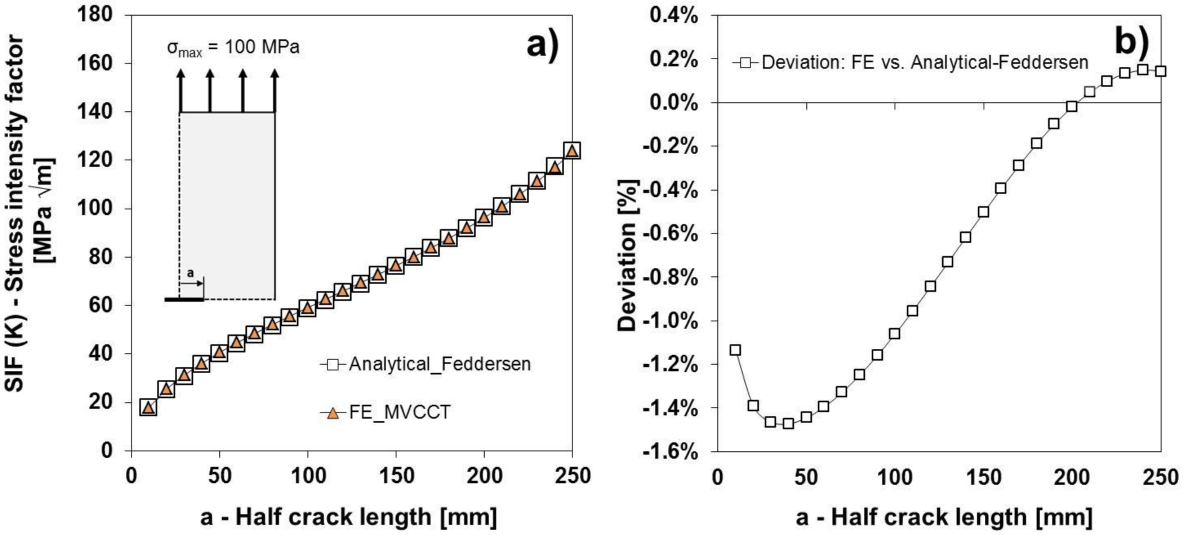

Figure 6-6: Comparison of FE model versus Feddersen's analytical SIF model. a) Total SIF (K_{tot}) vs half crack length (a) and b) Deviation (K_{Fed}/K_{Fed}) in percentage vs half crack length (a).

6.2.3 Step 3: Fatigue Crack Growth Rates Predictions

FCGRs for AA 2524-T3 CCT-sample were predicted using Walker's empirical crack growth law by taking into account the test data for *CCT-BL* samples and subsequent derived material constants C_0 ($1.0*10^{-07}$ mm/cycle), m (2.86) and n (0.59) as previously determined in chapter 5.2. FCGRs were calculated by:

$$\frac{da}{dN} = \frac{C_0 \cdot \left(\Delta K_{LP,eff}\right)^m}{\left(1 - R_{LP,eff}\right)^{m(1-n)}} \; (Equation\ 6.5)$$

in which $\Delta K_{LP,eff}$ is determined by the totals SIF ($K_{tot,max}$ and $K_{tot,min}$) computed by the FE model including both the internal (RS field) and external loadings using:

$$\Delta K_{LP,eff} = K_{tot,max} - K_{tot,min} \; (Equation\ 6.6)$$

and where $R_{LP,eff}$ is the R-ratio calculated by the SIFs ($K_{tot,max}$ and $K_{tot,min}$) to account for the means stress effects caused by the internal RS field.

$$R_{LP,eff} = \frac{K_{tot,min}}{K_{tot,max}} \; (Equation\ 6.7)$$

The number of load cycles N to reach any crack length a can be calculated by the integration of the inverse of the predicted crack growth rate. For the Walker equation this integration leads to the following formula:

$$\int_0^N dN = \int_{a_0}^{a_f} \left(C_0 \left[\Delta K_{Lp,eff}(1 - R_{LP,eff})^{m-1}\right]^n\right)^{-1} da \; (Equation\ 6.8)$$

Number of cycles can be calculated from the initial crack length a_0 to any final crack length a_f by using discrete values of $\Delta K_{LP,eff}$ and $R_{LP,eff}$ as supporting points. Initial crack lengths of a_0 = 6 mm was applied in line with the experimental CCT-sample. Final crack lengths of a_f = 80 mm were considered during the crack life calculations, as this is the crack length observed during testing before failure.

6.3 Laser-Peening Design Case Study

Finding an optimised LP treatment for CCT-samples and hence an optimised LP application for aircraft fuselage skins giving increased damage-tolerance capabilities is a major task in the LP research. For that an extensive study was performed, using the crack growth modelling approach described in the previous chapter. The effects of the following parameters taking into account different **LP layouts** and process parameters causing different **RS conditions** and also **external loading conditions** on the relevant crack growth parameters and overall crack lives were investigated. The parameters are:

- **LP layout: Position (d_{LP}), size (w_{LP}) and the number ($\#_{LP}$) of laser peened regions (stripe/s)** on the CCT-samples, as specified in Figure 6-7 and defined for a single LPS ($\#_{LP}$ = 1) on each side of a centre crack and two LPSs ($\#_{LP}$ = 2) on each side of a centre crack in Table 6-1 and Table 6-2. For single LPS ($\#_{LP}$ = 1), seven different cases were investigated, in which three cases vary the size in terms of the width of the LPS (w_{LP}) from 20 mm (*FE-LP-1-1*) to 40 mm (*FE-LP-1-3*) with an intermediate case in between of 30 mm (*FE-LP-1-2*). Case ***FE-LP-1-2*** (in italic in Table 6-1) has the identical LP layout as defined for the experimental laser-peened CCT-sample definition of *LP 2-B* (recall Figure 3-4b). Therefore, it can be used to validate the prediction model. Five other cases analyse the positioning of (d_{LP}) a single LPS with a constant size of w_{LP} = 20 mm from d_{LP} = 25 mm to d_{LP} = 55 mm with a step of Δd_{LP} = 10 mm (*FE-LP-1-1* and *FE-LP-1-4* to *FE-LP-1-7).*

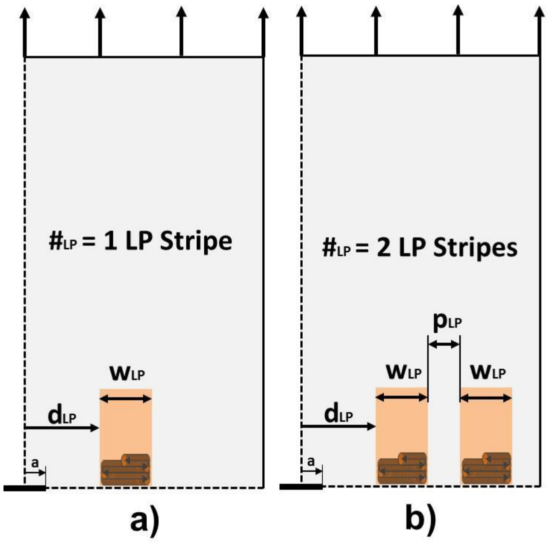

Figure 6-7: Illustration of the positioning of LPSs and relevant LP design parameters on a quarter CCT-samples. a) LP design parameters on a quarter CCT-samples for a single LPS ($\#_{LP}$ = 1) and b) LP design parameters on a quarter CCT-samples for two LPSs ($\#_{LP}$ = 2)

In the case of two LPSs ($\#_{LP}$ = 2) ten cases (*FE-LP-2-1* to *FE-LP-2-10*) were defined in which the position of the first LPS defined by d_{LP} and the relative position of the second peening stripe in relation to preceding one defined by p_{LP} were varied. Four values of d_{LP} (20 mm, 35 mm, 50 mm and 65 mm) and four p_{LP} values (15 mm, 30 mm, 45 mm and 60 mm) were considered and combined, as specified in Table 6-2.

Table 6-1: FE LP case study matrix for single LPS (#$_{LP}$ = 1) defining position and dimension of the single LPS as drawn in Figure 6-7a.

	FE-LP Case ID	d_{LP} [mm]	w_{LP} [mm]
Single LPS #LP = 1	**FE-LP-1-1**	25	**20**
	FE-LP-1-2	*25*	***30***
	FE-LP-1-3	25	**40**
	FE-LP-1-4	**25**	20
	FE-LP-1-5	**35**	20
	FE-LP-1-6	**45**	20
	FE-LP-1-7	**55**	20

Table 6-2: FE LP case study matrix for two LPSs (#$_{LP}$ = 2) defining position of the two LPSs as drawn in Figure 6-7b under a constant width of the LP of w_{LP} = 20 mm.

	FE-LP Case ID	d_{LP} [mm]	p_{LP} [mm]
Double LPS #LP = 2	**FE-LP-2-5**	20	15
	FE-LP-2-6	20	30
	FE-LP-2-7	35	15
	FE-LP-2-8	20	45
	FE-LP-2-9	35	30
	FE-LP-2-10	50	15
	FE-LP-2-11	20	60
	FE-LP-2-12	35	45
	FE-LP-2-13	50	30
	FE-LP-2-14	65	15

- **Level of compressive RS** within the LPS, as outlined in Table 6-3. Three level of compressive RS levels of σ_{RS} = -100 MPa, σ_{RS} = -130 MPa and σ_{RS} = -150 MPa were introduced into the FE model for the LP layout as described by *FE-LP-1-2*. For all other cases a constant value of σ_{RS} = -130 MPa was applied.

Table 6-3: FE cases for RS fields in the LP region.

FE-LP Case ID	RS

	[MPa]
FE-LP-1-2	**-100** **-130** **-150**
All other cases	**-130**

- **Level of applied external loads**, as given in Table 6-4. Three different maximum external applied stress levels of σ_{max} = 90 MPa, σ_{max} = 60 MPa and σ_{max} = 120 MPa were then selected and implemented to the case *FE-LP-1-2* while keeping a compressive RS of -130 MPa. The R-ratio for all load cases, however, remained constant at R = 0.1 simulating the situation on the aircraft fuselage. All other cases as described above were investigated using a constant external load of σ_{max} = 90 MPa and an R-ratio of 0.1.

Table 6-4: FE cases for external loads.

FE-LP Case ID	**σ_{max} [MPa]**	**σ_{min} [MPa]**	**R-ratio**
FE-LP-1-2	**90**	9	**0.1**
	60	6	**0.1**
	120	12	**0.1**
All other cases	**90**	9	**0.1**

6.4 Case Study Results

6.4.1 Balanced RSs in Laser-peened CCT-samples with a Single LP Stripe

A comparison of FE computed balanced RS field for FE cases FE-LP-1-1, FE-LP-1-2 and FE-LP-1-3 in which the width of the LPS (w_{LP}) is varied for a fixed position of d_{LP} = 25 mm. A compressive RS of -130 MPa was introduced by the FE PI controller process for the cases as presented in Figure 6-8 as stress contour maps. Stresses shown in the contour maps are longitudinal ones (σ_{yy}). In the maps, the effects of varying the dimension of the compressive RS field (w_{LP}) become evident. Balancing tensile RSs are significantly increased on the left-hand side (x = 0 mm to d_{LP} = 25 mm) with increased width of the peening stripe. Figure 6-11 summarises the maximum tensile RS for different configurations of LPSs. The maximum tensile RS increases linearly with the width (w_{LP}) from 20 mm (as shown in Figure 6-8a) to 30 mm (as shown in Figure 6-8b) and 40 mm (as shown in Figure 6-8c) to 42.3 MPa to 66.3 MPa and to 91.4 MPa. This is an increase of a factor of 2.16 taking into consideration the narrowest and widest peening stripe. On the right-hand side (d_{LP} + w_{LP} to 200 mm), the tensile RS values start lower than stresses on the left-hand side of the LPS at the boundary of the LPS and decline to zero at the edge of the sample. As for the more intense tensile RS between x = 0 mm to d_{LP} = 25 mm, it must be pointed out that there is a second peening stripe to the left of the peening stripe located at the other half of the CCT-sample behind the symmetry line which does not allow the RS to decline to zero as is the case for tensile RS on the right-hand side of the LPS.

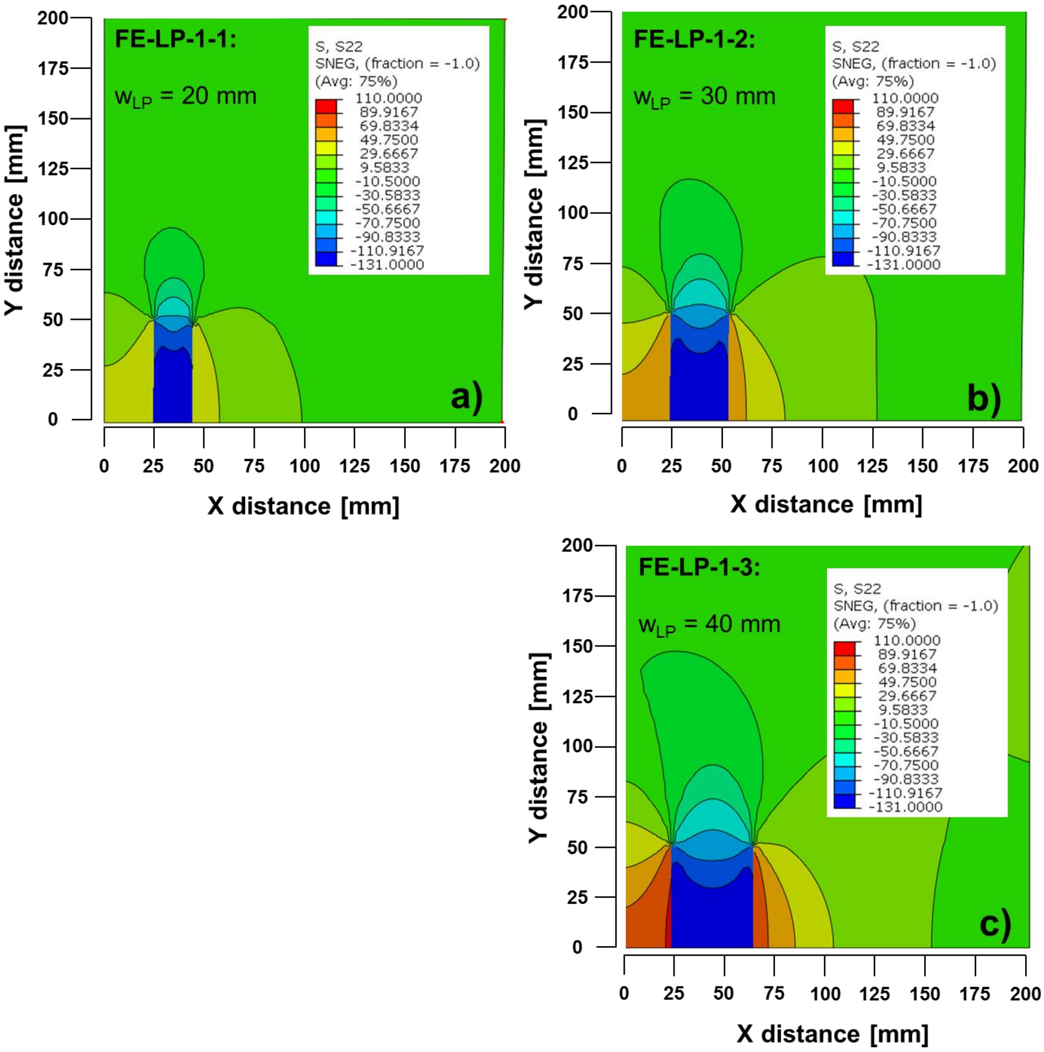

Figure 6-8: Stress contour plot results of the PI controller process varying the width (w_{LP}) of a single LPS showing the complete balanced longitudinal RS field Syy for a constant position of the peening (d_{LP}) stripe of 25 mm and RS of -130 MPa in the LP region. a) FE-LP-1-1, b) FE-LP-1-2 and c) FE-LP-1-2

In the example of varying the maximum compressive RS values in the peened area from σ_{RS} = -100 MPa to σ_{RS} = -130 MPa and finally to σ_{RS} = -150 MPa, a comparison of computed stress contour maps is given in Figure 6-9a, Figure 6-9b and Figure 6-9c for the position and dimension of the LPS as defined for case *FE-LP-1-2*. Tensile RSs are increased corresponding to more compressive RS within the LPS on both sides of the peening stripe. Comparing the maximum tensile RS values located in between the centre and the peening stripe (x = 0 mm to d_{LP} = 25 mm), the values alter from 32.5 MPa for σ_{RS} = -100 MPa, 42.3 MPa for σ_{RS} = -130 MPa to 48.8 MPa for σ_{RS} = -150 MPa, as seen in Figure 6-11. This is a relatively moderate increase by a factor of 1.5 when compared to the rise of tension by increasing the peening stripe dimension (w_{LP}).

Results of stress contour maps showing the RS field as the position of the peening stripe having a width of 20 mm and an introduced compressive RS value of -130 MPa are shifted away from the centre line of the CCT-sample are presented in Figure 6-10. As can be seen from the contours, the tensile RSs are not significantly decreased at the surrounding regions left and right of the peening stripe. In Figure 6-11, the maximum computed tensile RSs are plotted in relation to the position of the peening stripe which reveals that the position of d_{LP} = 25 mm results in a RS of 42.3 MPa whereas the maximum position of d_{LP} = 75 mm gives a tensile RS of 33.8 MPa. This decrease is insignificant in comparison of the effect of increasing dimension or compression of the peening stripe.

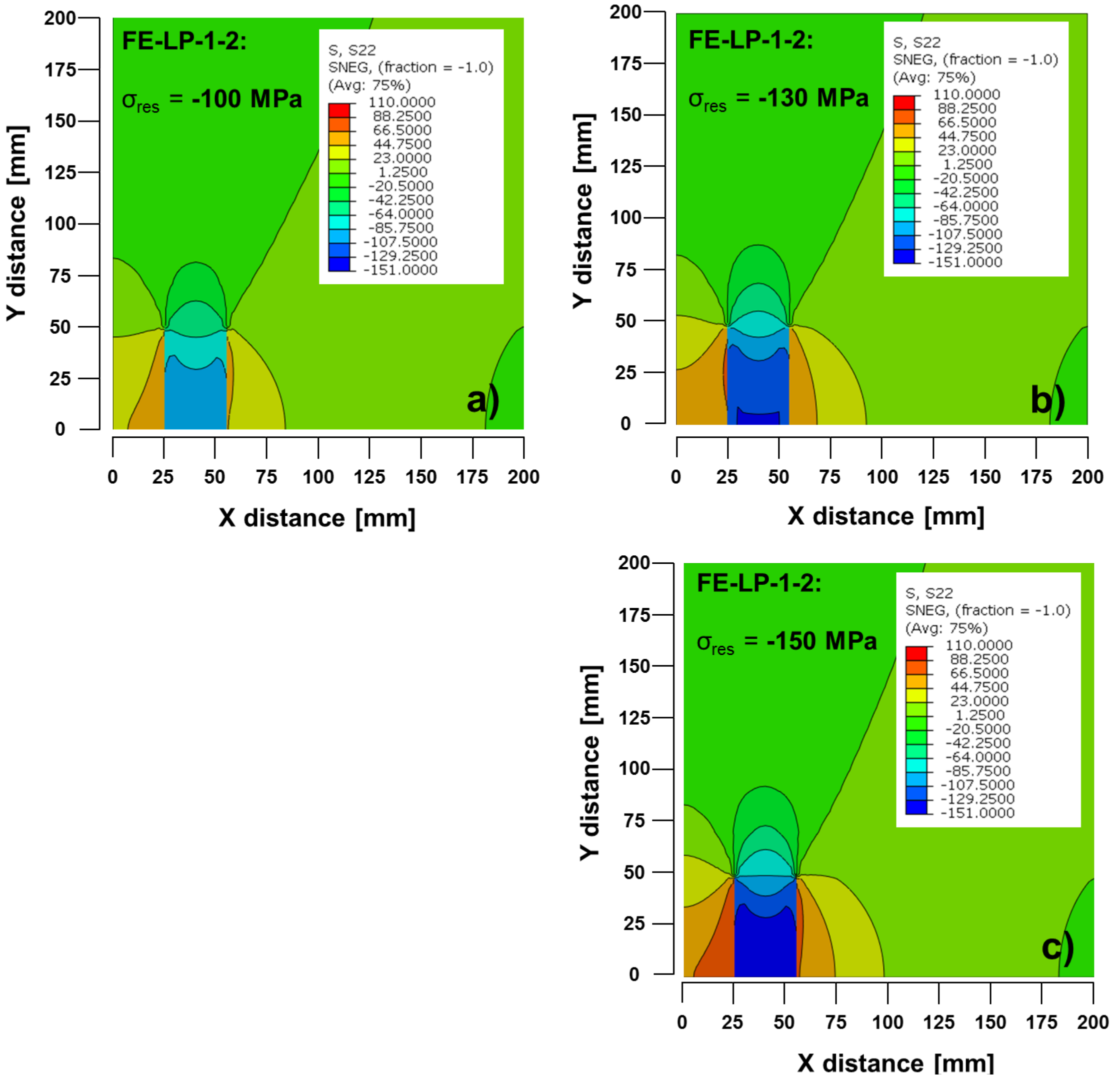

Figure 6-9: Stress contour plot results of the PI controller process varying the compressive RS values within a single LPS showing the complete balanced longitudinal RS field S_{yy} for a constant position (d_{LP}) and width (w_{LP}) of the peening stripe of 25 mm and 30 mm respectively (FE-LP-1-2). a) RS = -100 MPa, b) RS = - 130 MPa and c) RS = -150 MPa.

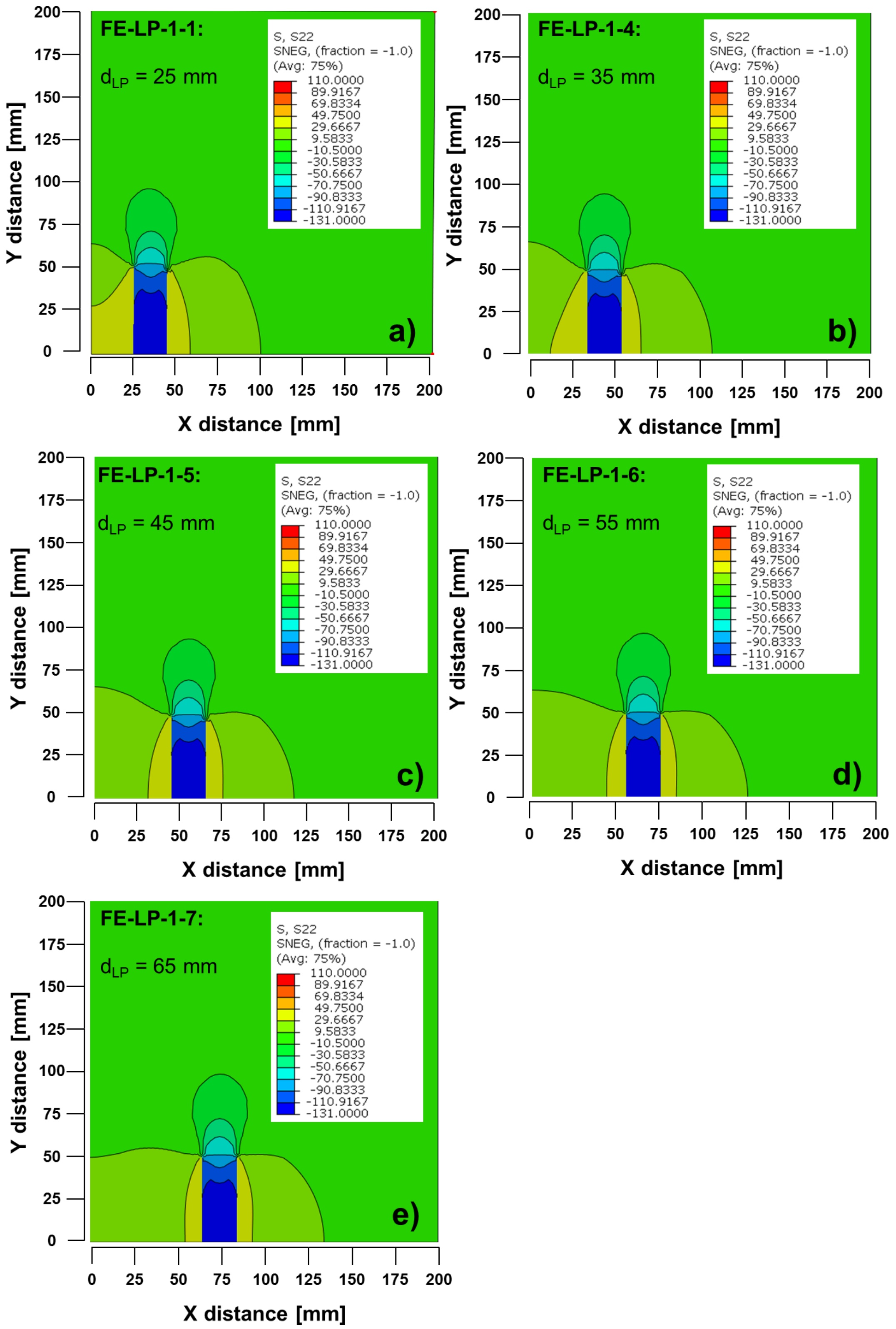

Figure 6-10: Stress contour plot results of the PI controller process varying the position of the peening (d_{LP}) stripe showing the complete balanced longitudinal RS field S_{yy} for a constant width (w_{LP}) of a single LPS of 20 mm and RS of -130 MPa in the LP region. a) FE-LP-1-1, b) FE-LP-1-4, c) FE-LP-1-5, d) FE-LP-1-6 and e) FE-LP-1-7.

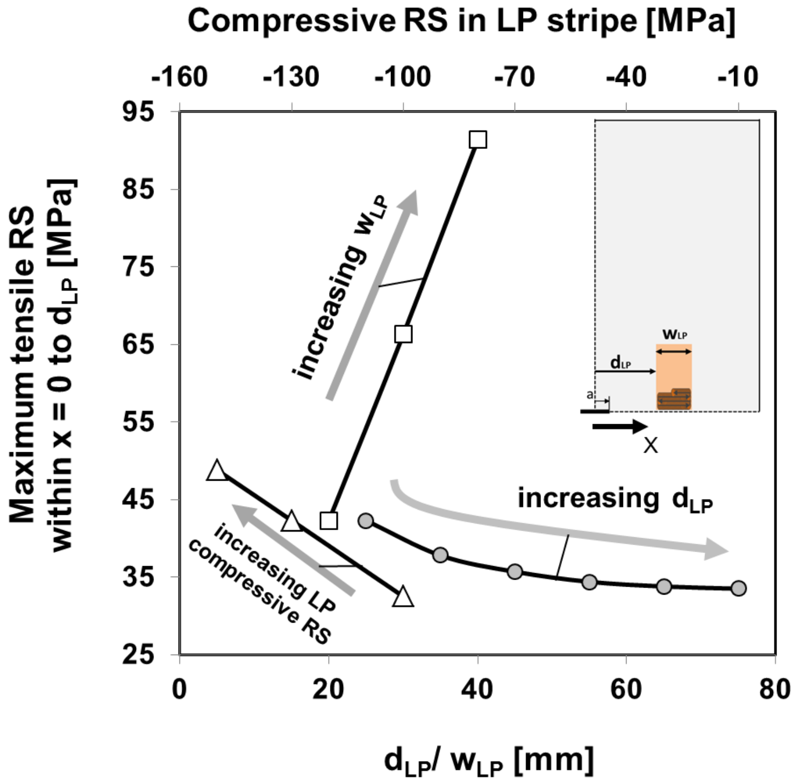

Figure 6-11: Summary of computed maximum tensile RSs as a result of the PI controller process in relation to varying parameters of w_{LP}, d_{LP} and σ_{RS}.

6.4.2 Balanced RSs in Laser-peened CCT-samples with Two LP Stripes

Contour maps for cases having two LPSs on each side of total CCT-sample are shown in Figure 6-12. Both peening stripes are (w_{LP} =) 20 mm wide and (σ_{res} =) -130 MPa in compression for all cases. The contour maps present the longitudinal stress component σ_{yy} as this is the direction which acts parallel to external loads. From the stress contour maps, it can be seen that *FE-LP-2-5* (d_{LP} = 20 mm and p_{LP} = 15 mm) has the highest tensile stress between the centre line and the first peening stripe (x = 0 to d_{LP}: 77.1 MPa) and also between the two peening stripes (x = d_{LP} + w_{LP} to x = d_{LP} + w_{LP} + p_{LP}: 82.8 MPa). A comparison of all computed maximum tensile RSs in between the centre line and the first peening stripe and between the two peening stripes is given in Table 6-5 and Table 6-6. Increasing the distance of two peening stripes (d_{LP}) with a constant pitch between them will decrease the tension in between the centre line and the first peening stripe as well as in between the two peening stripes. For instance comparing *FE-LP-2*-5 with *FE-LP-2-14* the tension reduced from 77.1 MPa to 55.4 MPa between the centre line and the first peening stripe and from 82.8 MPa to 51.5 MPa between the two peening stripes. Equivalently, the tension drops when the pitch between the peening stripes is increased.

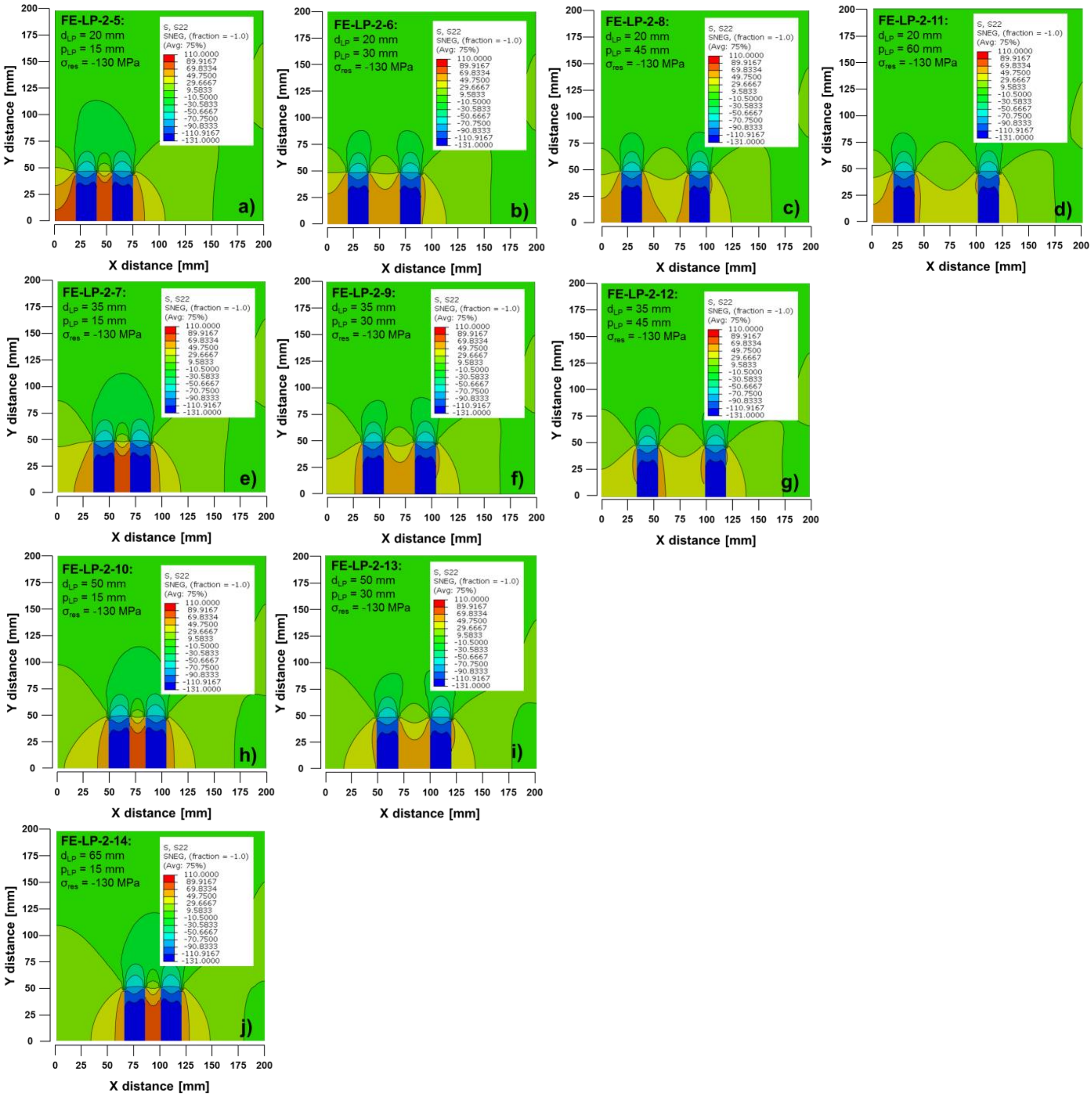

Figure 6-12: Stress contour plot results of the PI controller process varying the position two LPSs by the position of the first LPS (d_{LP}) and the relative position of the second LPS (p_{LP}) showing the complete balanced longitudinal RS field S_{yy} for a constant width (w_{LP}) of the stripes of 20 mm and RS of -130 MPa in the LP region. a) FE-LP-2-5, b) FE-LP-2-5, c) FE-LP-2-8, d) FE-LP-2-11, e) FE-LP-2-7, f) FE-LP-2-9, g) FE-LP-2-12, h) FE-LP-2-10, i) FE-LP-2-13 and j) FE-LP-2-14.

A summarising image of the data can be drawn that as more space and material is present between two peening stripes the lower the resulting tension will be around those laser-peened regions as the balancing tension can consequently be distributed more smoothly.

Table 6-5: Maximum tensile RS between the centre line of CCT-sample and the first peening stripe $x = 0$ to d_{LP} for all cases having two peening stripes. (All given stresses in MPa)

p_{LP} [mm]	d_{LP} [mm]	15	30	45	60
20		77.1	65.2	58.8	55.4
35		63.5	53.8	48.6	/
50		59.0	50.1	/	/
65		57.4	/	/	/

Table 6-6: Maximum tensile RS between first and second LPS $x = d_{LP} + w_{LP}$ to $x = d_{LP} + w_{LP} + p_{LP}$ for all cases having two peening stripes. (All given stresses in MPa)

p_{LP} [mm]	d_{LP} [mm]	15	30	45	60
20		82.8	66.5	56.6	51.5
35		75.2	60.2	51.3	/
50		72.7	58.1	/	/
65		71.8	/	/	/

6.4.3 Effect of Residual Stress on Effective Stress Intensity and R-ratio

Crack growth in laser-peened CCT-samples is predicted using the previously described modelling approach. FE model outputs of effective SIF range (ΔK_{eff}) and effective R-ratio (R_{eff}) are processed together with material properties (C_0, m and n) by applying Walker's empirical crack growth model. Figure 6-13a shows three different RS profiles corresponding to the FE case definition of FE-LP-1-2 (d_{LP} = 25 mm, w_{LP} = 30 mm) varying the compressive RSs (σ_{RS} =-100 MPa, σ_{RS} = -130 MPa and σ_{RS} = -150 MPa) within the LPS. Figure 6-13b and c then presents the computed effective SIF range (ΔK_{eff}) and effective R-ratio (R_{eff}) (refer to the equations in section 6.2.2) versus half crack length (a) for a maximum external applied stress of (σ_{max}=) 90 MPa and a nominal R-ratio of 0.1. Both graphs indicate the underlying mechanisms which cause FCGR retardation and acceleration in comparison with the BL condition as can be noticed in Figure 6-13d. The effective SIF range (ΔK_{eff}) which is the main driver of fatigue crack growth reduces significantly within the LPS depending on the level of compression and therefore causes the FCGR retardation within the LPS (see Figure 6-13d). For compressive RSs of σ_{RS} = -100 MPa, σ_{RS} = -130 MPa and σ_{RS} = -150 MPa within the LPS, ΔK_{eff} values dropped from ΔK_{eff} = 33.4 MPa√m for the un-peened condition to ΔK_{eff} = 17.1 MPa√m, ΔK_{eff} = 11.0 MPa√m and ΔK_{eff} = 7.0 MPa√m, for the respective LP condition. The effect of compressive RS on ΔK_{eff} is a result of the crack closure at the minimum external applied stress (σ_{min}). If for the amount of applied minimum stress the crack is closed due to the compression in the sample, the total minimum K (K_{min}) becomes zero. The total maximum K value ($K_{tot,max}$) is a sum of the SIF produced by RSs (K_{res}) and external load K values (K_{max}) and hence the ΔK_{eff} decreases when K_{res} is negative. The inversion of that argument is, however, that no effect of the RS field on values of ΔK_{eff} would occur if the minimum applied stress would not drop below the crack opening stress in the FE MVCCT model. Before the crack enters the LPS no effect of the tensile RS field on the FCGR was determined using the previous mentioned rationale.

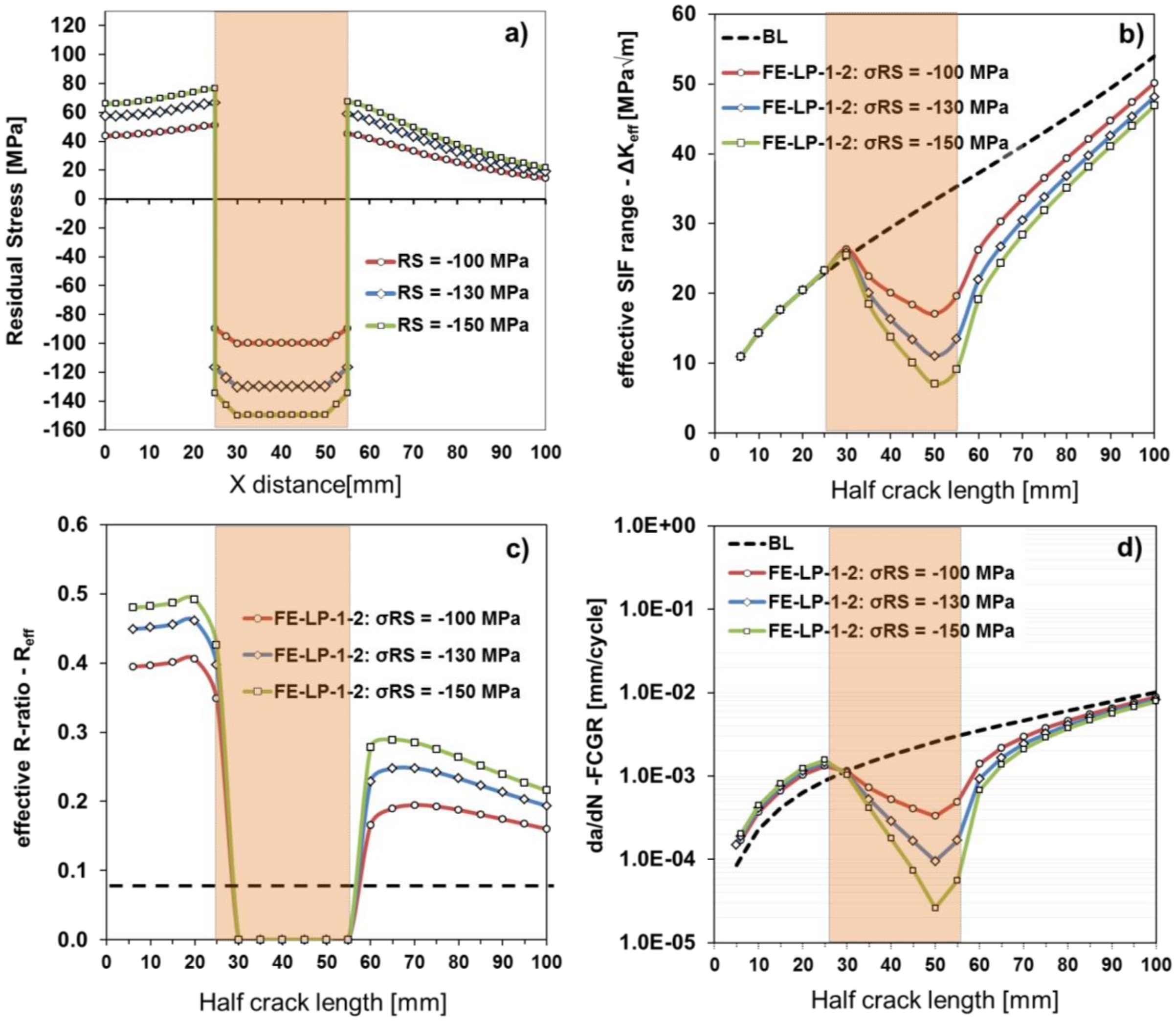

Figure 6-13: Modelling outputs for different conditions of RS under constant width (w_{LP}) of a single LPS of 30 mm and position of the peening (d_{LP}) stripe of 25 mm and an external maximum applied stress of σ_{max} =90 MPa and nominal R-ratio of 0.1. a) RS field varying level of compressive RS of σ_{RS} =-100 MPa, σ_{RS} =-130 MPa and σ_{RS} =-150 MPa b) effective SIF range ΔK_{eff} varying w_{LP} level of compressive RS of σ_{RS} =-100 MPa, σ_{RS} =-130 MPa and σ_{RS} =-150 MPa, c) effective R-ratio R_{eff} varying level of maximum level of external loading of σ_{max} = 60 MPa, σ_{max} = 90 MPa and σ_{max} = 120 MPa d) FCGR varying level of maximum level of external loading of σ_{max} = 60 MPa, σ_{max} = 90 MPa and σ_{max} = 120 MPa.

The effective R-ratio (R_{eff}) as shown in Figure 6-13c increases with increasing RS and vice-versa. In that case, effective R-ratios were increased for regions of tensile RS outside the LPS and decreased within the LPS in comparison to the nominal applied R-ratio of 0.1. As a result of that, FCGRs exhibited acceleration corresponding to higher values of R_{eff} which could be determined using Walker's model which takes into account the mean stress effect. Within the

LPS the lower limit of R_{eff} is to zero, as no negative K_{min} can be calculated due to crack flank contact in the FE model. FCGR retardation within the LPS is dominated by the decrease of ΔK_{eff} but however decreased values of R_{eff} will further decrease FCGRs.

To understand the acceleration which occurred in the tensile RS field before the LPS, the effective R-ratio, as shown in Figure 6-13c, provides an explanation. For instance, the effective R-ratio rises from R =0.1 to R = 0.5 for a RS of σ_{RS} = -150 MPa in that region and according to the mean stress effects as explained in chapter 2.1.2.3, FCGRs increase with increasing R-ratios. This is clearly noticeable in Figure 6-13d for the area before the LPS. The mean stress effect was explained by the underlying crack closure mechanics, as firstly referred to by Elber [46] (refer to chapter 2.1.2.3). The effect of compressive and tensile RSs on the mechanism of crack opening and closure were practically investigated by V. Lacarac *et al.* [20]. They demonstrated by experiments that the crack opening stress increased in the presence of compressive RSs which in turn caused a decrease of the effective ΔK_{eff} value and hence resulted in crack retardations. The ΔK_{eff} in this sense described the effective portion of the applied load cycles during which the crack is open and is capable of increasing the crack length. Analogously, the FCGRs within the LPS display crack growth retardation in comparison with the un-peened sample.

6.4.4 Crack Growth Results and the Effects of the LP Layout

6.4.4.1 Crack Growth of Laser-peened CCT-samples with a Single LP Stripe

Modelled FCGR versus half crack length (da/dN vs a) for cases that vary the LP layout hence the dimension and position of one LPS as illustrated in Figure 6-7a are presented in Figure 6-14a to Figure 6-14d. The FCGR and the normalised FCGR of different width of the LPS (w_{LP}) are contrasted in Figure 6-14a and Figure 6-14b and FCGR and the normalised FCGR of different positions of the LPS (d_{LP}) are compared in Figure 6-14c and Figure 6-14d individually. The normalised FCGR is calculated by the ratio of the FCGR for the LP case and the FCGR for the BL case ($[da/dN_{LP}]/[da/dN_{BL}]$). In this context, acceleration and retardation of FCGRs is referred to any value greater or lower than 1, as indicated in the figures.

Comparing FCGR coming from different widths of the LPS (w_{LP}) as shown in Figure 6-14a, the model data exhibit that for all three LPS widths of 20 mm (*FE-LP-1-1*), 30 mm (*FE-LP-1-2*) and 40 mm (*FE-LP-1-3*), an acceleration of crack growth occurs until the cracks propagate into the LPS equivalent to a half crack length of 25 mm. At this point, the crack growth rate drops down dramatically. However, the level of acceleration differs. Figure 6-14b presents the normalised FCGR and it can be noticed that the widest LPS produces acceleration of FCGR by a maximum factor of 2.1, the 30 mm wide stripe an acceleration effect by a maximum factor of 1.8 and the narrow stripe accelerates FCGRs by a maximum factor of 1.5. Analogously, the drop in FCGR can be quantified by the normalised FCGR. It can be noticed, that the retardation of FCGRs increases with increasing w_{LP} so that the case of a 20 mm, a 30 mm and a 40 mm wide LPS produces a retardation effect on the FCGR by a factor of 0.08, 0.04 and 0.02 correspondingly. The minimum of FCGR which was used to quantify the retardation effect is reached 5 mm (one crack increment in the FE model) before the end of the peening stripe and the crack penetrated through the LP area. At this point, the FCGR rise again but stay below the BL condition.

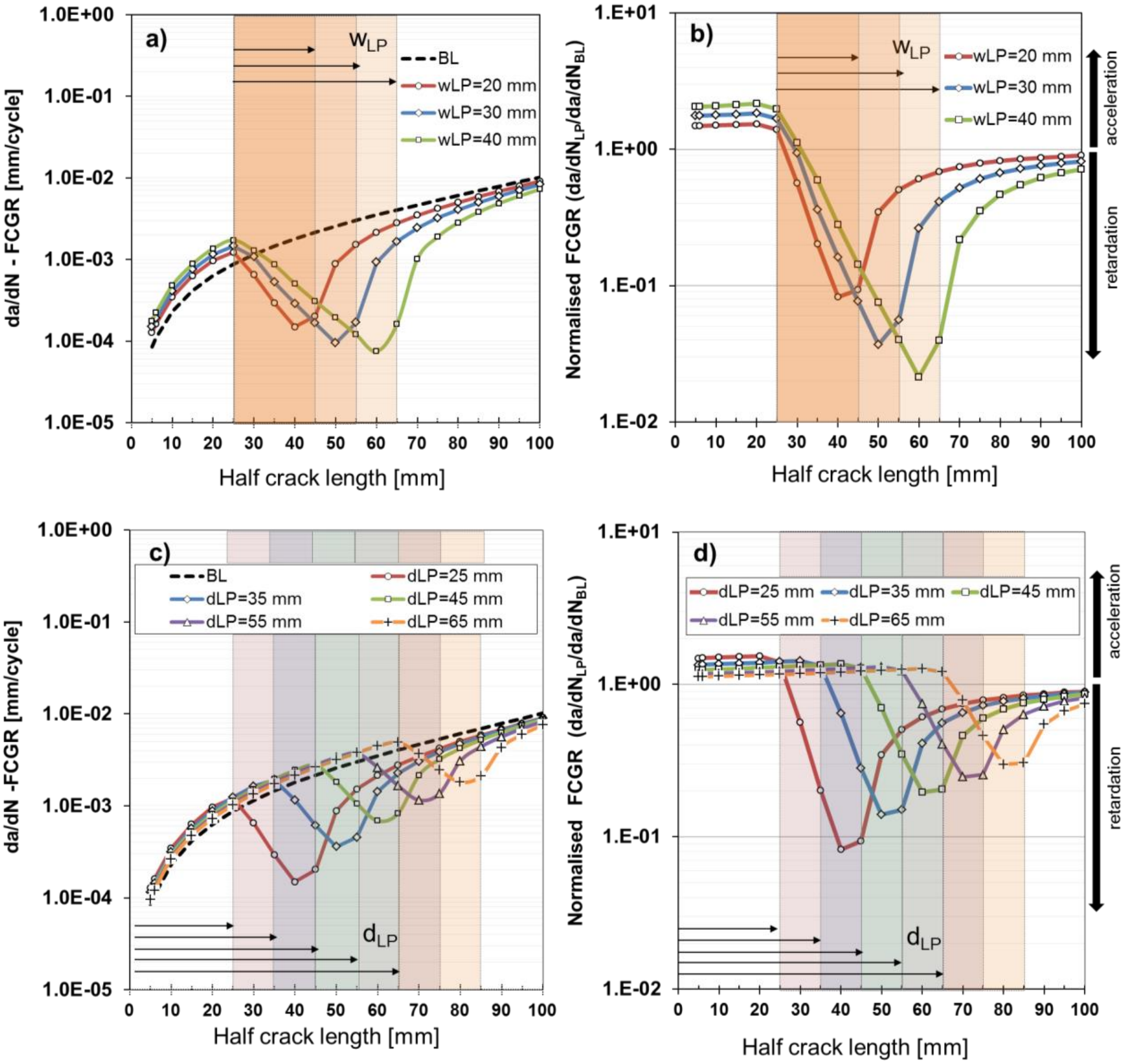

Figure 6-14: FCGR and normalised FCGR prediction for different LP layouts varying the width (w_{LP}) of a single LPS and position of the peening (d_{LP}) stripe of 25 mm and RS of -130 MPa in the LPS and an external maximum applied stress of σ_{max} =90 MPa and nominal R-ratio of 0.1. a) FCGR varying w_{LP}, b) normalised FCGR varying w_{LP}, c) FCGR varying d_{LP} and d) normalised FCGR varying d_{LP}.

For the case of changing positions of an LPS with a constant width of 20 mm, the FCG predictions are given in Figure 6-14c for FCGR and in Figure 6-14d for the normalised FCGR. Five different positions of the peening stripe were investigated corresponding to a distance of the peening stripe to the symmetry line of the CCT-sample of 25 mm (*FE-LP-1-1*), 35 mm

(*FE-LP-1-4*), 45 mm (*FE-LP-1-5*), 55 mm (*FE-LP-1-6*) and 65 mm (*FE-LP-1-7*). Similarly, predicted FCGRs are greater than the BL simulation until the crack length reaches the edge of the LPS. With increasing distance of the peening stripe (d_{LP}), the acceleration decreases moderately, see Figure 6-14d. As soon as the crack propagates into the LPS the FCGR drops down significantly. The retardation in FCG depends on the crack length at which the crack penetrates into the peened area. In Figure 6-14c and d the retardation decreases as to crack length at which the crack is affected by the compressive RS field increases. When again the cases of d_{LP} = 25 mm (*FE-LP-1-1*) and d_{LP} = 65 mm (*FE-LP-1-7*) are compared taking the minimum crack growth rates within the peening stripe into account retardation factors of 0.08 and 0.3 were found by the model. Intermediate cases (*FE-LP-1-5* and *FE-LP-1-6*) produce retardation effects in between those values. The pivot point where the FCGR increases again is 5 mm (one crack increment in the FE model) before the end of the peening stripe for all cases.

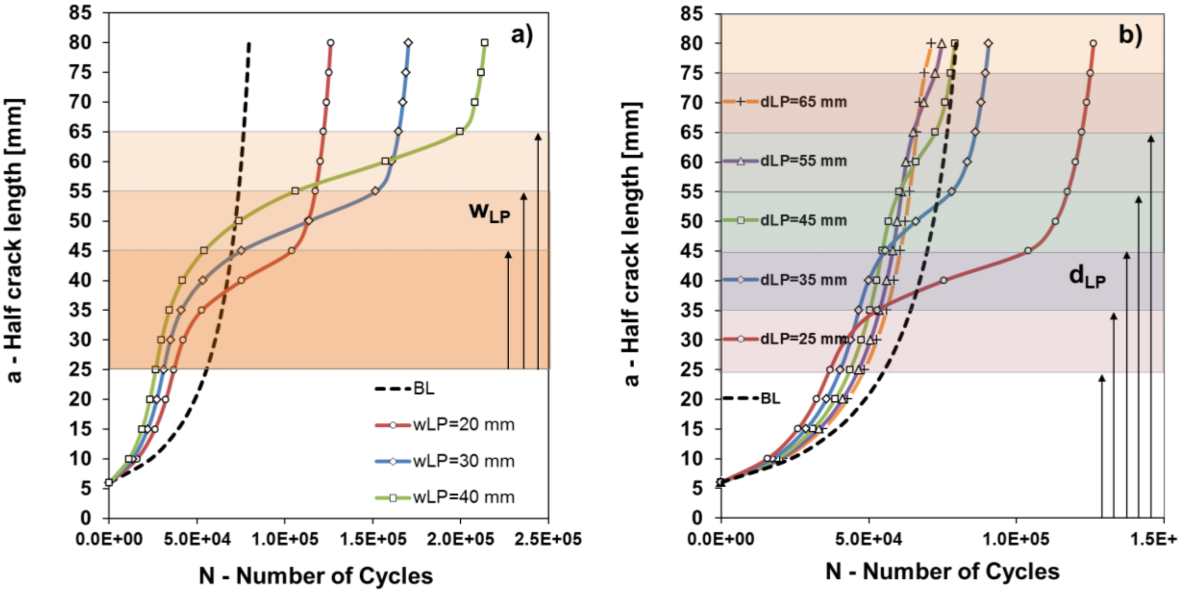

Figure 6-15: Modelling results of crack length (a) vs number of cycles (N) studying different LP layouts varying the width (w_{LP}) of a single LPS and position of the peening (d_{LP}) stripe of 25 mm and RS of -130 MPa in the LPS and an external maximum applied stress of σ_{max} =90 MPa and nominal R-ratio of 0.1. a) crack length (a) vs number of cycles(N) varying w_{LP} and b) crack length (a) vs number of cycles(N) varying d_{LP}.

The acceleration and retardation caused by different sizes and positions of peening stripes changes *a* vs *N* curves, as shown in Figure 6-15a and b. Crack lives *N* (*a* = 80 mm) of CCT-samples with laser-peened stripes positioned at d_{LP} = 25 mm and compressive RSs of σ_{RS} = -130 MPa within the LPS and increasing LPS widths in comparison with BL CCT-samples model results exhibit crack life extensions for all three values of w_{LP} (20 mm, 30 mm and 40 mm) with life increasing with w_{LP}. A w_{LP} of 20 mm, 30 mm and 40 mm result into lives of *N* (*a* = 80 mm) of 126,072 cycles, 170,370 cycles and 213,833 cycles respectively whereas for the BL condition a crack live *N* (*a* = 80 mm) = 79,533 cycles was predicted. Although, the acceleration of FCGR in the region between the initial crack length and the edge of the peening stripe result into a speedy crack growth, the retardation within the peening stripe gives an maximum overall extension of a factor of 2.6.

Different positions of the peening stripe (Figure 6-15b), decrease crack life N (a = 80 mm) with increased d_{LP} even to an extend that for two cases in which the LPS is positioned as far as d_{LP} = 55 mm (*FE-LP-1-6*) and d_{LP} = 65 mm (*FE-LP-1-7*) the crack life become as low as N (a = 80 mm) of 71,281 cycles and 74,826 cycles respectively. This is a reduction of life lower than life for the BL conditions (N (a = 80 mm) = 79,533 cycles). For d_{LP} of 45 mm, N = 79,127 cycles almost the same as the BL life. Only cases in which the crack propagates into the peening stripe at an earlier stage as for d_{LP} = 25 mm (*FE-LP-1-1*) and d_{LP} = 35 mm (*FE-LP-1-4*), crack life increases in comparison with BL results.

6.4.4.2 Crack Growth of Laser-peened CCT-samples with Two LP Stripes

Predicted FCGR versus half crack length (da/dN vs a) and normalised FCGR for FE cases that define two LPSs in the LP layout are shown for *FE-LP-2-5*, *FE-LP-11* and *FE-LP-2-14* to show the influence of the relationship of the first and second LPS on the FCGR and crack lives. Both LPSs had widths of (w_{LP} =) 20 mm and a compressive RS of -130 MPa within the LPSs. In Figure 6-16a and b the position of the first LPS is unchanged at d_{LP} = 15 mm and the position of the second peening (p_{LP}) stripe is varied from p_{LP} = 15 mm (*FE-LP-2-5*) to p_{LP} = 60 mm (*FE-LP-2-11*). Despite the unchanged position of the first LPS, the FCGRs are not equally retarded. In case of the longer p_{LP}, FCGRs are retarded by a maximum factor of 0.07 whereas a shorter p_{LP} results in a maximum retardation of 0.13. Between the LPSs, the FCGR accelerate until the crack grows into the second LPS where it slows down again. The extent of reduction depends on the p_{LP}. With increased p_{LP} the longer crack lengths at which the compressive RS acts on crack, the degree of retardation decreases consequently. A value of p_{LP} = 15 mm generated a maximum retardation in the second LPS of 0.13 and thus remained constant when compared with the preceding LPS. For the longer pitch of p_{LP} = 60 mm only has the potential of retarding the crack by a factor of 0.46.

Figure 6-16c and d show the effect of two LPSs with a constant pitch between them of p_{LP} = 15 mm, varying d_{LP}. As expected, FCGRs are less retarded by the compressive RS field at increased crack lengths with increased values of d_{LP}. Retardation of the FCGR of the first peening stripe are for d_{LP} = 15 mm and d_{LP} = 65 mm are by factors of 0.13 and 0.45 respectively. For the second peening stripe with equal pitch, the crack is retarded by factors of 0.13 and 0.37 for the two cases.

FCGRs were integrated into crack lives from an initial crack length of a_i = 6 mm to a final crack length (a_f =) of 80 mm. Half crack length (a) versus number of cycles (N) derived from FCGRs presented in Figure 6-16a and c are drawn in Figure 6-17a and b. For the cases in which the crack propagates into first peening stripe at a crack length of a = (d_{LP} =) 15 mm, overall crack lives were extended in comparison with the un-peened sample. Nevertheless, the extension differs due to the dissimilar FCGR retardation of the initial LPS depending on the pitch to the second LPS. If a pitch of p_{LP} = 15 mm is applied to the CCT-sample a crack life of $N(a$ = 80 mm) = 113,828 cycles can be achieved. As a result of increasing the pitch to p_{LP} = 60 mm, the crack life increases to $N(a$ = 80 mm) = 141,409 cycles. This is a surprising increase of 24% in crack life, since the crack never propagates into the second peening stripe if p_{LP} = 60 mm so that a total crack length of a = 95 mm must be reached before the second LPS could actually unfold the effect of the compressive RSs on FCGR. Although the crack grows into the second LPS for a shorter pitch of p_{LP} = 15 mm, the retardation which in effect is as strong as the first LPS could not add many cycles as the first peening stripe to the total crack life.

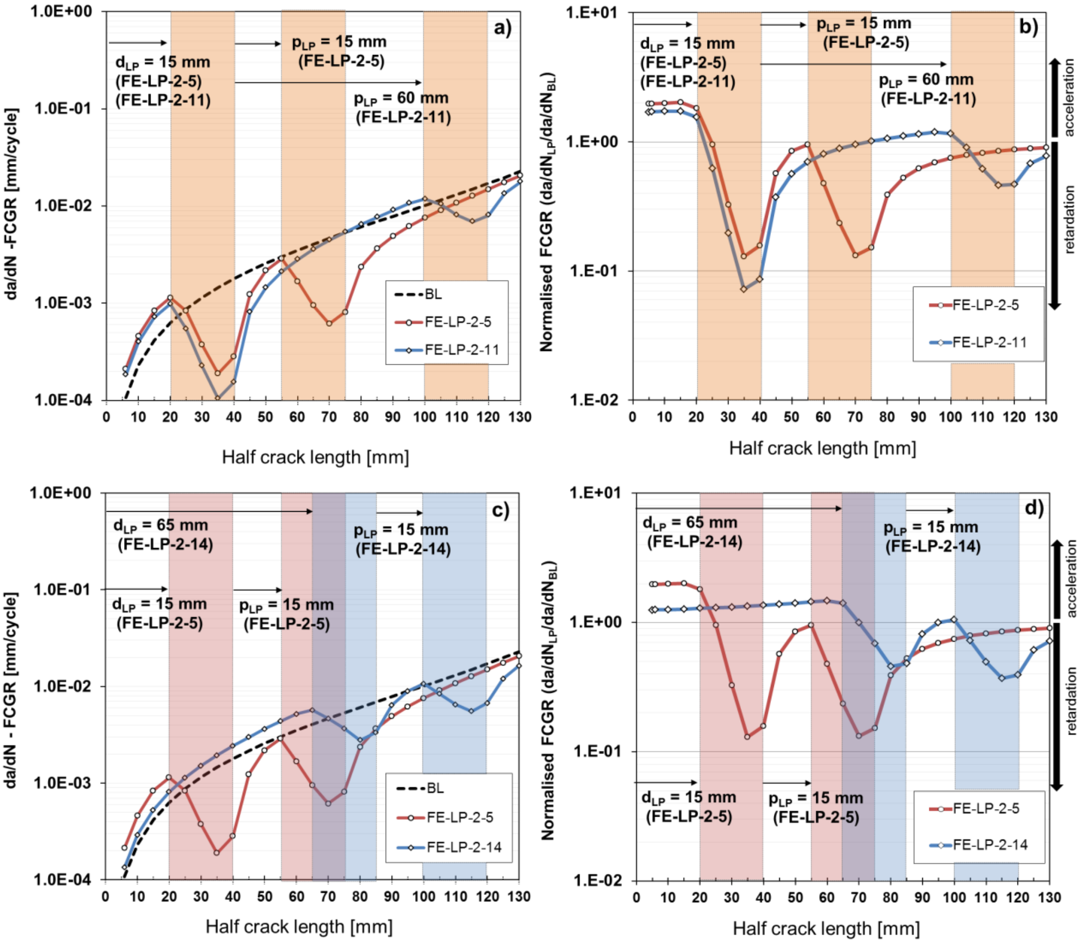

Figure 6-16: FCGR and normalised FCGR prediction for different LP layouts with two LPS varying the position of the first LPS (d_{LP}) and the pitch to the second LPS (p_{LP}) having a constant RS of σ_{RS} = -130 MPa and width of w_{LP} = 20 mm. a) FCGR varying p_{LP}, b) normalised FCGR varying p_{LP}, c) FCGR varying p_{LP} and d) normalised FCGR varying p_{LP}.

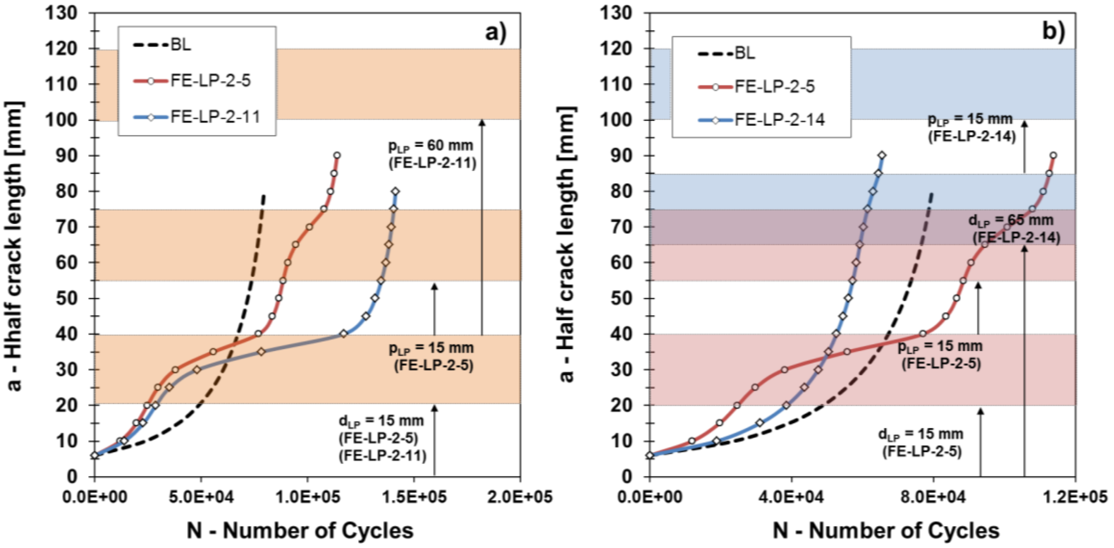

Figure 6-17: Modelling results of crack length (a) vs number of cycles (N) studying different LP layouts with two LPS varying the position of the first LPS (d_{LP}) and the pitch to the second LPS (p_{LP}) having a constant RS of σ_{RS} = -130 MPa and width of w_{LP} = 20 mm. a) crack length (a) vs number of cycles (N) varying p_{LP} and b) crack length (a) vs number of cycles (N) varying p_{LP}.

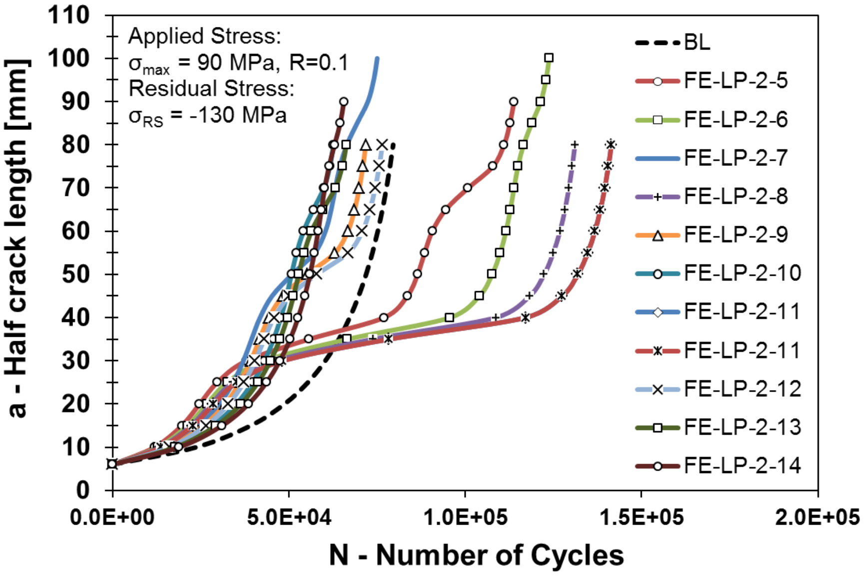

Figure 6-18: Modelling results of crack length (a) vs number of cycles (N) studying different LP layouts with two LPS varying the position of the first LPS (d_{LP}) and the pitch to the second LPS (p_{LP}) having a constant RS of σ_{RS} = -130 MPa, width of w_{LP} = 20 mm and an external maximum applied stress of σ_{max} =90 MPa and nominal R-ratio of 0.1 for all cases as described in Table 6-2.

Comparisons of crack length (*a*) vs number of cycles (*N*) for all cases with two LPSs in accordance to the definition of Table 6-2 are plotted in Figure 6-18. For all cases a compressive RS of -130 MPa and an external applied stress of 90 MPa have been defined. Significant changes in crack growth behaviour can be observed depending on the LP layout. Not all cases could provide a longer crack life than the BL condition. Six cases (*FE-LP-2-7*, *FE-LP-2-9*, *FE-LP-2-10*, *FE-LP-2-12*, *FE-LP-2-13* and *FE-LP-2-14*) in fact decreased the crack life whereas four cases (*FE-LP-2-5*, *FE-LP-2-6*, *FE-LP-2-8* and *FE-LP-2-11*) extended the number of cycles to failure. LP layouts such as *FE-LP-2-5* and *FE-LP-2-11,* as described in detail above, provide life improvement by positioning the first LPS with a short d_{LP} of 20 mm. Then life improvement increased with increasing p_{LP}. Life reductions were caused by positioning the first LPS with a d_{LP} greater than 20 mm. This circumstance indicates the importance of defining the LP strategy in a manner that leads to life improvements.

6.4.5 Crack Growth Results and Effects of Internal and External Loading

FCGR versus half crack length (*da/dN* vs *a*) and normalised FCGR for different compression stress within the LPS and level of externally applied stress are presented in Figure 6-19a to d. Three levels of compressive RS of σ_{RS} =-100 MPa, σ_{RS} = -130 MPa and σ_{RS} = -150 MPa were investigated using the LP layout defined for FE-LP-1-2 (d_{LP} = 25 mm and w_{LP} = 30 mm). The externally applied stress is σ_{app} = 90 MPa for all of those cases (refer to Table 6-4). All three values of stress within the LPS generate retardation of the FCGR and acceleration of the FCGR in the region between the initial crack length and the crack length which coincidence with the d_{LP} (= 25 mm).

Different amount of retardation are produced for different levels of compression (σ_{RS}). The retardation and acceleration is quantified in comparison with BL condition as shown in Figure 6-19b. A compressive RS of (σ_{RS} =) -100 MPa produces maximum retardation by a factor of 0.13, whereas the same LP layout has a factor of 0.01 if a compressive RS of (σ_{RS} =) -150 MPa is induced by LP. A RS of σ_{RS} = -130 MPa results in a retardation by a factor of 0.04.

Varying the externally applied maximum stress σ_{max}, affects the FCGR significantly under a compressive RS of -130 MPa, as presented in Figure 6-19c and d. Maximum retardation of FCGR within the LPS of ~ 0 was calculated for σ_{max} = 60 MPa. For applied stresses σ_{max} = 90 MPa and 120 MPa the retardation within the peened area weakens to maximum factors of 0.04 and 0.14.

Crack lives *N* (*a* = 80 mm), produced by integrating FCGR of Figure 6-19a and b are shown in Figure 6-20a and b for different values of RS and external loading conditions. For increased compressive stresses, predicted crack life increases consequently. A minor increase of crack life in comparison with the BL case of N (*a* = 80 mm) = 101,209 cycles was predicted for RS of (σ_{RS} =) -100 MPa whereas in contrast, a level of compression of σ_{RS} = -150 MPa provided 343,515 cycles. This is a difference of 242,306 cycles or an increase in crack life by a factor of 3.4 if the level of compression is increased by 50 MPa or by a factor of 1.5. A crack which grows in a RS field of σ_{RS} = -150 MPa accumulated *N* (*a* = 80 mm) = 170,370 cycles.

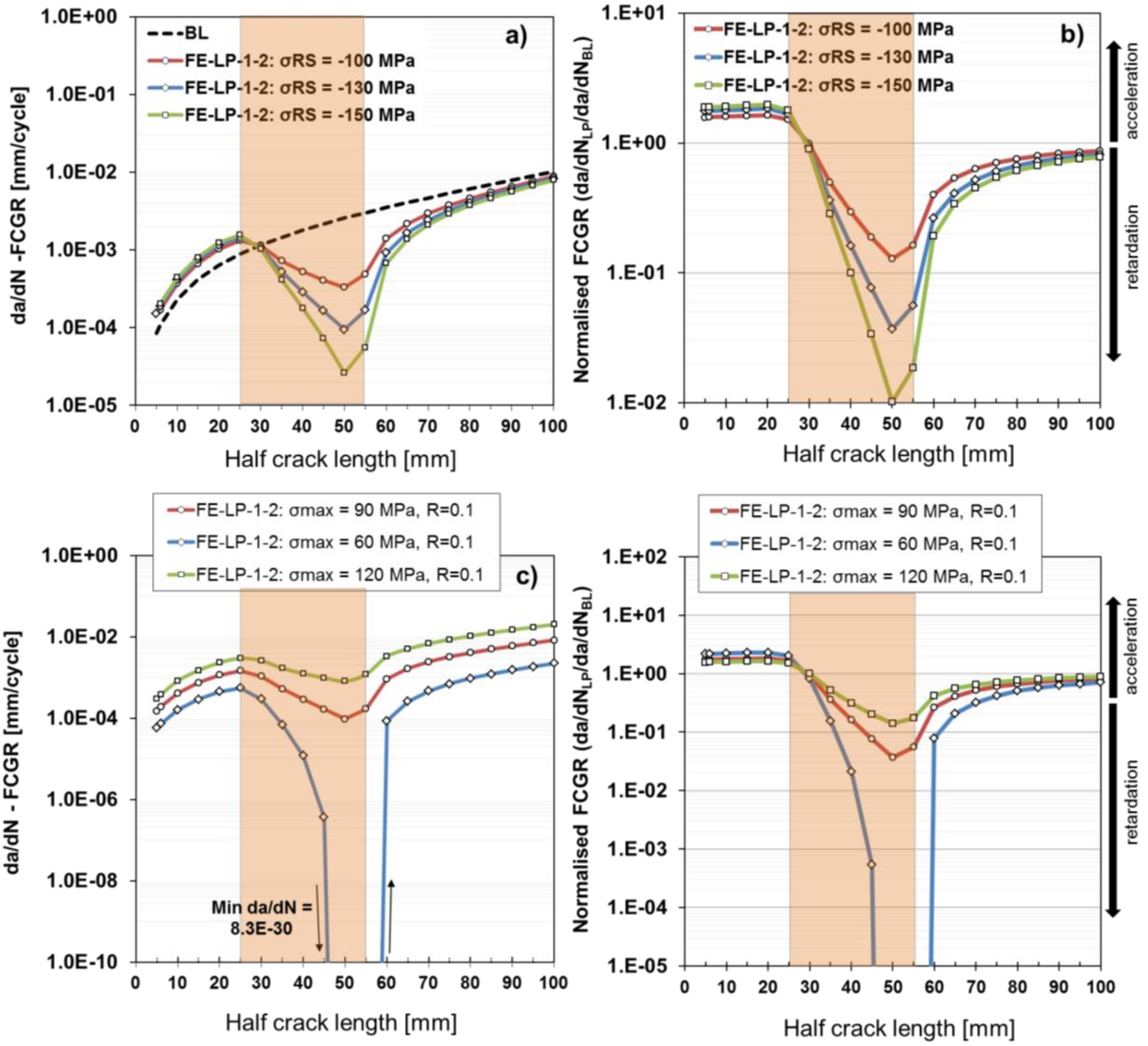

Figure 6-19: FCGR and normalised FCGR prediction for different conditions of internal and external loading under constant width (w_{LP}) of a single LPS of 30 mm and position of the peening (d_{LP}) stripe of 25 mm. a) FCGR varying level of compressive RS of σ_{RS} =-100 MPa, σ_{RS} =-130 MPa and σ_{RS} =-150 MPa under an external maximum applied stress of σ_{max} =90 MPa and nominal R-ratio of 0.1, b) normalised FCGR varying w_{LP} level of compressive RS of σ_{RS} =-100 MPa, σ_{RS} =-130 MPa and σ_{RS} =-150 MPa under an external maximum applied stress of σ_{max} =90 MPa and nominal R-ratio of 0.1, c) FCGR varying level of maximum level of external loading of σ_{max} = 60 MPa, σ_{max} = 90 MPa and σ_{max} = 120 MPa d) normalised FCGR varying level of maximum level of external loading of σ_{max} = 60 MPa, σ_{max} = 90 MPa and σ_{max} = 120 MPa.

As described before the level of externally applied stress can have a striking effect on the FCGR and most importantly on retardation and acceleration of the RS field. This is mirrored in the crack lives. As it can be seen from Figure 6-20b, an externally applied stress condition of σ_{max} = 60 MPa stops the crack with the LPS so that a theoretical crack live of N (a = 80 mm) = 9.7*10^{27} cycles. This is can be considered a run-out with a crack arrest within the LPS. On the other and if the externally applied stress of σ_{max} = 120 MPa, the crack life decreases to N (a = 80 mm) = 43,338 cycles which is a reduction of crack life in comparison the un-peened condition. 90 MPa external applied stress as described before provides a larger crack life on the same RS.

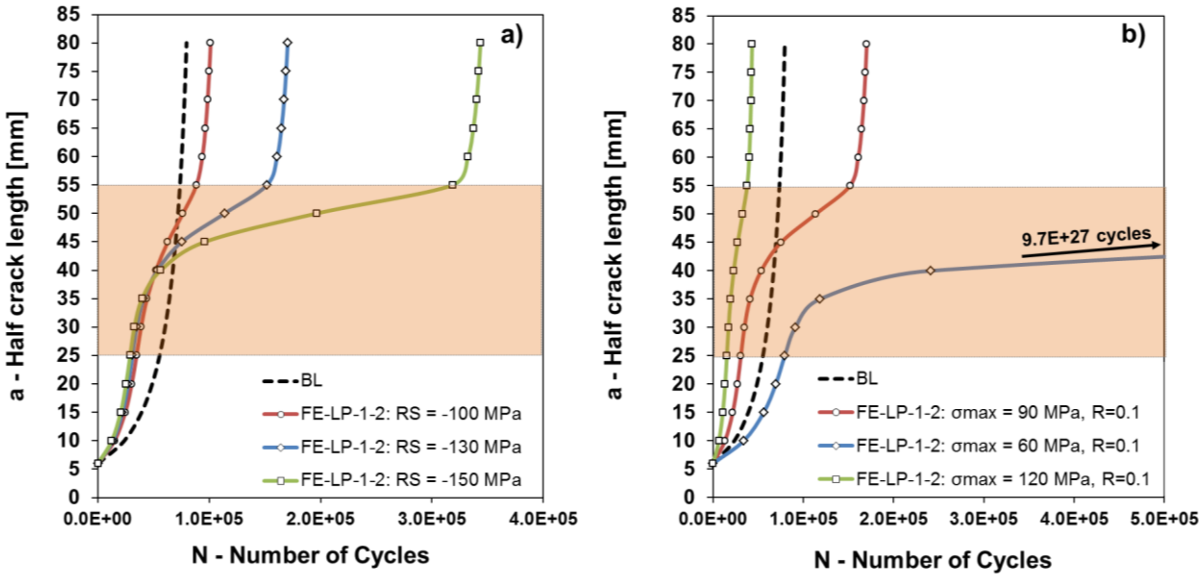

Figure 6-20: Modelling results of crack length (a) vs number of cycles (N) for different conditions of internal and external loading under constant width (w_{LP}) of a single LPS of 30 mm and position of the peening (d_{LP}) stripe of 25 mm. a) crack length (a) vs number of cycles (N) varying level of compressive RS of σ_{RS} =-100 MPa, σ_{RS} =-130 MPa and σ_{RS} =-150 MPa under an external maximum applied stress of σ_{max} =90 MPa and nominal R-ratio of 0.1 and b) crack length (a) vs number of cycles (N) varying level of maximum level of external loading of σ_{max} = 60 MPa, σ_{max} = 90 MPa and σ_{max} = 120 MPa.

6.5 Discussion of Model Predictions

Modelling results will be discussed in the following section. Initially predictions of RS field, FCGR and crack life are compared to experimental results which were presented in chapter 4 and 5 in order to validate and reflect on the accuracy of the modelling approach. After that, the results of the LP design study are discussed in the light of published work and applications to fuselage type structures.

6.5.1 Modelling Result in the Light of Experimental Data

Experimental and numerical results of RS fields and FCGRs have been determined and in order to validate the 2D numerical prediction model, those results will be contrasted with each other. RSs were obtained for CCT-sample, which were laser-peened according to the *2-B* denomination (recall Table 3-5; d_{LP} = 25 mm, w_{LP} = 30 mm, Power Density: 2.5 GW/cm^2, Pulse Density: 750/ 500 spots/ cm^2). In terms of the LP layout, the FE design for *FE-LP-1-2* and *2-B* samples is identical so that they will be used for comparisons.

For 1.6 mm 2524-T3 BL-CCT-samples, the methodology of predicting FCGR proved to produce results which are in very close agreement with respective test results of FCGRs (recall Figure 5-3) and analytical SIF solutions (recall Figure 6-6). For those reasons, the numerical approach using a 2D model and the MVCCT methodology and the Walker material model, as previously developed are accurate modules of the overall modelling approach.

6.5.1.1 Residual Stress Fields – Test vs FEA

For laser-peened CCT-sample, RS fields have been artificially introduced into the FE model (Step1: PI controller process in the modelling approach) before FCGRs were computed (Step 2 and Step 3). It is therefore important to compare not only the output data (FCGRs) of the three step modelling approach but also to compare the model output data (RS fields) after the individual steps, before statements about the results can be made. The understanding of the RS state in the 2-B CCT-sample is limited to the restricted RS data determined by ND, as presented in chapter 4.1.2. It would be preferably to achieve a sharper picture about the RS condition and distribution in laser-peened CCT-samples by performing additional experimental measurement techniques such as synchrotron XRD. However, this is not always possible, as the equipment needed for those techniques are not straightforwardly accessible and material and laser-peening supply resources are limited.

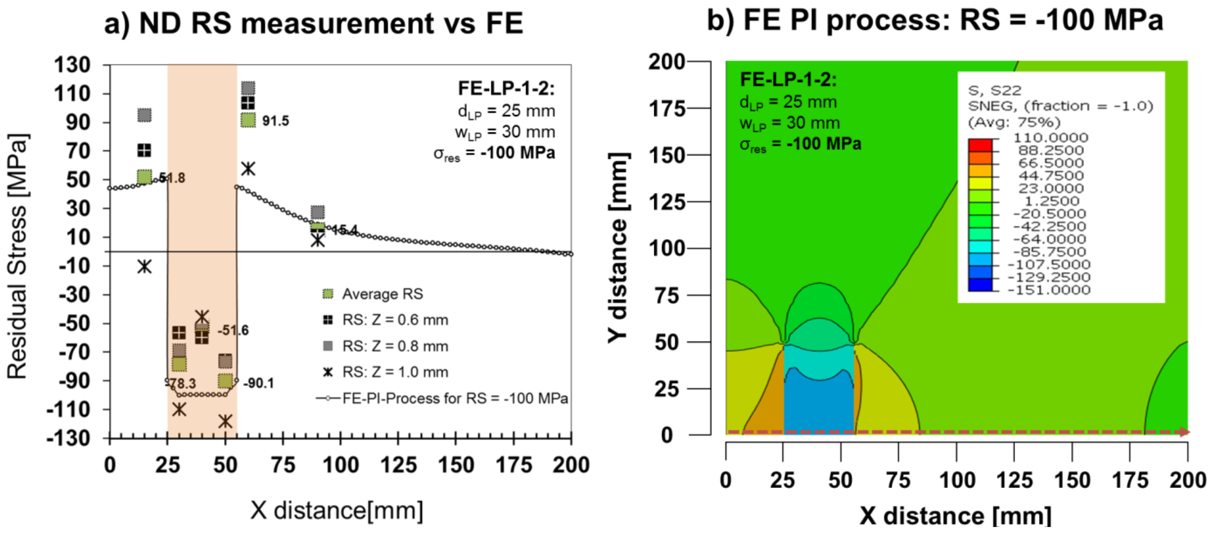

Figure 6-21: Comparison of experimentally measured (*CCT-LP 2-B*) and the numerically computed RS field (*FE-LP-1-2*). a) Comparison test vs FE and b) full longitudinal RS field as computed by FEM.

The ND RS data (which was previously presented in chapter 4.1.2) within the LPS showed variation of RS laterally and through the thickness (see Figure 6-21). The 2D FE model, conversely, is inherently not capable of describing RS distributions across the thickness direction. Therefore, the numerical data is best compared to an average value. For simplification reasons, the lateral distribution of RS within the LPS was not taking into account during the PI controller process, as this was reckoned to be a product of distortions (recall the discussions of chapter 4.3.2) and not of the LP process. Since no initial distortions were enforced on the FE model, this approach seems reasonable. An average through the thickness compressive RS of $\sigma_{RS,yy}$ = -90.1 MPa was calculated taking the three positions of the gauge value (z = 0.6/ 0.8/ 1.0) at the edge of the LPS, where distortions were the smallest. Finally, a constant compressive RS of $\sigma_{RS,yy}$ = -100 MPa (estimation of RS with zero distortion) was used to simulate the conditions in a *CCT-LP 2-B* sample to determine the distribution of tensile RSs.

A comparison of the experimentally measured (*CCT-LP 2-B*) and the numerically computed RS field (*FE-LP-1-2*) is shown in Figure 6-21a. In Figure 6-21b the FE prediction of the complete RS field is shown for the longitudinal stress direction. The RS distribution in Figure 6-21a refers to y = 0 mm as indicated by the red arrow. Recall, the compressive field within the LPS is pre-defined according to the input RS values ($\sigma_{RS,yy}$ = -100 MPa) and the FE algorithm then computes the tensile RS field in order to equalise the overall stress state. A single measurement was taking in the region between the centre line and the LPS at x = 15 mm. Experimental and numerical determined RS show close agreement with each other, if the average value of the ND measurement is considered. For the position of x = 60 mm, so 5 mm after the end of the LPS, the agreement between test data and FE is poor. The FE code significantly underestimates the tensile RS immediately after the LPS. ND measurement further indicates a rapid drop of tensile RS with increasing distance from the LPS in the direction of the sample edge. The trend is confirmed by the FE data and at x = 90 mm, measurements and predictions again come to a close agreement.

The deviations of RS at the position of x = 60 mm, can have a range of different causes. Three main causes were identified:

(1) The superposition of RSs and distortion induced bending stress displayed in the experimental RS data.

(2) Experimental errors in x-direction especially in regions with high stress gradients which arise from the transition from compressive to tensile RSs at the boundaries of the LPS.

(3) The procedure which was followed for the PI controller process. As the algorithm was stopped if the longitudinal RS stress within the LPS show good agreement. The transverse RS component was not taking into account but can have an impact on the outcome on the longitudinal RS direction, if considered during the PI controller process.

6.5.1.2 Fatigue Crack Growth in Laser-peened CCT-samples – Test vs FEA

A comparison of experimental and numerical crack growth data is presented in Figure 6-22. The compressive stress within the LPS are ($\sigma_{RS,yy}$ =) -100 MPa and ($\sigma_{RS,yy}$ =) -130 MPa) presented for the *FE-LP-1-2* case. In Figure 6-22a, the crack growth lives (*a* vs *N*) are compared. The FE prediction of crack growth for both compressive RS levels follows the same qualitative trend than the experimental data. In quantitative terms, the correlation is fair (deviation within 20%). Consequently, the same is observed for the FCGRs and normalised FCGRs, as shown in Figure 6-22b and Figure 6-22c. Overall, the modelling result brings about a shorter crack life for a RS of $\sigma_{RS,yy}$ = -100 MPa and a longer life for a RS of $\sigma_{RS,yy}$ = -130 MPa than the experimental determined result. Since there is limited RS data available for laser-peened CCT-samples, the predictions can be improved by gathering more information about the RS conditions which can be used as input to the PI controller process. Also, the laser-peening process can be directly simulated and after validation it can be exploited to generate realistic RS field to be inserted in the fracture mechanics FE model.

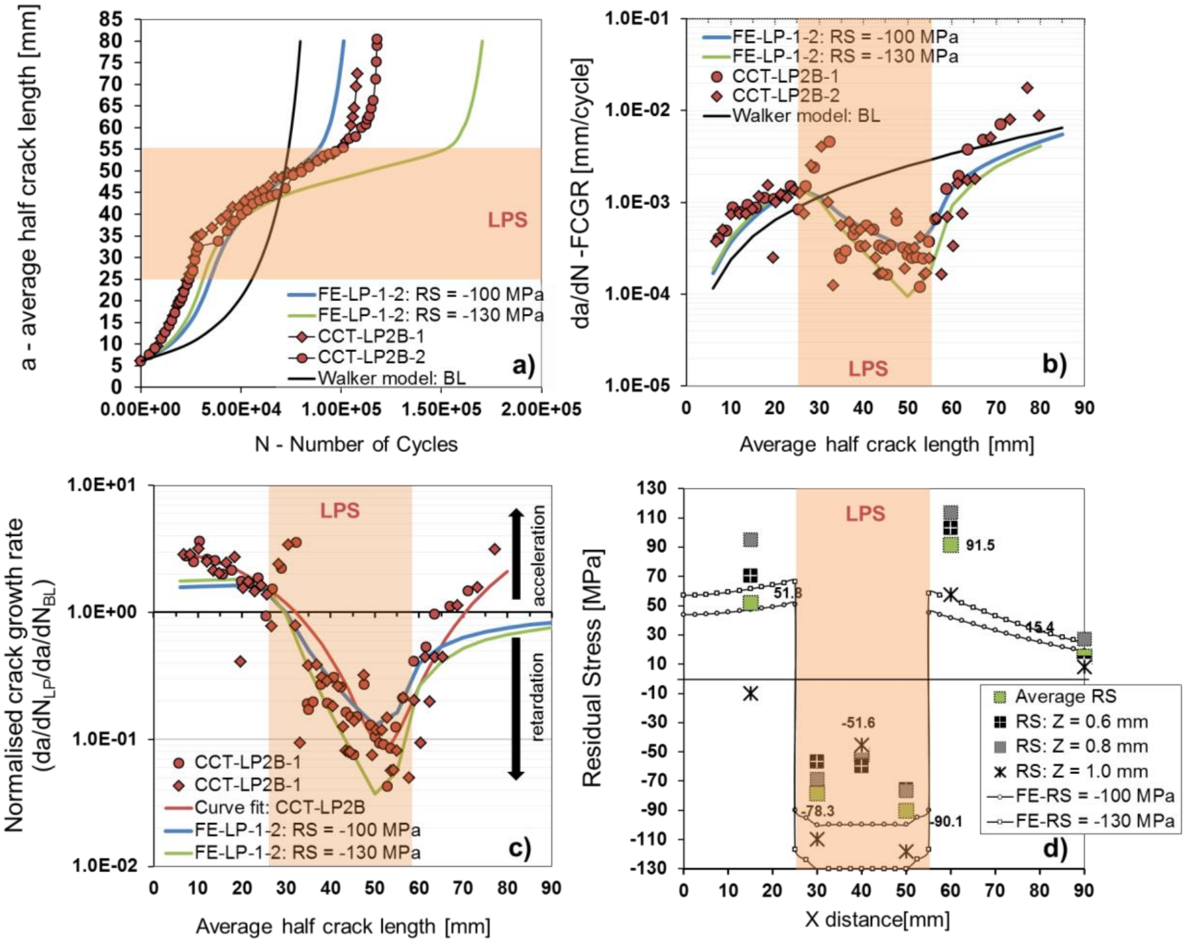

Figure 6-22: Comparison of fatigue crack growth determined by experiment versus predicted by numerical FEM. a) Experiment vs FEM for crack growth life: a vs N, b) Experiment vs FEM for FCGRs: da/dN vs a and c) Experiment vs FEM for normalised FCGR and d) Experiment versus predicted RS field, as discussed in section 6.5.1.1.

The modelling approach which was followed to determine FCGRs in presence of RSs was very similar to the methodology as outlined and applied by D. Schnubel [12,18] who achieved accurate FCG prediction for laser heated aluminium samples (as previously mentioned in chapter 2.3.4). The fracture mechanics part is based on the SIF computation via MVCCT and FCGR calculation using Walker's crack growth law without simulating the plastic wake around the crack tip. The approach to determine ΔK_{eff} and R_{eff} had improvements in comparison to the modelling approaches which were used by many researchers [11,125–127] before which is based on a linear superposition of K_{res} and K_{app}. When negative K values are set to zero in the post-processing step, the method is known as modified superposition. Schnubel [12,18] pointed out the crack flank contact is the physical more sound representation of the condition when a crack travels through a compressive RS field. On the other hand, the contact condition violates the linear principle of superposition so that K_{tot} values must be calculated which increases the computational efforts. Those extra efforts were justified by more accurate prediction achievements. No contact conditions underestimated crack lives by 14% [18,132]. Jones and Dunn [172] who compare the superposition, modified superposition and crack contact methodology came to the same conclusion that defining crack contact in the FE model produces the most accurate results. As mentioned plasticity induced crack closure (PICC) was not included in the model since N. Smyth [173] showed in his thesis that PICC is negligible when analysing crack closure in RS fields. The RS field dominate the closure behaviour in his FEA study. However, as PICC increases with increased crack length and N. Smyth modelled much smaller crack lengths in the range between 50 µm to 300 µm in comparison to the present model, PICC could have more effect.

6.5.2 Effect of the LP layout on Crack Growth and LIF

Modelling FCGR (*da/dN*) and subsequent crack lives (*N*) for different LP layouts (d_{LP}, w_{LP} and number of LPS) and external (σ_{max}) and internal loading (σ_{RS}) conditions clearly showed that all of those investigated parameters can have a significant effect on the performance of a CCT-sample like structure as the fuselage skin field for instance. Judging the fracture mechanics performance of laser-peened structures a Life Improvement Factor (LIF = N_{LP}/N_{BL}) can help as a quantifier of either the beneficial or detrimental effects in terms of overall crack life extension produced by LP.

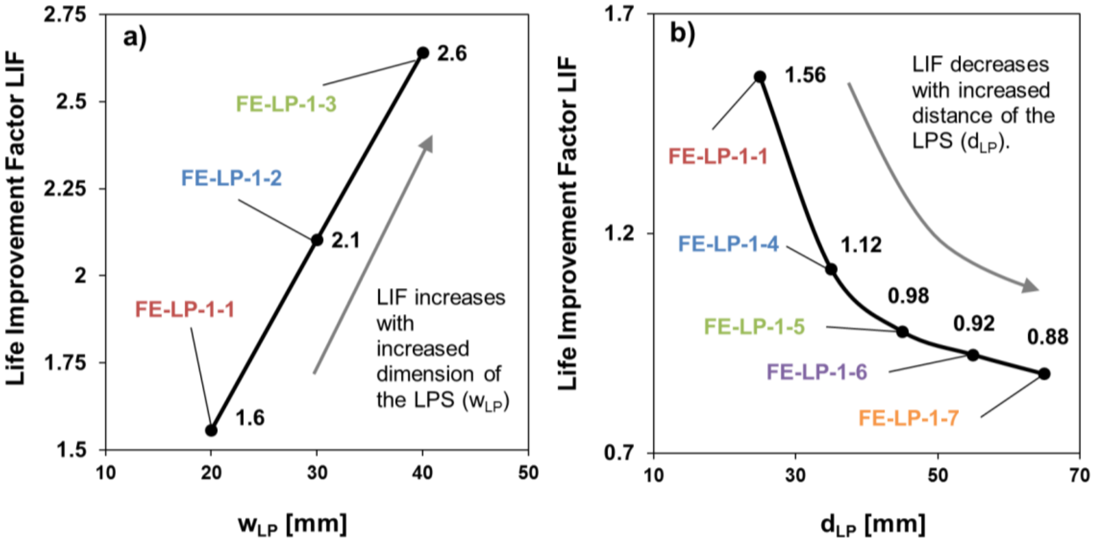

Figure 6-23: Life Improvement Factors for LP layouts with one LPS having a constant compressive RS of σ_{RS} = -130 MPa within the LPS and a maximum applied external stress of σ_{max} = 90 MPa. a) LIF vs w_{LP} and b) LIF vs d_{LP}.

A summary of LIFs is plotted against the investigated parameters which define the LP layout with one LPS in Figure 6-23. As a general note, LIFs between 0.88 – 2.60 were predicted for the set of LP layout parameters, RS and external load conditions chosen here. This means crack growth performance could be decreased by a factor 0.88 or increased by a factor of 2.6 merely by the spatial definition of the pre-defined laser-peened area on the CCT-sample.

- In Figure 6-23 a) LIF results of the investigated dimension of the LPS (w_{LP}) are shown. It is clearly seen from the plot that by increasing the w_{LP} the crack life extension can also be linearly proportionally enlarged. Increasing the w_{LP} by a factor of 2 will increase the LIF by a factor of 1.6.
- In Figure 6-23 b) LIFs are shown for different positions of the LPS (d_{LP}) in relation to the crack length and the data draws a striking picture that with increasing d_{LP} and consequently increased crack length when the crack is propagating into a compressive RS field the beneficial effect decreases. For this study, the results also show that detrimental effects on the crack growth performance in terms of life (N) can be expected if a 20 mm wide LPS is placed at a distance of $d_{LP} > 45$ mm.

S. Taddia and E. Troiani [27] found the same trends for a comparable laser-peened test sample (2024-T3, t = 2.0 mm, W = 160 mm, L = 400 mm), that the life improvement decreases or increases when a LPS is placed with a short or longer distance (d_{LP}) to the initial crack length. Also, as discussed above, their research presented numerically derived results, which confirm the above results, that increasing width of LPSs (w_{LP}), the life improvements increase consequently. Detrimental effect were likewise confirmed when the d_{LP} exceeds a certain value. A detailed analysis on the reasons for those observed trends were not presented.

Following this lack of explanation, experimental observations and the prediction of FCGRs as calculated by this modelling approach can be utilised. The model exhibits acceleration and retardation correlating with tensile and compressive RSs according to the discussions in section 6.4.3. These observations are needed to understand the impact of the LP layout on the crack growth performances. The FE study found that the LP layout has a significant impact on the overall life. All of the investigated LP layouts had a range of tensile RS fields outside the LPS. Consequently, propagating cracks are subjected to tensile and compressive stresses for a different amount of length and at different stages of the crack life (ΔK, a). This ultimately determines the overall crack growth life.

For a distance of the LPS of d_{LP} = 25 mm and increased widths of LPSs (w_{LP} = 20 mm, 30 mm, 40 mm), the tensile RS between the initial crack length and the LPS (x = 0 mm to d_{LP} = 25 mm) increased (refer to Figure 6-11). Consequently, the acceleration of the FCGR was predicted to result in different degrees which caused shorter crack lives in that region of tensile stresses (a = 6 mm to $a = d_{LP}$ = 25 mm). The adjacent region of compressive RSs within the LPS changed that trend, and slowed down cracks. With increasing widths of LPSs, fatigue cracks were subjected to compressive RSs for a longer growth period. Besides with longer propagation through compressive RSs, the retardation effect increased, which in combination resulted in the accumulation of a significantly large number of load cycles within the LPS. This outcome eventually produced crack life improvements.

Although tensile RSs accelerated FCGRs and caused a shorter crack life in the early stage of the crack (a = 6 mm to a = d_{LP} = 25 mm), in comparison to the BL sample, an overall life improvement is predicted due to the retardation within the LPS. With increasing distance of the LPS (d_{LP}) from the crack start, the overall ratio of detrimental effects caused by the tensile RS field to the beneficial effects produced by compressive stresses was altered. For a (w_{LP} =) 20 mm wide LPS, the LIF decreased (refer to Figure 6-23) when the position of the peening stripe was shifted away from the initial crack length (d_{LP} = 25 mm, 35 mm, 45 mm, 55 mm, 65 mm). The reduced LIF eventually become less than one if d_{LP} is sufficiently increased. Although the level of tensile RSs and in consequence FCGR decreased slightly for increasing d_{LP} values, the distance the crack propagated under reduced tensile RS increased. A substantial portion of the crack life is lost at that stage and cannot be recovered by a weaker retardation of FCGR for increased d_{LP} values. With increasing d_{LP} and consequently increasing crack length, the applied $K_{\mathrm{app},max}$ and $K_{\mathrm{app},min}$ values increases but the K_{res} values reduces due to elastic redistribution of the RS field [107,173] as the crack propagates through the samples. This decreases the significance of the K_{res} in the calculation of ΔK_{eff} as it can be seen by:

$$\Delta K_{eff} = (K_{res} + K_{app,max}) - (K_{res} + K_{app,min})$$

Although the FE model calculated K_{tot} values and the approach is different to the formula above which represents linear superposition, the concept describes the mechanics of decreasing influence of the compressive RS field with increasing crack lengths.

For the case of a LP layout with two sequential LPS, a contour map of LIF is shown in Figure 6-24 in which the distance to the first LPS (d_{LP}) and the pitch (separation of) (p_{LP}) from the first to the second peening stripe is put into relationship with resulting LIFs. When two LPS were designed onto the CCT-sample, LIF would increase and become maximal if the d_{LP} is minimal and the p_{LP} is maximised. A shorter pitch between peening stripes would decrease the crack life. If the distance to the first peening (d_{LP}) stripe exceeds 32 mm, detrimental effects on crack life would be predicted so that shorter lives than the un-peened BL conditions were possible.

The most beneficial LP layout design with two LPSs is when firstly the initial LPS is placed with a small distance to the initial crack length following the explanations for a single LPS and secondly when the pitch (p_{LP}) between the two LPS is maximised. There are two reasons for this trend. As mentioned the retardation of FCGRs drops down with increasing crack length at which a crack penetrates into a LPS. In this line, a large p_{LP} will give the LPS a larger crack length. Also, minimising the pitch (p_{LP}) will increase the tensile RS (recall section 6.4.2) in the region between the initial crack length and the edge of the first peening stripe producing higher accelerations in that region and thus a loss of crack life. It can be concluded that the second peening stripe in general has a detrimental effect on the crack growth behaviour. A single LPS with equal dimension and location will result in more life improvement than any solution which places an additional LPS on the CCT-sample as the second LPS increases the initial tensile RS field and consequently the acceleration.

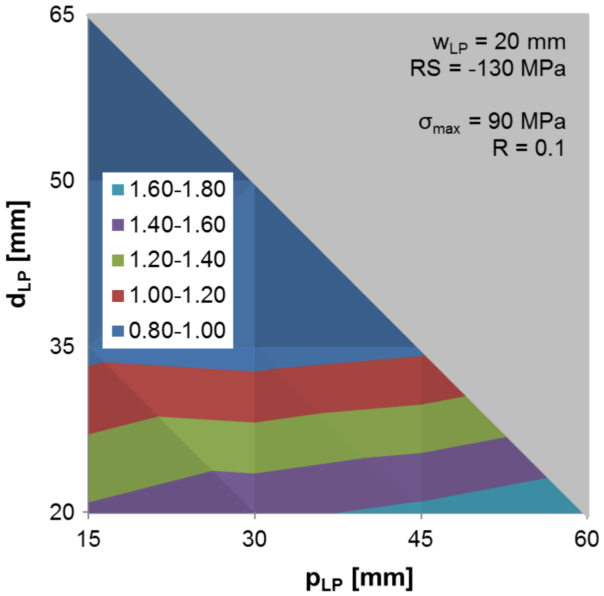

Figure 6-24: Life Improvement Factors for LP layouts with two LPSs having a constant compressive RS of σ_{RS} = -130 MPa within the two (w_{LP} =) 20 mm wide LPS and a maximum applied external stress of σ_{max} = 90 MPa.

6.5.3 Effect of Level Compression and of External Applied Loading on Crack Growth and LIF

In Figure 6-25a, LIF is plotted against different levels of compressive RS within the LPS. It can be noticed if the compressive RS is increased from σ_{RS} = -100 MPa to σ_{RS} = -150 MPa, the LIF increases from 1.2 to 4.2; a 50% increase in compressive RS will provide a 250% increase in crack growth life. Other researchers [89,92] also correlated more intense compressive RSs with larger crack retardation effects. Those results were experimentally determined which provided them the chance to directly correlate LP process parameter such a pulse density with FCGRs. In the present work, this causality was not possible to present, as the LP process was not simulated and the RS field was introduced via the model. The sensitivity of the fatigue crack growth life depending on the level of compressive RSs within the LPS has been shown to be significant. S. Taddia and E. Troiani [27] confirm this finding with their FE prediction. In order to qualify LP for the aerospace industry and integrate laser-peened induced RSs in the design of airframe structures, the variability of the RS field as a result of the LP process needs more attention in future academic research.

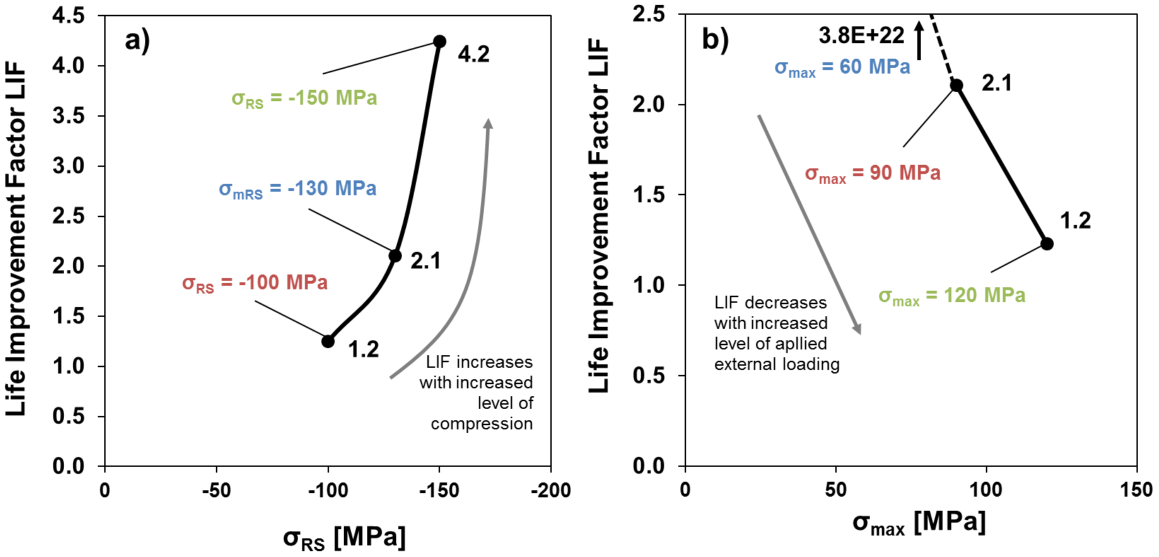

Figure 6-25: Life Improvement Factors for different RS and external load conditions with a constant LP layout with one LPS (d_{LP} = 25 mm and w_{LP} = 30 mm). a) LIF vs σ_{RS} and b) LIF vs σ_{max}.

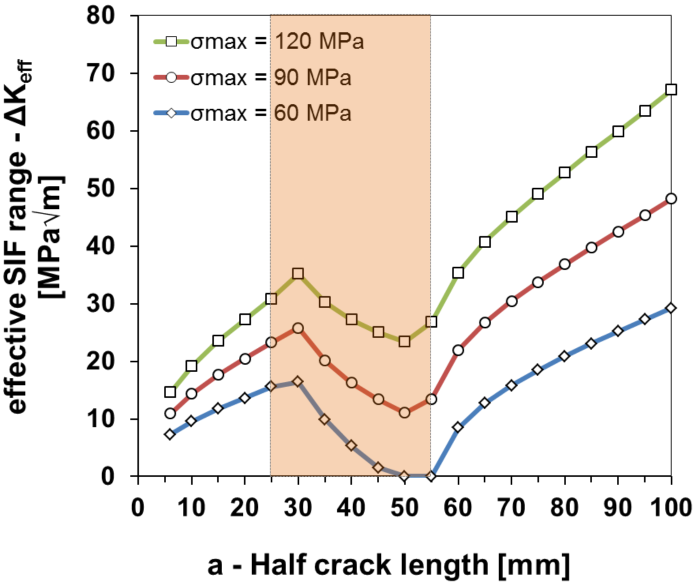

Figure 6-26: Effective SIF range (*ΔK_{eff}*) versus half crack length for different external load conditions with a constant LP layout with one LPS (d_{LP} = 25 mm and w_{LP} = 30 mm).

External applied load levels were also noticed to have a large influence on the crack growth improvements of laser-peened CCT-samples. As shown in Figure 6-25b, LIFs for applied nominal stresses of σ_{max} = 120 MPa and σ_{max} = 90 MPa result in (LIF =) 1.2 and (LIF =) 2.1 respectively. It means that a 33% increase of external loading will result in a 75% reduction in beneficial crack life improvements. However, it seems that there is a threshold cutting the lower limit of external applied loads in the sense that crack growth is not occurring within a LPS if the external load does not reach a certain level. Taking 60 MPa as that threshold level for instance, it must relate to the RS field. In this case, σ_{max} = 60 MPa and σ_{RS} = -130 MPa would result into a ratio of (60/-130=) -0.46. As it can be seen from Figure 6-25b, a σ_{max} = 60 MPa result into a theoretical LIF of $3.8*10^{22}$. In actual fact, the crack was stopped by the LPS. In Figure 6-26 the effective SIF range (ΔK_{eff}) is presented for all three levels of external applied maximum stress and it can be seen that ΔK_{eff} values for σ_{max} = 60 MPa become zero in the LPS which indicates that no crack growth is the results. For σ_{max} = 120 MPa and σ_{max} = 90 MPa ΔK_{eff} decreases within the LPS but it remained in a range between 11 – 24 MPa√m so that crack growth still occurred and could be stopped.

6.6 Conclusions

The following conclusion can be drawn from the model predictions of crack growth in laser-peened AA 2524-T3 1.6 mm CCT-samples:

- The 2D modelling approach provides predictions of FCGRs in laser-peened induced RS fields which exhibit accurate agreement with experimental test samples.
- The effects of the LP layout on the crack growth performance revealed that when designing an application of LP for fuselage skin structures, attention must be paid also on the tensile RS field besides the compression within a LPS to prevent detrimental consequences and find an optimised LP treatment.
- The optimised peening condition was found experimentally, when a LPS was peened on an initial crack length of (a_i =) 6 mm. Numerical results further concluded that with increasing the distance of a LPS (d_{LP}) to the initial crack length, detrimental effects on the improvements of crack growth lives are produced due to tensile RSs. Increasing the distance from d_{LP} = 25 mm to 65 mm will decrease improvements from LIF = 1.56 to 0.88 when the width of the LP is (w_{LP} =) 20 mm, the RS within the LPS is (σ_{RS} =) -130 MPa and an external maximum stress of (σ_{max} =) 90 MPa is applied. This reduction of LIFs is non-linear.
- Increasing the width of LPSs (w_{LP}) is an effective way to increase the beneficial effects of LP treatments. Increasing the width of LPS from w_{LP} = 20 to 40 for d_{LP} = 25 mm, σ_{RS} = -130 MPa and σ_{max} = 90 MPa, the LIF increased linearly from 1.6 to 2.6.
- The level of compressive RS within a LPS can have a very strong effect (non-linear) on the life improvements. Small amount of changes in compressive RS (± 20-30 MPa) can significantly affect the retardation effect within a LPS and result in different factors of improvement. An increase in compressive RS from -100 MPa

to -130 MPa will increase the LIF from 1.2 to 2.1. This indicates the importance of accurate knowledge of the RS state and its variability caused by the LP process to achieve accurate prediction results.

- External load levels in relation to the compressive RSs also determine the effectiveness of LP treatments. Therefore, it needs attention when designing a laser-peened structure. The ratio between external applied stress and RS (σ_{max} /σ_{RS}) seem to be the determining factor.

7 Fatigue of Laser-Peened Fastened Lap-Joints

This section will describe the experimental fatigue and fracture analyses of laser-peened LJ samples. LJ sheets were laser-peened as described in section 3.1.3 and the subsequent RSs were characterised in chapter 4.2. Finally, the fatigue and fracture results will be discussed in the light of the RS results in order to understand the effect of LP on fatigue and fracture of LJ samples.

7.1 Secondary Bending Stresses

Strain gauge measurement results according to the location on a LJ sample as specified in Figure 3-30 are given in Table 7-1. From the data, secondary bending effect, as described in section 2.2.2.2, can be analysed. Despite the measures taken during the LJ sample design (symmetrical design) to reduce secondary bending, it can be concluded from the strain gauge measurements that not insignificant secondary bending effects occurred during fatigue cycling of LJ samples.

Table 7-1: Strain gauge measurement results.

SG	Nominal applied max. tensile stress $\sigma_{applied}$ [MPa]	SG measured max. stress σ_{SG} [MPa]	Bending stress ($\sigma_{SG} - \sigma_{applied}$) σ_{Bend} [MPa]	Bending factor $k = \sigma_{Bend}/\sigma_{applied}$
1	***110***	***151***	***41***	***0.37***
2	110	48	-62	-0.56
3	110	37	-73	-0.66
4	***110***	***160***	***50***	***0.45***
5	110	22	-88	-0.8
6	110	19	-91	-0.83
7	110	15	-95	-0.86
8	110	11	-99	-0.9

As proposed by J. Schijve *et al.* [61] a bending factor *k* can be defined in order to characterise the amount of secondary bending as the ratio of bending stress (σ_{Bend}) and the tensile stress (here nominal applied tensile stress: $\sigma_{applied}$). The bending stress can be derived from the strain gauge measurements which reflect the total acting stress (tensile + bending) and the nominal tensile stress by subtracting the nominal tensile stress from the total stress.

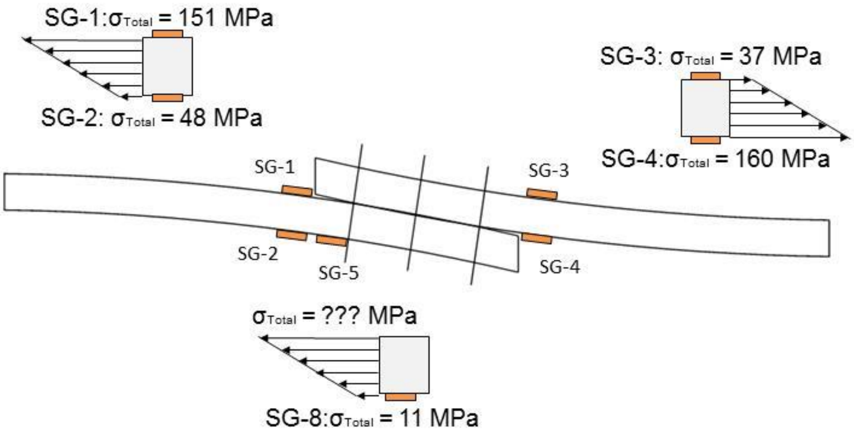

Figure 7-1: Illustration of strain gauge position and corresponding measurement results.

The trend that the secondary bending influence will decrease in longitudinal direction from the fastener row in the direction towards the free end, as predicted by J. Schijve *et al.* [61] neutral line model, is confirmed by the bending factor k from the data in Table 7-1 SG-1 to SG-4 positioned 12.5 mm remote from the fastener centre line where maximal secondary bending can be assumed under the simple assumption of the neutral line model exhibiting k values of 0.37 to 0.45 for the faying surface (in tension) and -0.56 to -0.66 for the free surface (in compression). In contrast SGs which are located nearer to the fastener centre row axis show higher bending factors of -0.8 to -0.9. Only the free surface could be measured at this position as the faying surface is hidden behind the sheet. In Figure 7-1 the secondary bending situation is summarised in an illustration showing the SG measurement results at their positions. As mentioned, no SG measurement could be taken at the near vicinity of the fastener hole on the faying surface but assuming that the bending factor k increases at the same rate from SG-1 to the unknown positon as marked in Figure 7-1 as it did from SG-2 to SG-8 for instance a bending factor of 0.6 and a total stress of 176 MPa could be estimated. Comparing 176 MPa against the nominal applied stress of 110 MPa, it can be grasped that secondary bending after all contributes to the local stress field under which fatigue damage will occur during testing.

7.2 Fatigue Test Data

Fatigue test data for the laser-peened and un-peened BL LJ samples are presented in the following section which is divided in two parts. Initially the effects of the different LP strategies on the fatigue performance are compared. Then the effect of different load levels on the fatigue and scatter will be contrasted on the basis of strategy-B samples only.

The fatigue performance will be assessed by defining a Life Improvement Factor (LIF) which is defined by equation 7.1:

$$LIF = \frac{N_{LP}}{N_{BL}} \; (Equation\ 7.1)$$

in which N_{LP} is the number of load cycles to failure of laser-peened LJ samples and N_{BL} is the equivalent for BL samples.

7.2.1 Fatigue Lives and LP Layout

Fatigue lives of *LJ-BL-1* to *LJ-BL-3*, *LJ-S-A-1* and *LJ-S-A-2*, *LJ-P-A-1* and *LJ-P-A-2*, and *LJ-S-B-1* to and *LJ-S-B-3* and *LJ-P-B-1* to *LJ-P-B-3* (refer to test matrix of Table 3-13) are presented in Figure 7-2 comparing the fatigue performance of BL LJ samples with LJ samples laser-peened using the strategies as defined in chapter 3.1.3. The obtained fatigue lives demonstrate that different LP strategies cause different degrees of life extension when compared to the BL fatigue lives. *P-B* LJ samples showed largest fatigue life with a maximum fatigue life in one sample of (N =) 911,714 cycles. In order to compare all results each data bar in Figure 7-3 represents the arithmetic mean of the fatigue lives obtained.

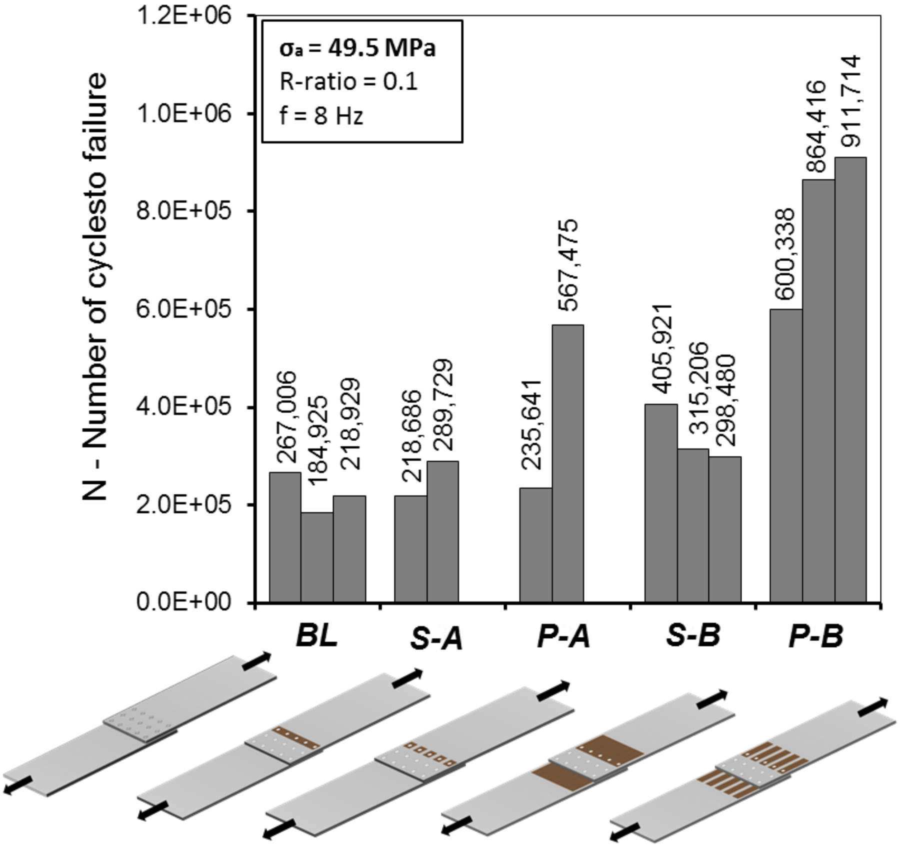

Figure 7-2: Obtained total fatigue lives of BL and laser-peened samples tested under tension-tension (R = 0.1) cyclic loading applying a stress amplitude of 49.5 MPa and a frequency of 8 Hz.

It can be seen that all LP strategies were able to give improvements in fatigue life. The extent of improvement depended on the LP strategy. Improvements can be quantified by using LIF calculated according equation 7.1.

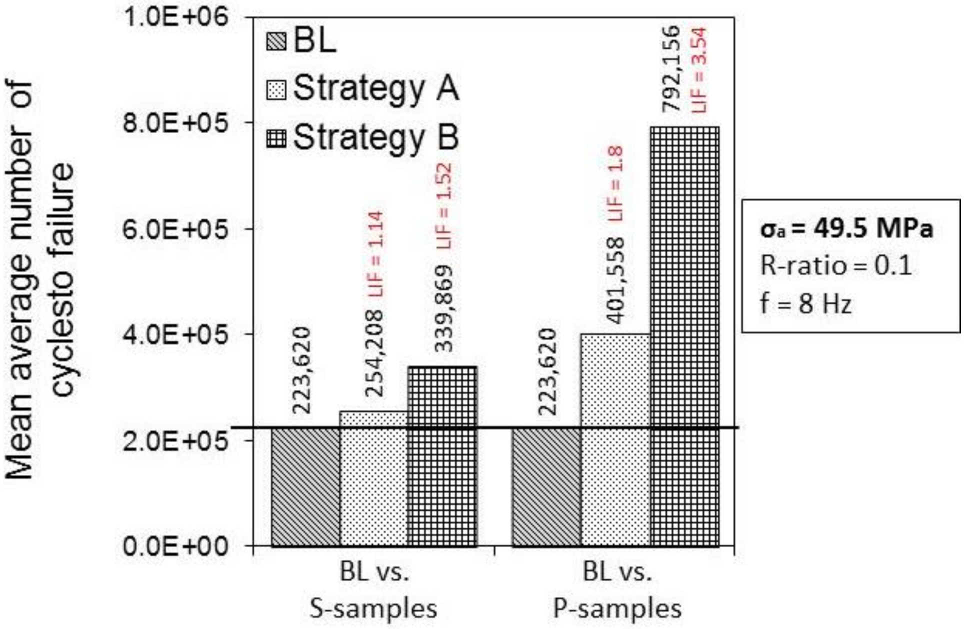

Figure 7-3: Comparison of fatigue life results of laser-peened and BL LJ samples tested under tension-tension (R = 0.1) cyclic loading applying a stress amplitude of 49.5 MPa and a frequency of 8 Hz.

P-samples in *strategy-A* (LIF = 1.80) and *B* (LIF = 3.54) condition showed superiority of effectiveness in improving fatigue performance of LJ when compared to *S-samples* which arguably could not significantly improve fatigue in *strategy-A* condition (LIF = 1.14) but were able to offer some improvement in *strategy-B* layout (LIF = 1.52).

For comparisons of *strategy-A* versus *strategy-B* for each *S*-and *P-sample*, it can be concluded that the *B* strategy is more effective in improving the fatigue performance than the *A* strategy for both *S*-and *P-LP layouts*. In fact, for *P-layout* the improvements from Strategy-*A* to *B* (97%) are greater than it is the case for *S-layouts* (34%).

7.2.2 Fatigue Lives at Different Load Amplitudes and Analysis of Scatter

Fatigue lives for *strategy-B* and *BL* LJ samples are plotted in Figure 7-4 for two different load levels. In Figure 7-4a, the results of three replicate LJ samples tested at a stress amplitude of σ_a = 49.5 MPa (σ_{max} = 110 MPa) are shown. Those results were already described and compared to *strategy-A* samples in the previous section. However in addition, fatigue test results of LJ samples tested at a stress amplitude of σ_a = 72.0 MPa (σ_{max} = 160 MPa) are complemented in Figure 7-4b, so that the effects of different load amplitudes (load levels) can be compared.

As expected the *BL* fatigue life decreases with increasing stress amplitude from (N =) 223,620 cycles to (N =) 79,257 cycles. On an absolute consideration, an equivalent trend is observed for LJ-*S-B* and *LJ-P-B* samples which fractured at a decreased accumulated load cycles of (N =) 124,746 and (N =) 150,061 compared with initial load cycles of (N =) 339,869 and (N =) 792,156 respectively. Analysing the effectiveness of LP on the two defined load levels, the LIF is plotted for *LJ-S-B* and *LJ-P-B* samples in Figure 7-5. From the LIF plots, it can be abstracted that for *P-samples* the overall superior effectiveness (LIF) dropped down to 1.89 from value of 3.54 indicating detrimental effects of increased nominal external loads on the benefits of laser-peened LJ samples. However, for *S-samples* (LIF [σ_a = 49.5 MPa] = 1.52 and LIF [σ_a = 72.0 MPa] = 1.57), a contradicting trend was observed since the LIF value remained on the same level.

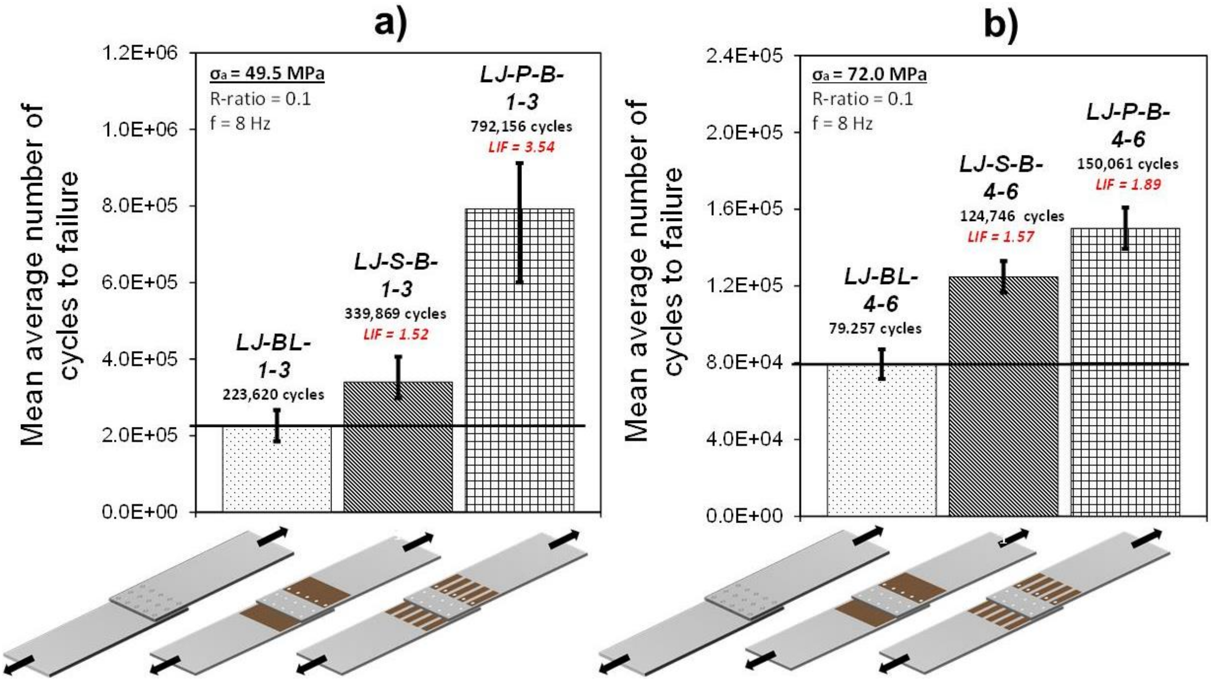

Figure 7-4: Data plots of fatigue life results of BL and LP strategy-B LJ samples for two different load amplitudes (load levels). a) Stress amplitude of σ_a = 49.5 MPa (σ_{max} = 110 MPa) and b) Stress amplitude of σ_a = 72.0 MPa (σ_{max} = 160 MPa).

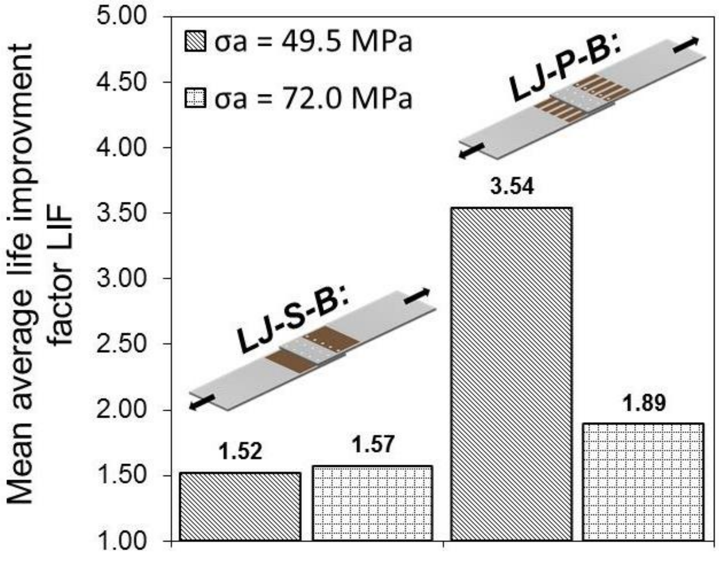

Figure 7-5: Data plots of LIF for *LJ-S-B* and *LJ-P-B* sample for stress amplitudes of σ_a = 49.5 MPa (σ_{max} = 110 MPa) and σ_a = 72.0 MPa (σ_{max} = 160 MPa).

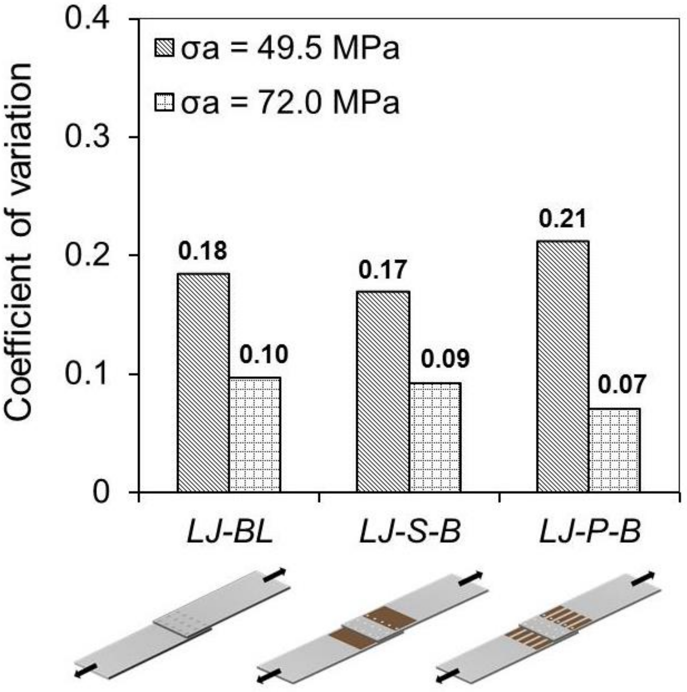

Figure 7-6: Data plots of coefficient of variation for *BL* and *strategy-B* LJ samples.

In order to determine the effect of LP on the scatter of fatigue test results originated in the stability and consistency of the LP process, statistical analysis were conducted using the coefficient of variation as defined as:

$$\widehat{C_V} = \frac{s}{\tilde{x}} \; (Equation\ 7.2)$$

in which $\widehat{C_V}$ is the coefficient of variation, *s* the standard deviation and $\tilde{x}$ the mean average value. Consequent results of $\widehat{C_V}$ values are plotted in Figure 7-6 for *LJ-BL* and *strategy-B* LJ samples (*LJ-S-B* and *LJ-P-B*). The statistical data obtained indicate that no effect of LP on the scatter for both stress levels under investigation as BL values of the coefficient of variation of 0.18 and 0.1 translate into 0.17 and 0.09 for *S-samples* and 0.21 and 0.07 for *P-samples* for stress amplitude of σ_a = 49.5 MPa and σ_a = 72.0 MPa respectively. As expected from published textbooks [32], in general, fatigue life scatter is lower at higher load levels than at lower loads. This is independent of LP and could have multiple different reasons, e.g. manufacturing variations such as surface finish or material variations.

Obtained fatigue lives for different applied LP strategies and BL LJ sample resulted in variations to BL samples measured by LIFs which were in the range of 1.14 to 1.8 for strategy A and 1.52 to 3.54 for strategy B LJ samples. Considering a variation in BL fatigue lives of 0.18 for a load amplitude of 49.5 MPa, obtained results for strategy-B are statistically significant. For strategy-A results, the LIF are low and comparable to the coefficient of variation for BL samples. Also only two LJs were tested and therefore for obtained results the statistical significance can be questioned.

7.3 Characterisation of Fatigue Crack Development

Fracture surfaces were examined in order to understand the mechanism of fatigue degradation and progression of fatigue cracks. Especially the role of LP induced RS field is investigated in order to analyse beneficial and detrimental effects.

7.3.1 Locations and Type of Fracture

The dominant crack initiation mechanism was identified as fretting-fatigue. An example of a typical observed fretting-fatigue crack is shown in the fracture surface as presented in Figure 7-7a and the SEM image in Figure 7-7b. Fretting-fatigue cracks which can be described as a combination of wear and fatigue cracking [18], emanated from multiple initiation sites on the faying surface (top surface in Figure 7-7) towards the free surface (bottom surface in Figure 7-7). These multiple initiation sites translated into various crack planes as found by Rans *et al.* [59]. Initiations started remote from the fastener hole edge at the boundary of a “fretted” zone which is situated around fastener-holes corresponding to the clamped area under the fastener head. The fretted zone can be seen from the top view perspective of the fastener hole as shown in Figure 7-8. The surface underneath the fastener head is clearly damaged and crack initiation occurs at the boundary of the fretted area.

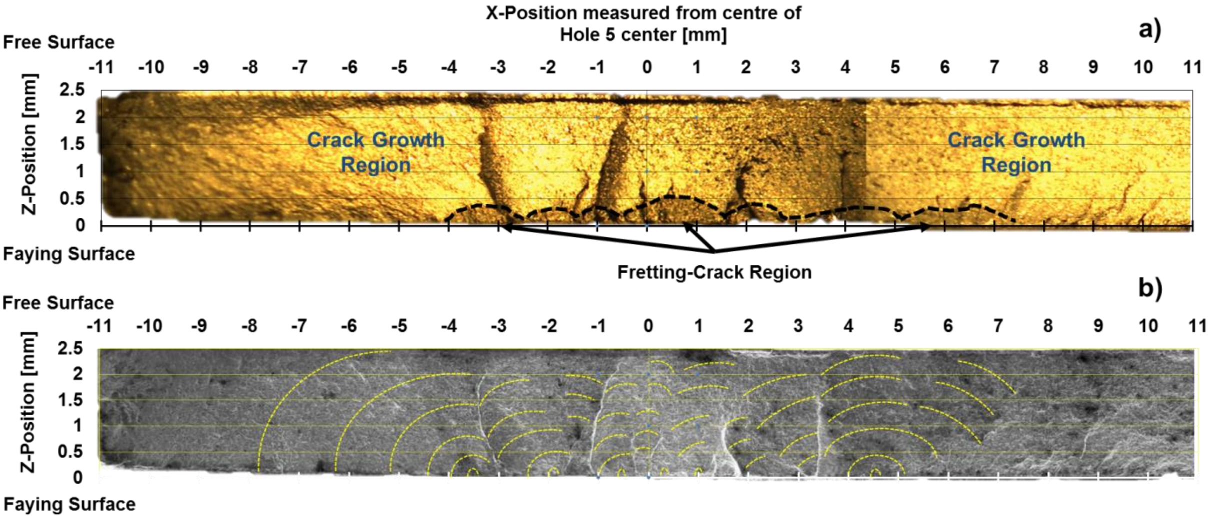

Figure 7-7: Micrograph and SEM image of example of a fretting-fatigue crack as observed in BL and LP samples (*LJ-BL-1*) tested under constant amplitude loading (σ_a = 49.5 MPa (σ_{max} = 110 MPa) and R = 0.1). Crack development marked in yellow.

The observed features of Figure 7-7a are also in agreement with observations of Gracia and Grandt [72] (section 2.2.2.6). Also Rans *et al.* [59] characterised in detail fretting-fatigue cracking of fastened LJs by means of advanced fractography and concluded that the maximum secondary bending moment coincided with this the boundary of the fretted area (refer to the review of chapter 2.2.2.2). Further research by Mueller [55] found that for high-clamping forces of solid rivet installations and consequent high load transfer via friction through the sheets fretting-fatigue occurs at the boundary of fretted zones around fastener holes. Fretted zones and detailed analyses of the fretting mechanism involved producing the surface damage as researched by Brown *et al.* [58] are also reflected in the micrographical evidence of fractured LJ-BL samples.

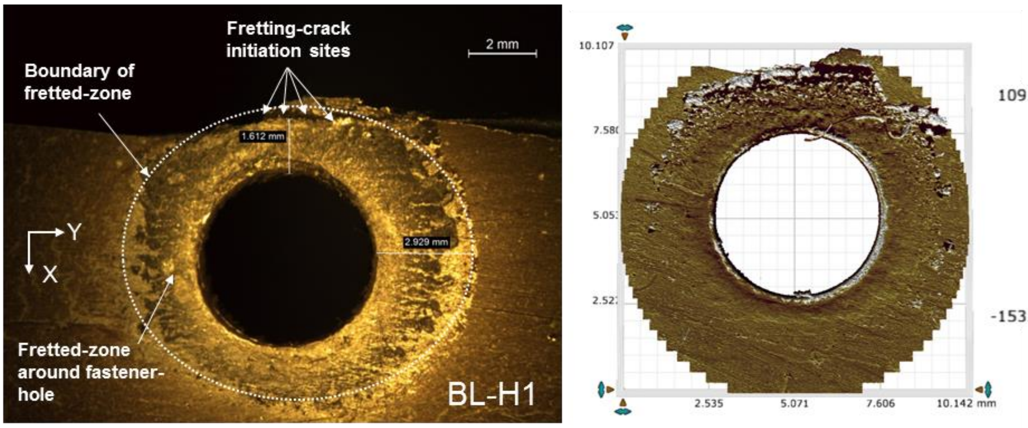

Figure 7-8: Micrograph example (left) and height profile (right) of fretted zone around fastener hole on faying surface (*LJ-BL-3*) tested under constant amplitude loading (σ_a = 49.5 MPa (σ_{max} = 110 MPa) and R = 0.1).

For LP LJ samples two different types of cracks were observed depending on the LP strategy. Beside fretting-fatigue cracks, fatigue cracks with distinctly different initiation appearance and location were found in LP samples. These initiated from a single location at LP-Zone Boundaries (LPZB) and grew on a single crack plane. In LP LJ sample both types of crack occurred in one sample. Examples of both, a fretting-fatigue crack and a fatigue crack at LPZB in a *LJ-LP-P* sample are shown in Figure 7-9. It can be seen that the fretting-fatigue crack (within the LP Patch in Figure 7-9) is a typical multiple initiation site and multiple crack planes leaving behind a fragmented surface. In contrast, LPZB cracks (outside the LP Patch Figure 7-9) initiate from a single location or near the boundary of the LP region. Fracture surfaces of those cracks are smooth and damaged the surface on single crack plane.

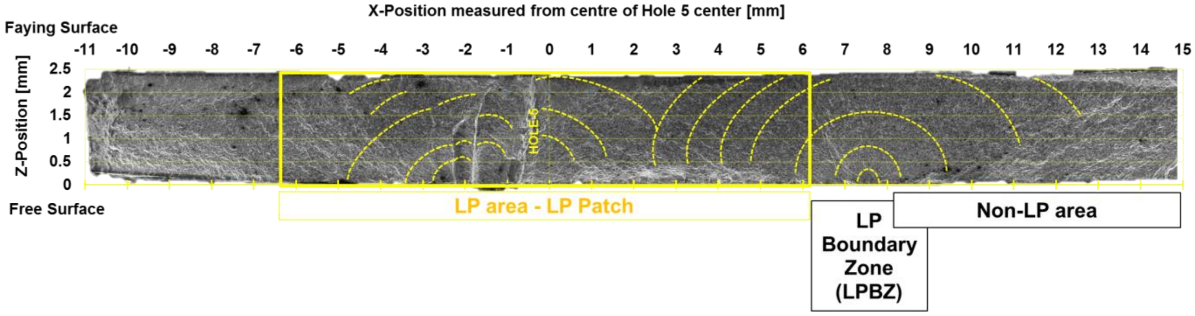

Figure 7-9: Example of fretting-fatigue crack and fatigue crack initiated at LPBZ (*LJ-P-A-1*) tested under constant amplitude loading (σ_a = 49.5 MPa (σ_{max} = 110 MPa) and R = 0.1).

Figure 7-10 presents another fatigue crack which was typical in *LJ-LP-P* samples. A fatigue crack initiated outside the peened area where tensile RSs dominate (RS data as described in section 4.2.3.2 superimposed to the fracture surface). As mentioned, fatigue cracks in contrast to fretting-fatigue cracks, scar the fracture surface differently and leave behind no intersecting crack planes. Likewise to all other crack initiation sites, fatigue cracks started at the faying surface and propagated towards the free surface.

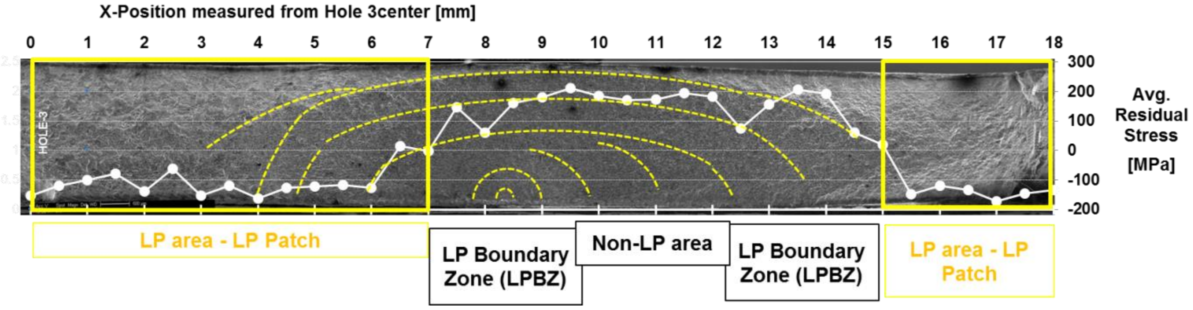

Figure 7-10: Example of fatigue crack which initiated at a LPBZ (*LJ-P-B-1*) tested under constant amplitude loading (σ_a = 49.5 MPa (σ_{max} = 110 MPa) and R = 0.1).Synchrotron XRD RS measurements as determined at DESY/Petra-III superimposed to the fracture surface.

A summary of identified cracks on BL and LP LJ samples are illustrated in Figure 7-11. These crack maps illustrate location, dimension and type (fretting-fatigue or fatigue) of cracking. In addition the top perspective of fractures (looking down on the fastener holes) is shown so that the fracture line can be analysed. For LP samples the region of LP are indicated with light red shading.

In section a. and b. of Figure 7-11, BL samples are shown. Section a. shows fretting-fatigue cracks which are located at Hole 4 (H4), Hole 5 (H5) (compare with Figure 7-7 and Figure 7-8) and partly at Hole 3 (H3). For BL and LP samples primary cracking starts from edge holes (edge effect). As expected final static failure proceeds through the weakest cross-section which is most likely the centre line of fastener hole row. Inner skin failure as in section a. and outer skin failure as a shown in section b. was found to be arbitrary for all conducted observations.

Fractures of LJ samples in conditions of LP *strategy-A*, are given in Figure 12 c. and d. These samples showed different cracking mechanisms when compared with BL samples. For both *S-* and *P-layouts* fatigue cracks initiate from the boundary between LP and non-LP regions (compare with right-hand crack examples in Figure 7-9 and crack shown in Figure 7-10) at LPBZ. However, cracking initiates not only at LPBZ transition regions in the x-direction but also in longitudinal y-direction as seen in section c. at the corner of the LP zone near *Hole 5* and in Figure 7-11d. on the corner of the LP regions around *Hole 4* (H4) and *Hole 5* (H5). Those localities are dominated by high local stress gradients (recall RS results of chapter 4.2.3). Those transition regions can be located between LP Patches or at the edge of the LP Stripe or Patch respectively.

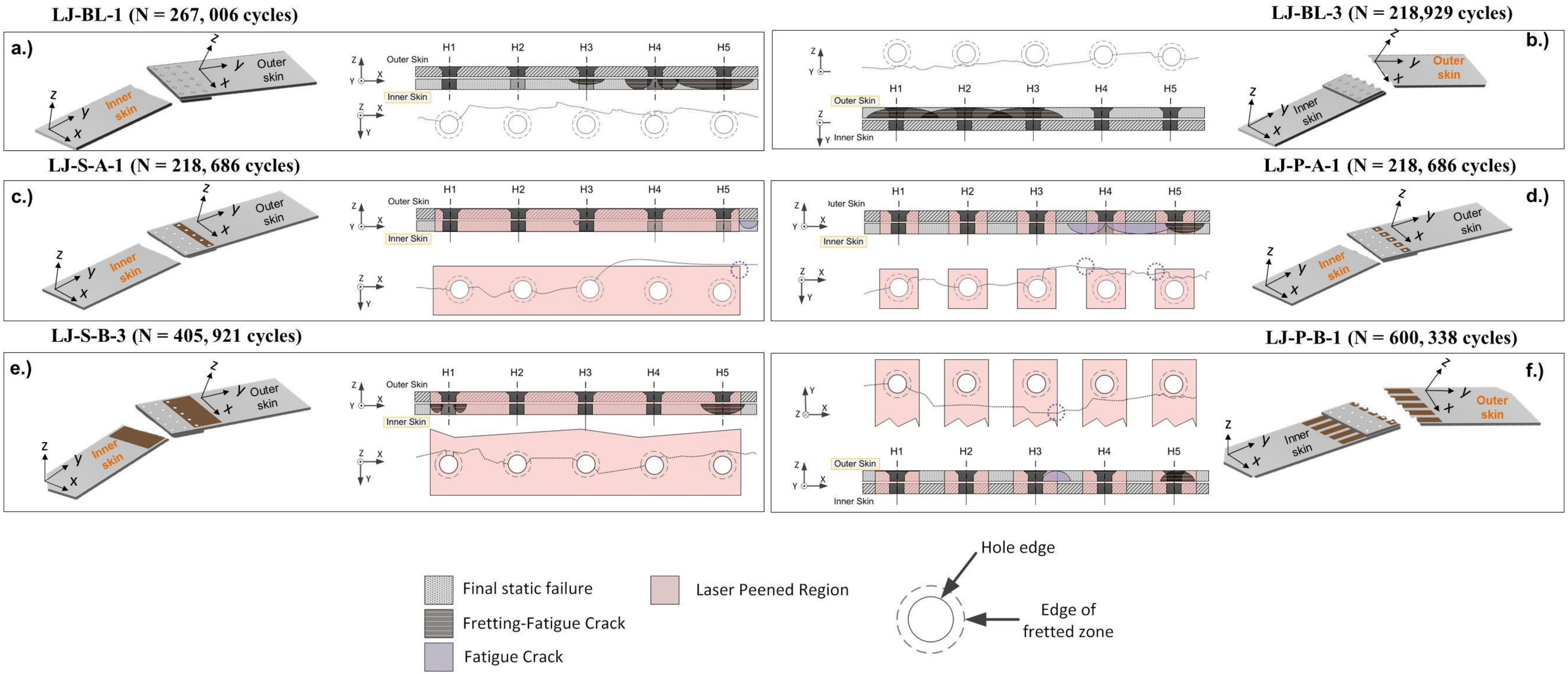

Figure 7-11: Examples of illustrations of fracture cross-sections and line of rupture. a.) and b.) typical and representative BL sample fracture, c.) *LJ-S-A* representative fracture, d.) *LJ-P-A* representative fracture, e.) *LJ-S-B* representative fracture, e.) *LJ-P-B* representative fracture.

For *strategy-B* samples presented in Figure 7-11e. and f. the observed fracture is different for *S*- and *P*-layouts. For *S-B samples*, the fracture mechanism returns to the BL mechanism; hence fretting-fatigue cracking is the cause of failure. Fretting initiation starting at zones around *Hole 1* (H1) and *Hole 5* (H5), compared with Figure 7-11e. The *P-B sample* fracture, however, indicates that both fretting-fatigue and local stress initiated crack mechanisms compete with each other and both kind of cracks were observed in *P-B samples*. As described, fretting-fatigue occurs at the boundary of the fretted zone around fastener-holes (H5 in *P-B*) while LPZB cracks (compare with Figure 7-10) initiate at a location remote from the fastener-hole (H3 in *P-B*) in longitudinal (y-direction) and at the LP-non-LP transition region in the transverse x-direction.

7.3.2 Fatigue Striations and Crack Growth Rates

Results of FCGRs (*da/dN*) determined by measuring striation spacing (as explained in section 3.4.2) on fracture surfaces of failed LJ samples (*LJ-BL-1* to *LJ-BL-3* and *LJ-P-B-1* to *LJ-P-B-3*) are shown in Figure 7-12a. Comparing *BL* to *P-B-samples*, the presented measurement data implies that there is no or very little effect of the LP treatment on the FCGR between a = 0.6 mm to a = 2.5 mm. No striation could be found for crack lengths less than 0.6 mm. During the examination striation spacing between 70 nm and 500 nm were observed. According to S. Lynch [174] this is the range of striation spacing typical observed for low and intermediate ΔK values. The lower limit of observed striation spacing is given as ~ 100 nm by Lynch's summary of "progression markings, striations, and crack-arrest markings on fracture surfaces" [174]. The obtained data points extracted from multiple samples were fitted using a fourth order polynomial function with coefficients as given in Table 7-2. The polynomial functions was used to calculate FCGRs and the subsequently crack growth life as presented in Figure 7-12b.

Table 7-2: Coefficient derived for the fitting procedure to describe FCGR vs crack length for BL and P-B samples.

Sample	a_4	a_3	a_2	a_1	a_0
LJ-BL	-1.68416E-04	1.17507E-03	-2.78936E-03	2.78988E-03	-8.27243E-04
LJ-P-B	6.93713E-05	-1.66502E-04	-1.71205E-04	6.84265E-04	-2.87707E-04

Crack growth life N_{CG} was calculate between crack lengths of a = 0.6 to a = 2.5 mm. For *LJ-BL* and *LJ-P-B* samples total crack growth lives of (N_{CG} =) 9,155 cycles and (N_{CG} =) 13,942 cycles were determined, respectively, indicating a minor effect of LP on the crack growth life. However, considering the total average fatigue life of respective LJ samples ($N_{LJ\text{-}BL}$ = 223,620 cycles and $N_{LJ\text{-}P\text{-}B}$ = 792,156 cycles), the obtained crack growth lives within the range of a = 0.6 to a = 2.5 mm are insignificant. In conclusion, it can be analysed that the overwhelming majority of the fatigue life is accumulated between crack initiation and crack length of a = 0.6 mm.

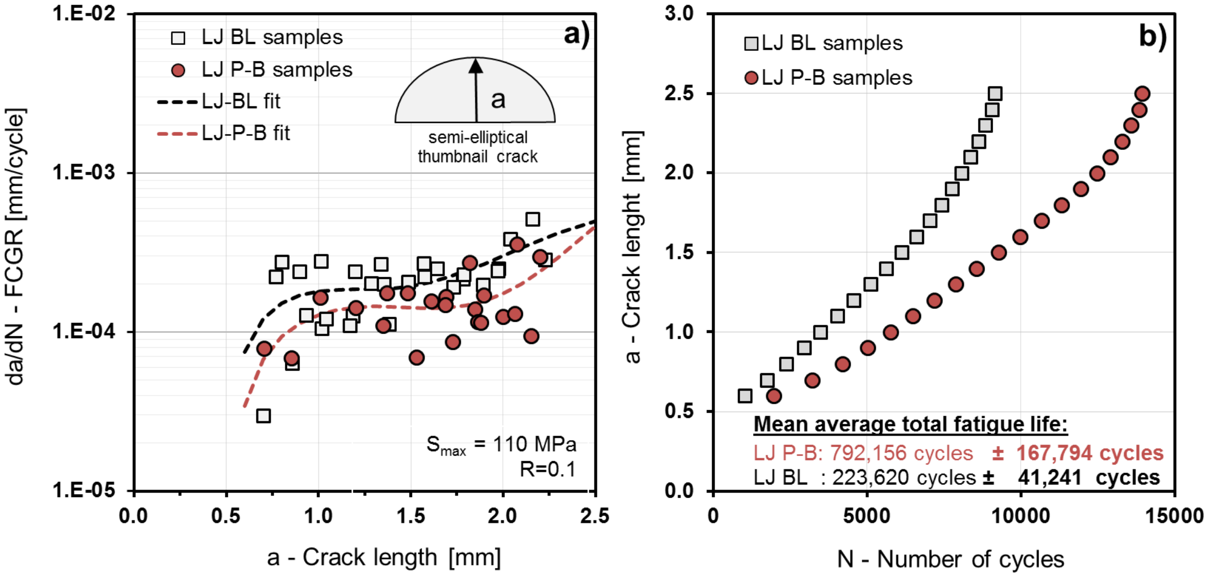

Figure 7-12: FCGR results determined by striation spacing measurements. a) FCGR (*da/dN*) vs crack length in thickness direction and b) Crack length vs number of cycles for the crack growth period.

7.4 Discussion of Laser-Peened Fastened LJs

7.4.1 Effect of Residual Stress on Crack Initiation and Crack Propagation

After the fracture surfaces were initially characterised as for location and type of fracture, the striation counting method was applied to determine FCGRs. Subsequent crack growth life calculations indicated that the majority of the total fatigue life is spent between crack initiation and crack lengths of a = 0.6 mm, as it is illustrated by the plot shown in Figure 7-13. This statement is true for both laser-peened and BL LJ samples and therefore the fatigue life improvements which were observed for laser-peened specimens must be assumed to occur during crack initiation or early crack growth. For *LJ-BL* samples the crack growth period consist of 4.1 % of the total fatigue life whereas *LJ-P-B* samples showed a 1.8 % fraction of the crack growth period of the total life, further indicating that LP improved the crack initiation rather than the crack growth period, since the propagation period did not increase for laser-peened samples. A similar result on the proportion of initiation and propagation stages of cracks in laser-peened specimens was also found by P. Peyre *et al.* [86] (also refer to Figure 2-36). The underlying mechanisms which delay crack initiation however remain unexplored and give motivation for further research. A detailed understanding of the initiation process and the role of RSs would provide more information which can be used to customise and optimise any LP strategy.

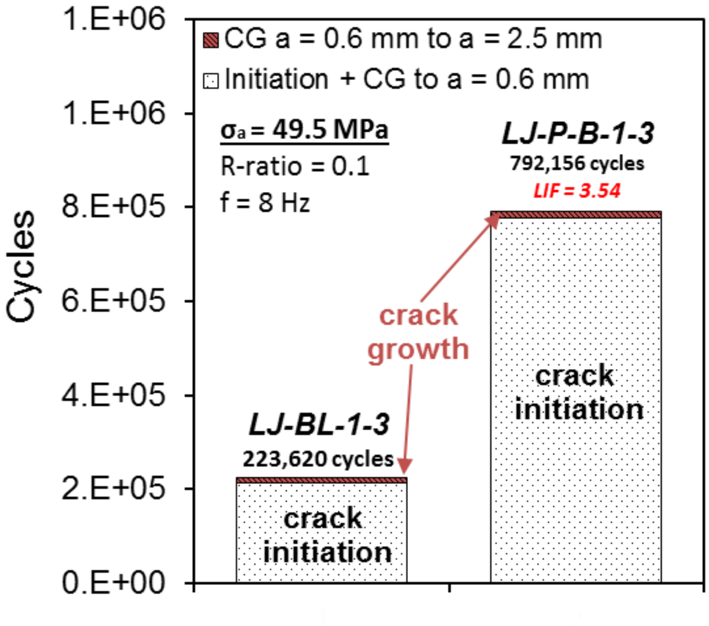

Figure 7-13: Comparison of initiation and cracking stages for BL and laser-peened *P-B* LJ samples derived from post-mortem fracture surface striation counting.

During the manufacturing of laser-peened LJ samples both surfaces were processed. Following the results that the compressive RS field on the free surface will not affect the crack growth as the initiation which occurs at the faying surface takes the bulk of the total life which gives further potential to reduce processing time and cost by avoiding peening on both surfaces and remain with processing merely the faying surface.

7.4.2 Effect of Residual Stress on Initial Failure Location and Fatigue Life

In the efforts of extending the fatigue life of aircraft longitudinal LJs, compressive RS were introduced into the structure using different strategies of LP. Compressive RS fields introduced by LP improved the fatigue life of LJ samples by delaying crack initiation which was promoted by fretting at the faying surfaces of LJ. Compressive RS fields, however, must be associated with balancing tension fields, which cause detrimental effects and promote crack initiation in new locations within the un-peened areas at the transition region from compressive to tensile RSs. The 2D stress contour map of Figure 4-10 and the 1D stress map of Figure 4-12 provide the evidence and quantify tensile RSs in laser-peened LJs (*strategy-B* samples). Therefore, enhancement of fatigue life in a surface treated component will depend on optimisation of the compressive fields, while minimising the associated tensile stress in vulnerable regions by controlling the LP layout and LP process parameters.

Table 7-3: Summary of ICHD determined RS profile values and corresponding fatigue and fracture key results.

Strategy	Max. Compr. RS σ_{yy}	Depth of Compr. RS	Unaffected by LP space through the thickness	LIF	Crack Initiation Mechanism	Location of Initiation
BL	*N/A*	*N/A*	*N/A*	*N/A*	***Fretting-fatigue***	***At fretted zone around fastener-hole***
S-A	-256 MPa	~700 µm	~1100 µm	1.14	Fatigue with tensile residual stress	LPBZ at sample edge hole
P-A	-280 MPa	~1000 µm	~500 µm	1.80	Fatigue with tensile residual stress	LPBZ at sample between Patches
S-B	-178 MPa	~700 µm	~1100 µm	1.52	Fretting-fatigue	At fretted zone around fastener-hole
P-B	-270 MPa	~800 µm	~900 µm	3.54	Mixed: Fretting-fatigue and tensile residual stress	At fretted zone around fastener-hole & LPBZ

The fatigue tests of LJ demonstrate the effects of both beneficial compressive and associated detrimental tensile RS fields on failure location and LIF. The RS field, mean fatigue life improvement (LIF) and initiation location are compared in Table 7-3. BL samples without LP always initiated in fretting-fatigue at the boundary of the wear region under the rivet head, as also found by several other researchers [58,59,64]. LP using *strategy-A* produced relatively small LIF values of 1.14 and 1.8, although these samples had the greatest compressive stress maxima. Both *S-A* and *P-A* samples had initiation locations shifted away from the fretting origin found in BL samples to locations at the laser-peen boundary zone (LPBZ), where balancing tensile stresses and large stress gradients are found (refer to RS maps of Figure 4-10 and Figure 4-12). Although, the referred RS data showing the stress gradient and tensile RS field for *strategy-B* LJ samples, high compressive stress maxima will tend to be associated with higher levels of balancing tension stresses. In the case of samples with *strategy-A* peening treatments, the superior compressive RSs have limited effect on life as the failure location has moved to the region of balancing tensile residuals at LPBZ which promote crack initiation and propagation. In addition to high tensile RSs occurring at the LPBZ, high secondary bending stresses, as estimated in section 7.1, superimpose on the nominal tensile stress at the same location of the LPBZ. The same mechanism of premature crack initiation which resulted in little or no life improvements due to unwanted balancing tensile RSs were also found by Achintha *et al.* [24] who laser-peened open-hole test samples. For that reason, two modifications were applied to the *strategy-A* to derive a *strategy-B* in order to achieve a more substantial fatigue life improvement:

1) Decrease the LP process parameters Power Density and Pulse Density to decrease most importantly the penetration depth to give space to the balancing tensile RS in the core of the LJ sheet and consequently decrease tensile stresses in lateral direction in order to prevent crack initiation promotion at the LPBZ.
2) Elongate the LP layout in longitudinal direction to place the LPBZ and its associated high stress gradients into region of lower secondary bending stresses.

The modified *strategy-B* peening treatment produces smaller compressive stress maxima; much smaller in the case of the *S-B* sample. In this case, the failure location and type has returned to fretting at the edge of the rivet head, and the LIF is increased to 1.52. The greatly reduced residual compressive stress has avoided creating large tensile balancing stresses at LPBZ which was shifted away in the case of the longitudinal direction. As a consequence the failure location is unchanged from the baseline and no cracking occurred at the LPBZ. Although the LIF increased, it is limited which can be rationalised by the relatively small compressive stresses. Sample *P-B* had the largest LIF of 3.54 among all test samples correlating with a strong compressive RS of -270 MPa. Although LP process parameters were decreased the maximum compressive stress was maintained. The penetration depth was on the other hand affected by the process parameter modification and more space for tensile RS in the core of the sheet was produced which is assumed to decreases the tensile RS at the LPBZ. However, further research is needed to better characterise the distribution of RSs and quantify the changes of penetration depths and resulting tensile RS in lateral direction in regard to the peened region.

Interestingly, *P-B* samples type had mixed failure modes and locations of fretting and balancing tensile stresses, suggesting that this LP treatment and patch geometry of the *P-B* LP layout has optimised both crack initiation mechanisms at both initiation locations, creating a situation in which both cracking mechanism compete with each other, leading to a greatly improved LIF of 3.54.

LP of LJ samples demonstrated that LP is more effective than applying the Cx process. In comparison to published work on cold-expanded fastener holes in LJ samples [76] (refer to literature review section 2.3.3.1) which suggested fatigue life improvement of 1.8, the obtained results exhibited that laser-peened LJ can offer a LIF of 3.54 in *P-B* configuration. This is the largest improvement in fatigue life of high-transfer LJ compared to the literature as far as the author knows. The superiority of LP can be either explained by the RS through the thickness profile or the RS distribution in lateral direction. The RS profile of Cx applications can outperform LP and can generate a greater peak compressive RS value [8,9,77] but Cx induced RS field are limited in lateral distribution of compressive RSs. The compressive RS field around a cold-expanded hole is limited to 1 to 1.5 fastener hole radii around the fastener hole. This can be disadvantageous when balancing tensile RS stresses can superimpose to high stresses induced by secondary bending in the same location as observed for *P-A* and *S-A* LJ samples. *P-A* samples had a comparable RS condition to anticipated Cx RS field in terms of lateral distribution of RSs. Also the same degree of fatigue life improvement (LIF) can be noticed. For *P-B* samples however the flexibility of the LP process was used. The LP layout was changed to avoid that detrimental superposition of balancing tensile and normal stresses from nominal and secondary bending loads and hence the LIF were increased to 3.54.

Giummarra and Zonker [124] (refer to literature review section 2.3.3.2) demonstrated fatigue life improvements of a factor of 2.16 on laser-peened low-transfer single LJs without further analysing the fracture and subsequently optimising the treatment, showing the importance of thoughtfully engineering the LP strategy to achieve higher degrees of improvements.

7.5 Summary and Conclusions

Aircraft longitudinal LJs were identified as a fatigue critical component of aircraft fuselages and the research objective was to extend the fatigue life using LP. Therefore, LP was applied and substantial measurable fatigue life improvements were achieved depending on the used LP strategies. Strategies which design the LP layout (*P-B*) and processing parameters to maximise the compressive RS on the faying surface which is most vulnerable for fatigue degradation processes and minimise balancing tensile RSs outside the treated areas exhibited the highest fatigue life improvements of (LIF =) 3.54. Also overlapping of balancing tensile stress field with area of high secondary bending stresses were avoided by merely changing the LP layout which increased the life improvements bringing to attention the importance of optimising the design of the LP layout on the target component in the pursuit of extending the fatigue life. From the investigation of laser-peened LJ samples the following conclusion can be made:

- Fatigue life improvements of longitudinal LJ samples between 1.14 to 3.54 were achieved by LP depending on the LP strategy.
- Compressive RSs in the laser-peened area inhibited crack initiation and early crack growth between a = 0 mm to a = 0.6 mm rather than retarded crack growth propagation.
- Balancing tensile RSs can promote crack initiation causing reductionist effect on the benefits of the compressive field. Also crack initiation location shifted from the BL condition to LPBZ which needs consideration when planning maintenance tasks of laser-peened damage-tolerance aircraft components.
- The LP layout was identified as a key parameter to extend the fatigue life. When defining the LP layout high tensile stresses should be avoided especially in regions of peak tensile stresses caused by external loadings. Minimalistic LP areas should be designated for processing to leave as much as possible elastic material to generate compressive RSs (refer to conclusion of chapter 4.4) and minimise balancing tensile stresses.
- Levels of expected external loading must be considered when fatigue life extension are planned as the maximum applied stress can reduce the beneficial effects of LP by a significant portion.

8 Conclusions

In recent decades, LP was research mainly by academic research groups and the superior performance to introduce compressive RS to extend the fatigue and crack growth life of metals has been highlighted. However, industrial applications of LP on realistic structures are still rare and the understandings of factors controlling the fatigue life extension beyond LP process parameters are still immature. Aiming to demonstrate and quantify the effectiveness of LP and the most relevant factors to extend the fatigue and fatigue crack growth performance in aircraft fuselage structures, an extensive experimental program was performed. This included mainly the application of a range of different RS measurements techniques, mechanical fatigue and crack growth testing methods using two different sample types: the CCT-sample as a representative for a fuselage skin type structure and the fuselage longitudinal LJ. Supplementary, a modelling approach has been developed to predict fatigue crack growth in laser-peened fuselage structures to analyse different LP strategies to explore the parameters which control the effectiveness of any LP treatment on fuselage structures. Based on the results and discussions the following overall conclusion can be drawn:

(1) Laser-peening of aerospace aluminium alloys 2524-T3 and 2024-T3 can produce a range of different RS profiles depending mainly on LP process parameters (Power Density and Pulse Density) and LP layouts. Obtained peak compressive RS of $\sigma_{res, compr.}$ = -200 to -350 MPa and penetration depths of compressive RSs between 700 μm to 1000 μm were measured. Deep penetration depth of RS profiles (700 - 1000 μm) in laser-peened samples show superior behaviour to SP induced RS profiles which have typical penetration depth of 100 – 200 μm.

(2) The behaviour that increasing LP process parameter will increase peak compressive stress was confirmed by experimental efforts. In addition, the LP layout was identified as an important factor to form RS profiles. It can also increase the amount of compression when limited area is laser-peened leaving enough unprocessed elastic material in the sample to allow elastic push back on the plasticised area and vice-versa. For that reason, a concentrated local LP treatment should be preferred when planning a LP application.

(3) Experimental and supplementary crack growth modelling demonstrated that the definition of the LP layout (d_{LP}, w_{LP}, and $\#_{LP}$) controls the life improvement effectiveness of the LP process. Life reductions and improvements between LIF = 0.88 - 4.2 were determined. Decreasing the distance of a LPS to the initial crack

initiation d_{LP} will increase fatigue crack growth life improvements and the optimum position is when a peening stripe is processed on top of a crack ($d_{LP} = 0$). In case of a critical distance of a LPS detrimental life reduction effects will be caused by the LP layout as for the acceleration of FCGR in areas of tensile RS. Increasing the $_{\mathrm{wLP}}$ will increase the beneficial effects linearly. LP layout having two LPS ($\#_{LP} = 2$) are disadvantageous compared to one LPS configurations as the second peening stripe ($\#_{LP} = 1$) increases the tensile RS field causing an increased acceleration effect which cannot be compensated by the retardation effect of the second LPS which does not affect the crack significantly.

(4) The crack growth model showed that the amount of compression within a LPS also determined the outcome of crack growth retardation in laser-peened CCT-samples. The more compression, the greater is the retardation effect. Interestingly, the ratio between external applied load and the compressive RS was identified as the determining factor of the level of retardation which can be achieved.

(5) For laser-peened LJ samples, the LP layout mainly affected the fatigue life improvements. Different LP layout` result in significantly different fatigue performances. Fatigue life improvement over un-peened samples were achieved for all LP samples. LIFs varied from 1.14 to 3.54. The maximum LIF was achieved when firstly a concentrated peening area (*P-samples*) which can generate higher peak compressive RSs was defined. Secondly, when the LP layout (*P-B* samples) was defined so that the LPBZ do not coincide with areas of high tensile stresses from secondary bending preventing premature crack initiation at the LPBZ as observed for *P-A* samples. Avoiding this circumstance a maximum LIF of 3.54 was achieved even by the sacrifice of reduction of peak compressive RS.

(6) Fatigue life improvement in LJ samples originates from delay of fatigue crack initiation and very early crack growth (> 600 µm) and had no effect on crack lengths greater than 600 µm which gives further indication that only a concentrated region of LP at regions susceptible to fatigue crack initiation (faying surface) is needed and advantageous.

(7) Crack initiation locations in laser-peened LJ sample can shift from a BL condition to different locations on the structure which contains high balancing tensile RSs as a result of large compressive RS. Those changes in failure location in peening treatments with greatest compressive stress maxima suggest that both compressive RS and the concurrent tensile RS must be managed carefully. Shift in failure location can have serious implication when planning maintenance inspections defined to find fatigue cracks especially when LP is applied post-certification of aircrafts.

9 Future Research

The following points were identified as relevant for future research within the scope of to further extending the fatigue and crack growth life of aircraft fuselage structure made of 2000 series aluminium alloys:

(1) It was shown that the LP layout affects the formation of the RS profile but the mechanisms and limitations on how un-peened regions and peened regions interact with each other remains mainly unclear. A fundamental study using either experimental RS measurements or a realistic LP simulation model could explore the mechanics of RS formation combining LP process parameters, LP layout and also LP pattern in a test matrix. Subsequent results can be used to define more tailored LP treatments and hence RS fields.

(2) LP produced distortions in test sample and it was rationalised that those distortions interfered with the RS field induced by the LP process. Those distortions may be either unwanted or wanted. Anyhow, the mechanism of the formation of distortions caused by LP must be analysed in order to control the distortion. A simulation model of the LP process can be used to study the mechanics. Also, techniques or laser-peening strategies of preventing distortion at all without compromising on the RS field must be explored to satisfy strict tolerances for manufacturing assemblies.

(3) Measured RS fields and described trends were all based on a single test sample. A more statistical sound quantification of the RS data need more test samples and subsequent RS measurements. Especially, RS measurements on laser-peened CCT-samples need more attention in future research as obtained RS data was limited.

(4) Both experimental crack growth data of laser-peened CCT-samples as well as fatigue data of peened LJs need a larger population of test samples to ground the obtained results on more solid statistics.

(5) Fractographical investigation on laser-peened LJ demonstrated that the majority of the fatigue life improvement occurred in the fatigue crack initiation and/or early crack life. The exact mechanism on how compressive RSs affects crack initiation process is unclear and must be researched when tailoring RS field to further extend the fatigue life. Interrupted fatigue tests can be conducted to examine the progression of fatigue cracks in the early crack growth period (> 600 µm) where no clear fatigue striations are formed on the fracture surface.

(6) Unlike tested samples in this work, real fuselage panels are curved. To prove the concept of fatigue life extension on fuselages, LP must be applied to curved panels or real fuselage assemblies. LP strategies can be derived from results presented in this thesis.

References

1. EASA. Certification Specifications for Large Aeroplanes. Cs-25 2008 p. 750. Available at: DOI:10.1002/9780470664797
2. Swift T. Damage tolerance capability. International Journal of Fatigue. 1994; 16(1): 75–94. Available at: DOI:10.1016/0142-1123(94)90446-4
3. Wanhill RJH. Milestone Case Histories in Aircraft Structural integrity Milestone Case Histories in Aircraft Structural integrity. National Aerospace Laboratory. 2002; : 1–25.
4. FAA-Lessons learned. U.S. Department of Transportation. Available at: http://lessonslearned.faa.gov/ (Accessed: 19 April 2017)
5. Pitt S., Jones R. Multiple-site and widespread fatigue damage in aging aircraft. Engineering Failure Analysis. 1997; 4(4): 237–257. Available at: DOI:10.1016/S1350-6307(97)00020-4
6. Jones R., Molent L., Pitt S. Study of multi-site damage of fuselage lap joints. Theoretical and Applied Fracture Mechanics. 1999; 32(2): 81–100. Available at: DOI:10.1016/S0167-8442(99)00029-4
7. Silva LFM., Gonçalves JPM., Oliveira FMF., De Castro PMST. Multiple-site damage in riveted lap-joints: experimental simulation and finite element prediction. International Journal of Fatigue. 2000; 22(4): 319–338. Available at: DOI:10.1016/S0142-1123(99)00129-2
8. Fatigue Technology Incorporated. FTI Process specification 8101. Seattle, Washington; 2011.
9. Lacarac VD., Garcia-Granada AA., Smith DJ., Pavier MJ. Prediction of the growth rate for fatigue cracks emanating from cold expanded holes. International Journal of Fatigue. 2004; 26(6): 585–595. Available at: DOI:10.1016/j.ijfatigue.2003.10.015
10. Ivetic G., Meneghin I., Troiani E., Molinari G., Ocaña J., Morales M., et al. Fatigue in laser shock peened open-hole thin aluminium specimens. Materials Science and Engineering A. 2012; 534: 573–579. Available at: DOI:10.1016/j.msea.2011.12.010
11. Im J., Grandhi R V. Residual Stress Intensity Factor Based Fatigue Crack Growth Life Prediction for Laser Peened Structures. 2010; (April): 2938.
12. Schnubel D., Huber N. Retardation of fatigue crack growth in aircraft aluminium alloys via laser heating - Numerical prediction of fatigue crack growth. Computational Materials Science. Elsevier B.V.; 2012; 65: 461–469. Available at: DOI:10.1016/j.commatsci.2012.07.047
13. Muhammed Burak TOPARLI. Analysis of Residual Stress Fields in Aerospace Materials After Laser Peening. The Open University; 2012.

14. Spradlin TJ., Hodges JL. Predictive Crack Growth Technique for Laser Peening Process Development. The Journal of Engineering. 2015; : 1–6. Available at: DOI:10.1049/joe.2015.0110

15. McClung RC. A literature survey on the stability and significance of residual stresses during fatigue. Fatigue and Fracture of Engineering Materials and Structures. 2007; 30(3): 173–205. Available at: DOI:10.1111/j.1460-2695.2007.01102.x

16. Spanrad S. Fatigue crack growth in laser shock peened aerofoils subjected to foreign object damage. 2011; Available at: http://hdl.handle.net/10068/980535%5Cnfile:///Users/marina/Library/Application Support/Zotero/Profiles/xqldzces.default/zotero/storage/I6RXDCW2/980535.html

17. Schnubel D., Horstmann M., Ventzke V., Riekehr S., Staron P., Fischer T., et al. Retardation of fatigue crack growth in aircraft aluminium alloys via laser heating - Experimental proof of concept. Materials Science and Engineering A. Elsevier B.V.; 2012; 546: 8–14. Available at: DOI:10.1016/j.msea.2012.02.094

18. Schnubel D. Laser heating as approach to retard fatigue crack growth in aircraft aluminium structures. 2012;

19. Metal Improvement Company. Shot Peening Applications. 2005;

20. Lacarac V., Smith DJ., Pavier MJ., Priest M. Fatigue crack growth from plain and cold expanded holes in aluminum alloys. International Journal of Fatigue. 2000; 22(3): 189–203. Available at: DOI:10.1016/S0142-1123(99)00126-7

21. Coratella S. Evaluation of Residual Stress Fields after Laser Shock Peening Treatment of Aerospace Components. Coventry University; 2015.

22. Busse DO., Irving PE., Ganguly S., Furfari D., Polese C. Improving Fatigue Performance of AA 2024-T3 Clad Aeronautical Riveted Lap-Joints Using Laser-Peening. 2017; (June): 7–9.

23. S. Coratella., Glaser D., Pavan M., Polese C., Marais D., Venter AM., et al. Residual stress distribution in Laser Shock Peened samples with non-uniform geometries. ICRS-10, 10th International Conference on Residual Stresses. 2016.

24. Achintha M., Nowell D., Fufari D., Sackett EE., Bache MR. Fatigue behaviour of geometric features subjected to laser shock peening: Experiments and modelling. International Journal of Fatigue. Elsevier Ltd; 2014; 62: 171–179. Available at: DOI:10.1016/j.ijfatigue.2013.04.016

25. Sticchi M., Schnubel D., Kashaev N., Huber N. Review of Residual Stress Modification Techniques for Extending the Fatigue Life of Metallic Aircraft Components. Applied Mechanics Reviews. 2014; 67(1): 10801. Available at: DOI:10.1115/1.4028160

26. Heckenberger UC., Hombergsmeier E., Holzinger V., Bestenbostel W Von., Heckenberger UC., Hombergsmeier E., et al. Laser shock peening to improve the fatigue resistance of AA7050 components. 2011; Available at: DOI:10.1108/17579861111108581

27. Taddia S., Troiani E. Effect of Laser Shock Peening on the Fatigue Behavior of Thin Aluminum Panels. Materials Today: Proceedings. Elsevier Ltd.; 2015. 5006-5014 p. Available at: DOI:10.1016/j.matpr.2015.10.090

28. Curtiss-Wright Surface Technologies. Shot Peening. Available at: https://cwst.com/shot-peening/overview/ (Accessed: 10 April 2017)

29. de los Rios ER., Walley A., Milan MT., Hammersley G. Fatigue crack initiation and propagation on shot-peened surfaces in A316 stainless steel. International Journal of Fatigue. 1995; 17(7): 493–499. Available at: DOI:10.1016/0142-1123(95)00044-T

30. Hammond DW., Meguid SA. Crack propagation in the presence of shot-peening residual stresses. Engineering Fracture Mechanics. 1990; 37(2): 373–387. Available at: DOI:10.1016/0013-7944(90)90048-L

31. Mcelhone M., Rugg D. Experimental Evaluation of the Fatigue Performance of Aero-Engine Fan Blade Dovetails. Aeromat 2005. 2005.

32. Jaap Schijve. Fatigue of Structures and Materials. Dordrecht: Kluwer Academic Publishers; 2004.

33. Anderson TL. Fracture Mechnics - Fundamentals and Applications. CRC Press LLC; 1995.

34. Broek D. The Practical Use of Fracture Mechanics. Kluwer Academic Publishers; 1988.

35. Perez N. Fracture Mechanics. Kluwer Academic Publishers; 2004.

36. Rice RC., Jackson JL., Bakuckas J., Thompson S. Metallic Materials Properties Development and Standardization. Washington, D.C.; 2003.

37. Murakami Y. Stress intensity factors handbook. Pergamon; 1987.

38. Glinka G. Development Of Weight Functions And Computer Integration Procedures For Calculating Stress Intensity Factors Around Cracks Subjected To Complex Stress Fields. Hampton, VA 23666, USA; 1996.

39. Krueger R. The Virtual Approach Crack Closure Technique : History , and Applications. ICASE Report. Hampton, VA; 2002.

40. Newman JC., Raju IS. Stress-Intensity Factor Equations for Cracks in Three-Dimensional Finite Bodies Subjected to Tension and Bending Loads. In: Atluri SN (ed.) Computational Methods in the Mechanics of Fracture. Elsevier Science Publisher; 1986.

41. ASTM 647 - Standard Test Method for Measurement of fatigue Crack Growth Rate. ASTM International;

42. Kranenburg C Van. Fatigue crack growth in Aluminium Alloys Fatigue crack growth in Aluminium Alloys.

43. Paris PC., Gomez MP., Anderson WE. A Rational Analytic Theory of Fatigue. 1961.

44. Servetti G. Modelling and Predicting Fatigue Crack Growth Behaviour in Weld Induced Residual Stress Fields. 2011; Available at: https://dspace.lib.cranfield.ac.uk/handle/1826/5617

45. Walker K. The Effect of Stress Ratio During Crack Propagation and Fatigue for 2024-T3 and 7075-T6 Aluminum. Effects of Environment and Complex Load History on Fatigue Life. 1970; : 1–14. Available at: DOI:10.1520/STP32032S

46. ELBER W. Fatigue Crack Closure Under Cyclic Tension. Engineering Fracture Mechanics. 1970; 2(1): 37–45. Available at: DOI:10.1016/0013-7944(70)90028-7

47. Mann T. International Journalof Fatigue The influence of mean stress on fatigue crack propagation in aluminium alloys. 2007; 29(0142): 1393–1401. Available at: DOI:10.1016/j.ijfatigue.2006.11.010

48. Skorupa A., Skorupa M. Riveted Lap Joints in Aircraft Fuselage. 2012.

49. Michael Chun-Yung Niu. AIRFRAME Stress Analysis and Sizing. Hong Kong: Conmilit Press Ltd.; 1997.

50. Dursun T., Soutis C. Recent developments in advanced aircraft aluminium alloys. Materials and Design. Elsevier Ltd; 2014; 56: 862–871. Available at: DOI:10.1016/j.matdes.2013.12.002

51. Hudson CM. Effect of Stress Ratio on Fatigue-Crack Growth in 7075-T6 and 2024-T3 Alumium-Alloy Specimen. Langley Station, Hampton, Va.;

52. Verma BB., Atkinson JD., Kumar M. Study of fatigue behaviour of 7475 aluminium alloy. Bull. Mater. Sci. 2001; 24(2): 231–236. Available at: DOI:10.1007/BF02710107

53. Hartman A., Schijve J. The Effect Of Secondary Bending On The Fatigue Strenght Of 2024-T3 Alclad Riveted Joints. 1956.

54. Skorupa M., Machniewicz T., Skorupa A., Korbel A. Fatigue strength reduction factors at rivet holes for aircraft fuselage lap joints. International Journal of Fatigue. Elsevier Ltd; 2015; 80: 417–425. Available at: DOI:10.1016/j.ijfatigue.2015.06.025

55. Mueller RPG. An Experimental and Analytical Investigation on the Fatigue Behaviour of Fuselage Riveted lap Joints. Delft University of Technology; 1995.

56. Starikov R. Mechanically fastened joints: critical testing of single overlap joints. FOI Swedish Defence Research Agency, Scientific. 2002. Available at: http://foi.se/ReportFiles/foir_0441.pdf

57. Rans CD. The Role of Rivet Installation on the Fatigue Performance of Riveted Lap Joints. Carleton University; 2007.

58. Brown AM., Straznicky P V. Simulating fretting contact in single lap splices. International Journal of Fatigue. Elsevier Ltd; 2009; 31(2): 375–384. Available at: DOI:10.1016/j.ijfatigue.2008.07.012

59. Rans CD., Alderliesten RC., Straznicky P V. Assessing the effects of riveting induced residual stresses on fatigue crack behaviour in lap joints by means of fractography. International Journal of Fatigue. Elsevier Ltd; 2009; 31(2): 300–308. Available at: DOI:10.1016/j.ijfatigue.2008.08.005

60. Szolwinski MP., Farris TN. Mechanics of fretting fatigue crack formation. Wear. 1996; 198(1): 93–107. Available at: DOI:10.1016/0043-1648(96)06937-2

61. Schijve J., Campoli G., Monaco A. Fatigue of structures and secondary bending in structural elements. International Journal of Fatigue. Elsevier Ltd; 2009; 31(7): 1111–1123. Available at: DOI:10.1016/j.ijfatigue.2009.01.009

62. Rans C., Straznicky P., Alderliesten R. Effects of Rivet Installation on Residual Stresses and Secondary Bending Stresses in a Riveted Lap Joint. 48th AIAA/ASME/ASCE/AHS/ASC Structures, Structural Dynamics, and Materials Conference. 2007; 7(April): 7378–7390. Available at: DOI:10.2514/6.2007-2307

63. Rans C., Straznicky P V., Alderliesten R. Riveting Process Induced Residual Stresses Around Solid Rivets in Mechanical Joints. Journal of Aircraft. 2007; 44(1): 323–329. Available at: DOI:10.2514/1.23684

64. Skorupa A., Skorupa M., Machniewicz T., Korbel A. Fatigue crack location and fatigue life for riveted lap joints in aircraft fuselage. International Journal of Fatigue. Elsevier Ltd; 2014; 58: 209–217. Available at: DOI:10.1016/j.ijfatigue.2013.01.014

65. Hills DA., Nowell D. Mechnics of Fretting Fatigue. Kluwer Academic Publishers; 1994.

66. Szolwinski MP., Harish G., Mc Veigh P., Farris TN. The Role Of Fretting Crack Nucleation In The Onset Of Widespread Fatigue Damage: Analysis And Experiments. FAA-NASA Symposium on the Continued Airworthiness of Aircraft Structures. Atlanta; 1996.

67. Hills DA., Nowell D., O’Connor JJ. On the mechanics of fretting fatigue. Wear. 1988; 125(1–2): 129–146. Available at: DOI:10.1016/0043-1648(88)90198-6

68. Iyer K., Rubin CA., Hahn GT. Influence of interference and clamping on fretting fatigue in single rivet-row lap joints. Journal of Tribology. 2001; 123(4): 686–698. Available at: DOI:10.1115/1.1352746

69. Piascik RS., Willard S a. The Characteristics of Fatigue Damage in the Fuselage Riveted Lap Splice Joint. 1997; (November 1997).

70. Faact- DOT. Literature Review and Preliminary Studies of Fretting and Frettinf Fatigue Including Special Application to Aircraft Joints. 1994.

71. Fawaz SA. Fatigue Crack Growth in Riveted Joints. Delft University of Technology; 1997.

72. Garcia DB., Grandt AF. Fractographic investigation of fretting fatigue cracks in Ti-6Al-4V. Engineering Failure Analysis. 2005; 12(4): 537–548. Available at: DOI:10.1016/j.engfailanal.2004.10.006

73. Wither PJ. Residual Stress and its Role in Failure. Reports on Progress in Physics. 2007; 70: 2211–2264. Available at: DOI:10.1088/0034-4885/70/12/R04

74. Amrouche A., Mesmacque G., Garcia S., Talha A. Cold expansion effect on the initiation and the propagation of the fatigue crack. International Journal of Fatigue. 2003; 25(9–11): 949–954. Available at: DOI:10.1016/S0142-1123(03)00127-0

75. de Matos PFP., McEvily AJ., Moreira PMGP., de Castro PMST. Analysis of the effect of cold-working of rivet holes on the fatigue life of an aluminum alloy. International Journal of Fatigue. 2007; 29(3): 575–586. Available at: DOI:10.1016/j.ijfatigue.2006.04.004

76. Buxbaum O., Huth H. Expansion of cracked fastener holes as a measure for extension of lifetime to repair. Engineering Fracture Mechanics. 1987; 28(5–6): 689–698. Available at: DOI:10.1016/0013-7944(87)90062-2

77. Zhang X., Wang Z. Fatigue life improvement in fatigue-aged fastener holes using the cold expansion technique. International Journal of Fatigue. 2003; 25(9–11): 1249–1257. Available at: DOI:10.1016/S0142-1123(03)00152-X

78. Yanishevsky M., Li G., Shi G., Backman D. Fractographic examination of coupons

representing aircraft structural joints with and without hole cold expansion. Engineering Failure Analysis. 2013; 30: 74–90. Available at: DOI:10.1016/j.engfailanal.2012.12.008

79. Hill MR., DeWald AT., Demma AG., Hackel LA., Chen H-L., Dane CB., et al. LASER PEENING TECHNOLOGY. asminternational. 2003; 161(8).

80. Jensen D. Adaptation of LSP Capability for Use on F-22 F-22 Mobile LSP Maturation Raptor Primary Structure at an Aircraft Modification Depot. 2nd International Conference on Laser Peening. 2010.

81. P.R. Smith, M. J. Shepard, P.S. Prevéy III and AHC. Effect of Power Density and Pulse Repetition on Laser Shock Peening of Ti-6AI-4V. Journal of Materials Engineering and Performance JMEPEG. 2000; 9(9): 33–37. Available at: DOI:10.1361/105994900770346259

82. Clauer AH., Fairand BP., Ford SC., Walters CT. Laser shock processing in Shock Waves and High-Strain-Rate Phenomena in Metals. 1983;

83. Fairand BP. Laser shock-induced microstructural and mechanical property changes in 7075 aluminum. J. Appl. Phys. 1974; 25(8): 431.

84. Clauer A., Walters C., Ford S. The effects of laser shock processing on the fatigue properties of 2024-T3 aluminum. Lasers in materials processing. 1983; (January): 7–22.

85. Fairand BP., Clauer AH., Jung RG., Wilcox BA. Quantitative assessment of laser-induced stress waves generated at confined surfaces. Applied Physics Letters. 1974; 25(8): 431–433. Available at: DOI:10.1063/1.1655536

86. Peyre P., Fabbro R., Merrien P., Lieurade HP. Laser shock processing of aluminium alloys. Application to high cycle fatigue behaviour. Materials Science and Engineering: A. 1996; 210: 102–113. Available at: DOI:10.1016/0921-5093(95)10084-9

87. Fabbro R., Fournier J., Ballard P., Devaux D., Virmont J. Physical study of laser-produced plasma in confined geometry. Journal of Applied Physics. 1990; 68(2): 775–784. Available at: DOI:10.1063/1.346783

88. Berthe L., Fabbro R., Peyre P., Tollier L., Bartnicki E. Shock waves from a waterconfined laser-generated plasma. J. Appl. Phys. 1997; 82: 2826.

89. Rubio-González C., Felix-Martinez C., Gomez-Rosas G., Ocaña JL., Morales M., Porro JA. Effect of laser shock processing on fatigue crack growth of duplex stainless steel. Materials Science and Engineering A. 2011; 528(3): 914–919. Available at: DOI:10.1016/j.msea.2010.10.020

90. Rubio-González C., Gomez-Rosas G., Ocaña JL., Molpeceres C., Banderas A., Porro J., et al. Effect of an absorbent overlay on the residual stress field induced by laser shock processing on aluminum samples. Applied Surface Science. 2006; 252(18): 6201–6205. Available at: DOI:10.1016/j.apsusc.2005.08.062

91. Gomez-Rosas G., Rubio-Gonzalez C., Ocaña JL., Molpeceres C., Porro JA., Chi-Moreno W., et al. High level compressive residual stresses produced in aluminum alloys by laser shock processing. Applied Surface Science. 2005; 252(4): 883–887. Available at: DOI:10.1016/j.apsusc.2005.01.150

92. Rubio-González C., Ocaña JL., Gomez-Rosas G., Molpeceres C., Paredes M., Banderas A., et al. Effect of laser shock processing on fatigue crack growth and fracture toughness

of 6061-T6 aluminum alloy. Materials Science and Engineering: A. 2004; 386(1–2): 291–295. Available at: DOI:10.1016/j.msea.2004.07.025

93. Gomez-Rosas G., Rubio-Gonzalez C., Ocaña JL., Molpeceres C., Porro JA., Morales M., et al. Laser Shock Processing of 6061-T6 Al alloy with 1064 nm and 532 nm wavelengths. Applied Surface Science. 2010; 256(20): 5828–5831. Available at: DOI:10.1016/j.apsusc.2010.03.043

94. Sánchez-Santana U., Rubio-González C., Gomez-Rosas G., Ocaña JL., Molpeceres C., Porro J., et al. Wear and friction of 6061-T6 aluminum alloy treated by laser shock processing. Wear. 2006; 260(7–8): 847–854. Available at: DOI:10.1016/j.wear.2005.04.014

95. Ocaña JL., Porro JA., Díaz M., Ruiz de Lara L., Correa C., Gil-Santos A., et al. Induction of engineered residual stresses fields and enhancement of fatigue life of high reliability metallic components by laser shock processing. Proceedings of SPIE - The International Society for Optical Engineering. 2013; 8603: 86030D. Available at: DOI:10.1117/12.2003935

96. Correa C., Peral D., Porro J a., Díaz M., Ruiz de Lara L., García-Beltrán a., et al. Random-type scanning patterns in laser shock peening without absorbing coating in 2024-T351 Al alloy: A solution to reduce residual stress anisotropy. Optics & Laser Technology. Elsevier; 2015; 73: 179–187. Available at: DOI:10.1016/j.optlastec.2015.04.027

97. Troiani E., S.Taddia., Meneghin I., Molinari G., Polese C. Effect of LSP-generated Residual Stresses on Fatigue Crack Propagation in Thin Panels. Proceedings of the 34th Conference and the 28th Symposium of the international Committee on Aeronautical Fatigue and Structural Integrity. Helsinki, Finland; 2015.

98. Sano Y., Obata M., Kubo T., Mukai N., Yoda M., Masaki K., et al. Retardation of crack initiation and growth in austenitic stainless steels by laser peening without protective coating. Materials Science and Engineering A. 2006; 417(1–2): 334–340. Available at: DOI:10.1016/j.msea.2005.11.017

99. Sano Y., Mukai N., Okazaki K., Obata M. Residual stress improvement in metal surface by underwater laser irradiation. Beam Interaction with Material & Atoms. 1971; 21(I 997): 42–45.

100. Montross CS., Wei T., Ye L., Clark G., Mai YW. Laser shock processing and its effects on microstructure and properties of metal alloys: A review. International Journal of Fatigue. 2002; 24(10): 1021–1036. Available at: DOI:10.1016/S0142-1123(02)00022-1

101. Gujba AK., Medraj M. Laser peening process and its impact on materials properties in comparison with shot peening and ultrasonic impact peening. Materials. 2014. 7925-7974 p. Available at: DOI:10.3390/ma7127925

102. Correa C., Ruiz De Lara L., Díaz M., Gil-Santos A., Porro JA., Ocaña JL. Effect of advancing direction on fatigue life of 316L stainless steel specimens treated by double-sided laser shock peening. International Journal of Fatigue. Elsevier Ltd; 2015; 79: 1–9. Available at: DOI:10.1016/j.ijfatigue.2015.04.018

103. Cuellar SD., Hill MR., Dewald AT., Rankin JE. Residual stress and fatigue life in laser shock peened open hole samples. International Journal of Fatigue. Elsevier Ltd; 2012; 44: 8–13. Available at: DOI:10.1016/j.ijfatigue.2012.06.011

104. Luong H., Hill MR. The effects of laser peening and shot peening on high cycle fatigue in 7050-T7451 aluminum alloy. Materials Science and Engineering A. 2010; 527(3): 699–707. Available at: DOI:10.1016/j.msea.2009.08.045

105. Liu KK., Hill MR. The effects of laser peening and shot peening on fretting fatigue in Ti-6Al-4V coupons. Tribology International. Elsevier; 2009; 42(9): 1250–1262. Available at: DOI:10.1016/j.triboint.2009.04.005

106. Rodopoulos C a., Romero JS., Curtis S a., de los Rios ER., Peyre DP. Effect of Controlled Shot Peening and Laser Shock Peening on the Fatigue Performance of 2024-T351 Aluminum Alloy. Journal of Materials Engineering and Performance. 2003; 12(4): 414–419. Available at: DOI:10.1361/105994903770342944

107. Ma YE., Staron P., Fischer T., Irving PE. Size effects on residual stress and fatigue crack growth in friction stir welded 2195-T8 aluminium - Part II: Modelling. International Journal of Fatigue. 2011; 33(11): 1426–1434. Available at: DOI:10.1016/j.ijfatigue.2011.05.008

108. Hatamleh O., Lyons J., Forman R. International Journalof Fatigue Laser and shot peening effects on fatigue crack growth in friction stir welded 7075-T7351 aluminum alloy joints. 2007; 29: 421–434. Available at: DOI:10.1016/j.ijfatigue.2006.05.007

109. Hong Z., Chengye Y. Laser shock processing of 2024-T62 aluminum alloy. Materials Science and Engineering: A. 1998; 257(2): 322–327. Available at: DOI:10.1016/S0921-5093(98)00793-X

110. Tan Y., Wu G., Yang JM., Pan T. Laser shock peening on fatigue crack growth behaviour of aluminium alloy. Fatigue & Fracture of Engineering Materials & Structures. 2004; 27(8): 649–656. Available at: DOI:10.1111/j.1460-2695.2004.00763.x

111. Ren XD., Zhang YK., Zhang T., Jiang DW., Yongzhuo HF., Jiang YF., et al. Comparison of the simulation and experimental fatigue crack behaviors in the nanoseconds laser shocked aluminum alloy. Materials and Design. 2011; 32(3): 1138–1143. Available at: DOI:10.1016/j.matdes.2010.11.002

112. Ren NF., Yang HM., Yuan SQ., Wang Y., Tang SX., Zheng LM., et al. High temperature mechanical properties and surface fatigue behavior improving of steel alloy via laser shock peening. Materials and Design. Elsevier Ltd; 2014; 53: 452–456. Available at: DOI:10.1016/j.matdes.2013.07.009

113. Zhou JZ., Huang S., Zuo LD., Meng XK., Sheng J., Tian Q., et al. Effects of laser peening on residual stresses and fatigue crack growth properties of Ti – 6Al – 4V titanium alloy. Optics and Lasers in Engineering. Elsevier; 2014; 52: 189–194. Available at: DOI:10.1016/j.optlaseng.2013.06.011

114. Huang S., Zhou JZ., Sheng J., Luo KY., Lu JZ., Xu ZC., et al. Effects of laser peening with different coverage areas on fatigue crack growth properties of 6061-T6 aluminum alloy. 2013; 47: 292–299. Available at: DOI:10.1016/j.ijfatigue.2012.09.010

115. Huang S., Zhou JZ., Sheng J., Lu JZ., Sun GF., Meng XK., et al. Effects of laser energy on fatigue crack growth properties of 6061-T6 aluminum alloy subjected to multiple laser peening. 2013; 99: 87–100. Available at: DOI:10.1016/j.engfracmech.2013.01.011

116. Bergant Z., Trdan U., Grum J. Effects of laser shock processing on high cycle fatigue

crack growth rate and fracture toughness of aluminium alloy 6082-T651. INTERNATIONAL JOURNAL OF FATIGUE. Elsevier Ltd; 2016; 87: 444–455. Available at: DOI:10.1016/j.ijfatigue.2016.02.027

117. Chahardehi A., Brennan FP., Steuwer A. The effect of residual stresses arising from laser shock peening on fatigue crack growth. Engineering Fracture Mechanics. Elsevier Ltd; 2010; 77(11): 2033–2039. Available at: DOI:10.1016/j.engfracmech.2010.03.033

118. Zhang XQ., Li H., Yu XL., Zhou Y., Duan SW., Li SZ., et al. Investigation on effect of laser shock processing on fatigue crack initiation and its growth in aluminum alloy plate. Materials & Design (1980-2015). 2015; 65: 425–431. Available at: DOI:10.1016/j.matdes.2014.09.001

119. Zhang L., Lu JZ., Zhang YK., Luo KY., Zhong JW., Cui CY., et al. Effects of different shocked paths on fatigue property of 7050-T7451 aluminum alloy during two-sided laser shock processing. Materials and Design. 2011; 32(2): 480–486. Available at: DOI:10.1016/j.matdes.2010.08.039

120. Liu Q., Yang CH., Ding K., Barter SA., Ye L. The effect of laser power density on the fatigue life of laser-shock-peened 7050 aluminium alloy. 2007; : 1110–1124. Available at: DOI:10.1111/j.1460-2695.2007.01180.x

121. Ren XD., Zhan QB., Yang HM., Dai FZ., Cui CY., Sun GF., et al. The effects of residual stress on fatigue behavior and crack propagation from laser shock processing-worked hole. Materials and Design. Elsevier Ltd; 2013; 44: 149–154. Available at: DOI:10.1016/j.matdes.2012.07.024

122. Yang JM., Her YC., Han N., Clauer A. Laser shock peening on fatigue behavior of 2024-T3 Al alloy with fastener holes and stopholes. Materials Science and Engineering A. 2001; 298(1–2): 296–299. Available at: DOI:10.1016/S0921-5093(00)01277-6

123. Zhang XQ., Chen LS., Li SZ., Duan SW., Zhou Y., Huang ZL., et al. Investigation of the fatigue life of pre- and post-drilling hole in dog-bone specimen subjected to laser shot peening. Materials & Design. December 2015; 88: 106–114. Available at: DOI:10.1016/j.matdes.2015.08.136 (Accessed: 22 January 2016)

124. Giummarra C., Zonker H. Improving the fatigue response of aerospace structural joints. ICAF 2005 Proceedings. 2005; : 1–12. Available at: http://www.lambda-research.com/html/resources/258.pdf

125. Beghini M., Bertini L. Fatigue crack propagation through residual stress fields with closure phenomena. Engineering Fracture Mechanics. 1990; 36(3): 379–387. Available at: DOI:10.1016/0013-7944(90)90285-O

126. Ren XD., Zhang YK., Zhou JZ., Lu JZ., Zhou LC. Influence of compressive stress on stress intensity factor of hole-edge crack by high strain rate laser shock processing. Materials & Design. Elsevier Ltd; 2009; 30(9): 3512–3517. Available at: DOI:10.1016/j.matdes.2009.03.005

127. Zhang YK., Ren XD., Zhou JZ., Lu JZ., Zhou LC. Investigation of the stress intensity factor changing on the hole crack subject to laser shock processing. Materials and Design. Elsevier Ltd; 2009; 30(7): 2769–2773. Available at: DOI:10.1016/j.matdes.2008.09.033

128. Song PS., Wen CC. Crack closure and crack growth behaviour in shot peened fatigued

specimen. Engineering Fracture Mechanics. 1999; 63(3): 295–304. Available at: DOI:Doi 10.1016/S0013-7944(99)00010-7

129. Gozin MH., Aghaie-Khafri M. 2D and 3D finite element analysis of crack growth under compressive residual stress field. International Journal of Solids and Structures. Elsevier Ltd; 2012; 49(23–24): 3316–3322. Available at: DOI:10.1016/j.ijsolstr.2012.07.014

130. Lam YC., Lian KS. The effect of residual stress and its redistribution on fatigue crack growth. Theoretical and Applied Fracture Mechanics. 1989; 12: 59–66.

131. LaRue JE., Daniewicz SR. Predicting the effect of residual stress on fatigue crack growth. International Journal of Fatigue. 2007; 29(3): 508–515. Available at: DOI:10.1016/j.ijfatigue.2006.05.008

132. Schnubel D., Huber N. The influence of crack face contact on the prediction of fatigue crack propagation in residual stress fields. Engineering Fracture Mechanics. 2012; 84: 15–24. Available at: DOI:10.1016/j.engfracmech.2011.12.008

133. ASTM. Standard Test Method for Determining Residual Stresses by the Hole-Drilling Strain-Gauge Method. Standard Test Method E837-13a. 2013; 03: 1–16. Available at: DOI:10.1520/E0837-13A.2

134. Grant P V., Lord JD., Whitehead PS. Measurement Good Practice Guide No . 53 - Issue 2 The Measurement of Residual Stresses by the Incremental Hole Drilling Technique.

135. Prime MB. Cross-Sectional Mapping of Residual Stresses by Measuring the Surface Contour After a Cut. Journal of Engineering Materials and Technology. 2000; 123(2): 162–168. Available at: DOI:10.1115/1.1345526

136. Prime MB., Kastengren AL. Experimental and Applied Mechanics, Volume 4. 2017; 6: 233–250. Available at: DOI:10.1007/978-3-319-42028-8

137. Prime MB. Residual stress measurement by successive extension of a slot: the crack compliance method. Appl Mech Rev. 1999;

138. Fitzpatrick M., Fry A., Holdway P., Kandil F., Shackleton J., Suominen L. Determination of Residual Stresses by X-ray Diffraction - Issue 2. Measurement Good Practice Guide. 2005; (52): 74. Available at: DOI:10.1007/s00028-005-0194-y

139. Reimers W., Pyzalla AR., Schreyer A., Clemens H. Neutrons and Synchrotron Radiation in Engineering Materials Science. Reimers W, Pyzalla AR, Schreyer A, Clemens H (eds.) 2008.

140. Cohen ICNJB. Residual Stress: Measurement by Diffraction and Interpretation. New York: Springer Science+Business Media; 1987.

141. Dorman M., Toparli MB., Smyth N., Cini A., Fitzpatrick ME., Irving PE. Effect of laser shock peening on residual stress and fatigue life of clad 2024 aluminium sheet containing scribe defects. Materials Science and Engineering A. 2012; 548: 142–151. Available at: DOI:10.1016/j.msea.2012.04.002

142. Coratella S., Sticchi M., Toparli MB., Fitzpatrick ME., Kashaev N. Application of the eigenstrain approach to predict the residual stress distribution in laser shock peened AA7050-T7451 samples. Surface and Coatings Technology. Elsevier B.V.; 2015; 273(1): 39–49. Available at: DOI:10.1016/j.surfcoat.2015.03.026

143. Maawad E., Sano Y., Wagner L., Brokmeier HG., Genzel C. Investigation of laser shock peening effects on residual stress state and fatigue performance of titanium alloys. Materials Science and Engineering A. Elsevier B.V.; 2012; 536: 82–91. Available at: DOI:10.1016/j.msea.2011.12.072

144. Oliveira JP., Braz Fernandes FM., Miranda RM., Schell N. Residual Stress Analysis in Laser Welded NiTi Sheets Using Synchrotron X-ray Diffraction. Materials & Design. Elsevier Ltd; 2016; 100: 180–187. Available at: DOI:10.1016/j.matdes.2016.03.137

145. British Standard Institute Staff. Non-destructive testing - Standard test method for determining residual stresses by neutron diffraction. 2005; 2008: 1–2.

146. Moat RJ., Pinkerton AJ., Li L., Withers PJ., Preuss M. Residual stresses in laser direct metal deposited Waspaloy. Materials Science and Engineering A. 2011; 528(6): 2288–2298. Available at: DOI:10.1016/j.msea.2010.12.010

147. Pirling T., Bruno G., Withers PJ. SALSA-A new instrument for strain imaging in engineering materials and components. Materials Science and Engineering A. 2006; 437(1): 139–144. Available at: DOI:10.1016/j.msea.2006.04.083

148. Alcoa. ALCLAD Alloy 2024-T3 Data Sheet. 2008. Available at: https://www.arconic.com/mill_products/catalog/pdf/alloy2024techsheet.pdf (Accessed: 1 January 2017)

149. ASTM Standard. E112-12:Standard Test Methods for Determining Average Grain Size. ASTM International. 2012; E112-12: 1–27. Available at: DOI:10.1520/E0112-12.1.4

150. Shou WB., Yi DQ., Liu HQ., Tang C., Shen FH., Wang B. ScienceDirect Effect of grain size on the fatigue crack growth behavior of 2524-T3 aluminum alloy. 2016; 6. Available at: DOI:10.1016/j.acme.2016.01.004

151. ASTM Standard. E8/E8M - Standard Test Method for Tension Testing of Metallic Materials. ASTM International; 2013.

152. HI-LOK specification. 2014. Available at: http://www.lisi-aerospace.com/_layouts/CentralDocConnector/DCConnector.aspx?id=148&listId=HI-LOK PINS&downloaded=HL11&type=nominal_size_shank (Accessed: 18 April 2017)

153. Huntsman. Aerospace adhesives. 2000; (July): 1. Available at: https://www.silmid.com/MetaFiles/Silmid/0f/0fe65000-9138-4ebb-8e64-4829b5a52e13.pdf

154. Sheet SD. Naftoseal MC-630 C-2 Hardener Naftoseal MC-630 C-2 Hardener. 2014; (1907): 1–11.

155. Sheet SD. Naftoseal MC-630 C-2 Base Naftoseal MC-630 C-2 Base. 2014; (1907): 1–14.

156. Schajer G. Measurement of Non-Uniform Residual Stresses Using the Hole-Drilling Method. Part II—Stress Calculation Procedures. ASME. J. Eng. Mater. Technol. 1988; Available at: DOI:10.1115/1.3226059

157. Albertini G., Bruno G., Dunn BD., Fiori F., Reimers W., Wright JS. Comparative neutron and X-ray residual stress measurements on Al-2219 welded plate. Materials Science and Engineering: A. 1997; 224(1–2): 157–165. Available at: DOI:10.1016/S0921-5093(96)10546-3

158. Clausen B., Lorentzen T., Leffers T. Self-consistent modeling of the plastic deformation of f.c.c polycristals and its implications for diffraction measurements of internal stresses. Acta Materialia1. 1998; 9(9): 3087–3098.

159. Genzel C., Denks IA., Gibmeier J., Klaus M., Wagener G. The materials science synchrotron beamline EDDI for energy-dispersive diffraction analysis. Nuclear Instruments and Methods in Physics Research, Section A: Accelerators, Spectrometers, Detectors and Associated Equipment. 2007; 578(1): 23–33. Available at: DOI:10.1016/j.nima.2007.05.209

160. Schell N., King A., Beckmann F., Ruhnau HU., Kirchhof R., Kiehn R., et al. The High Energy Materials Science Beamline (HEMS) at PETRA III. AIP Conference Proceedings. 2010; 1234: 391–394. Available at: DOI:10.1063/1.3463221

161. Connors WC. Fatigue striation spacing analysis. Materials Characterization. 1994; 33(3): 245–253. Available at: DOI:10.1016/1044-5803(94)90046-9

162. Hershko E., Mandelker N., Gheorghiu G., Sheinkopf H., Cohen I., Levy O. Assessment of fatigue striation counting accuracy using high resolution scanning electron microscope. Engineering Failure Analysis. 2008; 15(1–2): 20–27. Available at: DOI:10.1016/j.engfailanal.2007.01.005

163. Goudar DM., Smith DJ. Validation of Mechanical Strain Relaxation Methods for Stress Measurement. Experimental Mechanics. 2013; 53(2): 267–286. Available at: DOI:10.1007/s11340-012-9638-9

164. Withers PJ., Preuss M., Steuwer A., Pang JWL. Methods for obtaining the strain-free lattice parameter when using diffraction to determine residual stress. Journal of Applied Crystallography. 2007; 40(5): 891–904. Available at: DOI:10.1107/S0021889807030269

165. Colegrove PA., Coules HE., Fairman J., Martina F., Kashoob T., Mamash H., et al. Microstructure and residual stress improvement in wire and arc additively manufactured parts through high-pressure rolling. Journal of Materials Processing Technology. Elsevier B.V.; 2013; 213(10): 1782–1791. Available at: DOI:10.1016/j.jmatprotec.2013.04.012

166. Ding J., Colegrove P., Mehnen J., Williams S., Wang F., Almeida PS. A computationally efficient finite element model of wire and arc additive manufacture. International Journal of Advanced Manufacturing Technology. 2014; 70(1–4): 227–236. Available at: DOI:10.1007/s00170-013-5261-x

167. Kostov V., Gibmeier J., Lichtenberg K., Wanner A. Effect of Preloading on Local Residual Stresses Induced by Laser Surface Hardening of Steel. Advanced Materials Research. 2014; 996: 562–567. Available at: DOI:10.4028/www.scientific.net/AMR.996.562

168. Melson JH. Fatigue Crack Growth Analysis With Finite Element Methods And A Monte Carlo Simulation. 2014; : 160.

169. Leski A. Implementation of the virtual crack closure technique in engineering FE calculations. Finite Elements in Analysis and Design. 2007; 43(3): 261–268. Available at: DOI:10.1016/j.finel.2006.10.004

170. Rybicki EF., Kanninen MF. A finite element calculation of stress intensity factors by a

modified crack closure integral. Engineering Fracture Mechanics. 1977; 9(4): 931–938. Available at: DOI:10.1016/0013-7944(77)90013-3

171. Lei Y., Dowd NPO., Webster GA. Fracture mechanics analysis of a crack in a residual stress field. 2000; : 195–216.

172. Jones KW., Dunn ML. Fatigue crack growth through a residual stress field introduced by plastic beam bending. Fatigue and Fracture of Engineering Materials and Structures. 2008; 31(10): 863–875. Available at: DOI:10.1111/j.1460-2695.2008.01274.x

173. Smyth N. Effect on Fatigue Performance of Residual Stress induced via Laser Shock Peening in Mechanically Damaged 2024- T351 Aluminium Sheet. Cranfield University; 2014.

174. Lynch SP. Progression markings, striations, and crack-arrest markings on fracture surfaces. Materials Science and Engineering A. 2007; 468–470(SPEC. ISS.): 74–80. Available at: DOI:10.1016/j.msea.2006.09.083

175. Withers PJ., Turski M., Edwards L., Bouchard PJ., Buttle DJ. Recent advances in residual stress measurement. International Journal of Pressure Vessels and Piping. 2008; 85(3): 118–127. Available at: DOI:10.1016/j.ijpvp.2007.10.007

176. Nau A., Scholtes B. Evaluation of the High-Speed Drilling Technique for the Incremental Hole-Drilling Method. Exp. Mech. 2013; 53(4): 531–542.

Appendix A: Example of implemented PI controller in Python

```
#  Result Reader
#  PI controller process, generating new input values for next iteration step
#import SIGINIShellScript
import sys
import os
from odbAccess import *
odb = openOdb(jobName+'/'+odbfileName+'.odb')
print ('odb opened')
#Target stress, variable, according to measurements
targetValues_S2 = [-117,-130,-130,-130,-130,-130,-130,-130,-130,-130,-130,-117]
#
l = 11
# output values
#S1_out = [0.00]*12
S2_out = [0.00]*12
#
for i in range(1579-1,1590):
  #S1_out[l] = odb.steps['Equilibrium_Step'].frames[1].fieldOutputs['S'].values[i].data[0]
  S2_out[l] = odb.steps['Equilibrium_Step'].frames[1].fieldOutputs['S'].values[i].data[1]
#
  l=l-1
# Question: If output values is matching with target values. If yes-STOP, IF no-CONTINUE
#print S1_out
print S2_out
fulfil = 1
for i in range(0,12):
  if not S2_out[i] > 0.95*targetValues_S2[i] and S2_out[i] < 1.05*targetValues_S2[i]:
     fulfil = 0
#
if fulfil==1:
  j = 11
# initial values from previous iteration step
  #S1_ini_inp = [0.00]*12
  S2_ini_inp = [0.00]*12
#
  for i in range(1579-1,1590):
    #S1_ini_inp[j] = odb.steps['Equilibrium_Step'].frames[0].fieldOutputs['S'].values[i].data[0]
    S2_ini_inp[j] = odb.steps['Equilibrium_Step'].frames[0].fieldOutputs['S'].values[i].data[1]
    #round
    #
```

```
    j=j-1
  #print S1_ini_inp
  print S2_ini_inp
# PI controller: Generating new input values for next iteration step
  #global S1
  #S1 = [0.00]*13
  #global S2
  S2 = [0.00]*12
#PI controller
  for k in range(0,12):
    #S1[k] = S1_ini_inp[k] + (targetValues_S1[k] - S1_out[k])
    S2[k] = S2_ini_inp[k] + (targetValues_S2[k] - S2_out[k])
  #print S1
  print S2
  #os.system('python LauncherJOBSIGINIv0.py')
  execfile('WRITE_SIGINI_130.py')
else:
  print ("JOB DONE!")
```

Appendix B: Example of SIGNI FORTRAN Subroutine

```
    SUBROUTINE   SIGINI                      C
    C                                            C
    C*******************************************************************
C
    C     Input Residual Stress to ABAQUS 2-D model                    C
    C                                            C
    C*******************************************************************
C
          SUBROUTINE SIGINI(SIGMA,COORDS,NTENS,NCRDS,NOEL,NPT,LAYER,
         1 KSPT,LREBAR,NAMES)
    C*******************************************************************
C
    C  SIGMA(1):  First stress component.                       C
    C  SIGMA(2):  Second stress component.                        C
    C  SIGMA(3):  Third stress component.                        C
    C  COORDS:    An array containing the initial coordinates of this     C
    C            point.                                      C
    C  NTENS:     Number of stresses to be defined, which depends on the  C
    C            element type.                                   C
    C  NCRDS:     Number of coordinates.                            C
    C  NOEL:      Element number.                               C
    C  NPT:       Integration point number in the element.              C
    C  LAYER:     Layer number (for composite shells and layered solids). C
```

```
C  KSPT:      Section point number within the current layer.          C
C  LREBAR:    Rebar flag. If LREBAR=1, the current integration point  C
C             is associated with element rebar. Otherwise, LREBAR=0.  C
C  REBARN:    Name of the rebar to which the current integration      C
C             point belongs, which is the name given on the *REBAR    C
C             option or on the *REBAR LAYER option. If no name was    C
C             given on the *REBAR option or on the *REBAR LAYER       C
C             option, this variable will be blank. This variable is   C
C             relevant only when LREBAR=1.                            C
C******************************************************************************C
C
      INCLUDE 'ABA_PARAM.INC'
C
      DIMENSION SIGMA(NTENS),COORDS(NCRDS)
      CHARACTER NAMES(2)*80
      DIMENSION X_FE(12),Y_FE(20),S2(12),READSTRESS(12)
C
      DATA X_FE/26.25,28.75,31.25,33.75,36.25,38.75,41.25,43.75,46.25,
     +   48.75,51.25,53.75/
      DATA Y_FE/1.25,3.75,6.25,8.75,11.25,13.75,16.25,18.75,21.25,
     +   23.75,26.25,28.75,31.25,33.75,36.25,38.75,41.25,43.75,
     +   46.25,48.75/
C
      DATA S2/-184.498100281,-199.343170166,-199.343170166,
     +   -199.858581543,-200.042831421,-199.864822388,
     +   -199.306594849,-198.363800049,-197.045562744,
     +   -195.374008179,-193.382095337,-178.112365723/
C
      DO I=1,NTENS
        SIGMA(I)=0.0
      ENDDO
C
      X = COORDS(1)
      Y = COORDS(2)
C
      DO I=1,12
       DO J=1,20
C
        IF ((X .EQ. X_FE(I)).AND.(Y .EQ. Y_FE(J))) THEN
          SIGMA(1) = 0.0
          SIGMA(2) = S2(I)
          SIGMA(3) = 0.0
          CONTINUE
        ENDIF
       ENDDO
      ENDDO
C
      END
```